Physical Layer Modelling of Optical Fibre Communication Systems in the Nonlinear Regime

Daniel Francis Semrau

A thesis submitted to the
University College London (UCL)
for the degree of
Doctor of Philosophy

Optical Networks Group
Department of Electronic & Electrical Engineering
University College London

1 March 2020

I, Daniel Francis Semrau, confirm that the work presented in this thesis is my own. Where information has been derived from other sources, I confirm that this has been indicated in the work.

To my mother ***Simone Semrau***
for her love and care.

To my father ***Marcel Semrau***
for keeping me grounded and his words of encouragement.

To my grandparents ***Helga & Dieter Ertel***
for their unconditional support, wherever I am in the world.

Abstract

This thesis describes substantial advances in the physical layer modelling of optical fibre communication systems in the nonlinear regime. Optical communication networks are currently limited by the optical Kerr nonlinearity which imposes an upper bound on the information throughput that can be achieved in such systems. Novel analytical descriptions of the fibre channel are required, to accurately predict this performance limitation and to develop effective algorithms to potentially mitigate it.

Novel, low complexity models are proposed, that predict the nonlinear distortions arising from the Kerr effect, particularly in the context of next-generation, ultra-wideband transmission systems, where optical bandwidths exceed the conventional 5 THz window (C-band). Over such wide bandwidths, the delayed nature of the nonlinear fibre response becomes significant, giving rise to inter-channel stimulated Raman scattering (ISRS). A new low-complexity model is derived: based on a first-order regular perturbation approach, it accurately describes the impact of ISRS on the nonlinear distortions. Furthermore, approximations in closed-form are proposed, enabling efficient system design and real-time optimisation. The results are significant to enable rapid modelling of ultra-wideband communication systems in the nonlinear regime.

Additionally, it is theoretically and experimentally shown that nonlinear interactions between signal and noise from the transceiver sub-system become performance limiting in nonlinearity-compensated fibre transmission. These interactions, which have previously been overlooked, challenge state-of-the art proposals on the optimal design of digital nonlinearity compensation algorithms, such as digital back-propagation. Enabled by the new model, a new optimal design is proposed suggesting substantial gains of around 25% in reach with respect to previously published designs. The research results can be directly applied to enable more rapid, efficient and accurate analysis and design of large bandwidth optical networks.

Impact statement

Optical fibre communications underpin the global telecommunication infrastructure, an integral and indispensable pillar of modern society. Capacity demands are forecast to continue to grow exponentially, driven mainly by cloud services, the internet of things and consumer appetite for high quality video-on-demand. Although optical fibres could adequately fulfill these capacity needs in the past, fundamental physical and information-theoretic limitations are imminent. The most significant limitation is imposed by the instantaneous nonlinear fibre response, the Kerr nonlinearity. The Kerr nonlinearity leads to signal distortions that potentially sets an upper limit on the achievable capacity using conventional transmission approaches. There are two main strategies that can be pursued to further increasing the throughput per individual fibre core to address future capacity demands. The first approach involves extending the optical bandwidth beyond the conventional transmission band to the ultra-wideband regime, utilising the entire low-loss region of single-mode fibres. The second method mitigates the nonlinear Kerr effect through digital signal processing, leading to noise reductions and higher achievable throughput for a given signal bandwidth.

In the research described in this thesis new analytical models are proposed that provide physical insight and allow the quantification of nonlinear distortions in the ultra-wideband transmission regime and regimes where the Kerr effect is partly mitigated.

In the ultra-wideband regime, the delayed nature of the nonlinear fibre response is significant, giving rise to inter-channel stimulated Raman scattering (ISRS). ISRS amplifies redistributed power within the optical spectrum during propagation, imposing new challenges on system design and operation. For the first time, the Gaussian Noise (GN) model, a widely used tool to predict transmission performance, was extended to account for the impact of ISRS on the nonlinear distortions. This new analytical result is a significant contribution in the field of nonlinear transmission modelling and paramount in the design and operation of next-generation systems. Additionally, closed-form approximations were derived that enable real-time performance estimates for uniform and shaped quadrature ampli-

tude modulation formats. Such closed-form formulas are vital for the optimisation and design of physical layer-aware optical networks. The proposed models are validated by experiments over an optical bandwidth of 9 THz, representing the first experimental investigation of ISRS on the nonlinear transmission performance for coherent systems.

Another major contribution of this thesis is in the field of digital nonlinearity compensation (NLC). When nonlinear distortions are mitigated though digital signal processing, nonlinear signal noise interactions (NSNI) become performance limiting. Contrary to the established literature, it was shown that NSNI between the signal and co-propagating amplified-spontaneous emission (ASE) noise are not sufficient to predict performance limitations in systems that deploy NLC. A new formula is derived, capable of predicting the impact of NSNI between the signal and transceiver noise. Transceiver noise originates from any non-ideal transmitter and receiver, arising from the optical as well as the digital domain. The derived formula closed the performance estimation gap between theoretical predictions and NLC gains that were observed in state-of-the art experiments. Furthermore, established schemes on the optimum ratio between digital pre-distortions and back-propagation are challenged and improved designs are proposed, yielding gains of around 25% in reach. The new analytical model can be used to predict ultimate capacity limits in optical fibre transmission systems.

Overall, the results obtained in the course of the PhD research led to 33 publications, but most importantly, can be used in the design of future optical communication systems. A joint experiment performed with XTera, utilising the models described in this thesis, led to a record transmission result (item 23. in List 1.4). The research led to a IEEE Photonics Society award, given to the top 10 PhD students in the world. The research was also top-scored in the 45th European Conference on Optical Communication ([P19] in Sec. 1.4).

Acknowledgements

This thesis is a culmination of years of aspiration and perseverance none of which would have been conceivable without the individuals who have challenged, supported and stuck with me along the way. Although it is impossible to name every person who has mentored or otherwise influenced me during my education, I would like to acknowledge the following people for their contributions.

First and foremost I wish to express my sincere gratitude to my supervisor, Polina Bayvel, for providing me with steadfast support, guidance and faith in my ideas throughout my PhD research. Her enthusiasm for new frontiers in optical networks and tireless dedication to my personal success has not only made my studies possible, but worthwhile.

I must also voice my appreciation for Robert Killey, for his invaluable research advise and open door policy. His counsel about nonlinear fibre optics have left their mark on my work indelibly.

In addition to my advisors, I would like to recognise the many friends and colleagues I have known during my years as a member of the Optical Networks Group (ONG) team at UCL. I am grateful to Domaniç Lavery and Lidia Galdino for their constructive and engaging discussions about optical transmission experiments, the scientific community and the trappings of British politics. Their brilliant input has been indispensable on countless projects and shaped me as a researcher. Eric Sillekens, my friend and desk mate for the last four years, has been a constant source of insight and my first line of defense in the face of bothersome challenges with CentOS Linux and TikZ. Gabriel Saavedra not only shared my fondness for Mate beverages, but also provided crucial experimental validations for my proposed models, adding 'points on top of lines'. Sezer Erkılınç for his advise and cheerful conversations over numerous pints. Xianhe Yangzhang shared a flat with me on Fitzjohns Avenue for a significant portion of my PhD studies, which made working on weekends much less of a chore. To the rest of the team in office 808, it has been a tremendous pleasure to work amongst your collective expertise, especially on days I managed to attend work in person.

My gratitude is extended to Keren Bergman and Madeleine Glick from

Columbia University for hosting me in their group and giving me the opportunity to work on the cutting edge of data centre and supercomputer architectures.

I would also like to thank Piero Castoldi from Scuola Superiore Sant'Anna, Keith Blow from Aston University and Ken-ichi Kitayama, Akihiro Maruta and Yuki Yoshida from Osaka University for their academic direction and genuine hospitality during my masters programme terms abroad. I must also thank Nouman Malik for our road trips into the blue during reading weeks and all the stories that I will never forget.

From Technische Universität Berlin where I completed my undergraduate studies, I would like to sincerely thank Klaus Petermann, Stefan Warm and Georg Rademacher for nurturing my interest in 'Hochfrequenztechnik 1' into a lifelong passion for optical communications.

I am endlessly grateful for the opportunities that I have been given which profoundly enriched my professional and personal life.

Above all I am deeply indebted to my family for their constant encouragement in all my pursuits. The loving support of my parents Simone and Marcel, and my grandparents Helga and Dieter has inspired everything I have accomplished. Likewise I want to thank my girlfriend Emily, for her years of patience and convincing attempts to make even the most minute details of my research appear interesting to her. This thesis is dedicated to all of you.

Contents

List of Figures

List of Tables

Chapter 1

Introduction

The internet has revolutionised the communications and computer world like no other technology before. It is at once a world-wide broadcasting capability, a powerful tool for information dissemination, and a medium for collaboration and interaction between individuals and digital devices irrespective of their geographic location.

Since its introduction, the traffic carried by the internet protocol (IP) has been experiencing astonishing growth rates. It is forecast that the global internet traffic will reach 3.3 zettabytes ($3.3 \cdot 10^{21}$ bytes) by the year 2021 [23]. According to this prediction, the IP traffic will have grown at a compound annual growth rate of 24% from 2016 to 2021. The largest portion of the traffic carries video data with 82% of all consumer traffic by 2021, of which 26% will be internet to TV videos and 13% are live internet videos. Furthermore, traffic from conventional computers will be overtaken by smartphone traffic and the number of devices will be three times as high as the global population in 2021.

Optical fibre communications have supported this unprecedented traffic growth over the past three decades and now stands alone as the enabling technology that underpins the global information infrastructure. Capacity of lightwave communication systems increased from 100 Mb/s in 1970 to 10 Tb/s in present day commercial systems. The technical milestones that unlocked the feasibility of these high rates were wavelength division multiplexing (WDM), improved fibre design and fabrication, optical amplification, coherent detection and digital signal processing.

The evolution of optical fibre capacity, demonstrated in state-of-the art laboratories, is shown in Fig. 1.1a) for trans-Atlantic distances of at least 6000 km. The results were taken from [1–9]. Fig. 1.1 shows significant capacity increases over the years from 2011 to 2015. In subsequent years, the optical fibre capacity appears to have saturated to throughputs of around 70 Tbit/s. The corresponding optical bandwidths used for the same experimental demonstrations are shown in

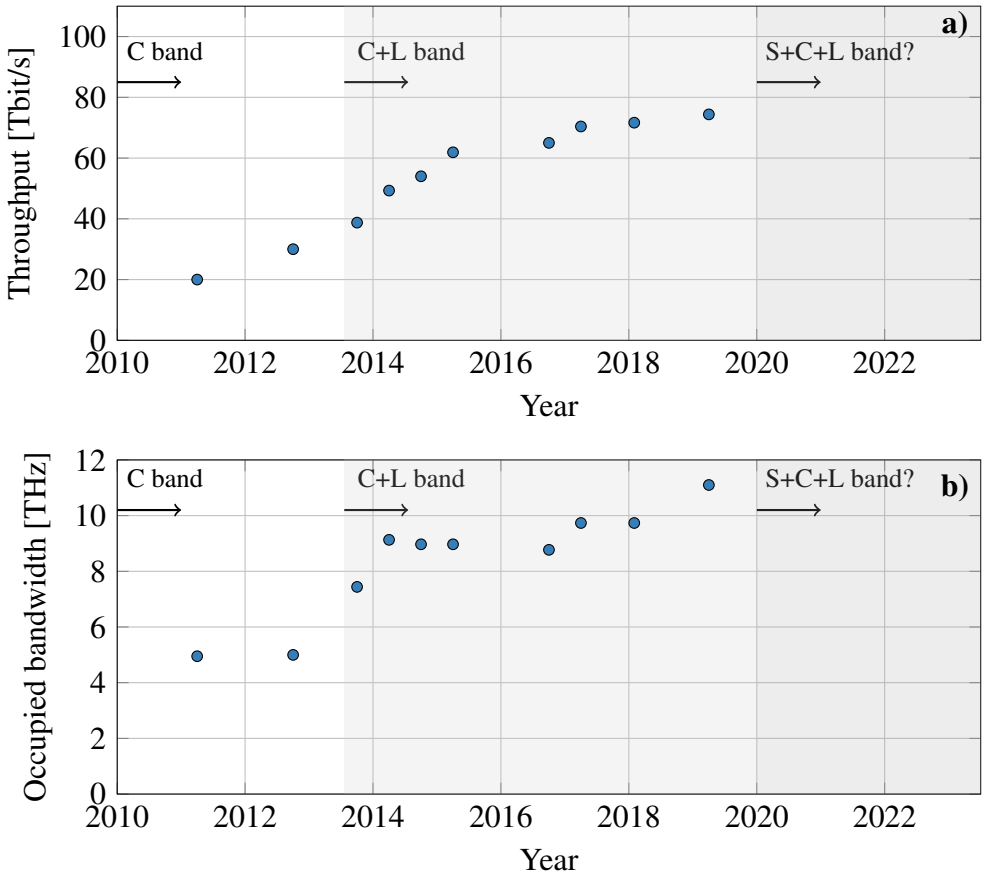

Figure 1.1: Laboratory throughput demonstrations together with their respective optical bandwidth used taken from [1–9]. Only experiments with trans-Atlantic transmission distances of at least 6000 km are shown.

Fig. 1.1b). Up to 2013, state-of-the art experiments utilised the C-band, a 5 THz low-loss transmission window in optical fibres, while subsequent demonstrations utilise the entire C+L band , an extended 10 THz transmission window. Fig. 1.1b) suggests that most capacity gains over trans-Atlantic distances have been achieved by extending the optical bandwidth beyond the C-band. Erbium-doped fibre amplifiers in the L-band (a transmission band ranging from 1565-1625 nm) and Raman fibre amplifiers have made it possible to extend the usable fibre bandwidth.

While C+L band transmission (10.8 THz optical bandwidth) was demonstrated in laboratory experiments since 2014, most terrestrial networks are still operating within the C-band only. Fig. 1.1 shows that the network capacity can be approximately doubled, when these networks are upgraded to the C+L band. However, beyond C-band transmission, the delayed nature of the nonlinear fibre response becomes significant. A non-instantaneous nonlinear fibre response, with respect to the optical field, results in inter-channel stimulated Raman scattering. ISRS effectively transfers power from high frequencies to lower frequencies during propaga-

tion, causing signal distortions and imposing new challenges on system design and operations. Current analytical descriptions of nonlinear distortions do not account for ISRS as it has been negligible over the C-band. However, for transmission bandwidths beyond the C-band, complex interactions between the instantaneous and the delayed part of the fibre response must be analytically modelled. This is necessary because numerical simulations become unmanageable in the ultra-wideband regime even using state-of-the art graphical processing units (GPUs). Furthermore, an accurate understanding of these new challenges is key to integrate the gains, achieved in laboratory setups, into heterogeneous and less controllable optical network environments. Better understanding of the nonlinear fibre response and more accurate mathematical modelling in ultra-wideband regimes will also result in better engineered system designs. Additionally, they will help answer questions on how much gain can be achieved by further increasing the optical bandwidth to the S+C+L band (15-20 THz) and how potential gains can be achieved and maximised.

Alternatively, the throughputs can be further increased by improved digital signal processing that reduce the distortions due to the nonlinear fibre response. While some of the experiments shown in Fig. 1.1 deploy advanced DSP to mitigate fibre nonlinearity, there were still large discrepancy between the theoretically achievable gains [24, 25] and the ones achieved in experiments. This further suggests that the fibre capacity can be increased by improved and advanced digital signal processing.

This thesis will explore the challenges that arise with ultra-wideband transmission systems with special emphasis on distortions caused by fibre nonlinearity. New analytical models are proposed that accurately describe the nonlinear distortions that are jointly imposed by the Kerr nonlinearity and ISRS. Furthermore, closed-form approximations are derived that enable performance estimations carried out within micro seconds. These formulas allow efficient system design and the real-time optimisation of ultra-wideband optical networks.

The second major contribution of this research is the discovery of fundamental limitations when nonlinear distortions are mitigated by means of digital signal processing. Through state-of-the art experiments and accurate modelling, it is shown that nonlinear interactions between transceiver (TRX) noise and signal are performance limiting when NLC is applied. These interactions have been overlooked in the established literature and based on the new model, improved NLC designs are proposed.

Overall, this PhD thesis proposes novel mathematical models that enable to quantify achievable gains and to derive optimum system design and operation for future optical fibre communication networks.

1.1 Research problem

The optical Kerr effect represents a significant physical limitation currently imposed on optical signals propagating through optical fibres. For additive white Gaussian noise (AWGN) channels, an idealised description suitable to model numerous real world communication channels, the throughput is monotonically increasing with the SNR and can be scaled arbitrarily by increasing the signal power. However, the optical Kerr effect imposes distortions on the propagating lightwave that are proportional to the cube of the signal power itself. The optical Kerr effect denotes the dependence of the refractive index on the electrical field itself. The refractive index describes the ratio of the phase velocity of the lightwave in a material compared to a vacuum. As a result, the SNR cannot be arbitrarily increased by simply increasing the signal power and the achieved throughput is fundamentally limited. Due to the monotonic increase of nonlinear distortions as a function of launch power, fibre systems exhibit an optimum launch power giving a maximum achievable SNR (for a given link, TRX and digital signal processing (DSP)). Most optical communication systems operate at this optimum operation point leaving little room for fundamental breakthroughs using conventional approaches and techniques. According to Shannon's celebrated capacity formula [26], there are only two strategies in order to increase the throughput that can be delivered by optical fibres. First, increasing the number of independent communication channels and, second, increasing the SNR per channel. Both strategies are covered in this thesis and addressed in more detail in the following.

The first can be achieved by transmitting more independent channels at different wavelengths, denoted as WDM. However, as the Kerr effect is dependent on the total launch power, more WDM channels lead to larger nonlinear distortions. However, the overall gain in capacity is positive as the increasing nonlinear penalties do not outweigh the throughput gains of the additional channels. Most systems currently utilise the entire C-band window (5 THz) for transmission, accommodating hundreds of wavelengths. However, it is not clear up to which optical bandwidths this trade-off remains beneficial. Diminishing returns may arise due to additional effects, namely inter-channel stimulated Raman scattering, that scales exponentially with optical bandwidth. ISRS becomes significant beyond C-band transmission and before the research described in this thesis, there were no efficient ways of predicting the nonlinear distortions due to ISRS. Split-step simulations, accurate numerical simulations of fibre propagation, quickly become unmanageable due to the extensive (and required) use of Fourier transforms. Although, accurate, low complexity, first-order perturbation models exist for C-band transmission systems [20, 27–31, 31–34], they are not suitable for ultra-wideband transmission, as

they do not account for ISRS. On the other hand, early studies have been carried out predicting power limitations due to ISRS in the context of non-coherent transmission [35–38]. However, those studies neglected the impact of ISRS on nonlinear distortions and thus cannot be applied to state-of-the art coherent transmission systems. Thus, new efficient modelling frameworks are required that efficiently and accurately predict the nonlinear performance in systems that operate beyond the C-band. They can then be applied to system analysis and operation and for the evaluation of potential gains when extending the optical bandwidth beyond 5 THz.

The second way to increase the throughput is by mitigating the nonlinear distortions and, hence, increase the SNR of a particular WDM channel. While the nonlinear distortions cannot be mitigated entirely, the maximum achievable SNR can be increased with advanced DSP (e.g., implementing digital NLC) which leads to higher capacity. The reason that the nonlinear distortions cannot be entirely compensated is due to NSNI. Experiments and theoretical investigations suggest that those fundamental limitations are set by nonlinear mixing between the signal and co-propagating ASE noise, originating in periodically placed, optical amplifiers [25, 39–42]. Mathematical models have been developed to describe those interactions [25, 41] and optimum digital NLC structures have been derived, by splitting the digital compensation between transmitter and receiver [41, 43]. However, the theoretically predicted gains have not been matched by state-of-the art experiments [44–46] and forecast gains expected from splitting the digital NLC algorithm evenly between transmitter and receiver have not been experimentally shown. This suggests that the current models do not accurately represent all impairments arising in systems that utilise nonlinearity compensation . An accurate model for such systems is vital for accurate gain predictions and system (re-)design.

The overall goal of this thesis was to develop accurate and efficient models for the predictions of performance limitations in next-generation optical communication networks. Particular emphasis was drawn to nonlinear distortions in the context of the two main strategies that potentially satisfy future capacity demand, the utilisation of larger optical bandwidths and advanced DSP for nonlinearity mitigation.

1.2 Thesis outline

The remainder of this thesis is organised as follows.

Chapter 2 introduces the main theoretical literature that is required for the later chapters. Fundamental concepts of digital communications are described as well as the most relevant propagation effects in optical fibres. Furthermore, Ch. 2 describes existing, state-of-the art modelling approaches in the context of coherent

optical communication.

Chapter 3 proposes new mathematical models that are able to predict distortions arising from the nonlinearities. The analytical results extend the Gaussian Noise model and account for inter-channel stimulated Raman scattering, significant for ultra-wideband transmission systems. The proposed models are validated by numerical simulations as well as by state-of-the art experiments.

Chapter 4 introduces closed-form approximations of the results derived in Chapter 3. Formulae are derived for the Gaussian contribution as well as for the modulation format dependent contribution of the nonlinear distortions. Additionally, strategies are discussed that enable those results to be applied to ultra-wideband systems, covering the entire S+C+L band (20 THz). All results have been validated by numerical simulations in point-to-point transmission and mesh optical network scenarios.

Chapter 5 reviews fundamental limitations in transmission systems that deploy digital nonlinearity compensation. It is shown that, contrary to the previous belief, nonlinear interactions between transceiver noise and the signal become performance limiting. A new formula is proposed to accurately model such nonlinear interactions. The model is supported by numerical and experimental results. Enabled by the new formula, new digital nonlinearity compensation approaches are proposed. In particular, optimum split ratios between digital pre-compensation and back-propagation are identified, outperforming previously reported schemes.

Finally, a summary of the thesis is given in Chapter 6, highlighting the most important contributions, and suggesting future work directions.

1.3 Key contributions

The key contributions of this thesis are listed below. The referencing in this Section refers to the list of publications as a result from this PhD research, shown in Sec. 1.4.

- The Gaussian Noise model in integral form was extended to account for inter-channel stimulated Raman scattering. The results represent the first model able to predict nonlinear distortions in the presence of ISRS. The approach was enabled by approximating the signal power profile by exponential decays. Numerical validations were carried out, showing agreements of 0.2 dB in nonlinear SNR. The work is described in Chapter 3; and the results led to the publication of [P13]. The results were further used in the publications [P8, P22, P29].

- The new model, proposed in Sec. 3.2 was validated by experimental results.

The transmitted optical bandwidth was 9 THz, occupying both the C-and L-band, and an average deviation of 0.4 dB was found between experiment and modelling results. The experiment was the first experimental investigation of the effect of inter-channel stimulated Raman scattering on the signal-to-noise ratio in ultra-wideband coherent transmission systems. The work is described in Sec. 3.3; and the results led to the publication of [P29].

- The model proposed in Sec. 3.2 was used to estimate the achievable rate degradation, due to ISRS, when the optical bandwidth is extended beyond the C-band to the entire S+C+L band (20 THz). It was found that, although ISRS degrades the capacity by around 40%, this degradation can be reduced to only 10% using adaptive modulation formats and code rates for every channel. The work was the first investigation of the impact of ISRS on the capacity of coherent optical transmission systems. The work is described in Sec. 3.4; and the results were published in [P13].

- The Gaussian Noise model was rederived, denoted as ISRS GN model, in order to account for arbitrary (as opposed to frequency independent) signal power profiles. This enables the Gaussian Noise model to be applied in regimes with strong power transfer due to ISRS as well as in distributed Raman amplified systems. The work represents an improved formalism with respect to the model in Sec. 3.2. The result was the first exact, first-order perturbation analysis of the Manakov equation, describing pulse propagation in fibres, with arbitrary signal power profiles and Gaussian constellations. Furthermore, analytical results were derived based on available closed-form approximations of ISRS. Numerical validations were carried out with negligible deviation compared to the proposed model. The work is described in Sec. 3.5; and the results led to the publication of [P8]. The results were further used in the publications of [P2, P4, P6, P19, P20, P22, P24, P26, P27].

- A comparison was performed between the analytical models derived in Sec. 3.2 and the ISRS GN model. Excellent agreements were found, with deviations of less than 0.1 dB, for ISRS power transfers of up to 6.5 dB (launch power of 4 dBm/ch.). However for stronger power transfers, the ISRS GN model was found to be more accurate with excellent agreements (<0.1 dB) compared to numerical simulations. The work is described in Sec. 3.6; and the results led to the publication of [P29].

- The ISRS GN model was extended to account for variably loaded spans in an analytical form. The main contribution was an analytical integral expression

(3.11) that can be applied in the modelling of mesh optical networks, where different optical spectra are launched into different network edges. The results were compared to numerical simulations of Gaussian signals, uniform 64-quadrature amplitude modulation (QAM) and Maxwell-Boltzmann shaped 64-QAM. Average deviations of 1.1 dB and 0.6 dB in nonlinear penalties were found comparing the modelling results with uniform and shaped 64-QAM, respectively. The work is described in Sec. 3.7; and the results led to the publication of [P27]. The results in this work were further used in the publications of [P4, P6, P19].

- A closed form approximation of the ISRS GN model was derived. The result was a closed-form formula that estimated the amount of nonlinear distortions in the presence of ISRS, enabling ultra-wideband performance estimates in real-time. The approach was enabled by a first-order description of ISRS. The work represents the first closed-form formula that accounts for ISRS, arbitrary launch power distributions and the dispersion slope. The formula was compared to numerical simulations over the entire C+L band and a maximum deviation of 0.3 dB is found. The work is described in Sec. 4.1; and the results were published in [P6]. The results in this work were further used in the publications of [P3, P4, P19, P22].

- The ISRS GN model in closed-form, derived in Sec. 4.1 was extended to correct for the modulation format dependent contribution to the nonlinear distortions. In particular, the result was a closed-form formula correcting for the modulation format dependence in the cross-phase modulation contributions of the nonlinear distortions. Numerical validations showed average deviations between model and simulations of 0.3 dB and 0.2 dB for 16-QAM in low dispersive and high dispersive fibres, respectively. The analytical result was the first analytical investigation of the modulation format dependence in the presence of ISRS and the first closed-form formula correcting for it. The work is described in Sec. 4.2; and the results led to the publication of [P4]. The results in this work were further used in the publication of [P19].

- A strategy was proposed in order to apply the ISRS GN model to optical bandwidths beyond 15 THz. The ISRS GN model is based on a triangular approximation of ISRS and only valid to bandwidths of up to 15 THz. However, enabled by parameter matching, the formula can be applied to bandwidths beyond 15 THz, where currently no analytical solutions of the Raman gain equations exist. The work enables real-time performance estimates and opti-

misation of transmission systems covering SCL band (20 THz). The results were the first closed-form formula that can be applied to SCL band systems and the first numerical validation of first-order perturbation approaches over 20 THz. The work is described in Sec. 4.3; and the results were published in [P19] and rated 'top-scored' in the peer-review process.

- It was shown that nonlinear interactions between transceiver noise and the signal are significant in transmission systems that exhibit digital nonlinearity compensation. The main contribution was a new formula that predicts the nonlinear distortions arising from these residual interactions. The model was compared to numerical and experimental results with good agreement between the theoretical predictions and the experiment. The work is described in Sec. 5.1; and the results led to the publication of [P15]. The results in this work were further used in the publications [P9, P21, P25, P31].

- The new formula, derived in Sec. 5.1, was used to derive an optimum scheme for digital nonlinearity compensation, deriving the optimum split ratio between digital pre-compensation and digital back-propagation. It was shown that this ratio depends on the transmission distance and the noise that is introduced by the transmitter and receiver. The work disproves previous designs, where it was suggested that the optimum split ratio is always half. The new design yields reach improvements of around 25%. The work is described in Sec. 5.2; and the results were published in [P9].

1.4 List of publications

The following publications are the result of the work carried out as part of the PhD research programme

Journal papers

(P1) M. Ionescu, D. Lavery, A. Edwards, E. Sillekens, **D. Semrau**, L. Galdino, R. I. Killey, W. Pelouch, S. Barnes, P. Bayvel, "74.38 Tb/s Transmission Over 6300 km Single Mode Fibre Enabled by C+ L Amplification and Geometrically Shaped PDM-64QAM", IEEE/OSA *Journal of Lightwave Technology* Early Access (2019).

(P2) L. Galdino, **D. Semrau**, M. Ionescu, A. Edwards, W. S. Pelouch, S. R. Desbruslais, J. James, E. Sillekens, D. Lavery, S. Barnes, R. I. Killey, P. Bayvel, "Study on the Impact of Nonlinearity and Noise on the Performance of High-Capacity Broadband Hybrid Raman-EDFA Amplified System", IEEE/OSA *Journal of Lightwave Technology* Early Access (2019).

(P3) A. Mitra, **D. Semrau**, N. Gahlawat, A. Srivastava, P. Bayvel, and A. Lord, "Effect of reduced link margins on C+L band elastic optical networks", IEEE/OSA *Journal of Optical Communications and Networking* **11** 10, pp. C86-C93 (2019).

(P4) **D. Semrau**, E. Sillekens, R. I. Killey, P. Bayvel, "A Modulation Format Correction Formula for the Gaussian Noise Model in the Presence of Inter-Channel Stimulated Raman Scattering", IEEE/OSA *Journal of Lightwave Technology* **37** 19, pp. 5122-5131 (2019).

(P5) W. Yi, Z. Li, M. S. Erkılınç, D. Lavery, E. Sillekens, **D. Semrau**, Z. Liu, P. Bayvel, R. I. Killey, "Performance of Kramers-Kronig Receivers in the Presence of Local Oscillator Relative Intensity Noise", IEEE/OSA *Journal of Lightwave Technology* **37** 13, pp. 3035-3043 (2019).

(P6) **D. Semrau**, R. I. Killey, P. Bayvel, "A closed-form approximation of the Gaussian Noise model in the presence of inter-channel stimulated Raman scattering", IEEE/OSA *Journal of Lightwave Technology* **3**7 9, pp. 1924-1936 (2019).

(P7) T. Sherborne, B. Banks, **D. Semrau**, R. I. Killey, P. Bayvel, D. Lavery, "On the Impact of Fixed Point Hardware for Optical Fiber Nonlinearity Compensation

Algorithms", IEEE/OSA *Journal of Lightwave Technology* **36** 20, pp. 5016-5022 (2018).

(P8) **D. Semrau**, R. I. Killey, P. Bayvel, "The Gaussian Noise Model in the Presence of Inter-channel Stimulated Raman Scattering", IEEE/OSA *Journal of Lightwave Technology* **36** 14, pp. 3046-3055 (2018).

(P9) **D. Semrau**, D. Lavery, L. Galdino, R. I. Killey, P. Bayvel, "The Impact of Transceiver Noise on Digital Nonlinearity Compensation", IEEE/OSA *Journal of Lightwave Technology* **36** 3, pp. 659-702 (2018).

(P10) G. Saavedra, M. Tan, D. Elson, L. Galdino, **D. Semrau**, M. Iqbal, I. Phillips, P. Harper, A. Ellis, B. C. Thomsen, D. Lavery, R. I. Killey, "Experimental Analysis of Nonlinear Impairments in Fibre Optic Transmission Systems up to 7.3 THz", IEEE/OSA *Journal of Lightwave Technology* **35** 21, pp. 4809-4816 (2017).

(P11) **D. Semrau**, G. Saavedra, D. Lavery, R. I. Killey, P. Bayvel, "A Closed-Form Expression to Evaluate Nonlinear Interference in Raman-Amplified Links", IEEE/OSA *Journal of Lightwave Technology* **35** 19, pp. 4316-4328 (2017).

(P12) D. Elson, G. Saavedra, K. Shi, **D. Semrau**, L. Galdino, R. I. Killey, B. C. Thomsen, P. Bayvel, "Investigation of Bandwidth Loading in Optical Fibre Transmission using Amplified Spontaneous Emission Noise", OSA *Optics Express* **25** 16, pp. 19529-19537 (2017).

(P13) **D. Semrau**, R. I. Killey, P. Bayvel, "Achievable Rate Degradation of Ultra-Wideband Coherent Fiber Communication Systems due to Stimulated Raman Scattering", OSA *Optics Express* **25** 12 pp. 13024-13034 (2017).

(P14) G. Saavedra, **D. Semrau**, L. Galdino, R. I. Killey, P. Bayvel, "Digital Back-Propagation for Nonlinearity Mitigation in Distributed Raman Amplified Links", OSA *Optics Express* **25** 5, pp. 5431-5439 (2017).

(P15) L. Galdino, **D. Semrau**, D. Lavery, G. Saavedra, C. Czegledi, E. Agrell, R. I. Killey, P. Payvel, "On the Limits of Digital Back-Propagation in the Presence of Transceiver Noise", OSA *Optics Express* **25** 4, pp. 4564-4578 (2017).

(P16) D. Lavery, R. Maher, G. Liga, **D. Semrau**, L. Galdino, P. Bayvel, "On the Bandwidth Dependent Performance of Split Transmitter-Receiver Optical Fiber Nonlinearity Compensation", OSA *Optics Express* **25** 4, pp. 4554-4563 (2017).

(P17) T. Xu, N. Shevchenko, D. Lavery, **D. Semrau**, G. Liga, A. Alvarado, R. I. Killey, P. Bayvel, "Modulation Format Dependence of Digital Nonlinearity Compensation Performance in Optical Fibre Communications Systems", OSA *Optics Express* **25** 4, pp. 3311-3326 (2017)

(P18) **D. Semrau**, T. Xu, N. Shevchenko, M. Paskov, A. Alvarado, R. I. Killey, P. Bayvel, "Achievable Information Rates Estimates in Optically Amplified Transmission Systems using Nonlinearity Compensation and Probabilstic Shaping", OSA *Optics Letters* **42** 1, pp. 121-124 (2017).

Peer reviewed conference papers published in conference proceedings

(P19) **D. Semrau**, L. Galdino, E. Sillekens, D. Lavery, R. I. Killey, P. Bayvel, "Modulation Format Dependent, Closed-Form Formula for Estimating Nonlinear Interference in S+C+L Band Systems", *Proceedings of European Conference on Optical Communications (ECOC)*, Dublin, Ireland, 2019.

(P20) L. Galdino, **D. Semrau**, P. Bayvel, "Candidate Technologies for High-Capacity Optical Communication Systems", *Advanced Photonics Congress (AP)*, San Francisco, United States, 2019.

(P21) D. J. Elson, **D. Semrau**, H. Takahashi, T. Tsuritani, "Analytical Model for Transmission Performance of Single Mode Multicore Fibre with Nonlinearity Compensation", *OptoElectronics and Communications Conference (OECC)*, Fukuoka, Japan, 2019.

(P22) **D. Semrau**, R. I. Killey, P. Bayvel, "Overview and Comparison of Nonlinear Interference Modelling Approaches in Ultra-Wideband Optical Transmission Systems", *International Conference on Transparent Optical Networks (ICTON)* (invited), Anger, France, 2019.

(P23) M. Ionescu, D. Lavery, A. Edwards, E. Sillekens, L. Galdino, **D. Semrau**, R. I. Killey, W. Pelouch, S. Barnes, P. Bayvel, "74.38 Tb/s Transmission Over 6300 km Single Mode Fiber with Hybrid EDFA/Raman Amplifiers", *Proceedings of Optical Fiber Communication Conference (OFC)*, San Diego, United States, 2019.

(P24) L. Galdino, **D. Semrau**, P. Bayvel, "Breaking the Transmission Barriers in Ultra-broadband High-capacity Optical Fiber Transmission Systems", *Latin America Optics and Photonics Conference* (invited), Tu2E. 2, Lima, Peru 2018.

(P25) L. Galdino, **D. Semrau**, P. Bayvel, "The Impact of Transceiver Limited SNR on Digital Back Propagation Performance", *IEEE Photonics Society Photonics Conference (IPC)* (invited), Reston, United States 2018.

(P26) L. Galdino, **D. Semrau**, E. Sillekens, D. Lavery, R. I. Killey, P. Bayvel, "Impact of Transceiver Subsystems on High-Capacity Optical Transmision", *Signal Processing in Photonic Communiations (SPPCom)* (invited), Zurich, Switzerland, 2018.

(P27) **D. Semrau**, E. Sillekens, R. I. Killey, P. Bayvel, "The ISRS GN Model, an Efficient Tool in Modeling Ultra-Wideband Transmission in Point-to-Point and Network Scenarios", *Proceedings of European Conference on Optical Communications (ECOC)*, Tu4G.6, Rome, Italy, 2018.

(P28) E. Sillekens, **D. Semrau**, D. Lavery, P. Bayvel, R. I. Killey, "Experimental Demonstration of Geometrically-Shaped Constellations Tailored to the Nonlinear Fibre Channel", *Proceedings of European Conference on Optical Communications (ECOC)* , Tu3G.3, Rome, Italy, 2018.

(P29) G. Saavedra, **D. Semrau**, M. Tan, M. Iqbal, D. Elson, L. Galdino, P. Harper, R. I. Killey, P. Bayvel, "Inter-channel Stimulated Raman Scattering and its Impact in Wideband Transmission", *Proceedings of Optical Fiber Communication Conference (OFC)*, Th1C.3, San Diego, United States, 2018.

(P30) E. Sillekens, **D. Semrau**, G. Liga, N. Shevshenko, Z. Li, A. Alvarado, P. Bayvel, R. I. Killey, D. Lavery, "A Simple Nonlinearity-Tailored Probabilistic Shaping Distribution for Square QAM", *Proceedings of Optical Fiber Communication Conference (OFC)*, M3C.4, San Diego, United States, 2018.

(P31) L. Galdino, G. Saavedra, **D. Semrau**, D. Elson, D. Lavery, M. Tan, M. Iqbal, P. Harper, R. I. Killey, P. Bayvel, "Digital Back-Propagation in Wideband Optical Fibre Transmission Systems", *Proceedings of European Conference in Optical Communications (ECOC)*, Th.2.E.2, Gothenburg, Sweden 2017.

(P32) G. Saavedra, M. Tan, D. Elson, L. Galdino, **D. Semrau**, M. Iqbal, I. Phillips, P Harper, N. Suibhne, A. Ellis, D. Lavery, B. C. Thomsen, R. I. Killey, P. Bayvel, "Experimental Investigation of Nonlinear Signal Distortions in Ultra-Wideband Transmission Systems", *Proceedings of Optical Fiber Communication Conference (OFC)*, W1G.1, Los Angelos, United States 2017.

(P33) N. Shevshenko, T. Xu, **D. Semrau**, G. Saavedra, G. Liga, M. Paskov, L. Galdino, A. Alvarado, R. I. Killey, P. Bayvel, "Achievable Information Rates

Estimation for 100-nm Raman-amplified Optical Transmission System", *Proceedings of European Conference on Optical Communications (ECOC)*, W.4.P1.SC5.56, Duesseldorf, Germany, 2016

Chapter 2

Theory and literature review

The aim of this chapter is to introduce the main physical concepts in optical communication that are required in order to understand the goals (see Ch. 1) and research described in this thesis. The fundamentals of light propagation in the optical fibre channel are reviewed with special emphasis on nonlinear effects, as they are currently viewed as the main limitation to increasing the achievable information rates within a given optical bandwidth. Particular attention is drawn to ultra-wideband bandwidth scenarios, where the optical bandwidth is larger than in conventional transmission systems. Fibre properties, enabling amplification techniques and common system modelling approaches are introduced and reviewed.

2.1 System modelling

A coherent optical communication system is comprised of an optical transmitter, a transmission link and an optical receiver followed by some digital signal processing, schematically shown in Fig. 2.1. Optical modulators modulate the data onto

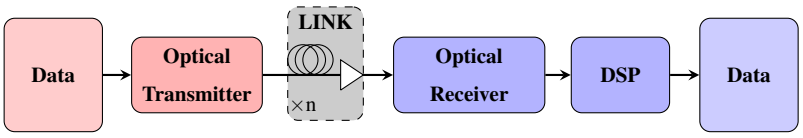

Figure 2.1: Transmission model in optical communication.

a light wave exploiting amplitude, phase and the polarisation state of the electric field. The modulated light then propagates through the optical fibre channel and is detected at the receiver side. Through the use of coherent detection and digital signal processing, the data is transferred from the optical into the electrical domain and then recovered, with errors originating from both the link and the transceiver sub-system [47]. In a coherent receiver, the received signal is mixed with a local oscillator and the resulting signal is subsequently detected using two photodiodes (per polarisation). This leads to beating terms from which the amplitude and phase

of the signal can be successfully extracted [48]. In the remaining sections of this chapter, the main concepts and transmission impairments of the light wave propagating in an optical fibre are introduced with focus on ultra-wideband transmission and nonlinear effects.

2.2 Modulation formats and mutual information

The electric field $\hat{Q}(t)$ of a WDM channel centered around f_c can be written as

$$\hat{Q}(t) = Q(T)\, e^{-j2\pi f_c t}, \tag{2.1}$$

where $Q(t)$ is the complex envelope of the WDM channel. As $Q(t)$ is complex valued, its real and imaginary parts can be used to transmit information. the Fourier transform is defined as in [11], i.e., the forward transform is given by $\mathscr{F}\{f(t)\}(f) = \int f(t)\, e^{j2\pi ft} dt$. In practice, the complex envelope of the electric field is generated by combining the output of two amplitude modulated optical waves that are phase shifted by $\frac{\pi}{2}$ (i.e. are orthogonal) with respect to each other. Utilising both real and imaginary parts of the electric field, is referred to as quadrature amplitude modulation, where the non-phase shifted and the $\frac{\pi}{2}$ phase shifted wave components are called the inphase component (I) and the quadrature component (Q). At the receiver, the complex electric field can be reconstructed by using a coherent receiver and coherent DSP.

QAM modulation formats are represented by a constellation diagram as shown in Fig. 2.2. As an example Fig. 2.2 a) shows a 16-QAM signal, using 4 different levels per I and Q component. Fig. 2.2 b) shows a Gaussian modulated signal, where the component of every constellation point is drawn from a Gaussian distribution. Gaussian constellations are not practically achievable as they require an infinite number of amplitude levels per I and Q component, however, they have three valuable properties. First, they upper bound the nonlinear distortions of QAM formats, leading to modulation format independent and guaranteed conservative performance estimates [31]. Second, Gaussian-modulated signals result in relatively simple analytical expressions enabling very efficient, low complexity models for the estimation of nonlinear interference [27, 29, 49]. Third, they maximise the achievable information rate in the presence of an additive white Gaussian noise channel. Fourth, Gaussian modulation is a good approximation for shaped constellation, which will be covered in this section. AWGN is defined as additive noise whose amplitude samples are drawn from a Gaussian distribution and whose power spectral density (PSD) is uniform over the signal bandwidth. Gaussian modulation and its benefits in the modelling of nonlinear distortions will be extensively

discussed in Section 2.6.2. It will be shown that Gaussian constellations result in simple integral expressions for analytical performance estimations, referred to as the GN model.

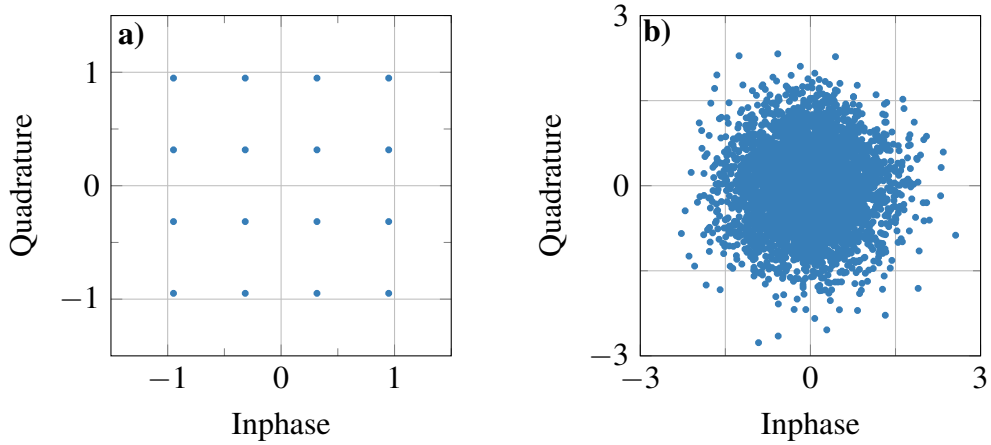

Figure 2.2: The inphase (real) and quadrature (imaginary) part of a 16-QAM format in a) and a Gaussian constellation in b). Both constellations are normalised to unit power.

Modulation formats are inherently tied to the achievable information rate (AIR) they can achieve given the channel statistics. AIR is an important figure of merit as it corresponds to the net data rate that can be achieved by a transceiver using soft-decision decoding. While hard-decision decoding operates on discrete quantities (i.e. bits that are either 1 or 0), soft-decision decoding operates on continuous quantities (soft bits) that additionally express the certainty of a bit estimation. This additional information results in better performance with respect to hard-decision decoders. A way to estimate the AIR is utilising mutual information (MI), which measures the amount of information obtained about the sent symbols X through observing the received symbols Y. The MI is given by [26]

$$\mathrm{MI}(X,Y) = \int\int dxdy\; p_{X,Y}(x,y) \log_2 \left(\frac{p_{X,Y}(x,y)}{p_X(x)\, p_Y(y)} \right), \tag{2.2}$$

where $p_{X,Y}(x,y)$ is the joint probabilty distribution of X and Y and $p_X(x)$, $p_Y(y)$ are the marginal probability distributions. For an AWGN channel, a Gaussian probability distribution (i.e. Gaussian modulation) maximises (2.2). The resulting MI is defined as (AWGN) channel capacity, and is given by the Shannon formula [26]

$$C = \log_2(1+\mathrm{SNR}), \tag{2.3}$$

where SNR is the signal-to-noise ratio. While Eq. (2.3) serves as a very useful

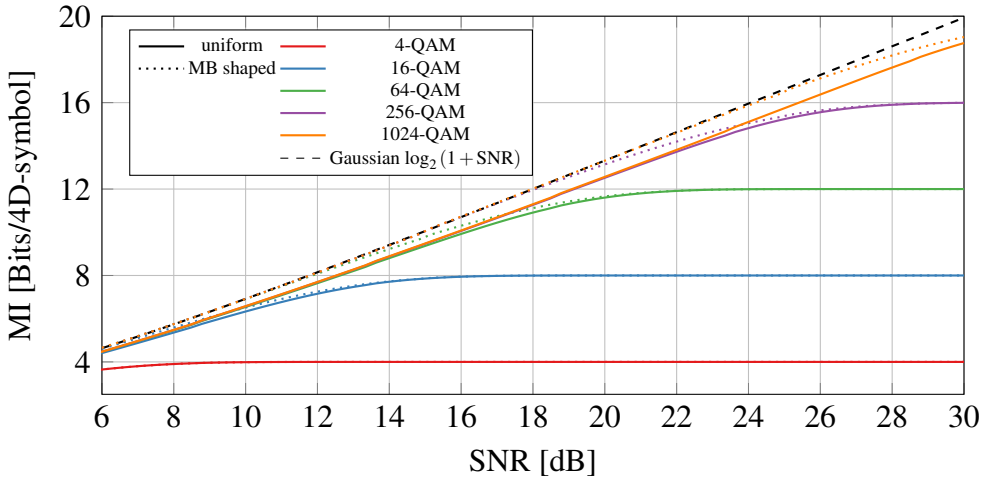

Figure 2.3: The mutual information as a function of SNR for a AWGN channel. Shown are uniform constellations and probabilistically shaped constellations.

upper bound on information throughput, it is difficult to (exactly) achieve in practice due to the requirement of infinite amplitude levels in I and Q components and infinite-length forward error correction code (FEC). However, the Shannon capacity can be approached by means of constellation shaping, where the location (i.e. geometric shaping) or the probabilities of occurance (i.e. probabilistic shaping) of each constellation point is varied. With respect to probabilistic shaping, it has been shown that the optimum probability distribution, under the constraint of a discrete constellation set and minimisation of average transmitted power, for the AWGN channel is the Maxwell-Boltzmann distribution [50] given as

$$p_{\mathrm{MB}}(x) = \frac{e^{-\lambda_{\mathrm{MB}}|x|^2}}{\sum_{\forall x' \in X} e^{-\lambda_{\mathrm{MB}}|x'|^2}}, \tag{2.4}$$

where λ_{MB} is the shaping parameter that is optimised for a given SNR. Note that $\lambda_{\mathrm{MB}} = 0$ describes a uniform constellation as in Fig. 2.2 a).

It should be stressed that the Shannon formula (2.3) holds for AWGN channels. However, the optical fibre channel does not strictly resemble an AWGN channel. E.g., it has been shown that the fibre channel exhibits a significant phase-noise component [51]. Additionally, the nonlinear interference noise is characterised by temporal correlations [32, 52]. However despite the non-AWGN nature of the fibre-optic channel, the Shannon formula (2.3) is of significant practical relevance as it offers an estimate of achievable throughputs using conventional (i.e. linear) transmission and detection schemes. Nonetheless, it should be emphasised that the *actual* capacity of the fibre-optic channel is unknown and still an open research ques-

tions [53].

To summarise, Fig. 2.3 shows the mutual information for several uniform and probabilistically shaped constellation formats as a function of the SNR. The results were obtained by numerically solving Eq. (2.2) (multiplied by 2, as two orthogonal polarisations are assumed) and using a gradient descent algorithm in order to maximise the shaping parameter in Eq. (2.4) for every SNR. As expected, a higher cardinality (i.e. unique elements) of the symbol alphabet results in higher MI, as the cardinality dictates the maximum achievable information rate for SNR $\to \infty$. Furthermore, Fig. 2.3 shows that probabilistic shaping, indeed, is able to close the gap to capacity (Gaussian modulation), yielding a maximum achievable shaping gain of 1.53 dB [50] (for SNR $\to \infty$). This shaping gain can be achieved by means of geometric or probabilistic shaping.

The calculation of mutual information is required to asses the net throughput that can be achieved for a given optical transmission system. Although the transmission models developed in this thesis (see Chapters 3, 4, 5) estimate the signal-to-noise ratio, the net throughput for the modelled system can be calculated using MI and the concepts discussed in this section.

2.3 Fibre propagation and impairments

In this section, the main concepts and transmission impairments of light wave propagation in an optical fibre are introduced with emphasis on ultra-wideband transmission. The evolution of the slow varying, complex envelope of the guided electric field $Q = Q(z,t)$ is well described by the nonlinear Schrödinger equation (NLSE) [11, Ch. 2]

$$\frac{\partial Q}{\partial z} + \underbrace{\frac{\alpha}{2}Q}_{\text{Loss}} + \underbrace{j\frac{\beta_2}{2}\frac{\partial^2 Q}{\partial T^2} - \frac{\beta_3}{6}\frac{\partial^3 Q}{\partial T^3}}_{\text{Dispersion}} = j\gamma\left(\underbrace{|Q|^2 Q}_{\text{Kerr effect}} - \underbrace{T_R\frac{\partial |Q|^2}{\partial T}Q}_{\text{Raman effect}}\right), \tag{2.5}$$

where α is the loss coefficient, β_2 is the group velocity dispersion parameter, β_3 is the group velocity dispersion slope at reference wavelength λ_{ref}, z is the propagation distance, $T = t - \frac{z}{v_g}$ is the time of the reference time window moving at group velocity v_g at reference wavelength λ_{ref}, γ is the nonlinearity parameter and T_R is the Raman time constant. The nonlinear parameter can be computed via $\gamma = \frac{2\pi n_2}{\lambda_{\text{ref}} A_{\text{eff}}}$, with effective mode area A_{eff} and nonlinear refractive index n_2 [11, Ch. 2]. The Raman gain constant captures the delayed nature of the nonlinear fibre response, leading to inter-channel stimulated Raman scattering. The Raman time

constant is related to the slope of the Raman gain $T_R = \frac{1}{2\pi\gamma f_r}\frac{\partial}{\partial f}g_r(f)\Big|_{f=0}$ with the fractional contribution of the delayed nonlinear response f_r. The Raman gain spectrum describes the power coupling of two frequency components as a function of their frequency separation (see Fig. 2.7). The Raman gain becomes relevant for bandwidths beyond 5 THz and is only valid for bandwidths up to the peak of the Raman gain coefficient (approximately 15 THz). Beyond 15 THz, an integral form of the Raman term has to be considered, which can be found in [54]. Eq. (2.5) is valid for the case of single polarisation. In Section 2.3.3, the case of dual polarisation is discussed.

For later use, Eq. (2.5) is written in the frequency domain by applying the Fourier transform. The NLSE in the frequency domain is

$$\begin{aligned}\frac{\partial}{\partial z}Q(f) = &\overbrace{\left(-\frac{\alpha}{2}+j2\pi^2\beta_2 f^2+j\frac{4}{3}\pi^3\beta_3 f^3\right)Q(f)}^{\text{Linear effects}}\\ &+\underbrace{j\gamma\{Q(f)*Q^*(-f)*Q(f)-jT_R[2\pi f\,(Q(f)*Q^*(-f))]*Q(f)\}}_{\text{Nonlinear effects}},\end{aligned} \tag{2.6}$$

with $Q(f)=\mathscr{F}\{Q(t)\}$ (note that both also depend on distance z), where $\mathscr{F}$ denotes the Fourier transform and $u(x)*v(x)$ denotes the convolution operation. Eq. (2.5) is key for the calculation of the transmission performance of optical fibre communication. As such, the analytical models developed in this thesis (Ch. 3, 4, 5) are extensively validated against numerical solutions of the NLSE. The prevailing numerical method to solve (2.5) is discussed in Section 2.3.4. Eq. (2.5) and (2.6) can be separated into linear and nonlinear effects.

It should be noted that throughout this thesis, Eq. (2.6) is not directly integrated. In particular, the Raman term in (2.6) is neglected and the Raman effect is indirectly accounted for in numerical simulations as well as in the analytical modelling. The Raman effect in (2.6) results in ISRS (formally introduced in Sec. 2.3.2.2) and it can be accounted for by introducing a signal power profile (i.e. a suitable loss function), such that the profile resembles the power transfer caused by ISRS. Mathematically, the signal power profile is obtained from the Raman gain equations (see Sec. 2.3.2.2). The approach neglects the temporal gain dynamics of ISRS which will be extensively discussed in Sec. 3.2 and the approach will be experimentally validated as part of this thesis in Sec. 3.3. The negligible nature of such dynamic effects is motivated by the averaging of many independent sources which has been theoretically shown for on-off keyed systems [55, 56]. Additionally, the Raman effect couples frequencies that exhibit large frequency spacings (>5 THz).

Such frequency spacings exhibit large channel walk-off (see Sec. 2.3.1), that reduces the effect of the impact of temporal gain dynamics.

2.3.1 Linear propagation

When nonlinear effects are negligible, Eq. (2.5) reduces to a linear differential equation, and it is convenient to analyse the signal evolution in the frequency domain, given by

$$\frac{\partial}{\partial z}Q(f) = \left(-\frac{\alpha}{2} + j2\pi^2\beta_2 f^2 + j\frac{4}{3}\pi^3\beta_3 f^3\right)Q(f), \tag{2.7}$$

with solution

$$Q(z,f) = Q(0,f)\exp\left(-\frac{\alpha}{2}z + j2\pi^2\beta_2 f^2 z + j\frac{4}{3}\pi^3\beta_3 f^3 z\right). \tag{2.8}$$

Eq. (2.7) and (2.8) model the intrinsic fibre loss and the effect of dispersion that cause a temporal spread of propagating pulses. Both linear effects are compensated by means of optical amplification, at the expense of linear noise, and chromatic dispersion compensation through dispersion maps [57] or digital filters [48]. A good understanding of both, linear and nonlinear effects, is necessary as their interplay is currently viewed as a fundamental limitation to increase capacity [58,59]. Additionally, the linear solution (2.8) plays a fundamental role in the derivation of first-order perturbation models, which are addressed in Section 2.6

2.3.1.1 Fibre loss

In general, the intrinsic fibre loss is a function of frequency, due to the interaction of a few different frequency-dependent absorption mechanisms. Neglecting dispersion and extending Eq. (2.8) for frequency dependent loss, we obtain a simple exponential relationship before and after propagation

$$Q(z,f) = Q(0,f)\exp\left(-\frac{\alpha(f)}{2}z\right), \tag{2.9}$$

in terms of the electric field and

$$P(z,f) = P(0,f)\exp\left(-\alpha(f)z\right), \tag{2.10}$$

in terms of optical power, with $P(z,f) = |Q(z,f)|^2$. The attenuation coefficient of a SMF is shown in Fig. 2.4. The profile was obtained from a fitting function to match experimental results [10]. The main absorption mechanisms that contribute to the overall fibre loss are Rayleigh scattering ($\propto \lambda^{-4}$), infrared absorption ($\propto \exp(q_1\lambda)$),

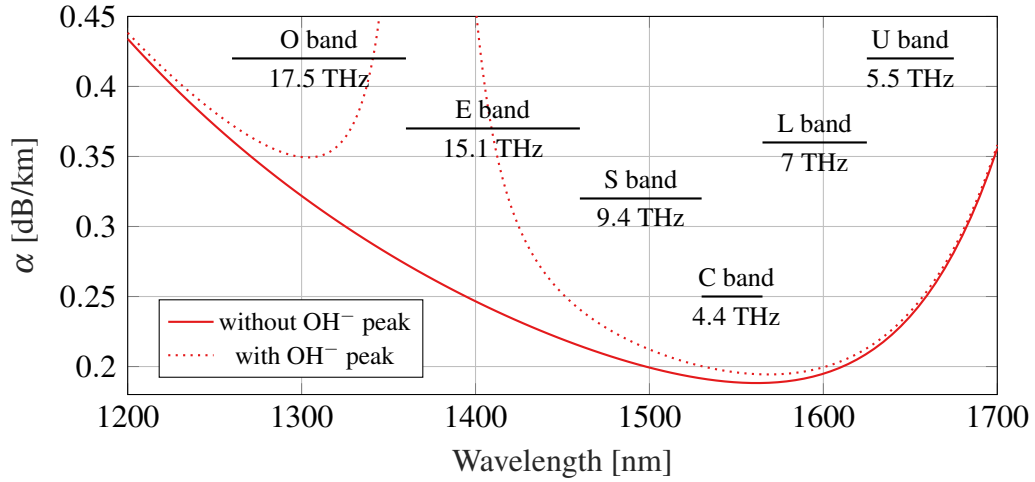

Figure 2.4: Attenuation profile of a standard single mode fibre (SMF) taken from [10].

ultra-violet absorption ($\propto \exp(-q_2\lambda)$) and waveguide imperfections, where q_1 and q_2 are fibre dependent fitting parameters.

The fundamental limit is imposed by Rayleigh scattering [60] for lower wavelengths and infrared absorption for longer wavelengths. Fig. 2.4 shows the so-called second (around 1300 nm) and third telecom windows (around 1500 nm) which are further subdivided into transmission bands. Both transmission windows were in earlier fibres separated by a loss peak imposed by hydroxide ions (OH^-). However since 1982, efficient fibre manufacturing processes are known to effectively remove the OH^- content [61]. As a result, the entire low-loss region of the SMF is accessible in state-of-the art optical networks. Utilising all transmission bands, yields an increase in bandwidth of 13.4 times with respect to C-band (as defined by the availability of erbium-doped fibre amplifiers, see Section 2.4.1) alone, a great potential to increase fibre capacity.

2.3.1.2 Dispersion

Another linear effect occurring during propagation is dispersion. The term group velocity dispersion (GVD) means that different frequencies travel with different velocities, leading to a temporal spreading of the propagating pulse. Dispersion leads to inter-symbol interference impairing signal demodulation, if left uncompensated. Additionally, to the effect that pulses located at different centre frequencies travel at different velocities, the pulses themselves become spread in time. This is because the frequency components within the same pulse also propagate at different

velocities. Neglecting attenuation in Eq. (2.8) yields

$$Q(z,f) = Q(0,f)\exp\left(j2\pi^2 f^2\left[\beta_2 + \frac{2}{3}\pi\beta_3 f\right]z\right), \tag{2.11}$$

in the frequency domain. Eq. (2.11) shows that dispersion introduces a frequency dependent phase shift while the amplitude stays constant. As mentioned dispersion leads to a velocity difference when two pulses are separated by a frequency $\Delta\omega = 2\pi\Delta f$. The corresponding separation time (ignoring the dispersion slope) between the two pulses, after a propagation distance L, can be calculated from

$$\Delta T = \frac{\partial}{\partial\omega}\left(\frac{L}{v_g}\right)\Delta\omega = \frac{\partial^2}{\partial\omega^2}(\beta)\,\Delta\omega L = \beta_2\Delta\omega L. \tag{2.12}$$

Applying the relation $\Delta\omega = -\frac{2\pi c}{\lambda_{\text{ref}}^2}\Delta\lambda$ to (2.12) yields a similar equation with respect to a wavelength separation

$$\Delta T = -\frac{2\pi c}{\lambda_{\text{ref}}^2}\beta_2\Delta\lambda L = D\Delta\lambda L, \tag{2.13}$$

where D is called the chromatic dispersion parameter. The chromatic dispersion parameter D is approximately $17\frac{\text{ps}}{\text{nm}\cdot\text{km}}$ at 1550 nm for a SMF. Regarding SMF, the reported value for the chromatic dispersion parameter typically varies in $D \in [16,20]\frac{\text{ps}}{\text{nm}\cdot\text{km}}$ depending on fibre specifications. The two n-th channels that are located at wavelength $1550\,\text{nm} \pm n\Delta\lambda$ are dispersed by

$$m = 2LDn\Delta\lambda\frac{1}{T_s}, \tag{2.14}$$

symbol slots, where $R_\text{b} = \frac{1}{\Delta T}$ with symbol rate R_b. For a symbol rate of $R_\text{b} = 32$ GBd and a spacing of $\Delta f = 32$GHz or $\Delta\lambda = 0.256$ nm (Nyquist-spacing), the $\pm$154-th channels (10 THz, approximately the entire C+L band) are dispersed by 4188 symbol time slots after 100 km in a SMF. A symbol time slot has time duration $T_s = \frac{1}{R_b}$. In ultra-wide bandwidth simulations this number must be kept within a few percent relative to the number of simulated symbols. This prevents that the signal leading edge of the signal wraps around the simulation window (i.e. keeps its impact low) as, in the simulation, the signal is assumed to be periodically extended across time.

Additionally, for large bandwidth signals, it is important to consider the change of the dispersion parameter D over the optical bandwidth. Similar to β_3

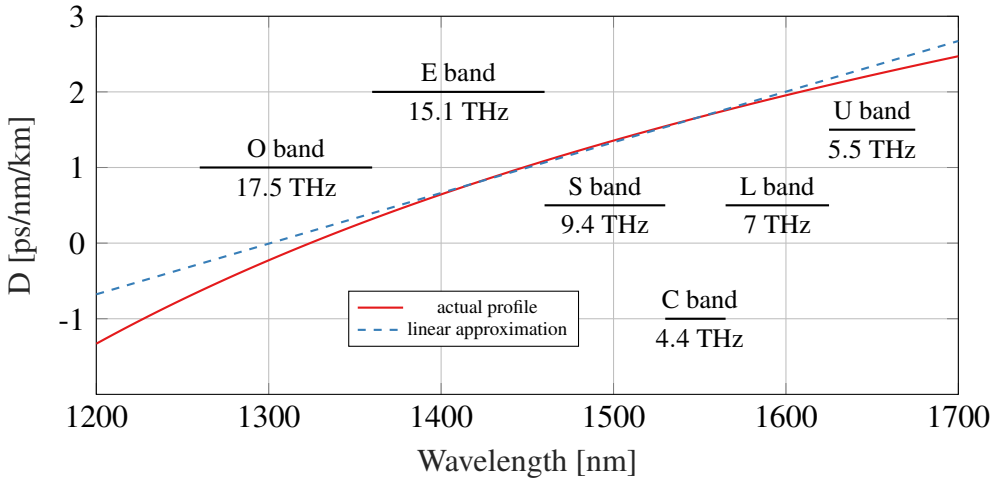

Figure 2.5: Dispersion profile for a standard single mode fibre together with its linear approximation. The dispersion profile satisfies $D(\lambda) = \frac{1}{4} S_{\text{ZDW}} \left(\lambda - \frac{\lambda_{\text{ZDW}}^4}{\lambda^3} \right)$, with zero-dispersion wavelength $\lambda_{\text{ZDW}} = 1324$ nm and zero-dispersion slope $S_{\text{ZDW}} = 0.092 \, \frac{\text{ps}}{\text{nm}^2\text{km}}$ [11].

the linear change of the dispersion coefficient D is given by

$$S = \left(\frac{\partial D}{\partial \lambda} \right)_{\lambda = \lambda_{\text{ref}}} = \frac{4\pi c}{\lambda_{\text{ref}}^3} \beta_2 + \frac{(2\pi c)^2}{\lambda_{\text{ref}}^4} \beta_3. \tag{2.15}$$

A SMF has a slope S of $0.067 \frac{\text{ps}}{\text{nm}^2 \cdot \text{km}}$ at 1550 nm. The dispersion parameter D together with its linear approximation for a standard single mode fibre, is shown in Fig. 2.5. It can be seen, that the linear dispersion approximation (via S or β_3) is fairly accurate from 1380 nm to 1620 nm which contains all bands except the O and U band.

It is essential to compensate for dispersion to prevent inter-symbol interference. Before the introduction of coherent detection, dispersion compensation was performed by means of dispersion maps (dispersion management) where some fibre spans along the transmission link use negative dispersion coefficients resulting in reduced accumulated dispersion at the receiver. Dispersion compensation modules usually consist of long (10 km) pieces of dispersion compensating fibres (DCF) [62, 63] or compact, chirped fibre bragg gratings [64]. Alternatively, the accumulated dispersion can be reversed electronically by applying a digital filter, following coherent detection, with transfer function

$$H(f) = \exp\left(-j2\pi^2 f^2 \left[\beta_2 + \frac{2}{3} \pi \beta_3 f \right] L \right), \tag{2.16}$$

after transmission distance L to compensate for chromatic dispersion [65].

2.3.2 Nonlinear propagation

As dispersion can be mitigated by digital filters and equalisers, the current limitation of optical communication systems is imposed by Kerr nonlinearities [58, 66, 67]. In order to obtain a better understanding of fibre nonlinearity, Eq. (2.5) in the absence of dispersion ($D = 0$ and $S = 0$), yields

$$\frac{\partial Q}{\partial z} = -\frac{\alpha}{2}Q + j\gamma\left(|Q|^2 Q - T_R\frac{\partial |Q|^2}{\partial T}Q\right). \tag{2.17}$$

The second term in (2.17) is related to the instantaneous Kerr effect while the third term describes the delayed nonlinear Raman response giving rise to inter-channel stimulated Raman scattering [68, 69]. Although there are no instantaneous physical processes, the nonlinear response can be separated into a quasi-instantaneous and a delayed contribution of the fibre response with respect to the frequency of the optical field. The nearly instantaneous part originates from electronic contributions while the delayed part originates from induced vibrations of the silica molecules. ISRS effectively redistributes power from high frequency to lower frequency components during fibre propagation. More specifically, the delayed Raman response arises from the non-instantaneous nature of the interaction between the incident optical waves and the vibrational modes. Eq. (2.17) is valid for bandwidths up to approximately 15 THz, as it relies on a linear approximation of the Raman gain spectrum. This assumption will be addressed in more detail in Section 2.3.2.2. Nonlinear effects include phenomena such as self-phase modulation (SPM), cross-phase modulation (XPM), four-wave mixing (FWM) and stimulated Brillouin and Raman scattering. In the following section these effects are described in more detail.

2.3.2.1 Instantaneous Kerr effect

First, the instantaneous Kerr effect is analysed in more detail. Neglecting ISRS in (2.17) yields

$$\frac{\partial Q}{\partial z} = -\frac{\alpha}{2}Q + j\gamma|Q|^2 Q. \tag{2.18}$$

with the solution

$$Q(z,T) = Q(0,T)\exp\left(-\alpha z + j\gamma|Q(0,T)|^2 L_{\text{eff}}\right), \tag{2.19}$$

in the time domain, where $L_{\text{eff}} = \int_0^L \exp(-\alpha\zeta)\,d\zeta$. Eq. (2.19) describes a phase shift in the time domain, dependent on the instantaneous power of the waveform Q

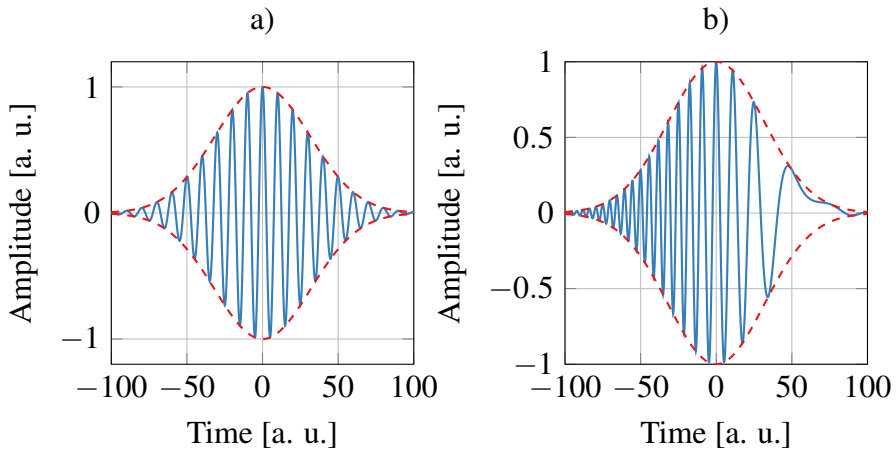

Figure 2.6: Illustration of chirp with a) being an unchirped pulse and b) being a chirped pulse as a result of SPM.

itself. It can also be noted that the intrinsic fibre loss reduces the relevant length scale from the span length L to the effective length L_{eff}. The effective length of a SMF ($\alpha = 0.2$ $\frac{\text{dB}}{\text{km}}$) is $L_{\text{eff}} = \frac{1-\exp(-\alpha L)}{\alpha} \approx \frac{1}{\alpha} = 21715$ m, which shows that the Kerr effect is only significant at the start of the fibre span. This can be exploited in numerical simulations and analytical modelling of the fibre channel, by tailoring the distance resolution to the exponential power loss profile [70]. Given an initial pulse envelope $Q(0,T) = Q_0(T)\exp(j\phi_0)$, the phase and angular frequency at distance L are

$$\phi(L,T) = \phi_0 + \gamma |Q_0(T)|^2 L_{\text{eff}}, \tag{2.20}$$

and

$$\omega(L,T) = -\frac{\partial}{\partial T}\phi(L,T) = -\gamma L_{\text{eff}} \frac{\partial}{\partial T} |Q_0(T)|^2 . \tag{2.21}$$

Eq. (2.21), shows that while the envelope of the pulse in time is not varying, the leading edge of the pulse experiences a frequency shift towards higher frequencies and the trailing edge of the pulse a frequency shift towards lower frequencies. In other words, the pulse acquires a time-dependent change of the instantaneous frequency, also called chirp. An illustration is shown in Fig. 2.6 with an un-chirped and a chirped pulse as a result of self-phase modulation.

SPM is the process whereby a pulse nonlinearly interacts with itself, in fibres first demonstrated in 1967 [71, 72]. On the other hand, cross-phase modulation is the process whereby a pulse nonlinearily interacts with another pulse [73, 74].

2.3.2.2 Delayed nonlinear effect

In recent years much attention has been drawn to the study and mitigation of Kerr nonlinearities such as SPM, XPM and FWM, which limit the achievable data rates and are the prevailing nonlinear effects for optical bandwidths within the C-band, where conventional Erbium fibre amplifiers operate. As mentioned, the nonlinear response can be considered instantaneous within these bandwidths, with respect to changes in the optical signal, and the delayed part of the response is negligible. However, for optical bandwidths beyond C-band, the delayed nonlinear fibre response must be taken into account. Neglecting dispersion and Kerr nonlinearity, and writing out the convolution operations in Eq. (2.6) yields

$$\begin{aligned}&\frac{\partial}{\partial z}Q(f) = -\frac{\alpha}{2}Q(f)\\&-2\pi\gamma T_R\int\int f_2 Q(f_1)Q^*(f_1-f_2)Q(f-f_2)df_1df_2.\end{aligned} \tag{2.22}$$

To analyse the effect of a delayed nonlinear response, a transmitted signal consisting of only two continuous waves with powers $P_1 = |Q_1|^2$ and $P_k = |Q_k|^2$ at (relative) frequencies 0 and f_k, respectively, can be considered. The waveform is then given by

$$Q(f) = Q_1\delta(f) + Q_k\delta(f-f_k), \tag{2.23}$$

note that $Q_1(z)$ and $Q_k(z)$ are distance-dependent, which is suppressed for notational convenience. Inserting the signal at the transmitter Eq. (2.23) into Eq. (2.22) yields

$$\begin{aligned}&\frac{\partial}{\partial z}\left[Q_1\delta(f) + Q_k\delta(f-f_k)\right] = -\frac{\alpha}{2}\left[Q_1\delta(f) + Q_k\delta(f-f_k)\right]\\&-2\pi\gamma T_R\int\int df_1df_2\ f_2\left[Q_1\delta(f_1) + Q_k\delta(f_1-f_k)\right]\\&\left[Q_1\delta(f_1-f_2) + Q_k\delta(f_1-f_2-f_k)\right]\left[Q_1\delta(f-f_2) + Q_k\delta(f-f_2-f_k)\right].\end{aligned} \tag{2.24}$$

The convolution integrals are only non-zero for two frequency combinations which are $\{f_1 = 0 \text{ and } f_2 = -f_k\}$ and $\{f_1 = f_k \text{ and } f_2 = f_k\}$. The resulting equation is

$$\begin{aligned}&\frac{\partial}{\partial z}\left[Q_1\delta(f) + Q_k\delta(f-f_k)\right] = -\frac{\alpha}{2}\left[Q_1\delta(f) + Q_k\delta(f-f_k)\right]\\&-2\pi\gamma T_R f_k\left[|Q_1|^2 Q_k\delta(f-f_k) - |Q_k|^2 Q_1\delta(f)\right].\end{aligned} \tag{2.25}$$

As the two Dirac delta functions are orthogonal, (2.25) can be written as two coupled differential equations and further translated to the power evolution of the continuous wave, using the relation $\frac{\partial P}{\partial z} = \frac{\partial Q^*}{\partial z}Q + \frac{\partial Q}{\partial z}Q^*$, as

$$\begin{aligned} \frac{\partial}{\partial z}P_1 &= -\alpha P_1 + \overbrace{4\pi\gamma T_R f_k P_1 P_k}^{\text{ISRS gain}}, \\ \frac{\partial}{\partial z}P_k &= -\alpha P_k - \underbrace{4\pi\gamma T_R f_k P_1 P_k}_{\text{ISRS loss}}. \end{aligned} \tag{2.26}$$

Eq. (2.26) reveals that a delayed nonlinear response, leads to a power transfer between propagating frequencies. If we have that $f_k > 0$, the wave P_k amplifies wave P_1 at the expense of its own depletion as described by (2.26). This power transfer from high to low frequency components is referred to as inter-channel stimulated Raman scattering. As mentioned, ISRS is caused by elastic scattering with optical phonons, the quantisation of vibrational modes of the glass lattice.

In fact, (2.26) can be generalised to the Raman gain equations, a set of M coupled differential equation that describe power evolution of each continuous wave channel, where M is the total number of channels [75]

$$\frac{\partial P_i}{\partial z} = \underbrace{-\sum_{j=i+1}^{M} \frac{f_j}{2f_i} g_R(\Delta f) P_j P_i}_{\text{ISRS loss}} + \underbrace{\sum_{j=1}^{i-1} \frac{1}{2} g_R(\Delta f) P_j P_i}_{\text{ISRS gain}} - \alpha P_i, \tag{2.27}$$

with the optical power P_i, of channel i, the normalised Raman gain coefficient $g_R(\Delta f)$, the attenuation coefficient α and the frequency separation $\Delta f = |f_j - f_i|$ between channel j and i. The factor $\frac{f_j}{f_i}$ conserves the photon number and the factor $\frac{1}{2}$ accounts for polarisation averaging as the Raman gain coefficient is strongly polarisation dependent [76]. The channels are indexed such that the highest frequency channel has index $i = 1$. Eq. (2.27) can be solved numerically and it extends the simplistic ISRS model in Eq. (2.5) and Eq. (2.26) by accounting for energy conservation and the precise Raman gain spectrum. Figure 2.7 shows the Raman gain coefficient in silica for a frequency separation of up to 20 THz, as measured by Stolen and Ippen in 1973 [12]. Fig. 2.7 also shows a linear regression of the Raman gain spectrum, often referred to as the triangular approximation of the Raman gain function, valid for bandwidths up to 15 THz. The triangular approximation leads to simplified descriptions of ISRS such as Eq. (2.5) and Eq. (2.26). Additionally, Eq.

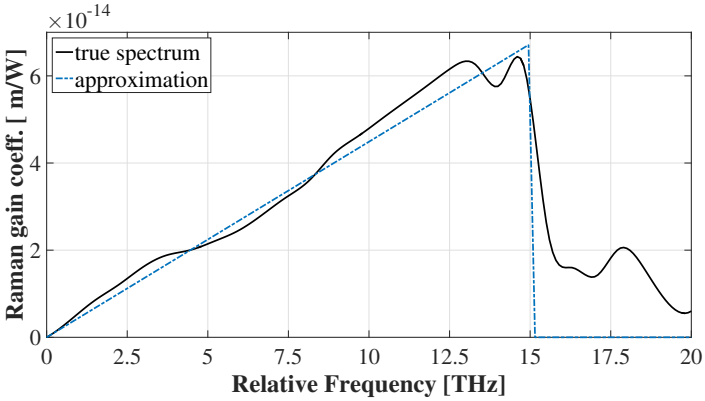

Figure 2.7: Raman spectrum at 1550 nm for a standard single mode fibre taken from [12] and a linear regression slope of $C_r = 0.028\ \frac{1}{\text{W}\cdot\text{km}\cdot\text{THz}}$.

(2.27) can be solved analytically under the triangular approximation [77, 78]

$$\rho(z,f) = \frac{P_{\text{tot}} e^{-\alpha z - P_{\text{tot}} C_{\text{r}} L_{\text{eff}} f}}{\int G_{\text{Tx}}(\nu) e^{-P_{\text{tot}} C_{\text{r}} L_{\text{eff}} \nu} d\nu}, \tag{2.28}$$

where C_{r} is the slope of a linear regression of the normalised, polarisation averaged Raman gain spectrum $\frac{1}{2} g_r(\Delta f)$, P_{tot} is the total optical power, $G_{\text{Tx}}(f)$ is the signal power spectral density at the transmitter and $L_{\text{eff}} = \frac{1-\exp(-\alpha z)}{\alpha}$. Eq. (2.28) yields the normalized signal power profile such that the signal power profile $P(z,f)$ at any distance and frequency is $P(z,f) = \rho(z,f)P(0,f)$. The z dependence in L_{eff} is suppressed for notational convenience.

The power evolution of the highest and lowest frequency channel is shown in Fig. 2.8. The results were obtained by numerically solving Eq. (2.27) with the Runge-Kutta method and its analytical approximation (2.28). The results assume a fully loaded (ideal Nyquist-spaced) WDM signal with a total optical bandwidth, B_{tot} of 10 THz, channel bandwidth, B_{ch} of 40 GHz, -2 dBm/ch. launch power, an effective fibre core area, A_{eff} of 80 μm^2 and a Raman gain spectrum as in Fig. 2.7. A very good agreement can be seen between the Raman gain equations and its analytical approximation, especially at the beginning of the fibre spans, where nonlinear distortions prevail. Therefore, (2.28) can be utilised as a simplified description of ISRS in the analytical modelling of nonlinear distortions in the ultra-wideband regime.

To date, the impact of ISRS has not been relevant for practical systems operating over bandwidths less than 5 THz. However, as bandwidths increase in the quest to increase channel throughput, the impact of inter-channel stimulated Raman scattering must be revisited in the context of exploring its impact on achievable communications rates in coherent WDM communication systems. The impact of

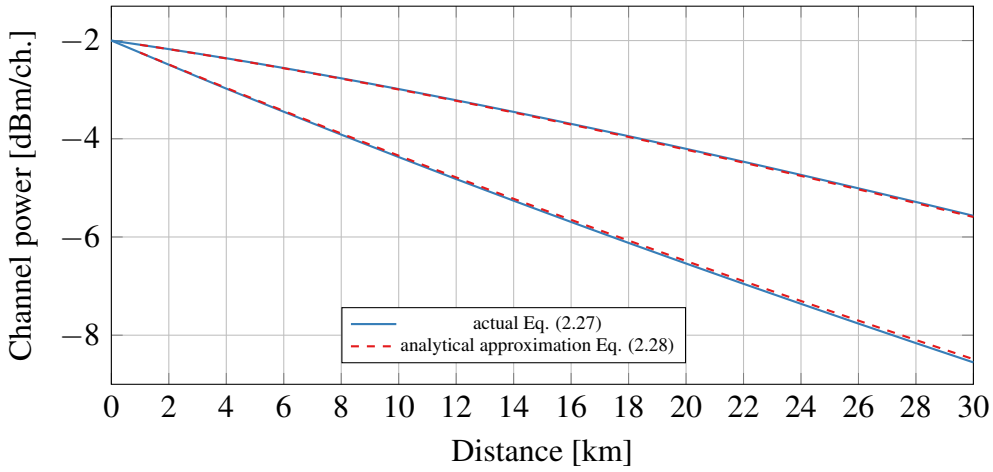

Figure 2.8: Power evolution of the highest and lowest frequency channel of a 10 THz signal (populating the entire C+L band), in the presence of ISRS. Results were obtained by numuerically solving the Raman gain equations (2.27) and its analytical approximation (2.28).

ISRS has been studied in early studies addressing on-off keyed transmission systems and neglecting the interaction between the Kerr effect and ISRS [35–38]. As outlined in Chapter 1, developing models that predict the impact of ISRS on the Kerr nonlinearity is a primary goal of this thesis. In Chapters 3, 4, new analytical models are derived in order to accurately predict such interactions and in Section 3.4, the impact of ISRS on the achievable information rate is investigated in the context of state-of-the art, coherent optical transmission systems.

2.3.3 Polarisation

The NLSE Eq. (2.5) is only valid for single polarisation. However, usually both orthogonal polarisation states of the optical wave are used for transmission. For this case, Eq. (2.5) can be extended to the Manakov equation [79] as

$$\begin{aligned}
\frac{\partial Q_x}{\partial z}+\frac{a}{2}Q_x+j\frac{\beta_2}{2}\frac{\partial^2 Q_x}{\partial T^2}-\frac{\beta_3}{6}\frac{\partial^3 Q_x}{\partial T^3}&=j\gamma\left(\frac{8}{9}\left|Q_x+Q_y\right|^2 Q_x-T_R\frac{\partial\left|Q_x+Q_y\right|^2}{\partial T}Q_x\right),\\
\frac{\partial Q_y}{\partial z}+\frac{a}{2}Q_y+j\frac{\beta_2}{2}\frac{\partial^2 Q_y}{\partial T^2}-\frac{\beta_3}{6}\frac{\partial^3 Q_y}{\partial T^3}&=j\gamma\left(\frac{8}{9}\left|Q_x+Q_y\right|^2 Q_y-T_R\frac{\partial\left|Q_x+Q_y\right|^2}{\partial T}Q_y\right),
\end{aligned} \tag{2.29}$$

where Q_x and Q_y are the complex envelopes of the signal in x and y polarisation, respectively. Eq. (2.29) models the average impact of birefringence on the pulse propagation [80]. Birefringence means that the refractive index of the material is polarisation dependent. However, in optical fibre transmission over tens of kilo-

metres, the birefringence varies so rapidly over the transmission distance that it is sufficient to analyse the average over the Poincaré sphere (i.e. all possible polarisation states). In the Manakov equation polarisation mode dispersion (PMD), arising from the velocity differences of the two polarisation states, is neglected. Eq. (2.29) can be extended to the Manakov-PMD equation in order to model the effect of PMD [81]. However, as a dispersive effect, PMD reduces the coherence between co-propagating frequency components and, as such, reduces nonlinear distortions [82]. Therefore, the Manakov equation serves as a good conservative estimate of the nonlinear distortions and the overall transmission performance.

2.3.4 The split-step Fourier method

To simulate the pulse propagation through an optical fibre, Eq. (2.5) (or Eq. (2.29) for dual polarisations) must be solved. Unfortunately, (2.5) has no analytical solution and efficient numerical methods are required. The prevailing numerical method to solve (2.5) is the SSFM and consists of dividing the entire transmission distance into small steps with length Δz [11]. Within a step, linear and nonlinear effects are decoupled and solved separately. Rewriting (2.8) and (2.19) as operators, the execution of a single split-step can be mathematically written as [11, Ch. 2]

$$Q(z+\Delta z,t) \approx e^{\int_z^{z+\Delta z}\hat{N}(\zeta)d\zeta} e^{\Delta z\hat{D}} Q(z,t), \tag{2.30}$$

with linear and nonlinear operators

$$\begin{aligned} \hat{L} &= -\frac{\alpha}{2} + j\frac{\beta_2}{2}\frac{\partial^2}{\partial T^2} + \frac{\beta_3}{6}\frac{\partial^3}{\partial T^3}, \\ \hat{N} &= j\gamma\left(|Q(z,T)|^2 - T_R\frac{\partial |Q(z,T)|^2}{\partial T}\right). \end{aligned} \tag{2.31}$$

The linear operator can be evaluated in the Fourier domain as

$$e^{\Delta z\hat{D}} Q(z,t) = \mathscr{F}^{-1} e^{\Delta z\mathscr{F}\hat{D}} \mathscr{F} Q(z,t) \tag{2.32}$$

Eq. (2.30) is then repeatedly applied until the end of the fibre span $z = L$ is reached. The accuracy of (2.30) can be improved by applying half the linear operator at the start and at the end of each split-step, referred to as the symmetric split-step Fourier method [11, Ch. 2].

The choice of the step size is key as the split-step Fourier method is more accurate for a smaller step size. The convergence of the step size can be improved when the step size distribution is logarithmic (tailored to an exponential loss of the signal

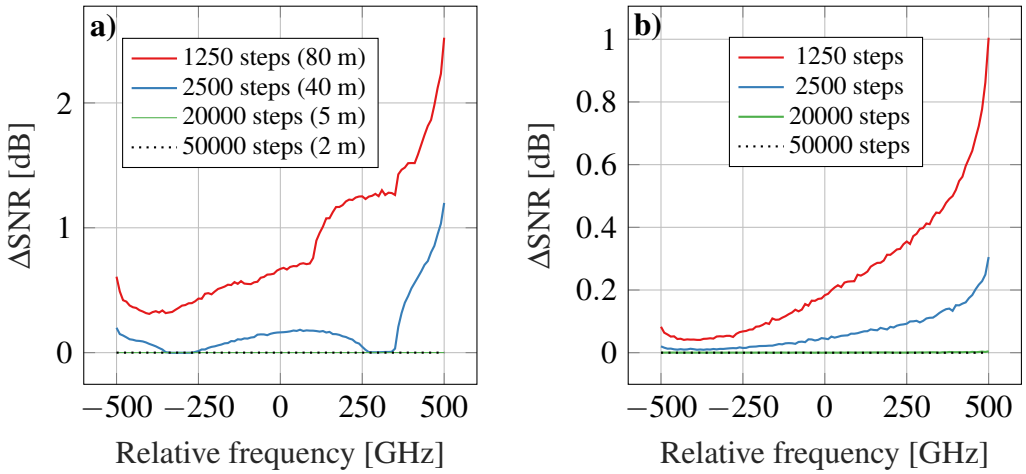

Figure 2.9: The SNR for different number of split-steps relative to the SNR for a converged number of steps for each WDM channel. Shown are a constant step size distribution a) and a logarithmically distributed step size distribution b). The results assume a 1 THz signal after 100 km of SMF with an artificially ten-fold increased Raman gain coefficient.

power profile) [70]. Fig. 2.9 shows the SNR relative to the converged (true) SNR for each WDM channel for different number of steps. The results were obtained by running the SSFM algorithm for different numbers of total steps per span for the same underlying transmission system. This way the convergence of the SSFM accuracy as a function of the step size can be studied. Additionally, the impact of using a uniform and a logarithmic step size distribution was investigated. The constant step size distribution is shown in Fig. 2.9a) and the logarithmic step size distribution is shown in Fig. 2.9b). The results assume a 1 THz signal after 100 km SMF using the symmetric SSFM (2.30). The nonlinear operator is evaluated at the effective step size (length). An artificially ten-fold increased Raman gain coefficient was assumed to yield an ISRS power transfer of 8.2 dB over 1 THz. It can be seen that the SSFM converges for increase step sizes with improved convergence when the step size is logarithmically distributed. A logarithmic step size distribution effectively reduces the step size at the beginning of the fibre span, where nonlinear distortions are significant, and increases the step size at the end of the fibre, where nonlinear effects are negligible (see Sec. 2.3.2).

The SSFM is extensively applied as a benchmark for computational complexity and in order to quantify the accuracy of the analytical models that are derived in Chapters 3, 4, 5.

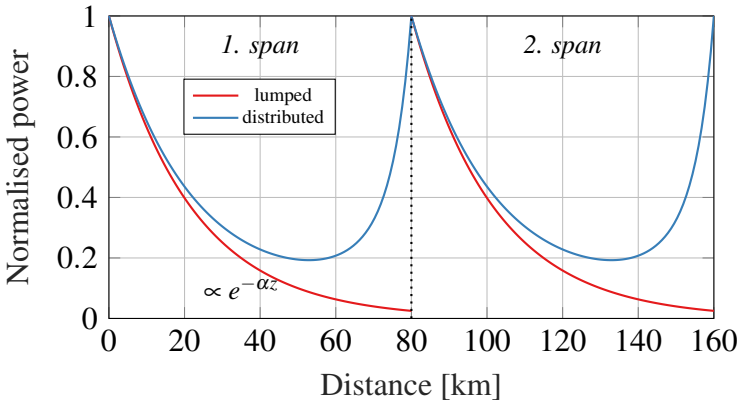

Figure 2.10: Signal power profiles within a SMF span using lumped and distributed amplification.

2.4 Optical amplification

Due to the intrinsic fibre loss, optical communication systems rely on the availability of optical amplifiers, for transmission over hundreds of kilometres and beyond. Optical amplification is the process of increasing the input signal power without the necessity of converting the signal into the electrical domain, allowing for transparent optical links. Optical amplification can be broadly categorised into lumped and distributed techniques. Both schemes result in different power profiles within the fibre span, resulting in different levels of nonlinear penalties. Therefore, a precise knowledge of the signal power profile is required for the modelling of nonlinear distortions. An illustration of the different signal power profiles by numerically solving Eqs. (2.35), for a SMF is shown in Fig. 2.10. In the former case the amplification is performed in a lumped amplifier at the end of every span. In the latter case the fibre itself functions as the gain medium during propagation. This is realised by exploiting stimulated Raman amplification (see Section 2.3.2.2), where a high power pump, with a frequency shift of around 13 THz, is injected into the propagation fibre. In the next sections, both amplification strategies are discussed in more detail.

2.4.1 Rare-earth-doped fibre amplifier

Although there are many different types of lumped amplification, the most common lumped amplifier is the Erbium-doped fibre amplifier (EDFA). The amplifier consists of an erbium-doped fibre acting as the active material in the wavelength region around 1550 nm. The early developments of the EDFA and its wavelength gain window motivated the definition of the C-band. EDFAs deliver high gain ($G > 20$ dB), enabling long-haul transmission without the necessity of optic-electronic conversion. However, co-propagating amplified-spontaneous emission noise will be gen-

erated within the doped fibre and injected into the transmission fibre. The ASE noise degrades the signal-to-noise ratio. It is well modelled by additive white Gaussian noise and its noise power over both polarizations can be calculated as

$$P_{\mathrm{ASE}} = 2n_{\mathrm{sp}}h\left(f+f_c\right)B_{\mathrm{ref}}\left(G-1\right), \tag{2.33}$$

where n_{sp} is the spontaneous emission factor, h is Planck's constant, f is the relative and f_c the reference frequency, B_{ref} is the reference bandwidth and G is the gain of the amplifier. The noise characteristic of an amplifier is typically measured in terms of noise figure F_{n}, defined and given by

$$\frac{\mathrm{SNR_{in}}}{\mathrm{SNR_{out}}} = F_{\mathrm{n}} = \frac{1}{G}\left[1+2n_{\mathrm{sp}}\left(G-1\right)\right] \approx 2n_{\mathrm{sp}}, \quad \text{for G} \gg 1, \tag{2.34}$$

where $\mathrm{SNR_{in}}$ and $\mathrm{SNR_{out}}$ are the SNR before and after the amplifier. The spontaneous emission factor is related to the population inversion in the gain media with $n_{\mathrm{sp}} \geq 1$ resulting in a minimum possible noise figure of $F_n > 2 = 3$ dB. A conventional EDFA offers high gain over an optical bandwidth of around 35 nm. This availability of the EDFA over the wavelength range of 1530 to 1565 nm motivating the definition of the C-band over the same wavelength range. With the use of longer erbium-doped fibres, the gain window can be shifted into the L band [83]. Similar to the definition of the C band, the availability of efficient optical amplification motivated the definition of the L band, ranging from 1565 to 1625 nm. A joint C+L band amplifier can then be realised by splitting the signal into the two bands, amplifying both separately and recombining both bands after the amplification stage. Using this technique, a lumped amplification window of around 77 nm can be realised [84].

The amplification window fundamentally depends on the used dopants in the active fibre. To increase the bandwidth beyond C+L band, alternative dopants must be used. A rare-earth material that can be used as a dopant for amplification in the S band is Thulium (Tm^{3+}), abbreviated as Thulium-doped fibre amplifier (TDFA) The first TDFA providing a peak gain of 8 dB over 1470-1540 nm was experimentally demonstrated in 2000 [85]. State-of-the art TDFA can provide over 30 dB gain for wavelengths ranging from 1460-1520 nm [13], unlocking the entire S+C+L-band for ultra-wideband transmission. Using the S+C+L band, a transmission rate of up to 150.3 $\frac{\mathrm{Tb}}{\mathrm{s}}$ over 40 km has been experimentally shown [86, 87].

Amplification in the E-band has been demonstrated by using Neodymium (Nd^{3+}) with a peak gain of 13.3 dB from 1376-1466 nm [14]. A promising dopant for lumped ultra-wideband transmission is Bismuth (Bi^{3+}), which has been shown

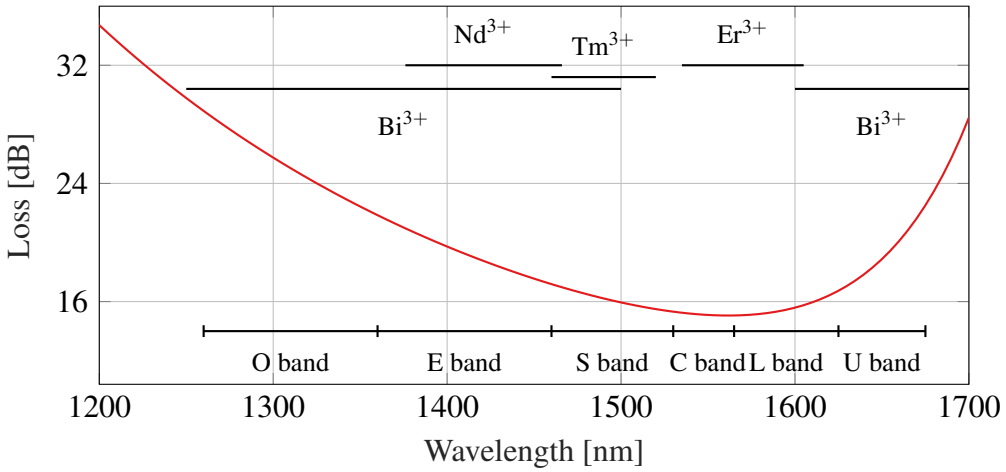

Figure 2.11: Loss (required gain) after propagation in a 80 km SMF based span using the profile shown in Fig. 2.4. Demonstrated amplification windows of a variety of rare-earth dopants are also shown [13–16]. The results shown in the figure neglect inter-channel stimulated Raman scattering.

to have an amplification window from 1250-1500 nm [15] and 1600-1700 nm [16]. Furthermore, it has been shown that the Bismuth-Erbium co-doped fibres can lead to a seamless amplification window with demonstrations of 15 dB gain from 1515-1775 nm [88]. Fig. 2.11 shows the required gain after propagating through 80 km of a SMF, using the loss profile as in Fig. 2.4, together with the demonstrated amplification bands for rare-earth-doped fibre-amplifiers. The power transfer due to inter-channel stimulated Raman scattering was not included. Fig. 2.11 shows that, in principle, the entire low-loss window of the SMF can be amplified and, thus, used to increase transmission rates. However as TDFAs are already readily available, this strongly relies on the commercial availability of Bismuth and Neodymium doped fibre-amplifiers providing gains of up to 30 dB gain.

2.4.2 Distributed Raman amplification

In addition to lumped implementations, optical amplification can be carried out in a distributed manner by utilising the effect of stimulated Raman scattering (see Sec. 2.3.2.2). A high power laser is injected into the propagating fibre, typically spaced by 13 THz with respect to the amplifying signal, in order to achieve the maximum Raman coupling (cf. 2.7). In contrast to doped-fibre amplifiers, the propagation fibre itself serves as the gain medium. Different configurations are possible including forward pumping, backward pumping or both at the same time. Typically, backward pumping is employed in order to reduce the relative intensity noise (RIN) [89]. RIN originates from the transfer of pump power fluctuations onto the signal wave, leading to signal distortions. These distortions are reduced using backward pumping

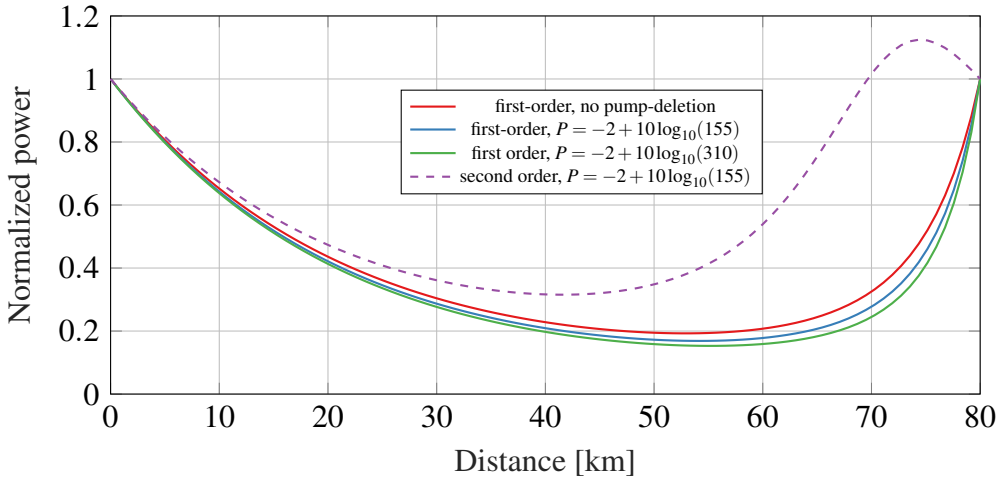

Figure 2.12: Signal power profiles for first-and second order-Raman pumping. Different optical bandwidths, a 155 channel and a 310 channel system, are shown to illustrate the effect of pump depletion.

as the pump and the signal propagate in opposite directions, leading to more averaging and reduced RIN as a consequence. Multiple Raman pumps can be used in order to achieve a flat gain profile across the signal (amplification) bandwidth [90]. Configurations, where the pump itself is amplified by another Raman pump, reduce the total ASE noise, referred to as second-order Raman amplification. This can be used to allow for reach extension [91] or to achieve more symmetric power profile, which is a key enabler for, e.g., optical-phase conjugation [92].

Similar to the mathematical description of ISRS (2.27), distributed Raman amplification is described by a system of coupled differential equations, depending on how many pumps are used [93–95]

$$\begin{aligned}
\frac{\partial P}{\partial z} &= \alpha P - g_{\mathrm{R}}\left(\left|f_c - f_{\mathrm{p}}\right|\right) P P_{\mathrm{p}}, \\
\frac{\partial P_{\mathrm{p}}}{\partial z} &= -\alpha_{\mathrm{p}} P_{\mathrm{p}} - \frac{\lambda_{\mathrm{ref}}}{\lambda_p} g_{\mathrm{R}}\left(\left|f_c - f_{\mathrm{p}}\right|\right) P P_{\mathrm{p}} + g_{\mathrm{R}}\left(\left|f_{\mathrm{p2}} - f_{\mathrm{p}}\right|\right) P_{\mathrm{p}} P_{\mathrm{p2}}, \\
\frac{\partial P_{\mathrm{p2}}}{\partial z} &= -\alpha_{\mathrm{p2}} P_{\mathrm{p2}} - \frac{\lambda_p}{\lambda_{p2}} g_{\mathrm{R}}\left(\left|f_{\mathrm{p2}} - f_{\mathrm{p}}\right|\right) P_{\mathrm{p}} P_{\mathrm{p2}},
\end{aligned} \tag{2.35}$$

where P_p is the power profile of the first-order pump with loss coefficient a_p at λ_p (frequency f_p), P_{p2} is the power profile of the second-order pump with loss coefficient a_{p2} at wavelength λ_{p2} (frequency f_{p2}), P is the signal power profile at reference wavelength λ_{ref} (frequency f_c). It should be noted that the distance z in (2.35) is defined relative to the propagation direction of the pumps (i.e. $z = 0$ defines the end of the fibre).

With the combination of forward, backward pumping as well as higher-order pumping, different signal power profiles can be realised with different nonlinear and ASE performances. Another effect that occurs using distributed amplification is pump depletion. The term $-\frac{\lambda_{\text{ref}}}{\lambda_p} g_{\text{R}} \left(\left| f_c - f_{\text{p}} \right| \right) P P_{\text{p}}$ in Eq. (2.35) ensures energy conservation and as the signal is being amplified the pump itself is being depleted. This effect increases with increasing total signal power and therefore with increasing channel count (assuming constant power per channel).

To illustrate different signal power profiles for first-and second-order backward pumping, Eq. (2.35) was numerically solved using the Runge-Kutta method. The results assume a symbol rate of 32 GBd and a channel power of -2 dBm per channel and are shown in Fig. 2.12. A signal containing 155x32 GBd channels (approximately the entire C-band) and one containing 310x32 GBd channels (C+L band) are shown. It can be seen that, indeed, pump depletion increases with the number of transmitted channels (i.e. with the total power).

The noise power for Raman amplified systems is obtained by integrating the signal power profile via

$$P_{\text{ASE}} = B_{\text{ref}} n_{\text{sp}} h f_0 G(L) \int_0^L \frac{P_p(z)}{\tilde{G}(z)} dz, \tag{2.36}$$

where $\tilde{G}(z) = \exp\left(\int_0^z g_R(f) \frac{P_p(\zeta)}{a_p} d\zeta \right)$. Raman amplification generally introduces less ASE noise with respect to doped fibre-amplifiers. Distributed Raman amplifiers exhibit excellent noise figures with respect to their lumped counterparts. Both effects combined result in improved overall system performance (SNR) in Raman amplified systems.

Recent high-capacity experiments for C+L band transmission include Raman amplification in combination with lumped amplification for better performance and to overcome the amplification gap between the C and L band [84, 96]. Ultra-wide bandwidth transmission using all-Raman has been shown in [97] where an amplification bandwidth of 94.5 nm was demonstrated. However, the high throughput of 102.3 Tb/s was only achieved over a rather short distance of 240 km. As part of the work of this thesis, a throughput of 74.38 Tb/s over 6300 km was achieved using a hybrid Raman/EDFA amplifier, covering a continuous bandwidth of 91 nm [98]. The use of hybrid Raman/EDFA amplifiers impose a strong wavelength dependence of the system performance due to ISRS as only part of the spectrum is amplified by the Raman amplifier. As a consequence of the strong wavelength dependence, the spectral distribution of the launch power must be optimised in order to maximise the total throughput. The new analytical model derived in Ch. 3 was applied to

perform the launch power optimisation in the experimental setup in [98].

2.5 Digital nonlinearity compensation

In addition to extending the optical bandwidth, the SNR can be improved in order to increase transmission throughput (cf. (2.3)). The SNR includes noise sources originating from transceiver, spontanenous ASE noise and fibre nonlinearity, where as the optical signal-to-noise ratio (OSNR) only includes noise from optical components (e.g. ASE noise). The SNR is formally defined in the next section 2.6.

For the remainder of this thesis, the receiver is assumed to consist of digital dispersion compensation (or digital-back propagation), ideal root-raised-cosine (RCC) matched filtering and constellation rotation. The SNR was then estimated as the ratio between the variance of the transmitted symbols $E[|X|^2]$ and the variance of the noise σ^2, where $\sigma^2 = E[|X-Y|^2]$ and Y represents the received symbols after digital signal processing. For the received symbols, only scaling and an ideal phase rotation (jointly applied to all symbols) was applied. It should be noted that different results in terms of SNR could be obtained using different approaches. For example, it has been shown that carrier phase estimation algorithms reduce the nonlinear interference power due to their temporal correlations [32, 52]. However, this effect is not considered in this thesis as no carrier phase estimation is performed.

To reduce the nonlinear distortions imposed by fibre nonlinearity, hence improve SNR, digital nonlinearity compensation has been proposed and investigated [24,99,100]. Most digital nonlinearity compensation techniques extend the physical link with a virtual link inverting the propagation equation and using the received signal as initial condition (see Eq. (2.5) with $\alpha \rightarrow -\alpha$, $\beta_2 \rightarrow -\beta_2$, $\beta_3 \rightarrow -\beta_3$, $\gamma \rightarrow -\gamma$, $T_R \rightarrow -T_R$). To date, three different implementations have been proposed in the literature, depending whether this virtual link is placed at the transmitter, called digital pre-compensation (DPC), receiver, called digital back-propgatation (DBP) or evenly split between them. This scheme is illustrated in Fig. 2.13, where the NLC algorithm is arbitrarily devided between transmitter and receiver. The link consist of n spans, where X spans are digitally pre-compensated at the transmitter and the remaining $n-X$ spans are digitally back-propagated at the receiver.

Digital back-propagation, has been the subject of numerous research papers as a method to enhance transmission performance [25, 99–103]. Reach increases of around 100% (from 640 km to 1280 km) have been experimentally demonstrated [44]. Overcoming the modest bandwidths of digital-to-analog converter and the use of mutually coherent sources (phase-locked spectral combs) enabled the application of DPC [104]. Reach gains of 100% (from 1530 km to 3060 km) [45] and even 200% (425 km to 1275 km) [46] have been experimentally shown using DPC.

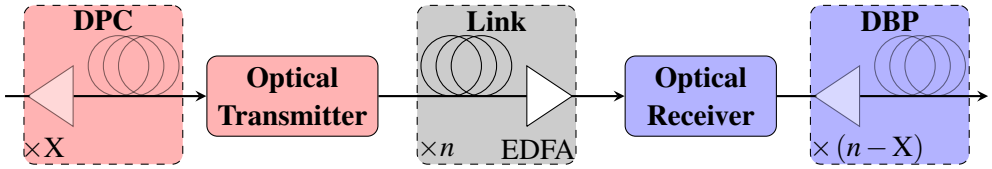

Figure 2.13: Illustration of digital nonlinearity compensation, where the digital nonlinearity compensation is arbitrarily divided between transmitter and receiver. The link consist of n spans, where X spans are digitally pre-compensated (DPC) at the transmitter and the remaining $n-X$ spans are digitally back-propagated (DBP) at the receiver.

It should also be mentioned that other digital nonlinear compensation techniques have been proposed which take advantage of the the long corrrelation time of the nonlinear inteference and use, e.g. Kalman filters, to reduce the induced nonlinear interference [32, 52]. However, in this section we will focus on digital nonlinearity compensation by means of digital back-propagation or pre-compensation.

Digital nonlinearity compensation is not able to fully compensate for stochastic effects, such as nonlinear interactions between the signal and co-propagating ASE noise or polarisation mode dispersion [40, 101]. In other words, as deterministic signal-signal nonlinearities are fully compensated by NLC, stochastic signal-noise interactions become performance limiting. The nonlinear signal-noise beating can be further minimised (and, therefore, performance maximised) by means of split NLC, as illustrated in Fig. 2.13 [41, 43, 105]. This implementation divides the virtual link evenly ($X = \lceil \frac{n}{2} \rceil$) between transmitter and receiver yielding SNR improvements of 1.5 dB compared to DBP ($X = 0$). However, up to date there is no experimental demonstration showing the benefits of split NLC. In chapter 4, it is experimentally demonstrated that nonlinear interactions between transceiver noise and the propagating signal become performance limiting, which has been overlooked in the literature prior to the research described in this PhD thesis. Using a new formula to predict nonlinear TRX noise signal interactions, it was proven that the optimum NLC split ratio is not one-half, which may explain why the predicted gains of split NLC have not been experimentally shown.

2.6 Analytical modelling

To accurately predict the performance of an optical fibre communication system, as in Fig. 2.1, the noise components arising from the transceiver sub-system, optical amplifiers (see Sec. 2.4) and fibre nonlinearity (see Sec. 2.3.2) must be taking into account, as they all degrade the SNR of the received signal. Assuming that all three noise sources are statistically independent, additive Gaussian noise sources,

the total SNR at the receiver can be written as

$$\mathrm{SNR} = \frac{P}{\kappa P + P_{\mathrm{ASE}} + P_{\mathrm{NLI}}} = \frac{P}{\kappa P + P_{\mathrm{ASE}} + \eta_n P^3}, \tag{2.37}$$

with $\kappa = \mathrm{SNR}_{\mathrm{TRX}}^{-1}$, where $\mathrm{SNR}_{\mathrm{TRX}}$ is the transceiver (i.e. back-to-back) SNR and P_{NLI} is the nonlinear interference power, describing the nonlinear distortions imposed by the optical Kerr effect. Eq. (2.37) assumes that all noise sources are AWGN. The total noise power (i.e. variance of the AWGN distribution) can therefore be obtained by simply adding the noise powers (variances) of the individual noise contributions. In order to express the launch power dependence of the SNR, it is convenient to introduce a nonlinear interference coefficient as $\eta_n = P_{\mathrm{NLI}} P^{-3}$, with η_n the nonlinear interference coefficient after span n. The nonlinear interference coefficient is a normalisation of the NLI noise power, such that the NLI coefficient becomes independent of the optical launch power.

All transceiver impairments are summarised by the transceiver SNR, which is the SNR in the absence of a transmission fibre and therefore the maximum achievable SNR for the transmission system. Transceiver impairments include quantisation noise due to the finite resolution of digital-to-analog converters (DAC) and analog-to-digital converters (ADC), noise contributions from linear electrical amplifiers as well as impairments due to optical transceiver components and blind DSP implementations. The transceiver noise contribution is often ignored in theoretical studies, however, it represents a significant noise contribution in the total system performance.

The optimum launch power and SNR can be obtained by setting the derivative of Eq. (2.37) to zero and solving for the optimum launch power P_{opt}. Inserting the optimum launch power in the SNR equation (2.37) yields the optimum SNR as

$$\mathrm{SNR}_{\mathrm{opt}} = \frac{1}{\kappa + \sqrt[3]{\frac{27}{4} P_{\mathrm{ASE}}^2 \eta_n}}, \tag{2.38}$$

with optimum launch power as

$$P_{\mathrm{opt}} = \sqrt[3]{\frac{P_{\mathrm{ASE}}}{2\eta_n}}. \tag{2.39}$$

Eq. (2.39) reveals that the maximum SNR is achieved when the nonlinear interference power is half the ASE noise power, mathematically $\eta_n P_{\mathrm{opt}}^3 = \frac{1}{2} P_{\mathrm{ASE}}$. Although, Eqs. (2.38) and (2.39) are often referred to in the literature as optimum SNR and launch power [106, 107], this is not strictly true. The reason is that the NLI coeffi-

cient itself is a function of the (normalised) launch power distribution which is not accounted for, in deriving Eq. (2.39), where it was assumed that the NLI coefficient is *independent* of the launch power distribution and that every channel can be optimised independently. However, the actual optimum launch power distribution only deviates slightly from Eq. (2.39) (≤ 0.3 dB as shown in [17]), and Eq. (2.38) serves as a good approximation.

2.6.1 First-order regular perturbation

While the ASE noise contribution can be obtained using the closed-form formula Eq. (2.33) and the transceiver SNR can be measured in back-to-back characterisations, the nonlinear SNR is obtained by solving the NLSE (2.5). This is done numerically using the SSFM (see Section 2.3.4), which has a very high computational complexity due to the repeated use of large fast Fourier transforms. As a low complexity alternative, the use of first-order perturbation theory has been proposed to obtain an analytical solution (to first order) of the NLSE [20, 27–29, 31, 32, 108]. These analytical models yield vast complexity reductions, enabling real-time performance estimation [109]. This is vital for efficient system design [110], physical layer aware optical networking [111] and real-time system optimisation [17]. Additionally, analytical models reveal unique insight into the underlying parameter dependencies.

Most analytical approaches rely on a regular first-order perturbation (RP1) approach, with the exception of [32] which proposes a logarithmic perturbation approach. Both approaches are accurate as long as the induced nonlinear perturbation (i.e. distortion, interference) is small with respect to linear distortions. The approach has been shown to be accurate (<0.1 dB error in NLI power) for optimum launch power [33]. Most communications systems are operated at or around the optimum launch power, making the RP1 approach a powerful tool for performance prediction. Within the RP1 approach, the electric field is written as a perturbation series with respect to the nonlinearity parameter γ as

$$Q(f) = Q^{(0)}(f) + \gamma Q^{(1)}(f) + \mathscr{O}\left(\gamma^2\right). \tag{2.40}$$

Inserting the perturbation series (2.40) into the NLSE (2.6), neglecting second-order terms $\mathscr{O}\left(\gamma^2\right)$ and separating zeroth and first-order terms yields

$$\begin{aligned} \frac{\partial}{\partial z} Q^{(0)}(f) &= \hat{\Gamma}(f)\, Q^{(0)}(f), \\ \frac{\partial}{\partial z} Q^{(1)}(f) &= \hat{\Gamma}(f)\, Q^{(1)}(f) + j Q^{(0)}(f) * Q^{*(0)}(-f) * Q^{(0)}(f), \end{aligned} \tag{2.41}$$

with the complex propagation constant $\hat{\Gamma}(f) = -\frac{\alpha}{2} + j2\pi^2\beta_2 f^2 + j\frac{4}{3}\pi^3\beta_3 f^3$. In principle, higher-order terms with respect to the nonlinearity coefficient can be easily included using the same procedure. However, higher-order terms are negligible around optimum launch power (2.39) and, therefore, of minor interest. The zeroth-order solution of (2.41) is simply the linear part of the NLSE (see 2.3.1) and its solution is given by (2.8). Using the initial condition for the first-order field $Q^{(1)}(z=0,f)=0$, the first-order solution is given by

$$Q^{(1)}(L,f) = e^{\hat{\Gamma}(f)L}\int_0^L \frac{Q^{(0)}(\zeta,f) * Q^{*(0)}(\zeta,-f) * Q^{(0)}(\zeta,f)}{e^{\hat{\Gamma}(f)\zeta}} d\zeta. \tag{2.42}$$

Eq. (2.42) represents the basis of first-order analytical models, where the RP1 is either carried out in the frequency domain as in (2.42) [20, 27–32] or in the time domain [31, 33, 34], which are both connected through a 3-dimensional Fourier transform [112]. While frequency domain models treat NLI as AWGN, time domain representations offer quantitative insight into the phase noise component of NLI as well as temporal correlations of the nonlinear interference [32, 33].

The published RP1 approaches can be mainly categorised into two groups, depending on the ability to account for arbitrary modulation formats. Those two groups can be further sub-divided whether those models are expressed in integral or in closed-form. Models, expressed in integral form, are highly accurate but rely on numerical integration whose execution times may range from minutes to hours. Closed-form approximations, on the other hand, can be computed in sub-seconds but are less accurate compared to their counterparts in integral form. The different modelling approaches are schematically shown in Fig. 2.14 and discussed in detail in the next sections.

2.6.2 The Gaussian Noise (GN) model

As shown in Fig. 2.14, available RP1 approaches can be categorised, depending on the assumed signal constellation at the transmitter (i.e. modulation format dependent or independent). Mathematically, this corresponds to the initial condition of the zeroth order solution in Eqs. (2.41)(2.42) (the initial condition of the first-order solution is zero).

The first analytical model in the context of modern coherent systems was derived assuming Gaussian constellations [27, 29] which later became widely known as the Gaussian Noise (GN) model [49]. To be more precise, the GN model assumes an infinitely narrow frequency comb, spectrally shaped according to the PSD of transmitted signal and where each spectral line carries a complex, circular Gaussian

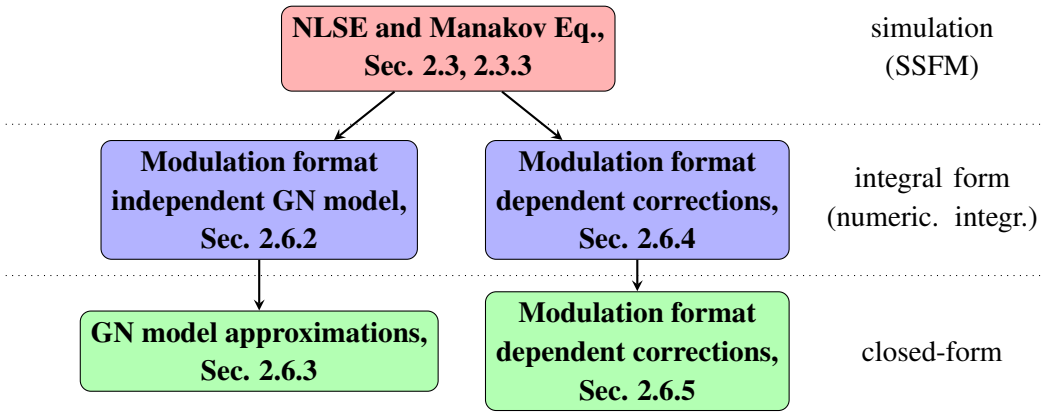

Figure 2.14: Approaches of modelling nonlinear distortions categorised into numerical simulations and analytical models in integral form and proposed closed-form approximation. The shown models do not account for utra-wideband effects such as ISRS.

distributed symbol ξ_n. The signal assumption of the GN model is written as [113]

$$Q(z=0,f) = \sqrt{f_0 G_{\mathrm{Tx}}(f)} \sum_{n=-\infty}^{\infty} \xi_n \delta\left(f - n f_0\right), \tag{2.43}$$

where $f_0 \to 0$ and $G_{\mathrm{Tx}}(f)$ is the power spectral density of the signal at the transmitter. Eq. (2.43) assumes the signal to be a Gaussian process. However, in [53] it was shown that arbitrary signals do not converge to a jointly Gaussian process due to fibre propagation (even in the presence of a dispersion only). However, (2.43) is defined for mathemtical convenience and it is shown in Sec. 2.6.4 that the definition overestimates the amount of nonlinear interference of regular QAM formats. Following the signal definition as in Eq. (2.43), it immediately follows that the GN model is modulation format and symbol rate agnostic. First, assuming a Gaussian constellation (see Fig. 2.2) overestimates the amount of nonlinear interference with respect to uniform and shaped QAM formats. Secondly, as the signal consists of infinite Gaussian modulated frequency components, the NLI as predicted by the GN model is independent of symbol rate within a fixed optical bandwidth, because the GN model is not capable of distinguishing between different channels. This means that the nonlinear perturbation of one channel modulated at 100 GBd is the same as compared to four channels modulated at 25 GBd. Therefore, the GN model is not suitable for symbol rate optimisation [114]. The symbol rate dependence can be included with modulation format dependent models which are discussed in Sec. 2.6.4.

Inserting Eq. (2.43) and the solution of the linear NLSE (2.8) into Eq. (2.42) and exploiting the statistical independence of the symbols at different frequencies,

the power spectral density of the nonlinear perturbation on frequency f can be written as [29, 30, 49, 115]

$$G(z,f) = 2\gamma^2 \int df_1 \int df_2 \; G_{\mathrm{Tx}}(f_1) G_{\mathrm{Tx}}(f_2) G_{\mathrm{Tx}}(f_1+f_2-f) \left| \frac{1-e^{-\alpha L - j4\pi^2(f_1-f)(f_2-f)[\beta_2+\pi\beta_3(f_1+f_2)]L}}{-\alpha + j4\pi^2(f_1-f)(f_2-f)\left[\beta_2+\pi\beta_3(f_1+f_2)\right]} \right|^2 . \tag{2.44}$$

Eq. (2.44) represents the GN model for one polarisation. The dual polarisation case can be obtained by replacing $2\gamma^2 \rightarrow \frac{16}{27}\gamma^2$ [116].

The GN model is often attributed to the group of Politecnico di Torino. However, Eq. (2.44) was first reported in 1995 in the PhD thesis of C. Kurtzke (with co-authors A. Splett and K. Petermann) [115, Eq. (13.22)], written in German. In English , Eq. (2.44) was first published in 1993 [27, Eq. (4)] in the absence of loss ($\alpha = 0$), and in 2002 including the loss coefficient [29, Eq. (7)].[1] The GN model can be derived for arbitrary signal power profiles (see Section 2.4). The GN model for backward-distributed Raman amplifications has been derived in [20]. The nonlinear interference coefficient can be simply obtained by integrating the NLI PSD (2.44) over the bandwidth of interest and normalising by the channel launch power as

$$\eta_n = \frac{1}{P^3} \int_{-\frac{B_{\mathrm{ch}}}{2}}^{\frac{B_{\mathrm{ch}}}{2}} |H(f)|^2 G(f)\, df \approx \frac{B_{\mathrm{ch}}}{P^3} G(f_i), \tag{2.45}$$

where $|H(f)|^2$ is the transfer function of the matched filter at the receiver. The approximation in Eq. (2.45) assumes a rectangular transfer function equal to the channel bandwidth and that the NLI is uniformly distributed over the channel bandwidth. The approximation error is negligible in WDM systems with very dense channel spacing (e.g. Nyquist-spacing). The approximation in Eq. (2.45) is particularly useful for the derivation of closed-form approximations of the GN model, as arbitrary matched filter shapes are difficult to include analytically.

The GN model after one span can be extended for the multi-span case by including the phased-array term in the integration of (2.44) [115]

$$\chi(f_1,f_2,f) = \left| \frac{\sin\left[n2\pi^2(f_1-f)(f_2-f)\left[\beta_2+\pi\beta_3(f_1+f_2)\right]L\right]}{\sin\left[2\pi^2(f_1-f)(f_2-f)\left[\beta_2+\pi\beta_3(f_1+f_2)\right]L\right]} \right|^2 . \tag{2.46}$$

[1] To aid comparison the third integral in the second term in [29, Eq. (7)] resolves with the Dirac delta function at $\omega_3 = \omega_0 - \omega_1 + \omega_2$. This leads to $f(\omega_0,\omega_1,\omega_2,\omega_3) = j\beta_2(\omega_0-\omega_1)(\omega_2-\omega_1)$. Change of integration variables leads to Eq. (2.44), with $\beta_3 = 0$.

The phased-array term, resembling the formula of the far-field of a phased-array antenna, captures the accumulation of NLI over multiple spans. Mathematically, the phased-array term is a result when all spans are considered identical in terms of fibre parameter and transmitted spectrum. In particular it captures the coherent accumulation of NLI, referred to as the *coherent* GN model. The coherent accumulation is the effect that the total NLI over multiple spans is larger than the sum of the individual NLI contributions of each span alone. It should be added that this holds for dispersion uncompensated transmission links and *not* for arbitrary dispersion maps. For ultra-wideband transmission, this coherent accumulation is very small ($\varepsilon \approx 0.04$ after [20]) and the NLI accumulation can be considered incoherent and linear with the number of spans n. The incoherent NLI accumulation of the GN model was first shown in [29] and later it was based on more mathematical arguments and referred to as the *incoherent* GN model [20]. The coherent GN model always overestimates the amount of NLI with respect to uniform or shaped QAM formats due to the neglected modulation format dependence. The modulation format dependence of the NLI is discussed in more detail in Sec. 2.6.4. Thus, the incoherent GN model appears to be more accurate in the prediction of QAM formats compared to its coherent counter-part [117]. However, this is a fallacy as the source of the improvement does not originate from a more precise model but from error cancellation between neglecting the coherence factor (i.e. coherent accumulation) and neglecting the impact of the modulation format correction. The Gaussian constellation assumption always overestimates the NLI, with respect to QAM formats. On ther other hand, the incoherent NLI addition always reduces the predicted NLI. The two arising approximation errors partly cancel each other, resulting in (so it seems) increased prediction accuracy with respect to QAM formats. The incoherent GN model is less accurate for Gaussian constellations, which the GN model is derived for.

Although the proposed RP1 based models, such as the GN model, are widely applied throughout research and industry, they cannot be applied to optical bandwidths beyond the C-band. This is because they neglect ISRS, which becomes significant in the transmission over C+L band and beyond (see Section 2.3.2.2). As part of this thesis, an extension of the GN model, that accurately accounts for ISRS, is derived and described in chapter 3 . The newly derived model overcomes a major shortcoming of all models presented in this chapter and has been published in [P8, P13, P27].

2.6.3 Approximations of the GN model in closed-form

The GN model relies on numerical integration of Eq. (2.44) which can take up a considerable amount of time, particularly in the context of real-time applications. Such applications include on-the-fly power optimisations, physical layer aware wavelength allocations in routing-wavelength allocations and other optimisation problems that contain a very large solution space. To avoid the need for numerical integrations, and, hence, obtain computational complexity reductions, the GN model can be approximately solved in closed-form. This enables real-time optimisation routines and further offers unique insight in the underlying parameter dependencies. Such insight reveals useful scaling laws which can be utilised in design and operations of fibre based communication systems. Several closed-form approximations have been proposed in the literature which approximate the nonlinear interference coefficient for the central channel after one span as $\eta_1 \approx \frac{B_{\text{ch}}}{P^3} G(0)$, following Eq. (2.45).

Closed-form approximations of the GN model have been proposed for lossless [27, 109] and lossy fibres. In the latter category, the published approximations mainly differ in the geometric approximation of the integration domain of Eq. (2.44), where circular and rectangular integration domains have been considered [20,28,49,118]. A comparable closed-form formula was also derived assuming OFDM signals [119]. The proposed formulas are summarised in Table 2.1. The formulas in [27, 28, 119] were derived for the NLSE, assuming only one polarisation, while the other reported formulae are derived base on the Manakov equation Eq. (2.29), to account for dual polarisation transmission.

Table 2.1: GN model approximations in closed-form for a single span η_1

Reference	**Formula for η_1**	**Improvements / assumptions**
1993, [27]	$\frac{4\gamma^2 L}{B_{\text{ch}}^2 \pi \beta_2} \left[1 + \ln\left(2\pi L \beta_2 B_{\text{tot}}^2\right)\right]$	lossless fibre
2003, [28]	$\frac{\gamma^2 L_{\text{eff}}}{\Delta f^2 \pi \beta_2} \ln\left[\pi^2 L_{\text{eff}} \beta_2 (N_{\text{ch}} \Delta f)^2\right]$	ext. [27] for loss & non-Nyquist
2010, [119]	$\frac{\gamma^2}{\Delta f^2 \pi a \beta_2} \ln\left(2\pi^2 \beta_2 \frac{(N_{\text{ch}} \Delta f)^2}{a}\right)$	derived for OFDM
2011, [49]	$\frac{8}{27} \frac{\gamma^2 L_{\text{eff}}}{B_{\text{ch}}^2 \pi \beta_2} \ln\left[\pi^2 L_{\text{eff}} \beta_2 (N_{\text{ch}} \Delta f)^2\right]$	extends [28] for dual pol.
2011, [109]	$\frac{8}{27} \frac{\gamma^2 L}{B_{\text{ch}}^2 \pi \beta_2} \ln\left[\pi^2 n L \beta_2 (N_{\text{ch}} \Delta f)^2\right]$	ext. [27] for dual pol., lossless fibre
2012, [20]	$\frac{8}{27} \frac{\gamma^2 L_{\text{eff}}^2 a}{B_{\text{ch}}^2 \pi \beta_2} \text{asinh}\left(\frac{\pi^2 \beta_2 B_{\text{tot}}^2}{2a}\right)$	
2013, [118]	$\frac{8}{27} \frac{\gamma^2 L_{\text{eff}}^2 a}{B_{\text{ch}}^2 \pi \beta_2} \text{asinh}\left(\frac{4\pi^2 \beta_2 B_{\text{tot}}^2}{3a}\right)$	extends [49] for low symbol rates

The difference of the closed-form approximations listed in Table 2.1 with respect to the numerical integration of Eq. (2.44) as a function of total optical bandwidth is shown in Fig. 2.15. The numerical integration of Eq. (2.44) can be considered as

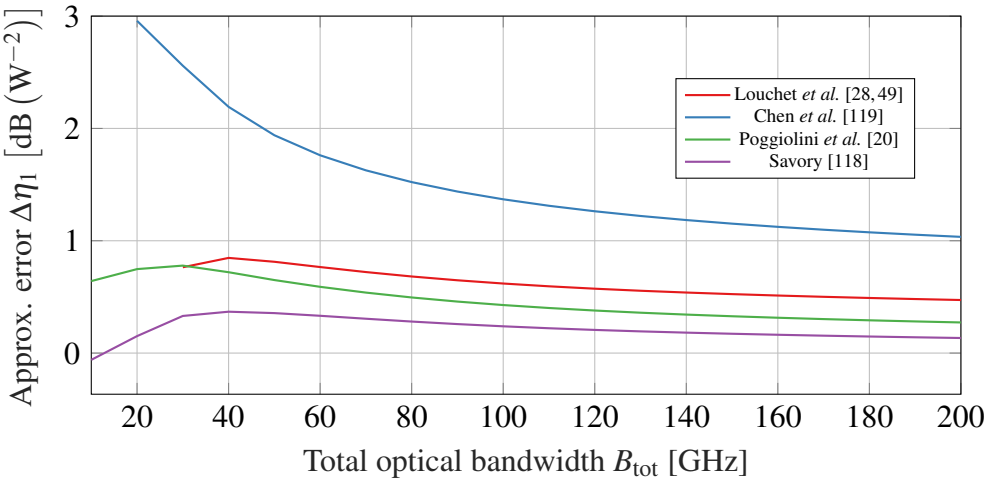

Figure 2.15: The approximation error of proposed closed-form approximations in the literature as a with respect to the GN model in integral form (2.44) as a function of optical bandwidth

the true NLI power. The excellent accuracy (<0.1 dB) of the GN model compared to SSFM simulation is shown in Fig. 2.16. The results were calculated assuming one span of SMF with $\gamma = 1.2\ \frac{1}{\text{W·km}}$ and length 80 km and a symbol rate of 10 GBd. WDM channels were successively added with a channel spacing of 10.001 GHz in order to sweep the total optical bandwidth. The formulas in [28,119] were extended for the dual polarisation case by replacing $2\gamma^2 \rightarrow \frac{16}{27}\gamma^2$. The formulae in [28,49,119] are not not plotted for bandwidths below 20 GHz and 30 GHz, as they were derived for large bandwidths ($\pi^2 L_{\text{eff}} \beta_2 (N_{\text{ch}} \Delta f)^2 > 1$). It can be seen from Fig. 2.15 that the approximation errors of the shown formulas become constant for sufficiently large optical bandwidths. This means that all shown formulas correctly predict the logarithmic growth of NLI for large optical bandwidths. However, the formula proposed in [118] exhibits the highest accuracy, particularly for low optical bandwidths. This is a consequence of the equivalent, circular integration area approach that was carried out in [118], resulting in better convergence for low bandwidths.

The closed-form formulas in Table 2.1 analytically address the NLI coefficient after a single span. All works consider an incoherent (i.e. linear) NLI accumulation over mutliple spans with the exception of [119], in the context of orthogonal frequency devision multiplexing (OFDM), and [20], in the context of Gaussian modulation. The impact of the coherent NLI accumulation, mathematically described by the phased-array function (2.46), can be defined as [20]

$$\eta_n = \eta_1 n^{1+\varepsilon}, \tag{2.47}$$

where $\varepsilon \in [0,1]$ is the coherence factor [29]. It should be emphasised that a scaling law, as in Eq. (2.47), is only valid for Gaussian signals. This is due to the fact that accumulated dispersion does not change the signal statistics of a Gaussian modulated signal. Therefore, the coherent accumulation over multiple spans is approximately constant. Available formulas in closed-form for the coherence factor are summarised in Table 2.2. Although [119] reveals parameter dependencies such as the attenuation coefficient and span length it does not account for the strong dependence on bandwidth [20, 29]. In fully populated, ultra-wideband transmission systems, the NLI accumulation is approximately incoherent which is correctly captured by [20].

Table 2.2: GN model approximations in closed-form for the coherent NLI accumulation

Reference	**Formula for coh. acc. ε**	**Major improvements**
2010, [119]	$\frac{1}{\ln(n)} \ln\left[1+\frac{2}{n}\frac{\left(n-1+e^{-aLn}-ne^{-aL}\right)e^{-aL}}{\left(e^{-aL}-1\right)^2}\right]$	
2012, [20]	$\frac{1}{\ln(n)} \ln\left[1+\frac{2}{naL}\frac{1-n+n\mathrm{Har}(n-1)}{\mathrm{asinh}\left(\frac{\pi^2}{a}\beta_2 B_{\mathrm{tot}}^2\right)}\right]$	imporves acc. of [119]

The formulas in Table 2.1 cannot be applied for arbitrary launch power distribution. However, the precise modelling of arbitrary signal spectra is important in the context of mesh optical networks. In mesh optical networks, different WDM spectra are launched into links connected by two reconfigurable optical add-drop multiplexer (ROADM) as a result of the routing-wavelength allocations (RWA) and time varying traffic demands. These conditions impose a strong NLI dependence depending on the frequency location of the channel under test [120]. To optimise, e.g., launch power, wavelength assignment, in such scenarios closed-form approximations capable of handling arbitrary WDM combs are required. The GN model (2.44) can be approximated in such a scenario by considering only self-phase modulation (SPM) and cross-phase modulation (XPM) terms. SPM denotes the NLI contribution that a channel imposes on itself and XPM denotes the NLI contribution that a single interfering channel (INT) imposes on the channel of interest (COI). This assumption is sometimes referred to as the XPM assumption. The XPM assumption neglects terms that are jointly generated by multiple interfering channels and the COI itself, denoted as the FWM contribution. However, the FWM contribution is negligible in systems with high symbol rates and channel spacings ($>$ 40 GHz) [121]. Based on the XPM assumption, the total NLI coefficient at frequency $f_i = 0$ can be approximated as

$$\eta_1(f_i) \approx \eta_{\mathrm{SPM}}(f_i) + \sum_{k=1,k\neq i}^{N_{\mathrm{ch}}} \eta_{\mathrm{XPM}}^{(k)}(f_i), \tag{2.48}$$

where η_{SPM} is the SPM contribution of the COI and $\eta_{\mathrm{XPM}}^{(k)}$ is the XPM contribution of a single interfering channel k on COI i. Both contributions can be be solved in closed-form as [20, 21]

$$\eta_{\mathrm{SPM}} \approx \frac{8}{27}\frac{\gamma^2 L_{\mathrm{eff}}^2 \alpha}{\pi^2 B_{\mathrm{ch}}^2 \beta_2} j\left[\mathrm{Li}_2\left(-j\pi^2\frac{\beta_2}{\alpha}B_{\mathrm{ch}}^2\right) - \mathrm{Li}_2\left(j\pi^2\frac{\beta_2}{\alpha}B_{\mathrm{ch}}^2\right)\right], \tag{2.49}$$

and

$$\begin{aligned}\eta_{\mathrm{XPM}}^{(k)}(f_i) \approx \frac{8}{27}\frac{\gamma^2 L_{\mathrm{eff}}^2 \alpha}{\pi^2 B_{\mathrm{ch}}^2 \beta_2}\frac{P_k^2}{P_i^2} \\ \left\{ j\left[\mathrm{Li}_2\left(-j\pi^2\frac{\beta_2}{\alpha}\left(f_k+\frac{1}{2}B_{\mathrm{ch}}\right)B_{\mathrm{ch}}\right) - \mathrm{Li}_2\left(j\pi^2\frac{\beta_2}{\alpha}\left(f_k+\frac{1}{2}B_{\mathrm{ch}}\right)B_{\mathrm{ch}}\right)\right]\right. \\ \left. - j\left[\mathrm{Li}_2\left(-j\pi^2\frac{\beta_2}{\alpha}\left(f_k-\frac{1}{2}B_{\mathrm{ch}}\right)B_{\mathrm{ch}}\right) - \mathrm{Li}_2\left(j\pi^2\frac{\beta_2}{\alpha}\left(f_k-\frac{1}{2}B_{\mathrm{ch}}\right)B_{\mathrm{ch}}\right)\right]\right\}\end{aligned} \tag{2.50}$$

where $\mathrm{Li}_2(x)$ denotes the di-logarithm function, f_k is the centre frequency of channel k and P_i and P_k the respective channel powers. Eq. (2.49)(2.50) are capable of handling arbitrary channel powers (including the absence of channel with launch power 0) and are suitable for various optimisation problems in point-to-point and mesh optical networks scenarios.

The advantages of the Gaussian Noise model are also its major drawbacks. Due to its simplicity, it is not capable of predicting certain features of the nonlinear interference. The major source of inaccuracy stems from the assumption that the signal is Gaussian, which significantly overestimates the actual NLI power for uniform or shaped QAM signal. However, correction formulae have been proposed which will be discussed in more detail in the next section. Other, less significant, features of NLI include symbol rate dependence [120, 122–125] (also addressed in the next section), nonlinear phase noise [33, 51], long temporal correlations [32, 33] and the dependence on the memory length (arising from dispersion) of the fibre-optic channel [126].

The closed-form formulas in this section, do not account for ISRS and are therefore not applicable in ultra-wideband transmission scenarios. However, in chapter 4 a closed-form approximation of the ISRS GN model is proposed. The formula is an approximation of the ISRS GN model, which was developed as part of this thesis and discussed in detail in chapter 3. Additionally, the closed-form approaches presented in this section (and published in the literature) are also applicable for lossless fibres or lumped-amplified transmission systems.

Table 2.3: Excess kurtosis of selected modulation formats.

Modulation format	Excess kurtosis Φ
uniform QPSK	-1
uniform 16-QAM	-0.6800
uniform 64-QAM	-0.6190
uniform 256-QAM	-0.6050
uniform ∞-QAM	-0.6000
geom. shaped 64-QAM (12 dB SNR, GMI) [127]	-0.3403
proba. shaped 64-QAM (12 dB SNR, MI) [50]	-0.1871
Gaussian modulation	0

2.6.4 Modulation format dependence of NLI

In 2012, based on a RP1 approach, it has been analytically shown that the nonlinear interference significantly depends on the chosen modulation format [31, 32]. Additionally, the authors were able to show that part of the overall NLI manifests itself as a pure phase-noise component. This phase-noise component is particularly significant for ideally distributed Raman amplification and low dispersion transmission systems [33, 51], but usually negligible in lumped, long-haul transmission systems. It could be shown that the XPM contribution of the nonlinear interference coefficient depends on higher-order moments of the transmitted constellation and can be written as

$$\eta_{\mathrm{XPM}}^{(k)}(f_i) = \eta_{\mathrm{XPM,\,GN}}^{(k)}(f_i) + \eta_{\mathrm{XPM,\,corr}}^{(k)}(f_i), \tag{2.51}$$

Interestingly, it seems that the total NLI can be written as a superposition of a Gaussian constellation (which is predicted by the GN model, Sec. 2.6.2) and a modulation format dependent correction term. Table 2.3 shows the excess kurtosis $\Phi = \frac{\mathrm{E}[X^4]}{\mathrm{E}^2[X^2]} - 2$, with expectation $\mathrm{E}[\cdot]$, of a few selected modulation formats. It can be seen that the kurtosis of common modulation formats is negative (being less peaky than a circular symmetric Gaussian distribution), meaning that the NLI is *reduced* by the modulation format correction term in (2.51).

Following up the work in [31, 33, 51], a complete set of formulas have been derived containing the modulation format correction for all arising terms (i.e. SPM, XPM+XCI, FWM terms) [117, 128], referred to as the enhanced Gaussian Noise (EGN) model. The derivation of the EGN model further revealed that the nonlinear interference, in addition to the fourth-order moment (kurtosis), depends on the sixth moment of the transmitted constellation. While the EGN model exhibits remarkable accuracy in terms of NLI power, it is, due to its description in the fre-

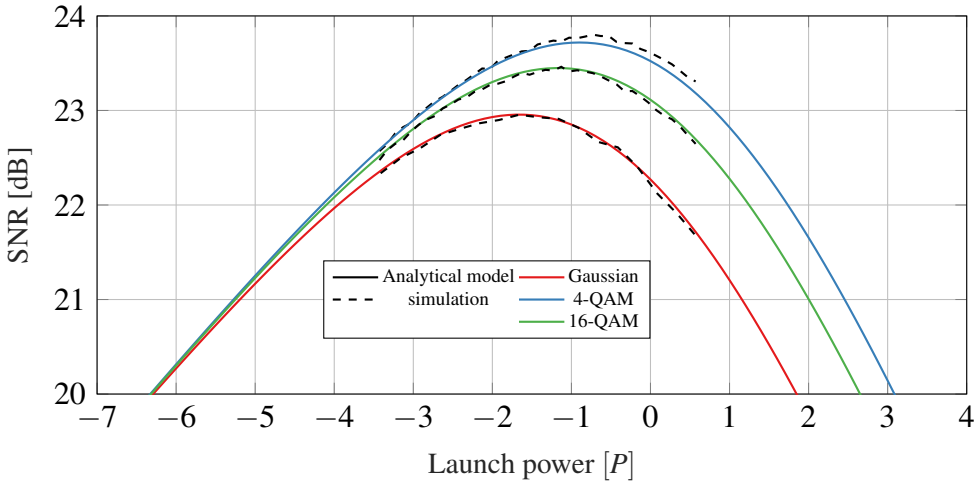

Figure 2.16: The SNR as a function of launch power for Gaussian modulation, uniform 4-and 16-QAM. The results were obtained from numerical simulation using the SSFM and using the EGN model. The results assume 5x32 GBd channels transmitted over lumped-amplified 5x80 km SMF based spans.

quency domain, not capable of predicting nonlinear phase noise and temporal NLI correlations. However, the EGN model represents a major improvement over the conventional GN model by improving the accuracy for arbitrary signal constellations.

Fig. 2.16 shows the SNR as a function of launch power, while Fig. 2.17 shows the SNR at optimum launch power (2.39) after 400 km of transmission. Both results were obtained by numerical simulations using the SSFM (see Sec. 2.3.4) and numerically integrating the EGN model. The fibre length was assumed to be 80 km based on SMF ($\alpha = 0.2$ $\frac{\text{dB}}{\text{km}}$, $D = 17$ $\frac{\text{ps}}{\text{km·nm}}$ and $\gamma = 1.2$ $\frac{1}{\text{W·km}}$) and amplified by an EDFA with a 4.5 dB noise figure. As transmitted signals, 5 channels modulated at 32 GBd and spaced by 32.1 GHz were assumed using Gaussian, 4-QAM and 16-QAM modulation. The step size was $\Delta z = 0.1$ km and the sequence length was 2^{15} symbols.

It can be seen that, indeed, the case of Gaussian modulation is always conservative, due to its high excess kurtosis shown in Tab. 2.3. As correctly predicted by the EGN model, the SNR (especially in the nonlinear regime at high launch powers) is increased for constellations with lower excess kurtosis. After 400 km, the optimum SNR for the 4-QAM and 16-QAM formats are 0.5 dB and 0.8 dB higher compared to Gaussian modulation, respectively. The gap between 4-QAM and Gaussian modulation reduces from 1.9 dB after 1 span to 0.6 dB after 30 spans. The GN model as in Eq. (2.44) is identical to the EGN model in the case of Gaussian modulation. In summary, the very simple GN model (2.44) is particularly useful in

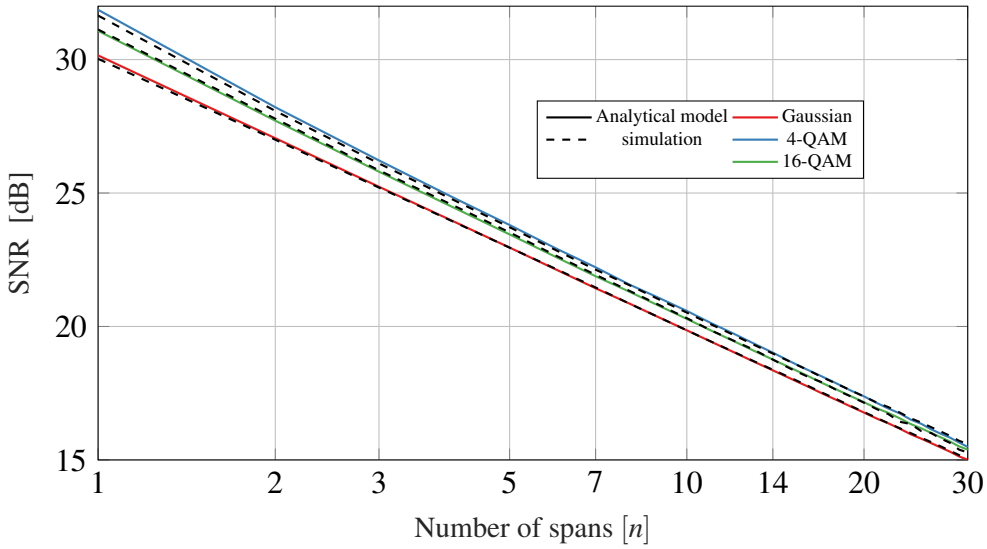

Figure 2.17: The optimum SNR (2.38) as a function of span number for Gaussian modulation, uniform 4-and 16-QAM. The results were obtained from numerical simulation using the SSFM and using the EGN model. The results assume 5x32 GBd channels transmitted over lumped-amplified 80 km SMF based spans.

long-haul systems, while the considerably more complex EGN model should be considered for short and medium-haul systems.

Experimental validations of the GN model can be found in [125, 129, 130], reporting accuracies within a few percent at maximum reach for several fibre types. The accuracy of the EGN model has been investigated in [131, 132] showing differences between experimental results for 16-QAM and EGN model of 0.2 dB in nonlinear interference coefficient and of around 1 dB with respect to the GN model [132]. As a caveat, accuracies reported in the literature may vary depending on the quantity that is subject to comparison. This is because analytical models only predict the nonlinear interference power (or coefficient) which is only one contribution of the total SNR (cf. Eq. (2.37)). Therefore, measurement inaccuracies with respect to other noise sources (transceiver noise, ASE noise) have an impact on the estimated accuracy of the nonlinear interference power.

2.6.5 Approximations of the modulation format dependence in closed-form

As addressed in Section 2.6.3, closed-form approximations that evaluate the nonlinear interference are key enabler for real-time performance estimations and optimisation routines. To improve the accuracy of the closed-form approximations of the GN model (see Section 2.6.3), approximations of the modulation format correc-

tion terms are desirable (see Section 2.6.4). The most dominant NLI contribution in WDM transmission, particularly in ultra-wideband systems, is the XPM contribution. Therefore, a closed-form approximation of the XPM modulation format correction, as in (2.51) would yield a large accuracy gain at little additional complexity respect to GN model closed-form formulas. A formula for the XPM modulation format correction for the central channel (a formula for any channel within the WDM comb can be found within the same work) has been derived in [22]

$$\eta_{\text{XPM, corr}}(0) \approx \frac{80}{81}\Phi\frac{\gamma^2 L_{\text{eff}}^2 n}{\pi B_{\text{ch}}\Delta f \beta_2 L}\text{Har}\left(\frac{N_{\text{ch}}-1}{2}\right), \tag{2.52}$$

where the harmonic number is $\text{Har}(n) = \sum_{k=1}^{n}\frac{1}{k}$. Eq. (2.52) has been derived in the asymptotic limit of a large number of spans $n \to \infty$. Thus, it does not sufficiently correct the modulation format dependence for short and metro-haul networks (consisting of only a few spans). However for long-haul systems, the relatively simple correction formula Eq. (2.52) exhibits very good accuracy of around 0.2 dB compared to numerical simulations for quasi Nyquist-spaced channels.

The formula proposed in Eq. (2.52) does not account for ISRS and cannot be applied for transmission systems that operate beyond the C-band. As part of this thesis, in chapter 4 a modulation format correction formula is derived, which accounts for the impact of ISRS. It therefore extends the published results in this chapter for ultra-wideband transmission systems.

2.6.6 Nonlinear signal-noise interactions

In scenarios where the nonlinear interference is partly or completely mitigated, Eq. (2.37) is not sufficient in the predicting of system performance and nonlinear signal noise interactions must be taken into consideration. In fact, for systems using, e.g., digital nonlinearity compensation (see Sec. 2.5), these signal-noise interactions become performance limiting [39].

The study of signal-noise interactions dates back to the 1960s, where it was referred to as modulation instability [133]. Early work of Gordon and Mollenauer resulted in a formula of the variance of the phase noise resulting from NSNI [134]. However, in the coherent age where links have high dispersion, the phase-noise character of the NSNI is broken down and mostly translated to amplitude noise. The first analytical approach to model NSNI was included in the work by Tang in [29] where signal constellation, as well as ASE noise, were assumed to follow a Gaussian process. Similar approaches in order to model NSNI as been carried out in [25,39–42]. In order to account for NLC and NSNI, Eq. (2.37) must be modified. In particular, DBP decreases the NLI coefficient and therefore ASE noise-signal in-

teractions, which were neglected previously, must be taken into consideration. The resulting SNR after NLC, assuming ideal, noiseless transceivers, can be estimated as [25, 41]

$$\mathrm{SNR} = \frac{P}{(\eta_n - \tilde{\eta}_n) P^3 + \kappa P + N P_{\mathrm{ASE}} + 3\tilde{\eta}_1 \xi_{\mathrm{ASE}} P_{\mathrm{ASE}} P^2}. \tag{2.53}$$

where ξ_{ASE} is the ASE noise-signal beating accumulation factor that depends on where nonlinearities are compensated (i.e. at the receiver or transmitter). For receiver based digital back-propagation $\xi = \sum_{i=1}^{n} i^{1+\tilde{\varepsilon}}$ and for transmitter based digital back propagation $\xi = \sum_{i=1}^{n-1} i^{1+\tilde{\varepsilon}}$. The NSNI coefficient $\tilde{\eta}_1$ is in general not the same as η_i as only 2 signal fields are involved and not 3 as in the case of η_i. The work in [135] shows that the modulation format dependent correction is smaller for $\tilde{\eta}_i$ than for η_i. This means that the modulation format dependence is less severe in the case of signal-noise interactions, which is plausible as only 2 modulated signal fields are involved in the four-wave mixing process. Additionally, NLC can only be applied over a portion of the entire optical bandwidth. In this case, the variables $\tilde{\eta}_i$ is evaluated over that particular bandwidth which is pre-compensated or back-propagated. Typically it is assumed that $\tilde{\eta}_i \approx \eta_i$ if NLC is jointly applied to the entire bandwidth (otherwise $\tilde{\eta}_i < \eta_i$). It has been shown that, Eq. (2.53) exhibits good accuracy with numerical simulations despite neglecting the impact of the modulation format dependence in calculating $\tilde{\eta}_i$ [43].

As part of this thesis, it was discovered that nonlinear interactions between the signal and transceiver noise become performance limiting in nonlinearly compensated transmission systems. As those interactions are not included in published SNR equations, such as Eq. (2.53), a new SNR formula was proposed for the performance computation. The formula was experimentally verified, showing inaccuracies of Eq. (2.53), and used in order to prove that the optimal split ratio of the DBP algorithm is distance dependent and not $X = \lceil \frac{N}{2} \rceil$ (half the link is compensated at each, the transmitter and receiver), as previously shown (see section 2.5).

Chapter 3

Inter-channel stimulated Raman scattering: Analytical modelling and its impact on ultra-wideband transmission

After describing the theoretical background in chapter 2, the novel contributions, as a result of this research, are presented and discussed. Increasing the transmitted optical bandwidth is key to maximise current throughput of optical fibre communication systems. With the increasing availability of rare-earth doped amplifiers beyond the C-band window or the use of hybrid Raman amplification techniques (see Ch. 2.4), ultra-wideband transmission is seen as a promising technology for next-generation optical networks. Additionally, ultra-wideband transmission makes use of the legacy infrastructure without the need for new fibre deployment.

However, for such ultra-wide bandwidths, the non-instantaneous nature of the nonlinear fibre response becomes significant, giving rise to inter-channel stimulated Raman scattering (ISRS) as described in Sec. 2.3.2.2. ISRS effectively transfers power from high to lower frequencies within the same optical signal. Although the physics of the interaction between the Kerr effect and ISRS are well understood (as described in Ch. 2.3.2.2), efficient low-complexity performance models for state-of-the art coherent systems were not available before the results of this PhD research. Low-complexity models are important for high-capacity transmission designs and technologies and they enable efficient operation and real-time optimisation of such systems in point-to-point and mesh optical network scenarios.

The analytical models published in the literature (prior to the research described in this thesis [P13]), and discussed in Sec. 2.6, do not account for ISRS and the wavelength dependence of the attenuation coefficient (cf. Fig. 2.4)

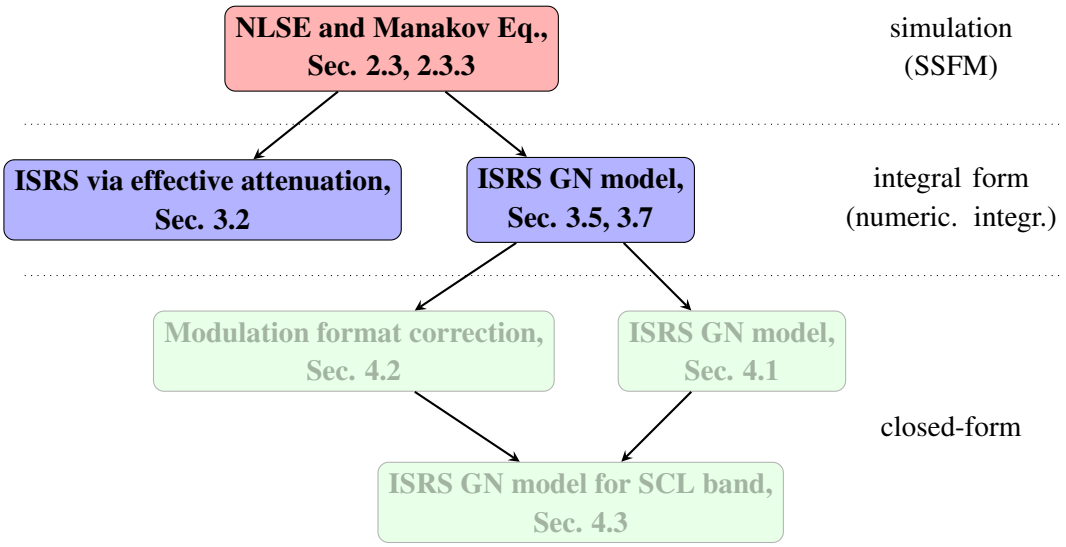

Figure 3.1: Approaches of modelling nonlinear distortions in the presence of inter-channel stimulated Raman scattering. Analytical models that account for ISRS in integral form are described in this chapter. Closed-form approximations and modulation format corrections of the nonlinear distortions are described in Ch. 4.

[20, 30–34, 113, 117, 119, 120, 122–125, 136]. It is, therefore, key to extend the RP1 models to account for ISRS, so that they can be applied to optical bandwidths beyond 5 THz.

The modelling of ISRS and its interplay with nonlinear distortions can be categorised into three groups: i) numerical simulations using SSFM, ii) analytical models in integral form using first-order regular perturbation (see. 2.6) and iii) closed-form approximations where RP1 models are approximated in closed-form. Models, expressed in integral form, are highly accurate but rely on numerical integration whose execution times may range from minutes to hours. Closed-form approximations, on the other hand, can be computed in sub-seconds but are less accurate compared to their counterparts in integral form. A schematic of those three groups in the context of ISRS modelling is shown in Fig. 3.1. This chapter describes approaches that analytically model nonlinear distortions in the presence of ISRS and whose results are expressed in integral form. In particular, an extension of the GN model is derived, that enables the quantification of ISRS and the wavelength dependent attenuation on the nonlinear distortions. This represents a key result of the research, described in this thesis, and is significant in the modelling of ultra-wideband transmission systems. In particular, two approaches are described to extend the conventional Gaussian noise model (see Sec. 2.6.2) for ISRS. However, the approaches are general and can be applied to a wider range of models, including the modulation format dependence (see Sec. 2.6.4).

First, an approach based on an effective attenuation coefficient is described in Sec. 3.1 and 3.2. The approach is based on an exponential decay approximation of the signal power profile and valid in the weak ISRS regime. The model is subsequently validated by an ultra-wideband transmission experiment, covering an optical bandwidth of 9 THz, in Sec. 3.3. Finally, enabled by the new model, the impact of ISRS on the achievable information rates is quantified, as the bandwidth is extended well beyond the C-band.

The second major contribution is a complete re-derivation of the GN model to account for arbitrary signal power profiles, i.e. those resulting from ISRS. The newly derived model is referred to as ISRS GN model and a major result of this PhD thesis. The model accounts for strong ISRS power transfers and, in contrast to the results in Sec. 3.2, is capable of modelling hybrid Raman amplified links. In Sec. 3.6, the effective attenuation approach, presented in 3.2, is compared to the ISRS GN model in terms of computational complexity and prediction accuracy. In Sec. 3.7, the ISRS GN model is extended to account for variably loaded spans in order to efficiently model mesh optical network transmissions.

The material presented in this chapter were published in peer reviewed conferences and journals [P8, P13, P22, P27]. The experimental results in Sec. 3.3 were published in collaboration with G. Saavedra [P29].

3.1 Modelling inter-channel stimulated Raman scattering

To quantify the impact of ISRS on the total SNR (2.37), the impact of ISRS on the ASE noise contribution and the nonlinear interference power must be modelled.

First, it is important to quantify the impact of ISRS on the ASE noise. To offset the wavelength dependent fibre loss and the power transfer induced by ISRS, a gain-flattening filter (GFF) can be used. At the end of a fibre span, the signal is amplified with a frequency dependent gain $G_{\mathrm{EDFA}}(f_i)$ provided by a lumped amplification device (e.g. an EDFA). A gain-flattening filter imposes a loss $l_{\mathrm{GFF}}(f_i)$ at the channel frequency f_i. The GFF is designed such that a particular, desired, output power spectral density is achieved. In order to offset wavelength dependent loss and ISRS, the frequency dependent loss must be chosen as

$$l_{\mathrm{GFF}}(f_i) = \frac{P_i(0)}{P_i(L)\, G_{\mathrm{EDFA}}(f_i)}, \tag{3.1}$$

where $P_i(0)$ and $P_i(L)$ is the power of channel i at the beginning and end of the fibre span, which can be obtained by numerically solving Eq. (2.27) or in closed-form

using Eq. (2.28). Setting the loss of the GFF according to Eq. (3.1) recovers the launch power at each fibre span.

The ASE contribution after the GFF results from the gain $G_{\mathrm{EDFA}}(f_i)$ and is then attenuated by the GFF loss $l_{\mathrm{GFF}}(f_i)$. It can be calculated by modifiyng (2.33) yielding

$$\begin{aligned} P_{\mathrm{ASE}}(f_i) &= 2n_{\mathrm{sp}}hf_iB_{\mathrm{ref}}\left(G_{\mathrm{EDFA}}(f_i)-1\right)l_{\mathrm{GFF}}(f_i) \\ &\approx 2n_{\mathrm{sp}}hf_iB_{\mathrm{ref}}\frac{P_i(0)}{P_i(L)}. \end{aligned} \tag{3.2}$$

Eq. (3.2) can be used to calculate the impact of ISRS on the ASE noise contribution (i.e. P_{ASE} in the SNR Eq. (2.37)) and it can be calculated in closed-form using Eq. (2.28).

In addition to the ASE contribution, the impact of ISRS on the nonlinear interference power is required. For this pupose, the Gaussian noise model is extended and re-derived in order to account for ISRS. The newly derived expressions are validated by numerical and experimental results.

3.2 The effective attenuation approach

In this section, the effective attenuation approach is presented. The effective attenuation approach enables the modelling of ISRS through effective attenuation coefficients that resemble the apparent loss in the fibre span. The major assumption of the approach is that the temporal effects of ISRS are neglected. As a result, only the average effect of ISRS on the signal power profile is considered. This assumption is discussed and motivated in more detail in Sec. 3.2.1 and experimentally validated in Sec. 3.3. The average power transfer of ISRS is given by the Raman gain equations Eq. (2.27). Within the effective attenuation approach, the Raman gain equations are used to change the intrinsic fibre attenuation coefficient α to an effective, channel dependent attenuation coefficient $\alpha_{\mathrm{eff},i}$, to approximate the actual signal power profile. The approach is explained in more detail in Sec. 3.2.2.

3.2.1 Temporal ISRS gain dynamics

As discussed in Sec. 2.3.2.2, ISRS leads to a power transfer from high to lower frequency components. However, this transfer depends on the complex interaction between intrinsic fibre attenuation, dispersion and Kerr nonlinearity, as these effects together alter the signal in the frequency domain during propagation, and hence the ISRS power transfer. These interactions are included by the ISRS term in the NLSE (2.5). However, this would require a (at least) second-order regular perturbation

approach to analytically quantify the impact of ISRS on the Kerr distortion (i.e. the NLI). This is because the ISRS term is not a linear effect and, therefore, not part of the linear solution of the NLSE. As a result, it would not appear in the first-order perturbation induced by the Kerr effect alone (cf. (2.42)). To overcome this and to include ISRS in RP1 models, it is assumed that ISRS manifests itself *only* as the average power transfer, described by the Raman equations (2.27). This approach neglects the interactions between dispersion, Kerr nonlinearity and ISRS on the signal power profile.

Additionally, the Raman equations (2.27) assume that channels can be modelled as continuous waves (cw). Actual channels, however, are modulated with higher-order modulation formats (Sec. 2.2). Therefore, the power of each channel fluctuates in time according to its modulation format and data pattern. A modulated channel does not resemble a continuous wave. These temporal fluctuations result in time-dependent ISRS gain and, hence, in signal distortions and cross talk. In [137], it was shown that inter-channel stimulated Raman scattering can be separated into two contributions, namely an average ISRS gain component (described by (2.27)) and a time dependent cross talk component, arising from the temporal power fluctuations of each channel. In [55, 56, 137], it has been theoretically shown that this cross talk component can be neglected as each channel is statistically independent, resulting in an averaged behaviour of ISRS. The validity of this approach was experimentally shown in [P29], which resulted from a collaboration with G. Saavedra and whose results are addressed in Sec. 3.3. Similar observations were independently made in [86]. Furthermore, the same effect was observed in distributed Raman amplifiers. In [138], it was found that replacing a single high power Raman laser with a broadband ASE source yields reduced distortions. This is a consequence of the same temporal averaging mechanism, discussed in this Section.

3.2.2 The effective attenuation approach

The effective attenuation approach approximates the signal power profile, resulting from the average ISRS power transfer as described in Sec. 3.2.1, as channel dependent exponential decays. Additionally, in the computation of the NLI of the COI i, it is assumed that all interfering channels exhibit the same modified attenuation coefficient as the COI itself. The channel dependent attenuation coefficient is then chosen such that its effective length matches the actual effective length present in the fibre. Mathematically, this can be written as

$$\int_0^L \frac{P_i(\zeta)}{P_i(0)} d\zeta = \frac{1-\exp(-\alpha_{\mathrm{eff},i}L)}{\alpha_{\mathrm{eff},i}}, \tag{3.3}$$

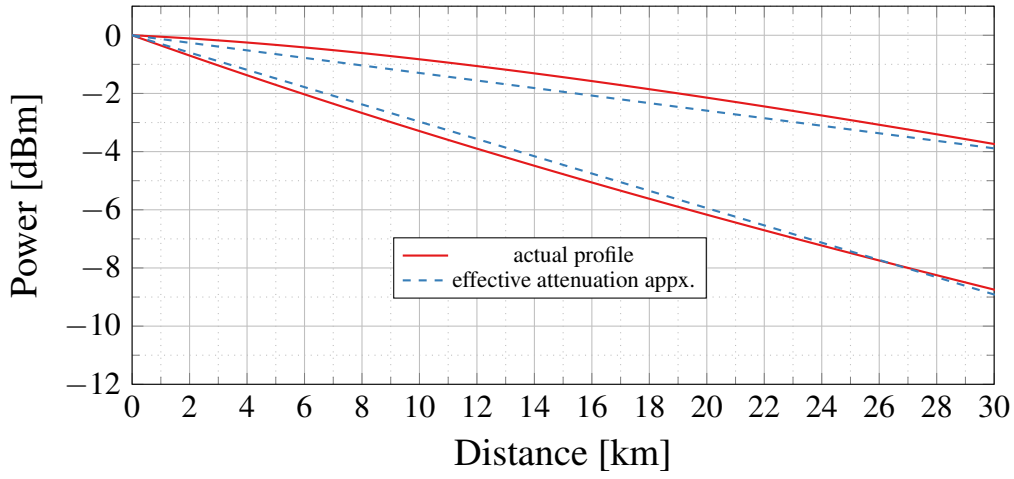

Figure 3.2: The power of highest and lowest frequency channel as a function of transmission distance. Shown are the actual signal power profile, obtained by numerically solving Eq. (2.27), and the signal power profile according to the effective attenuation approach (3.3).

where $\alpha_{\text{eff},i}$ is the effective attenuation coefficient of channel i. The left-hand side of Eq. (3.3) describes the actual effective length of the channel i present in the fibre span. The right-hand side of Eq. (3.3) represents the effective length of an exponential decay (cf. Eq. 2.19). Therefore, solving Eq. (3.3) for $\alpha_{\text{eff},i}$, yields an approximation of the actual effective length with an exponential decay. Fig. 3.2 shows the signal power profile for the highest and lowest frequency channel, obtained by numerically solving the Raman equations (2.27) and the effective attenuation approximation obtained by solving Eq. (3.3) for the same channels. It should be noted that, although a better exponential fit may be obtained in terms of matching the power profile itself, the effective attenuation approach minimises the fitting error in terms of effective length. This gives a better approximation in terms of nonlinear interference power.

The advantage of the effective attenuation approach is, that *any* model, that is derived for lumped amplified links, can be extended to account for ISRS. The only additional calculations that are necessary is to solve the Raman gain equations (2.27) and $\alpha_{\text{eff},i}$ using Eq. (3.3). The conventional Gaussian Noise model (2.44) (for dual polarisation) can be modified to account for ISRS as

$$G(z,f_i) = \frac{16}{27}\gamma^2 \int df_1 \int df_2\, G_{\text{Tx}}(f_1) G_{\text{Tx}}(f_2) G_{\text{Tx}}(f_1+f_2-f) \left| \frac{1-e^{-\alpha_{\text{eff},i}L - j4\pi^2(f_1-f)(f_2-f)[\beta_2+\pi\beta_3(f_1+f_2)]L}}{-\alpha_{\text{eff},i} + j4\pi^2(f_1-f)(f_2-f)\left[\beta_2+\pi\beta_3(f_1+f_2)\right]} \right|^2 . \tag{3.4}$$

The experimental and numerical validation of Eq. (3.4) is described in Sec. 3.3 and 3.6, respectively. In Sec. 3.4, enabled by the new model Eq. (3.4), the degradation of the AIR is quantified as the optical bandwidth is increased using multiple transmission bands of up to 20 THz.

The effective attenuation approach offers a simple way to extend published RP1 models to account for ISRS and offers initial conclusions on the impact of ISRS on the nonlinear interference, described in Sec. 3.4. However, the effective attenuation approach is only valid as long as the signal power profile can be approximated by an exponential decay. Therefore, an increasing approximation error of the approach is expected with increasing ISRS power transfers, where the signal power profile can no longer be approximated with exponential decays. This approximation error is quantified in Sec. 3.6 and lifted in Sec. 3.5, where the GN model is re-derived from scratch to precisely account for the signal power profile, induced by ISRS.

3.3 Experimental validation

In order to validate the effective attenuation approach introduced in Sec 3.2, its analytical predictions were compared to experimental results. The main goal of the experiment was to verify that temporal ISRS gain dynamics, due to channel modulation, can be neglected (see. 3.2.1). The validation was carried out over an optical bandwidth of 9 THz. The experimental setup is discussed in Sec. 3.3.1 and the results are shown in Sec. 3.3.2. The experimental measurements were mainly carried out by G. Saavedra, whereas the experimental setup and data interpretation was jointly designed and carried out.

3.3.1 Experimental setup

The experimental setup, used to verify the effective attenuation approach 3.2, is shown in Fig. 3.3 a). Within the C-band, fourteen external cavity lasers (ECL) were used with wavelengths between 1529 and 1540 nm and a frequency spacing of 100 GHz. Within the L-band, only one ECL was used at 1600 nm. All fifteen lasers were separated into two groups, where every second ECL was assigned the same group to separate the channels into odd and even channels. Every ECL within the same group was then modulated by the same dual polarisation IQ modulator. This was done to reduce temporal and spatial correlations between adjacent channels and therefore reduce artificial enhancement of the NLI. Electrically and offline generated 32 GBd 256-QAM signals were used to drive the IQ modulators. A root raised cosine pulse shape with a roll-off factor of 0.01 was used as pulse-shape. The remaining interfering channels were emulated using spectrally-shaped ampli-

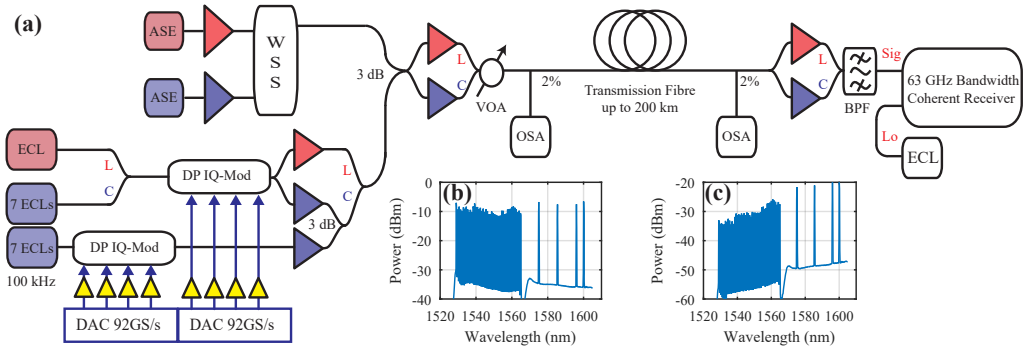

Figure 3.3: **(a)** Experimental transmission setup to validate the effective attenuation approach. **(b)** and **(c)** show the input and output spectrum at 10.7 dBm per channel measured using 0.1 nm resolution. The spectrum in **(c)** is tilted due to ISRS.

fied spontaneous emission (SS-ASE) noise. SS-ASE is the technique of populating optical bandwidth with ASE noise in order to mimic interfering channels. Similarly to the Gaussian Noise model, as shown in Sec. 2.6, this leads to a conservative estimate of the NLI with respect to uniform or shaped QAM formats. Futhermore, this leads to a more accurate validation of the GN model, as GN model approaches assume Gaussian constellations as the transmitted signal. In the experiment, the SS-ASE was shaped as 32 GHz channels spaced at 100 GHz in the C- and spaced at 1000 GHz in the L-band. The spacing in the L-band was larger, due to the limited output power available in the used L-band amplifier. The resulting optical spectrum that was launched into the transmission fibre is shown in Fig. 3.3b).

One fibre span with variable fibre length was considered for the transmission line. This was done to obtain a better controllable experimental environment and to prevent ISRS from accumulating over multiple fibre spans. The considerd span lengths were 100, 160 and 200 km with parameters $\alpha = 0.18\ \frac{\text{dB}}{\text{km}}$, $D = 0.18\ \frac{\text{ps}}{\text{nm}\cdot\text{km}}$ and $\gamma = 1.3\ \frac{1}{\text{W}\cdot\text{km}}$. The normalised Raman gain coefficient was measured to be $0.42\ \frac{1}{\text{W}\cdot\text{km}}$ at a frequency separation of 11.5 THz. The slope of the Raman gain coefficent was therefore $C_r = 0.036\ \frac{1}{\text{W}\cdot\text{km}\cdot\text{THz}}$. At the receiver, the optical signal was amplified using EDFAs in the C and L-band. The channel of interest was then selected using a band-pass filter and detected with a coherent detector.

The experimental results were then compared with analytical predictions of the effective attenuation approach (see Sec. 3.2), which are shown in the next section.

3.3.2 Experimental results

The experimental results were obtained using the experimental setup shown in Sec. 3.3. First, the impact of ISRS on the received power was investigated. This was done as a sanity check to validate the Raman equations Eq. 2.27 and the used parameters (transmitted spectrum, attenuation and Raman gain coefficient) that were

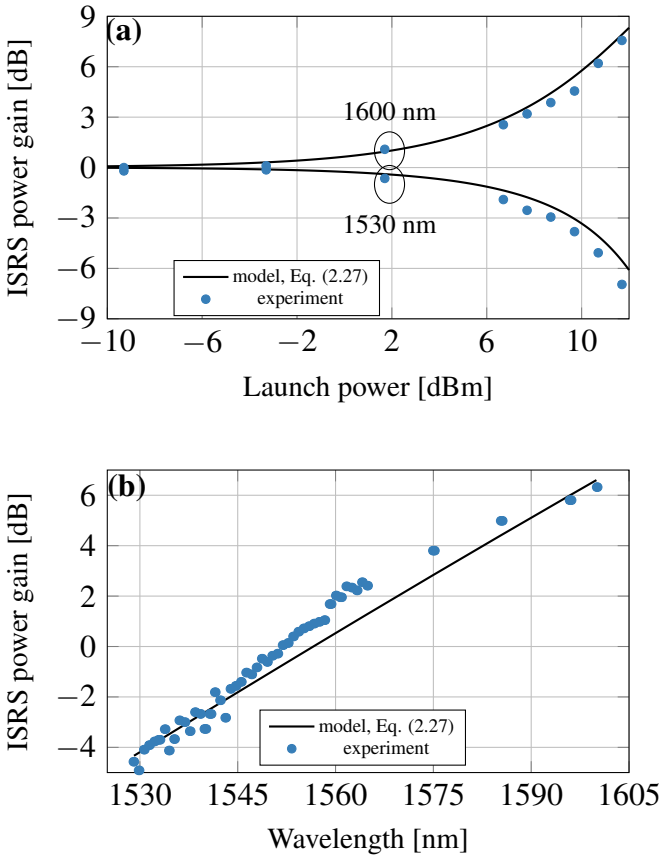

Figure 3.4: **(a)** The ISRS gain as a function of launch power for the channels located at 1530 and 1600 nm. **(b)** The ISRS gain as a function of the channel wavelength for a launch power of 10.7 dBm per channel.

used in the modelling results. The ISRS power gain as a function of launch power for the channels located at 1530 and 1600 nm is shown in Fig. 3.4a). The ISRS power gain for the entire spectrum for a high launch power of 10.7 dBm per channel is shown in Fig. 3.4b). The high launch power of 10.7 dBm/ch. was chosen to validate the Raman equations in the presence of significant ISRS power transfer. The results are independent of the fibre length used, as all three considered lengths are significantly larger than the effective length fibre length of $L_{\text{eff}} = 24.12$ km. It can be seen that the theory is in good agreement with the experimental results, showing that Eq. (2.27) can be reliably used to model the impact of ISRS in terms of modelling the ASE noise contribution and the nonlinear interference power.

The experimentally measured and the predicted SNR as a function of launch power for the channels located at 1530 and 1600 nm are shown in Fig. 3.5a) and b), respectively. The two channels are the ones that are most impacted by ISRS, as they are at the edges of the transmitted spectrum. The results for all three span lengths are shown. The SNR of the analytical predictons were obtained using Eq.

(2.37) with the ASE noise computed using Eq. (3.2) and the NLI was computed using Eq. (3.4). In order to study the impact of ISRS, two cases were considered. i) the C and L-band were transmitted alone and ii) both bands transmitted together. This way the effect of ISRS could be effectively switched on and off. It should be noted that the effect of ISRS is less pronounced for SNRs above 17 dB, due to the limited transceiver SNR.

In the launch power regime, where the ASE noise contribution dominates, Eq. (3.2) is in good agreement with the experimental results. In the low launch power regime, where ASE noise dominates, the experimental results show a gain in SNR for the 1600 nm channel and a penalty in SNR for the 1530 nm channel. This is because the high wavelength channel is effectively amplified during propagating, resulting in lower required gain at the end of the span. As a result, the ASE noise contribution is reduced and the SNR is increased. The opposite is true for the 1600 nm channel. As a reminder, Eq. (3.2) assumes no additional distortions due to temporal gain dynamics arising from channel modulation. Fig. 3.5 shows that the temporal gain dynamics are, indeed, negligible as the experimental results are good agreement with the predictions by Eq. (3.2).

The theoretical predictions in the nonlinear regime are based on the effective attenuation approach Eq. (3.4). The analytical results are in good agreement with the experimental measurements. The channel at 1530 nm loses power during propagation due to ISRS and experiences reduced nonlinear distortions as a consequence. The opposite holds for the channel at 1600 nm, which gains power during propagation, resulting in a larger NLI power. The experimental results show altered nonlinear distortions due to ISRS, as correctly predicted by the effective attenuation approach. The combination of linear and nonlinear effects result in increased and decreased SNRs at optimum launch power for the high and low wavelength channel, respectively. The reason is that, at optimum launch power, the ASE noise contribution is approximately twice as large as the nonlinear noise contribution (cf. Sec. 2.6). As a result, high wavelength channels experience a gain in SNR at optimum launch power, although they experience higher nonlinear penalties with respect to low wavelength channels.

In summary, the experimental results, shown in this section, validate the effective attenuation approach, described in Sec. 3.2. The experimental results show that, firstly, no cross-talk was observed due to temporal gain dynamics arising from channel modulation (see Sec. 3.2.1). The ASE noise contribution is correctly predicted by Eq. (3.2). Second, the impact of ISRS on the nonlinear penalties is correctly predicted by the Eq. (3.4), showing that ISRS can be approximated by exponential decays using effective attenuation coefficients. The effective attenuation approach

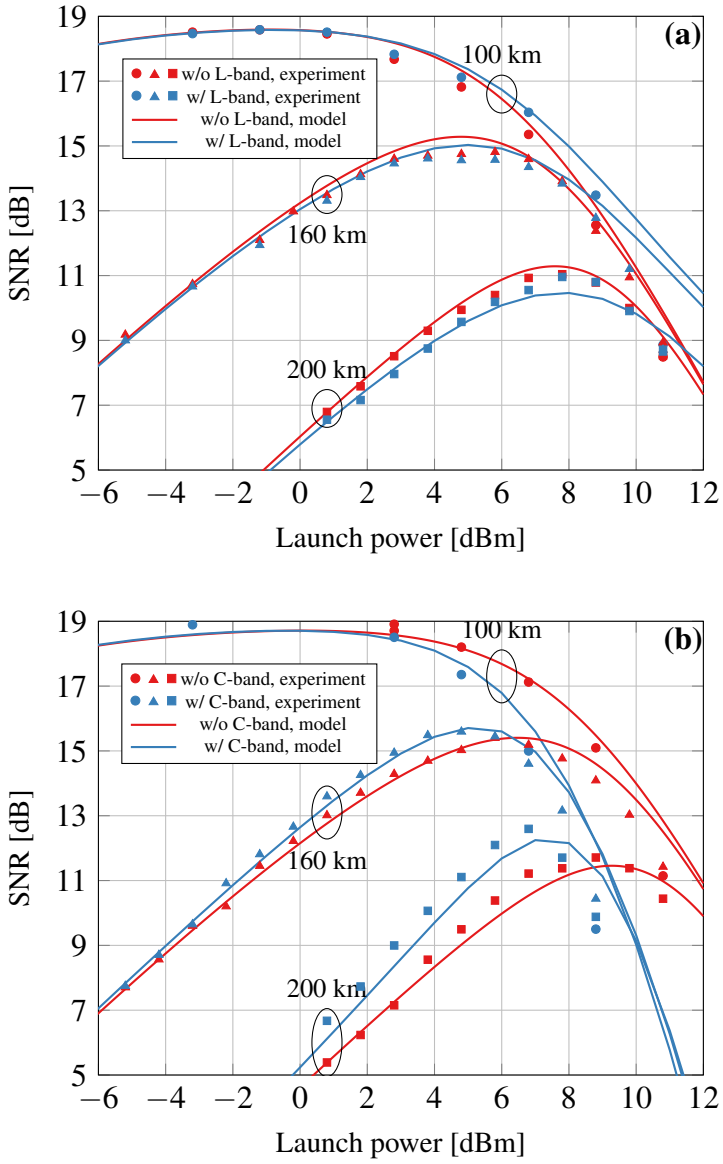

Figure 3.5: The SNR as a function of launch power for the channels located at **(a)** 1530 nm and **(b)** 1600 nm. Markers show experimental data and solid lines represent the effective attenuation approach Sec. 3.2. The transmission of the entire spectrum (9 THz), resulting in significant ISRS, is shown in blue and the transmission of either only C-band or L-band channels, resulting in negligible ISRS, are shown in red color.

is used in Sec. 3.4 to quantify the impact of ISRS on the AIR and is further validated through numerical simulations in Sec. 3.6.

3.4 Achievable rate degradation due to ISRS

After validating the effective attenuation approach in Sec. 3.2, the new model was used to estimate the degradation in achievable information rate as the opti-

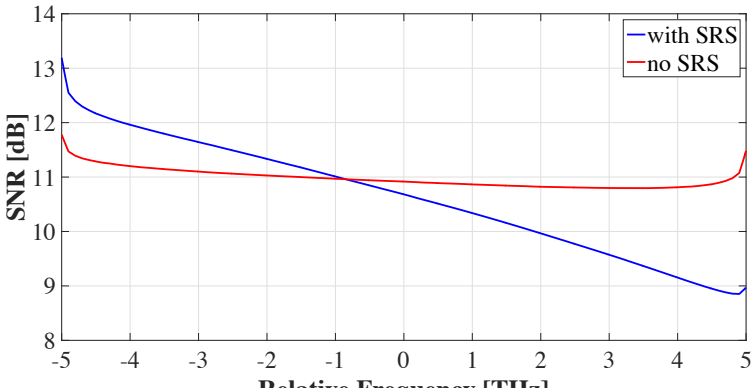

Figure 3.6: SNR of each channel in a 10 THz WDM signal after transmission of 3000 km of SMF based spans. Results are shown with and without the effect of ISRS.

cal bandwidth is extended beyond the C-band. To quantify the gains that can be expected using multiple transmission bands, it is important to assess the degradation due to ISRS for ultra-wideband system. A SMF based system is considered with parameters: attenuation coefficient $\alpha = 0.2\ \frac{\text{dB}}{\text{km}}$, group velocity dispersion $\beta_2 = -21.3\ \text{ps}^2\ \text{km}^{-1}$, group velocity dispersion slope $\beta_3 = 0.145\ \text{ps}^3\ \text{km}^{-1}$, span length $L = 100$ km, noise figure $F = 5$ dB and nonlinearity coefficient $\gamma = 1.2\ \frac{1}{\text{W}\cdot\text{km}}$. A total transmission distance of 3000 km and a symbol rate of 10 GBd (Nyquist-spaced) was considered. The Raman gain spectrum as in Fig. 2.7 was considered. For each transmission, the signal power profile was obtained by numerically solving Eq. (2.27). For the linear noise contribution Eq. 3.2 was used and for the nonlinear interference noise contribution Eq. (3.4) was used. An ideal transceiver was considered, to obtain fundamental transmission limits. The SNR as a function of frequency, obtained from the effective attenuation approach, is shown in Fig. 3.6. As experimentally shown in Sec. 3.3, high frequency channels experience a penalty due to ISRS. On the other hand, low frequency channels experience a gain in SNR due to ISRS. In other words, the effect of the ISRS power transfer is an increase or decrease of the SNR depending on the channel's spectral location. The spectral efficiency, obtained by using the Shannon capacity formula Eq. (2.3), is shown in Fig. 3.7. Again, the case with and without ISRS is shown. The results in Fig. 3.7 represent the maximum achievable information rate, assuming an AWGN channel. This means that, in principle, the spectral efficiencies shown in Fig. 3.7 can be achieved by means of adaptive modulation formats. This means that every channel is modulated with a uniform or shaped modulation format that maximises its respective spectral efficiency. The loss in spectral efficiency for high frequency channels is comparable with the gain in spectral efficiency for the low frequency channels. As a consequence, the use of adaptive modulation formats can minimise

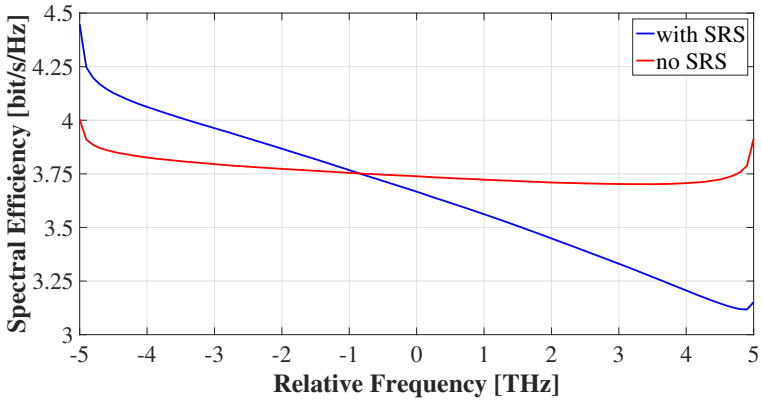

Figure 3.7: The maximum achievable efficiency as a function of frequency for a 10 THz WDM signal transmitted over 3000 km of SSMF based spans.

the overall throughput loss.

It should be emphasised that a uniform launch power was used to obtain the results in Fig. 3.7. While this enables initial conclusions on the achievable throughput in the presence of ISRS, a uniform launch power does not lead to optimum (total) performance as some channels are not operated at their respective launch power. Low frequency channels experience larger amounts of ASE noise compared to their high frequency counterparts and, as a consequence, have a higher optimum launch power. This issue can be overcome by introducing a spectral launch power distribution such that every channel is operating at its respective optimum. Therefore, the results in this section represent a lower (but easier to achieve) bound on the total achievable throughput. In general, spectral launch power optimisation is an optimisation problem with a very large solution space as every channel (e.g. 1000 channels in Fig. 3.7) can have a different optimum launch power. This is especially true in mesh optical network transmission which is addressed in Sec. 3.7.2. For this purpose the analytical models that are proposed in this section can be utilised. Due to their very low computational complexity, optimisation algorithms can be carried out that require thousands of function evaluations, which would not be manageable with conventional split-step simulations, particularly for ultra-wide bandwidths. Closed-form approximations (addressed in Sec. 4) are particularly useful as those enable performance estimations in sub-milliseconds, leading to execution times of the *entire* optimisation routine within seconds. In addition, the models proposed in this chapter can also be used to optimise gain flattening filters. However, the spectral power optimisation is not subject of this thesis and left for future investigations.

The total throughput, calculated as the AIR Eq. (2.3), summed over all transmitted channels, as a function of optical bandwidth is shown in Fig. 3.8. Two cases

are shown, one where the uniform launch power was optimised and one where the launch power was chosen such that, the SNR penalty due to ISRS is less than 0.5 dB. The latter case was investigated to study whether simply suppressing ISRS with low launch powers is a viable option in ultra-wideband transmission. Additionally for each case, the AIR using adaptive modulation formats and using the same worst-case modulation format for each channel is shown. In the worst-case modulation format case, each channel exhibits the same modulation format that is dictated by the channel with the lowest SNR. In order to quantify the penalty with respect to the absence of ISRS, the same AIR without considering ISRS is shown.

It can be seen that no throughput gain is achieved increasing the bandwidth from 8 THz to 14 THz, when the launch power is kept low in order to suppress the effect of ISRS. This shows that ultra-wideband transmission systems must be operated in a regime in which the impact of ISRS is significant. This emphasises the significance of ISRS, as operating in a low power regime, is not a viable option and next-generation systems are likely to be operated in a regime where ISRS is relevant. Approximately twice the throughput is achievable by operating in the regime of optimum launch power, using only one, worst-case modulation format. However, ISRS imposes a penalty of around 40% for an optical bandwidth of 15 THz, when the same modulation format is used throughout the WDM system. However, the use of adaptive modulation formats can limit the AIR penalty due to ISRS to only 10%. The results in Fig. 3.8 emphasise the importance of flexible modulation format adaption in the context of ultra-wideband transmission systems.

The analysis in this section shows that the penalties due to ISRS can be largely overcome by using adaptive modulation formats and gain flattening filters. The gain flattening filters fully reverse the nonlinear power transfer at the end of the span and prevent ISRS from accumulating over multiple fibre spans. As a result, the impact of ISRS becomes approximately independent of the transmission distance (number of spans). Finally, adaptive modulation formats enable to translate the SNR gain of low frequency components into a net gain in spectral efficiency to balance the SE degradation for high frequency components (cf. Fig. 3.7). It appears that, ISRS does not impose an insurmountable limit on the throughput gains obtained from increasing the optical transmission bandwidth. Based on the parameters in this section, using a transmission bandwidth of 20 THz, approximately corresponding to the entire S+C+L band, yields a four-fold increase in total achievable throughput compared to using the C-band (5 THz) alone.

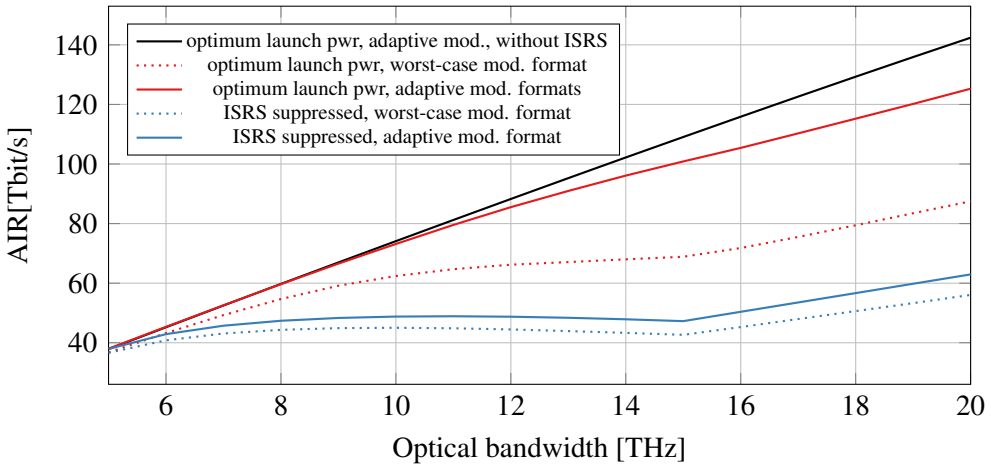

Figure 3.8: The achievable information rate (AIR) as a function of total optical bandwidth. Two scenarios are shown. One, where the uniform launch power is optimised and one where the launch power reduced such the penalties due to ISRS are <0.5 dB. Additionally, each launch power strategy shows the use of adaptive modulation formats and the case of using the same (worst-case) modulation format accross all channels. The case of no ISRS is shown for comparison.

3.5 The ISRS GN model

The effective attenuation approach, presented in Sec. 3.2, approximates the signal power profile with exponential decays. However, for strong ISRS power transfers, of more than 6 dB, the signal power profile does not strictly resemble exponential decays and the GN model needs to be re-derived based on the precise signal power profile.

In this section, the GN model is re-derived in order to account for any arbitrary signal power profile. Additionally, the analytical result of the ISRS power transfer Eq. 2.28 is used to derive a fully analytical extension of the GN model to account for ISRS. The newly derived model, referred to as ISRS GN model, represents a generalisation of the effective attenuation approach in Sec. 3.2, as ISRS is again modelled as a pure change of the power profile. However, the ISRS GN model exhibits high accuracy even in strong ISRS regime. Additionally, the ISRS GN model can be used for distributed Raman amplified systems. A comparison between the effective attenuation approach and the ISRS GN model is carried out in Sec. 3.6.

Defining $\rho(z,f) = \frac{P(z,f)}{P(0,f)}$ as the normalised signal power profile, with $P(z,f)$

being the power at distance z and frequency f, the ISRS GN model is written as

$$G(f) = \frac{16}{27}\gamma^2 \int df_1 \int df_2 \; G_{\mathrm{Tx}}(f_1) G_{\mathrm{Tx}}(f_2) G_{\mathrm{Tx}}(f_1+f_2-f) \cdot \left| \int_0^L d\zeta \sqrt{\frac{\rho(\zeta,f_1)\rho(\zeta,f_2)\rho(\zeta,f_1+f_2-f)}{\rho(\zeta,f)}} e^{j\phi(f_1,f_2,f,\zeta)} \right|^2, \tag{3.5}$$

where $\phi = -4\pi^2(f_1-f)(f_2-f)\left[\beta_2 + \pi\beta_3(f_1+f_2)\right]\zeta$. The detailed derivation of (3.5) can be found in Appendix A.1. Eq. (3.5) can be used to model arbitrary signal power profiles, for example the ones arising from ISRS or distributed hybrid Raman EDFA amplifiers (see Sec. 2.4). However, in the following only lumped amplified transmission systems are considered. As a check, inserting a passive fibre loss $\rho(z,f) = e^{-\alpha z}$, into Eq. (3.5) recovers the conventional GN model as in Eq. (2.44). Multiple fibre spans can be accounted for by inserting the phased-array term (2.46) into Eq. (3.5). Eq. (3.5) represents a key result of this chapter and this thesis.

The analytical solution of the Raman equations (2.28) can be used to write the semi-analytical model (3.5) in fully analytical form. For this purpose, a comparison of numerically solving the Raman equations (2.27) and its analytical approximation (2.28) is shown in Fig. 3.9. The results assume a fibre length of 100 km, an attenuation coefficient of $\alpha = 0.2$ $\frac{\mathrm{dB}}{\mathrm{km}}$, a Raman gain spectrum as in Fig. 2.7 and a Raman gain slope of 0.028 $\frac{1}{\mathrm{km\cdot W\cdot THz}}$. A total optical bandwidth of 10 THz was assumed and the results for several total launch powers are shown. The results in Fig. 3.9 show an excellent agreement between the Raman equations and its analytical approximation with maximum deviations of around 0.1 dB. This shows that the analytical approximation of the ISRS power transfer (2.28) is well suited for the modelling of nonlinear interference. Substituting Eq. (2.28) into Eq. (3.5) yields the ISRS GN model in analytical form as

$$G(f) = \frac{16}{27}\gamma^2 \int df_1 \int df_2 \; G_{\mathrm{Tx}}(f_1) G_{\mathrm{Tx}}(f_2) G_{\mathrm{Tx}}(f_1+f_2-f) \cdot \left| \int_0^L d\zeta \, \frac{P_{\mathrm{tot}} e^{-\alpha\zeta - P_{\mathrm{tot}} C_{\mathrm{r}} L_{\mathrm{eff}}(f_1+f_2-f)}}{\int G_{\mathrm{Tx}}(\nu) e^{-P_{\mathrm{tot}} C_{\mathrm{r}} L_{\mathrm{eff}} \nu} d\nu} e^{j\phi(f_1,f_2,f,\zeta)} \right|^2. \tag{3.6}$$

It should be noted that the effective length $L_{\mathrm{eff}}(\zeta) = \frac{1-\exp(-\alpha\zeta)}{\alpha}$ in Eq. (3.6) is a function of the integration variable ζ. Eq. (3.6) is a key result of this thesis, as it extends the conventional GN model to account for ISRS and is validated by SSFM simulations in Sec. 3.7 and Sec. 3.6.

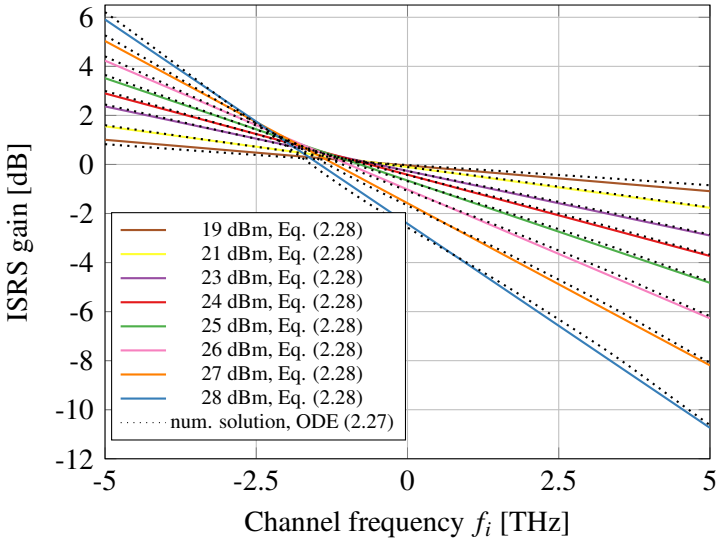

Figure 3.9: The gain due to ISRS against channel frequency obtained by solving the set of coupled differential equations (2.27) shown in dotted lines and its analytical triangle approximation (2.28) shown in solid lines for a variety of total optical launch power P_{tot}.

The nonlinear interference coefficient as a function of frequency for a variety of total launch powers is shown in Fig. 3.10a). The corresponding ISRS power transfers can be obtained from Fig. 3.9. The deviation of the nonlinear interference coefficient, with respect to the case of no ISRS, as a function of total launch power is shown in Fig. 3.10b). The results assume a transmission system with parameters listed in Table 3.1.

Table 3.1: System parameters

Parameters	
Loss (α) [dB/km]	0.2
Dispersion (D) [ps/nm/km]	17
Dispersion slope (S) [ps/nm^2/km]	0.067
NL coefficient (γ) [1/W/km]	1.2
Raman gain slope (C_r) [1/W/km/THz]	0.028
Raman gain ($C_\mathrm{r} \cdot 14$ THz) [1/W/km]	0.4
Fiber length (L) [km]	100
Symbol rate [GBd]	50
Channel spacing (B_ch) [GHz]	50.001
Number of channels	201
Optical bandwidth (B) [THz]	10.05
Roll-off factor [%]	0.01

The tilt of the nonlinear interference coefficient in the absence of ISRS is due to the dispersion slope. The group-velocity dispersion is larger for lower frequencies (around 14% for channels at the edge of the spectrum) and as a result those frequencies experience lower nonlinear distortions. For increasing launch powers, high frequency channel transfer power to lower frequency channels, reducing the amount of nonlinear interference. As a reference, the optimum uniform (total) launch power for the central channel is 24 dBm, assuming EDFAs with a noise figure of 5 dB. The same trend can be seen in Fig. 3.10b). Additionally, Fig. 3.10b) shows that for increasing transmission distances the impact of ISRS on the NLI increases. To further investigate this effect, the coherence factor (cf. Sec. 2.6.2) as a function of frequency is shown in Fig. 3.11. The coherence factor was calculated, similar to Eq. (2.47), as

$$(\eta_n)\,[\mathrm{dB}] - (\eta_1)\,[\mathrm{dB}] = (1+\varepsilon)\cdot(n)\,[\mathrm{dB}]\,, \tag{3.7}$$

where $(x)\,[\mathrm{dB}] = 10\log_{10}(x)$ stands for conversion to the decibel scale. As already indicated in Fig. 3.10b), Fig. 3.11 shows that ISRS impacts the coherent accumulation of NLI. High frequency channels lose power due to ISRS and, therefore, experience less coherent NLI accumulation. The opposite effect can be observed for lower frequency channels. This is because gaining power leads to an increased nonlinear interaction length (i.e. effective length) that increased the coherence of the signal.

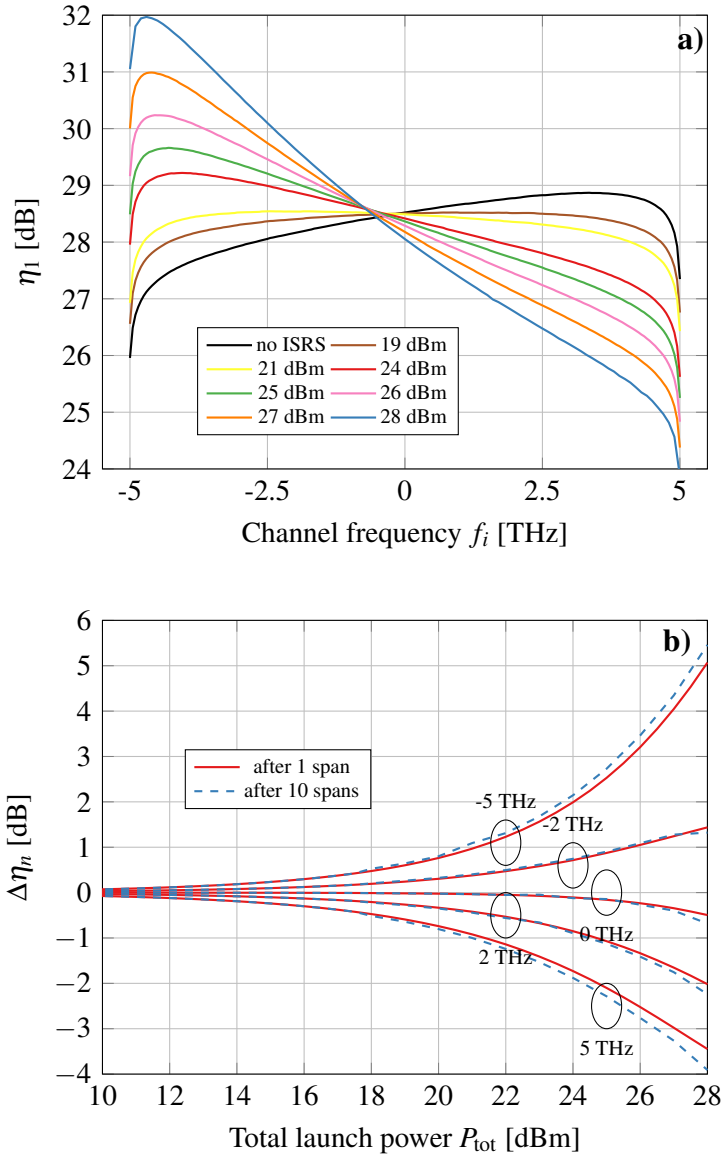

Figure 3.10: The nonlinear interference coefficient after 1 span as a function of channel frequency for different total launch powers is shown in a) and the NLI deviation as a function of total launch power is shown in b) obtained by the analytical ISRS GN model (3.6). The uniform optimum launch power for the system under test is 24 dBm.

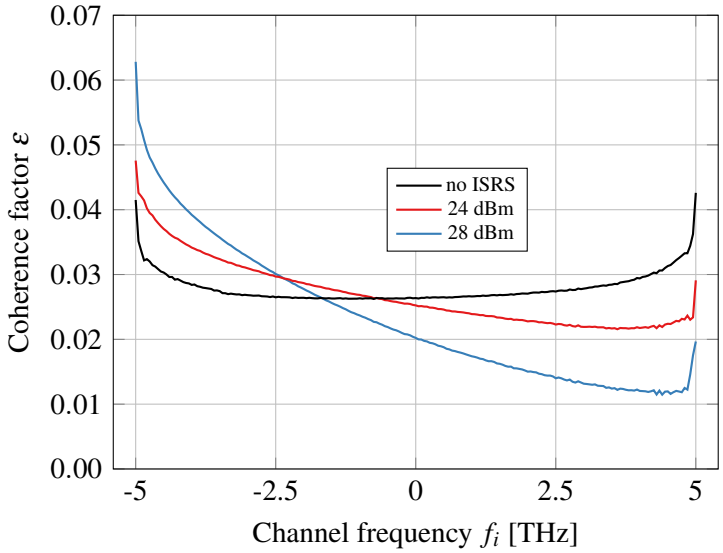

Figure 3.11: The coherence factor as a function of channel frequency for a variety of total launch powers obtained by the analytical ISRS GN model (3.5).

The formula proposed in this section (3.5) is different than those derived in [17, Eq. (16)], [18, Eq. (18)] and [139, Eq. (1)], where $\rho(\zeta, f_1+f_2-f)$ and $\rho(\zeta, f)$ in (3.5) are swapped. As a consequence of the different result, the f_1 and f_2 dependence vanishes in [17, 18, 139], for power profiles of the form $\rho(z, f) = e^{a(z)\cdot f+b(z)}$ (as the one resulting from ISRS). This means that in the nonlinear process all three frequencies in the triplet (f, f_1, f_2) attenuate according to frequency f which overestimates the impact of ISRS. This incorrectly overestimated the impact of ISRS. A comparison between Eq. (3.5) and the results derived in [17, 18, 139] is shown in Fig. 3.12. It can be seen that, indeed, the formula proposed in [17, 18, 139] overestimates the impact of ISRS on the nonlinear interference coefficient. In Sec. 3.7 and 3.6, it is shown, through numerical simulations, that Eq. (3.5) is the correct formula to extent the GN model for arbitrary signal power profiles. Additionally, after the publication of Eq. (3.5) in [P8], [17, 18, 139] were updated with [18, 140] correcting the formalism to match the result derived in this thesis Eq. (3.5).

3.6 Comparison between the effective attenuation approach and the ISRS GN model

This section serves two purposes; to validate the two analytical approaches in Sec. 3.2 and Sec. 3.5 with numerical simulations, and to compare their accuracy. The results from the SSFM and Eq. (3.5) using the actual Raman gain spectrum, as in Fig. 2.7, were compared to the effective attenuation approach Eq. (3.4) and the ISRS GN model in analytical form Eq. (3.5).

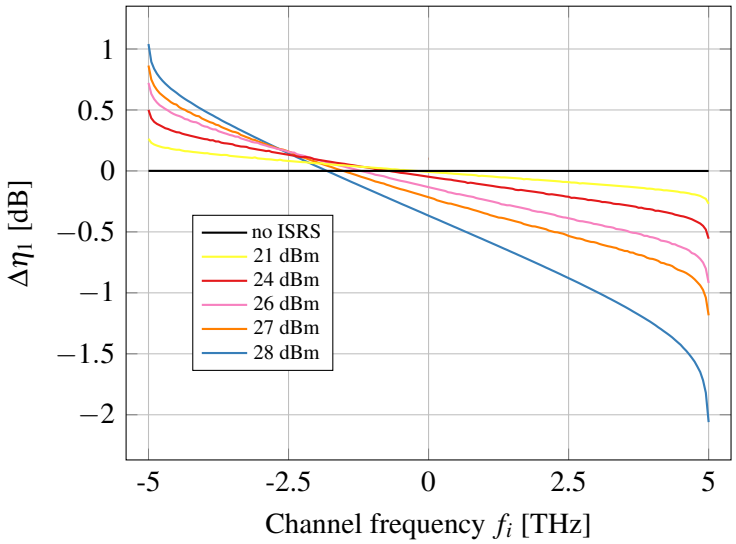

Figure 3.12: Deviation of the NLI coefficient after one span between the analytical ISRS GN model (3.6) and [17, Eq. (13) and (16)] [18, Eq. (18)]. The validity of the ISRS GN model is shown in Sec. 3.6 and 3.7.2.

A WDM signal that was studied consisted of 119×85 GBd Nyquist-spaced channels, occupying the entire C+L band (10.11 THz), centered at $\lambda_{\text{ref}} = 1570$ nm. Transmission over a link comprising three spans of standard single mode fibre was considered, with the parameters listed in Table 3.1. ISRS was implemented by a frequency-dependent loss at each simulation step (see Sec. 2.3.4), to yield the signal power profile $\rho\,(f,\zeta)$. Ideal gain equalisation after each span was assumed. A sequence length of 2^{17} symbols was considered and four data realisations were averaged to increase the accuracy of the SSFM. In order to accurately benchmark the proposed models against the simulations, Gaussian symbols were used for transmission. A comparison of the ISRS GN model with QAM signals is shown in Sec. 3.7.2.

The NLI coefficient (see Sec. 2.6.2) as a function of channel frequency and as a function of the ISRS power transfer is shown in Fig. 3.13. The ISRS power transfer is defined as the sum of the ISRS gain/loss in decibel of the outer most WDM channels. The ISRS power transfer can be calculated using Eq. (2.28) as

$$\Delta\rho\,(z)\,[\text{dB}] = 4.3 \cdot P_{\text{tot}} C_{\text{r}} L_{\text{eff}} B_{\text{tot}}. \tag{3.8}$$

The ISRS GN model, in semi-analytical form (3.5) and in analytical form (3.6), have a negligible error with respect to the split-step simulations. The effective attenuation approach is in very good agreement with simulations despite the exponential decay approximation; with a maximum mismatch of 0.1 dB for 4 dBm launch power.

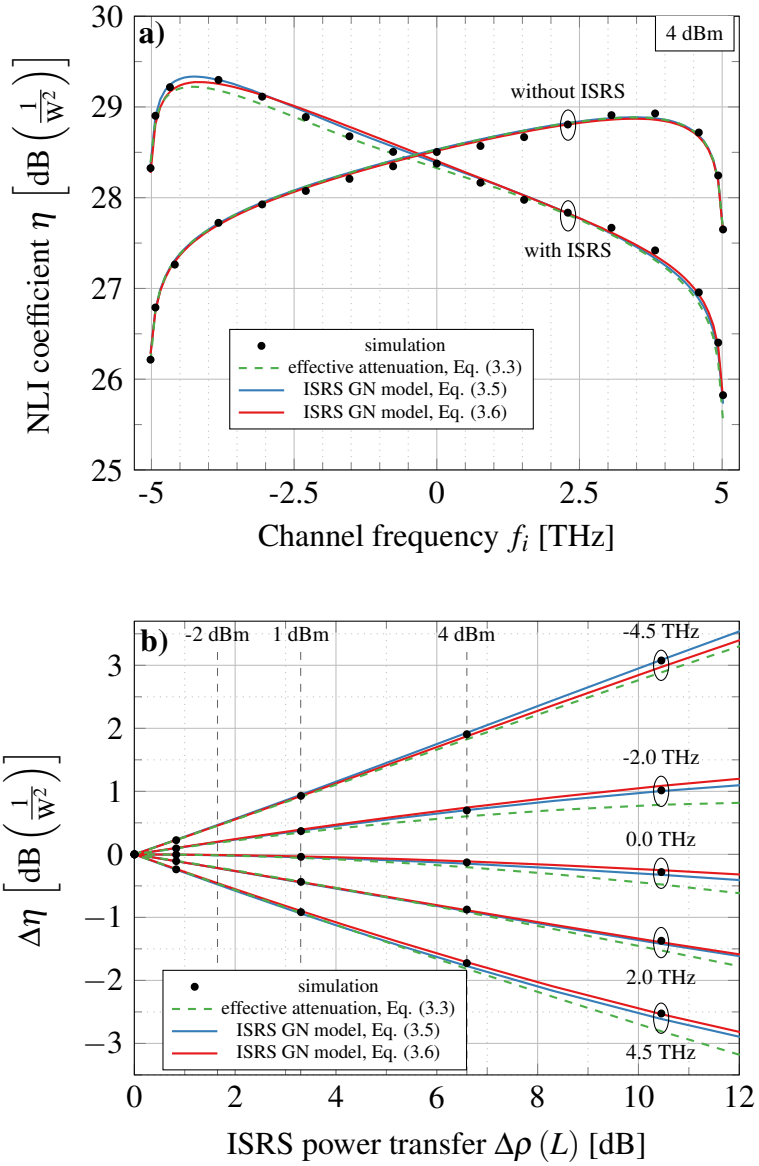

Figure 3.13: NLI coefficient, and its deviation, after 3 spans obtained by numerical simulations, the effective attenuation approach Eq. (3.3), the ISRS GN model in semi-analytical (3.5) and analytical (3.6) form.

However, this mismatch increases for increasing ISRS power transfers as ISRS does not resemble an exponential decay.

In conclusion, the NLI estimates of all integral approaches are similar within 0.1 dB for powers up to 4 dBm per channel. However, for stronger powers (i.e. ISRS power transfers) and higher required accuracy, the use of the ISRS GN model is recommended at the expense of higher computational complexity.

3.7 The ISRS GN model in network scenarios

In this section, the newly derived ISRS GN model (see Sec. 3.5) is numerically validated through SSFM simulations in a point-to-point and mesh optical network scenario. For the latter case, Eq. (3.6) is extended to account for variably loaded fibre spans. The extension is first carried out in Sec. 3.7.1 and then compared to numerical simulations in Sec. 3.7.2.

3.7.1 Extension of the ISRS GN model to variably loaded spans

In this section, the ISRS GN model in analytical form (3.6) is extended to account for varying signal power spectral densities at the input of each fibre span. This is important for the nonlinear interference prediction in optical mesh networks. In mesh optical networks, light paths are established according to traffic demands and routing and wavelength assignment (RWA) algorithms. As a result, transmission links between two ROADMs may exhibit dramatically different signal spectra. For these cases, the phased-array term (2.46) cannot be used as the transmitted signal is not identical at each span. Additionally, variably loaded spans can also occur in point-to-point transmission scenarios. For ultra-wideband transmission, it is unlikely that the signal power spectral density would be identical at the beginning of each fibre span. This is mainly due to the ISRS power transfer which may be difficult to compensate for each span using static gain flattening filters, ISRS is launch power dependent, requiring dynamic ISRS power transfer compensation. Additionally, ultra-wideband amplifiers may exhibit gain-ripples, resulting in the inabilty to precisely recover the spectral launch power distribution of each span.

To extend Eq. (3.6) to account for arbitrary signal PSDs at each span, the normalised signal power profile for the *entire* transmission is derived first. The signal power profile $P_k(z,f)$ within an arbitrary span k and in the presence of ISRS, is given by Eq. (2.28)

$$G_k(z,f) = G_k(f)\frac{P_{\text{tot},k}e^{-\alpha z - P_{\text{tot},k}C_{\text{r}}L_{\text{eff}}f}}{\int G_k(\nu)e^{-P_{\text{tot},k}C_{\text{r}}L_{\text{eff}}\nu}d\nu}, \tag{3.9}$$

where $G_k(f)$ is the signal power spectral density launch into span k with total launch power $P_{\text{tot},k} = \int G_k(\nu)d\nu$. Eq. (3.9) can be used to define the normalised signal power profile as

$$\rho(z,f) = \frac{1}{G_1(0,f)}\sum_{k=1}^{n} G_k\left[\text{mod}_L(z),f\right]\Pi\left(\frac{z-kL+\frac{1}{2}L}{L}\right), \tag{3.10}$$

with the rectangular function $\Pi(x)$ and the modulo operation $\text{mod}_a(x)$. The ISRS

GN model in analytical form, extended for an arbitrary signal PSD at each span is then obtained by inserting Eq. (3.10) in Eq. (3.5)

$$G(f) = \frac{16}{27}\gamma^2\, G_1(f) \int df_1 \int df_2 \left| \sum_{k=1}^{n} \int_0^{L_k} d\zeta\; S_k(f_1,f_2,f)\, \frac{P_{\mathrm{tot},k} e^{-\alpha\zeta - P_k C_r L_{\mathrm{eff}}(f_1+f_2-f)}}{\int G_k(\nu) e^{-P_k C_r L_{\mathrm{eff}}\nu} d\nu} e^{j\phi\left(f_1,f_2,f,\tilde{L}_k+\zeta\right)} \right|^2, \tag{3.11}$$

with $S_k(f_1,f_2,f) = \sqrt{\frac{G_k(f_1)G_k(f_2)G_k(f_1+f_2-f)}{G_k(f)}}$ and $\tilde{L}_k = \sum_1^{k-1} L_k$. The derivation steps can be found in Appendix A.2.

Eq. (3.11) represents an extension of Eq. (3.6) to account for abitrary signal power spectral densities at the input of each fibre span. For identical signal PSD, Eq. (3.11) reduces to Eq. (3.6). It can be applied to point-to-point transmission, where amplifier gain ripples are significant, and in mesh optical networks, where fibre spans are variably loaded due to RWA algorithms and traffic conditions.

3.7.2 Numerical validation

To check the validity of the developed Eq. (3.11), it is validated via SSFM simulations in a mesh optical network scenario. The considered network topology is shown in Fig. 3.14, which is a section of the British Telecommunications (BT) 20+2 topology of the United Kingdom core network [19]. The considered transmission path, that will be modelled in this section, is marked in red, going from node *A* to *B*. The equivalent physical layer representation is shown in Fig. 3.15. In this work, every node in Fig. 3.14 was assumed to consist of a ROADM and links longer than 100 km were split evenly into two fibre spans. Due to traffic conditions and the result of RWA algorithms, different signal PSDs are launched between two nodes ROADM as illustrated in Fig. 3.15. The total usable optical bandwidth was assumed to be 10 THz, corresponding to the entire C+L band. The validation was carried out for two scenarios. One where the entire C+L band was populated and one with variably loaded network spans. A standard single mode fibre was considered with parameters as in Table 3.1, where the WDM signal consisted of 251×40 GBd channels, occupying the entire C+L band (10.04 THz). Gaussian modulation, uniform and Maxwell-Boltzmann shaped 64- QAM optimised for a SNR of 15 dB was used as transmitted symbols. This was done to compare the analytical predictions to more commonly used modulation formats. Every transmitted channel exhibits a launch power of 0 dBm which is the optimum launch power for the central channel in the presence of an Erbium-doped fibre amplifier with 5 dB noise figure. The

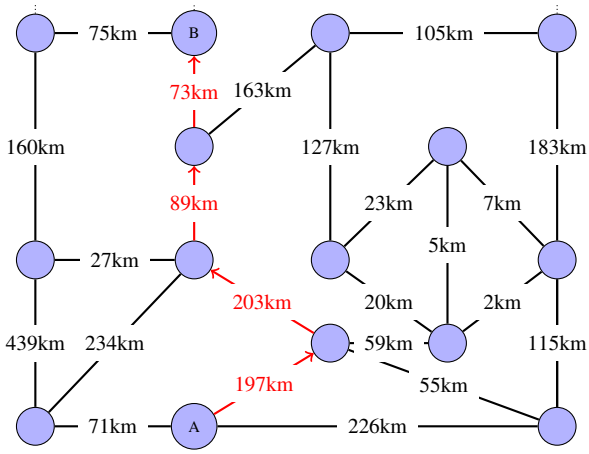

Figure 3.14: A section from the BT network taken from [19]. In Sec 3.7.2, the nonlinear performance of the red path (A-B) is modelled using the ISRS GN model (3.7.1) and numerical split step simulations

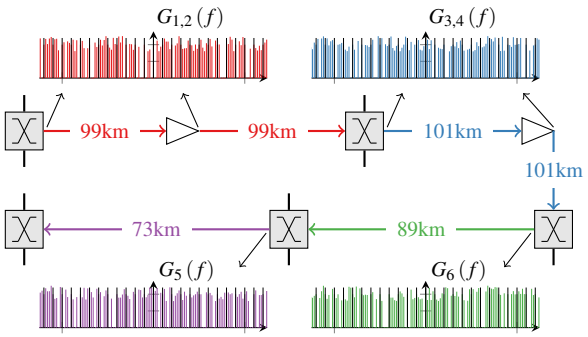

Figure 3.15: Physical layer representation of the transmission link, between nodes 15 and 13, shown in Fig. 3.14, showing interfering channels (in colour) added and dropped at each ROADM.

analytical results were obtained from the newly derived Eq. (3.11).

The nonlinear SNR, defined as $\mathrm{SNR}_{\mathrm{NLI}} = \frac{P}{P_{\mathrm{NLI}}}$, against channel frequency, calculated via SSFM and Eq. (3.11), is shown in Fig. 3.16. Transmission in the absence of ISRS is shown in Fig. 3.16a) while the transmission including ISRS is shown in Fig. 3.16b). The non-physical case in which ISRS is absent is shown for comparison and to quantify the impact of ISRS. The wavelength dependent gain due to ISRS along a span was ideally compensated to ease a comparison to the point-to-point case. The power difference after one span between the outer channels due to ISRS was 6.5 dB. The ISRS GN model shows excellent agreement in the case of Gaussian modulation with an average deviation of $<$0.1 dB. The average deviation to uniform and shaped 64- QAM is 1.9 dB and 1 dB after 3 spans and 1.6 dB and 0.8 dB after 6 spans. The tilt in Fig. 3.16a) is a result of the dispersion slope S. Due

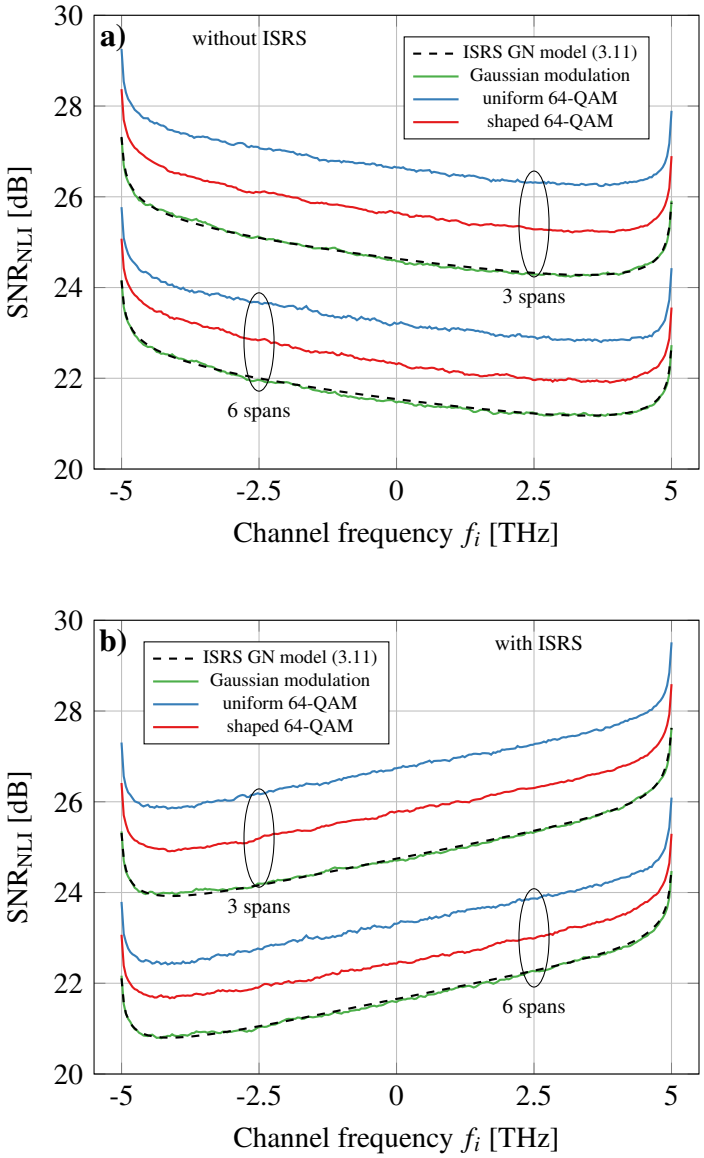

Figure 3.16: Nonlinear performance of a fully loaded C+L band point-to-point scenario a) without and b) with ISRS. The results are obtained from numerical simulations, shown in solid, and from the ISRS GN model in analytical form (3.11), shown in dashed.

to ISRS, the overall tilt in $\mathrm{SNR_{NLI}}$ is changed by -2 to 1.8 dB as a consequence of the effective power amplification and loss.

After validating the ISRS GN model (3.11) for fully populated spans, the case of variably loaded network links was investigated. It is assumed that channels are added and dropped at each ROADM to emulate a more realistic network environment as indicated in Fig. 3.15. Every fifth channel is transmitted along the entire path, which are shown in black in Fig. 3.15. Those 51 channels are referred to as signal channels and their nonlinear performance was evaluated. The remaining

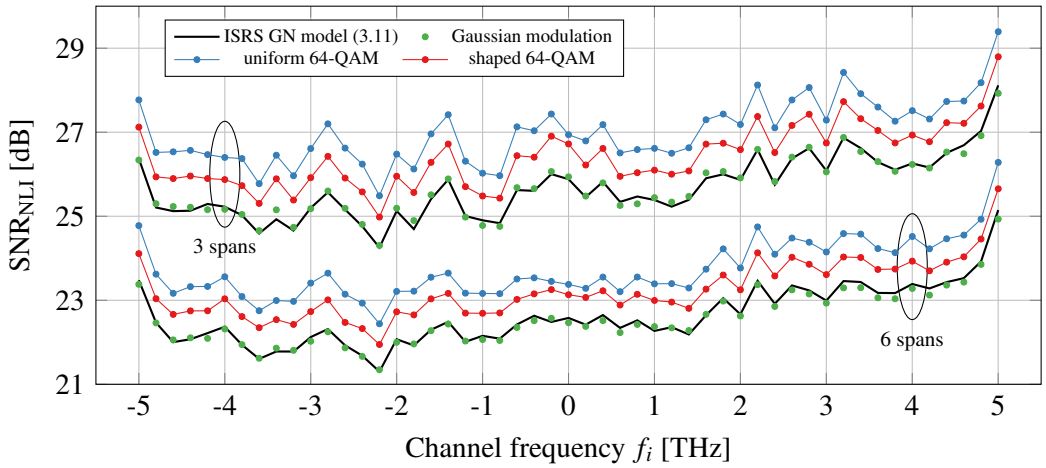

Figure 3.17: Nonlinear performance of the signal channels considering a network scenario as illustrated in Fig. 3.15. The results are obtained from numerical simulations SSFM, shown in markers, and from the ISRS GN model in analytical form (3.11), shown in black.

200 channel slots act as interfering channels which are continuously dropped and added at each ROADM. 80% of the interfering channels are dropped randomly (uniform) and channels are added randomly choosing an empty channel slot, until a 80% network utilisation is reached. Realistic network utilisations may vary and are generally strongly dependent on traffic conditions and network operation. In practice, those unused channel slots are the result of variably loaded network spans. The added channels exhibit a random power offset between ± 1 dB with respect to the signal channels to account for non-ideal power equalisation in ROADM nodes. It was assumed that the interfering channels use the same modulation format as the signal channels and were randomly pre-dispersed corresponding to a transmission distance between 0 and 1000 km to emulate the propagation from different lightpaths in the network. The wavelength dependent gain due to ISRS was perfectly compensated to ease a comparison to the case of fully occupied spans in Fig. 3.16.

The nonlinear performance against the signal channels, calculated using the ISRS GN model (3.11) and SSFM, is shown in Fig. 3.17. The $\mathrm{SNR}_{\mathrm{NLI}}$ exhibits less average tilt with respect to the fully occupied case as less average optical power is transmitted. The average power difference between the outer channels due to ISRS was 5.2 dB. The fluctuation of the SNR (as high as 2 dB) is a consequence of the lightpath configuration. It can be seen that this fluctuation is smaller after 6 spans due to averaging. The average deviation between the ISRS GN model and Gaussian modulation is only 0.1 dB which can be considered negligible. The average deviation to uniform and shaped 64-QAM is 1.3 dB and 0.7 dB after 3 spans and 1.1 dB and 0.6 dB after 6 spans. The deviation is smaller than in the point-to-point case

because the interfering channels exhibit in average more accumulated dispersion (due to their transmission history when they are entering the light pathof interest). More importantly, all formats exhibit similar SNR fluctuations as predicted by Eq. (3.11).

Based on the numerical validation, carried out in this section, it can be concluded that the ISRS GN model Eq. (3.11) predicts the nonlinear interference power with negligible error. It can therefore be used in the analytical modelling of transmission performance in ultra-wideband transmission systems for point-to-point and mesh optical networks.

3.8 Summary

Increasing the optical bandwidth, that is used for transmission, is a promising candidate to increase the total capacity of installed and future optical networks. In this chapter, new analytical models were derived that accurately describe the nonlinear distortions in ultra-wideband transmission, where the optical bandwidth exceeds 5 THz and ISRS becomes significant. The model was experimentally validated over an optical bandwidth of 9 THz. The model was then used to estimate the achievable rate degradation imposed by ISRS. The study suggested that the impact of ISRS on the AIR can be limited to only 10%. It can therefore be concluded that ISRS does not represent an insurmountable challenge and, indeed, represents a viable option to increase the capacity of fibre communication systems. The derived model was further extended to account for variably loaded spans which is key in the modelling of mesh optical networks. The results in this thesis can be used for the design, operation and optimisation for ultra-wideband point-to-point and mesh optical networks. The key results from this chapter are:

- For the first time, the widely used GN model was extended to account for inter-channel stimulated Raman scattering. Two approaches were proposed: i) the effective attenuation approach, a low complexity extension of the GN model valid up to 4 dBm/ch, and ii) the more complex but highly accurate ISRS GN model. Using the newly derived models, it was found that ISRS imposes a significant wavelength dependence on the SNR across the received spectrum. The models are extensively validated by numerical simulations with negligible deviations between modelling and simulation results using Gaussian constellations. The computational of the effective attenuation approach is lower than the ISRS GN model, as it contains one less integration dimension. Deviations of 1.6 dB and 0.8 dB were found between the model and uniform and Maxwell-Boltzmann shaped 64-QAM, respectively. The

results are a significant contribution in the modelling of ultra-wideband transmission systems which led to the publication of [P8, P13, P29].

- The described models were validated by experimental demonstrations of up to 9 THz optical bandwidths, occupying the entire C+L band. It was found that temporal gain dynamics of ISRS are negligible, confirming a fundamental assumption used in the derivation of the models, described in this section. It was shown that while high wavelength channels experience an increase in SNR, the SNR of low wavelength channels is decreased as a result of ISRS. For the outer most wavelengths, deviations of up to 0.4 dB were found between model and experiment. However, similar deviations were found with and without ISRS, suggesting that those deviations are not originating from shortcoming in the ISRS modelling. The work led to the publication of [P29].

- Using the derived models, the degradation in AIR imposed by ISRS was quantified. Suggested by modelling and experimental results, described in this chapter, ISRS leads to performance gain and loss of high and low wavelength channels, respectively. As a result of this balance, the degradation of ISRS on the AIR can be limited to only 10% by using gain flattening filters and adaptive modulation formats. The study indicated that expanding bandwidth beyond C-band is, indeed, a promising solution in increasing the capacity of next-generation optical networks. The work led to the publication of [P13].

- The described models were further extended to transmission in mesh optical network, where fibre spans are variably loaded due to traffic patterns and RWA. Fluctuation of up to 2 dB in terms of nonlinear distortions were found after 6 spans and passing 3 network nodes. The results were validated by numerical simulations showing negligible deviation between modelling and simulation using Gaussian constellations. A deviation of 1.1 dB and 0.6 dB was found between the model and uniform and Maxwell-Boltzmann shaped 64-QAM, respectively. The work led to the publication of [P27].

Chapter 4

Approximations and modulation format correction of the ISRS GN model

The ISRS GN model in integral form was derived in chapter 3 to accurately predict the impact of ISRS on the nonlinear distortions. Although the ISRS GN model yields vast time reductions compared to numerical simulations, it is not suitable for real-time applications as it relies on numerical integrations. To enable real-time applications and computation times in sub-second scale, closed-form approximations of the ISRS GN model need to be derived. Fig. 4.1 shows the approaches of modelling ISRS, categorised into numerical simulations, integral and closed-form approaches. Closed-form approximations are key for time sensitive applications and optimisation problems with large solution space such as launch power optimisation, RWA and network design.

In this chapter approximations and modulation format corrections of the ISRS GN model, presented in Sec. 3.5, are derived and presented. Novel formulas for Gaussian modulated signals as well as for real-world QAM constellations are derived in Sec. 4.2.4, to predict the nonlinear interference in the presence of inter-channel stimulated Raman scattering. Additionally, an approach is proposed in Sec. 4.3 that allows the derived formulas to be applied beyond 15 THz, where currently no analytical solutions of the Raman gain equations exist. The results in this chapter are significant in the design and real-time optimisation of ultra-wideband optical networks. The results in this chapter were peer-reviewed and published in [P4, P6, P19].

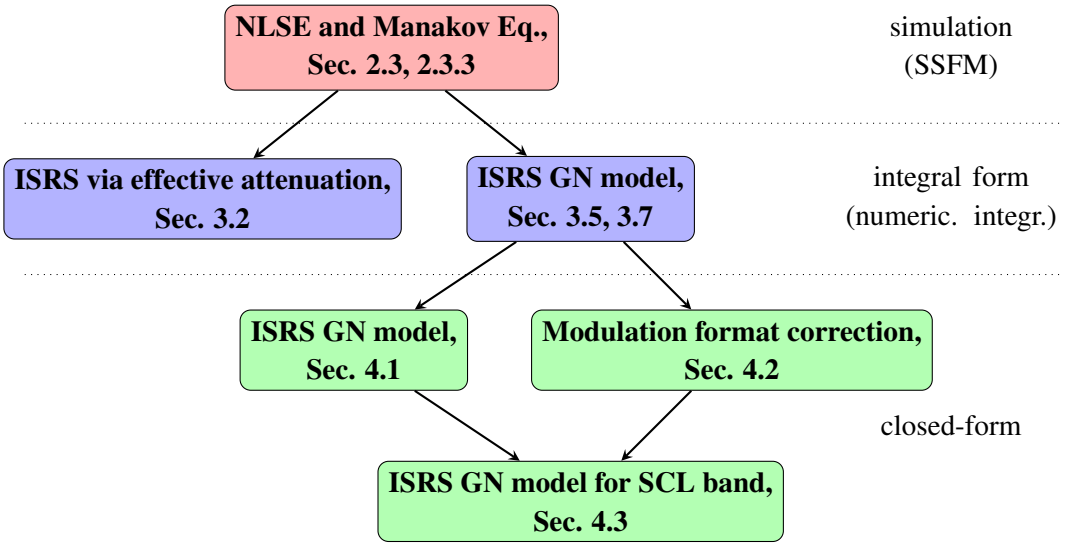

Figure 4.1: Approaches of modelling nonlinear distortions in the presence of inter-channel stimulated Raman scattering. Analytical models that account for ISRS in integral form are described in Ch. 3. Closed-form approximations and modulation format corrections of the nonlinear distortions are described in this chapter.

4.1 A closed-form approximation of the Gaussian Noise model in the presence of inter-channel stimulated Raman scattering

In this section, a closed-form approximation of the ISRS GN model (3.6) is derived. The proposed formula accounts for the SPM and XPM contributions of the NLI, which are discussed in Sec. 4.1 in more detail. The formula is presented in Sec. 4.1.2 and its key assumptions are addressed in Sec. 4.1.4. As a sanity check, the convergence to previously published results is addressed in Sec. 4.1.3. Finally, numerical validations are carried out in Sec. 4.1.5 for transmission in a fully occupied point-to-point link and a variably loaded mesh optical network.

4.1.1 SPM and XPM contributions of the ISRS GN model

Before presenting the proposed closed-form formula, one of the key assumption made in its derivation is described. The formula neglects FWM contributions, that are NLI contributions that are jointly generated by two interfering channels on a given COI. This assumption is often referred to as the XPM assumption [21, 31–33, 141]. The neglected FWM contributions are typically very small and can be neglected in high dispersive links, where high symbol rates or channel spacings are used [117, 121]. Neglecting the FWM contributions significantly simplifies the analytical modelling as fewer terms have to be accounted for. Applying the XPM assumption, the total (remaining) NLI contribution can be written as the sum

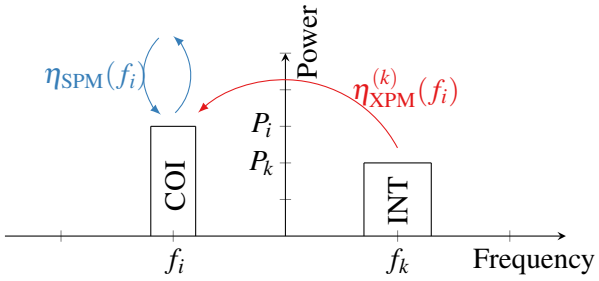

Figure 4.2: Illustration of the transmitted spectrum $G_{\mathrm{Tx}}(f)$ subject to the XPM assumption. Shown are the channel under test (COI) and a single interferer (INT) with arbitrary power levels, bandwidths and center frequencies. The total XPM is then obtained by summing over all interferers $k \in S_i$ as in (4.1).

over all individual XPM contributions of each interfering channel, reducing the NLI modelling to a single XPM integral. This XPM integral is now described in more detail.

Let $\eta^{(k)}_{\mathrm{XPM}}(f_i)$ be the nonlinear perturbation (i.e. the NLI contribution) of the COI i, caused by a single interferer (INT) k. The reader is reminded that NLI contributions caused by interfering channel (i.e. $i \neq k$) are denoted as XPM, whereas the NLI contribution caused by the COI itself (i.e. $k = i$) is denoted by SPM. Mathematically, the set of all XPM interferers, with respect to a given COI i, is written as

$$S_i = \{k \in \mathbb{N} \mid 1 \leq k \leq N_{\mathrm{ch}} \text{ and } k \neq i\}. \tag{4.1}$$

The SPM and XPM contribution of a COI and a single INT are schematically illustrated in Fig. 4.2. The COI and INT channel may exhibit different power levels, bandwidths and centre frequencies. It is assumed that the SNR for the entire transmission path is the sum of each individual link contribution, including the coherent accumulation of NLI. The nonlinear SNR at the receiver is then given by

$$\begin{aligned} \mathrm{SNR}_{\mathrm{NLI}}^{-1} &= \sum_{j=1}^{n} \mathrm{SNR}_{\mathrm{NLI},i}^{-1} \\ \Longleftrightarrow \mathrm{SNR}_{\mathrm{NLI}}^{-1} &= \eta_n(f_i) P_i^2 \approx \sum_{j=1}^{n} P_{i,j}^2 \left[\eta_{\mathrm{SPM,j}}(f_i) n^{\varepsilon} + \eta_{\mathrm{XPM,j}}(f_i)\right], \end{aligned} \tag{4.2}$$

where $\eta_{\mathrm{SPM,j}}(f_i)$ is the SPM contribution and $\eta_{\mathrm{XPM,j}}(f_i)$ is the total XPM contribution generated in the j'th span. $P_{i,j}$ is the power of channel i launched into the jth span. For the first fibre span we have that $P_{i,1} = P_i$. The approximation symbol in Eq. (4.2) is due to the XPM assumption of the total NLI. The coherent accumu-

lation along multiple fibre spans is included using the coherence factor ε (see Sec. 2.6.3).

As for example in Eq. (2.47), the coherence factor is typically defined for the entire optical signal. However in Eq. (4.2), only the SPM contribution is assumed to accumulate coherently and the coherence factor is *redefined* over the channel bandwidth B_i as proposed in [142]. The XPM contribution, on the other hand, is assumed to accumulate incoherently. The advantage of this approach is that the coherent accumulation is independent of the transmitted spectrum, the coherent accumulation is only a property of the COI which, by definition, always propagates from the transmitter to the receiver. This significantly simplifies the modelling of NLI in optical mesh networks where fibre spans can be variably loaded. The approach is consistent with the observations in [117]. As a result, the nonlinear SNR (or in turn the total NLI coefficient) can be written as in Eq. (4.2). The proposed formalism in this chapter assumes that the coherence factor itself is not altered by ISRS, which is not strictly true as shown in Fig. 3.11. However, this effect is neglected due to its small impact on the NLI. For SMF based spans and a 10 THz signal, this results in an approximation error of around 0.1 dB after 10 fibre spans as shown in Fig. 3.11.

Different fibre parameters and launch power distributions for each span can be modelled using Eq. (4.2) by utilising the span dependent NLI coefficients. The NLI coefficient for the entire path, normalised to the transmitted power is obtained from Eq. (4.2) as

$$\eta_n(f_i) \approx \sum_{j=1}^{n} \left[\frac{P_{i,j}}{P_i}\right]^2 \cdot \left[\eta_{\mathrm{SPM,j}}(f_i)\, n^{\varepsilon} + \eta_{\mathrm{XPM,j}}(f_i)\right]. \tag{4.3}$$

Eq. (4.3) essentially returns the NLI coefficient of each span, normalised to the launch power of the transmitter.

The total XPM contribution $\eta_{\mathrm{XPM}}(f_i)$ in Eq. (4.3) is obtained by summing over all interfering channels

$$\eta_{\mathrm{XPM}}(f_i) = \sum_{\forall k \in S_i} \eta_{\mathrm{XPM}}^{(k)}(f_i), \tag{4.4}$$

where $\eta_{\mathrm{XPM}}^{(k)}(f_i)$ is the XPM contribution of a single interfering channel k on channel i.

To obtain a closed-form solution of the NLI coefficient, we first derive an integral expression for the SPM and XPM contributions in Eq. (4.3). In the following, the NLI caused by a single interferer on the COI, is analytically eval-

uated. It is assumed that the channel of interest i has normalised pulse shape $g_i(f-f_i) = \frac{1}{B_i}\Pi\left(\frac{f-f_i}{B_i}\right)$, launch power P_i, channel bandwidth B_i and is centered at frequency f_i. The function $\Pi(x)$ denotes the rectangular function. The rectangular pulse shape implies a pulse shape roll-off of 0, assumed to simplify the formalism. The interfering channel has normalised pulse shape $g_k(f-f_k) = \frac{1}{B_k}\Pi\left(\frac{f-f_k}{B_k}\right)$, launch power P_k, bandwidth B_k and is centered at frequency f_k. The transmitted spectrum, consisting of the COI and a single INT channel, is then given by

$$G_{\mathrm{Tx}}(f) = P_i g_i(f-f_i) + P_k g_k(f-f_i-\Delta f), \tag{4.5}$$

where $\Delta f = f_k - f_i$ is the frequency separation between COI and INT channels. An illustration of (4.5) with the resulting nonlinear interactions on the COI is shown in Fig. 4.2.

The arising nonlinear perturbation (i.e. distortion, interference) can be obtained by utilising the results derived in Chapter 3. Substituting the transmitted spectrum (4.5) in the ISRS GN model in analytical form (3.6) yields six non-identical terms where only two are non-zero and contribute to the NLI of the COI. These two terms are the SPM and the XPM contribution. The XPM contribution is

$$\begin{aligned}\eta^{(k)}_{\mathrm{XPM}}(f_i) = \frac{32}{27}\frac{\gamma^2}{B_k^2}\left(\frac{P_k}{P_i}\right)^2 \int_{-\frac{B_i}{2}}^{\frac{B_i}{2}} df_1 \int_{-\frac{B_k}{2}}^{\frac{B_k}{2}} df_2\, \Pi\left(\frac{f_1+f_2}{B_k}\right) \\ \cdot \left| \int_0^L d\zeta\, \frac{P_{\mathrm{tot}} e^{-\alpha\zeta - P_{\mathrm{tot}} C_{\mathrm{r}} L_{\mathrm{eff}}\cdot(f_1+f_2+f_k)}}{\int G_{\mathrm{Tx}}(\nu) e^{-P_{\mathrm{tot}} C_{\mathrm{r}} L_{\mathrm{eff}} \nu} d\nu} e^{j\phi(f_1+f_i, f_2+f_k, f_i, \zeta)} \right|^2,\end{aligned} \tag{4.6}$$

and the SPM contribution is

$$\eta_{\mathrm{SPM}}(f_i) = \frac{1}{2}\eta^{(i)}_{\mathrm{XPM}}(f_i). \tag{4.7}$$

As mentioned previously, it can be seen that only one, multidimensional integral expression remains after applying the XPM assumption. It should be emphasised that in Eq. (4.6), P_{tot}, B_{tot} and $G_{\mathrm{Tx}}(\nu)$ refer to the launch power, bandwidth and transmitted spectrum of the *entire* WDM signal and *not* to a single COI-INT pair.

4.1.2 The ISRS GN model in closed-form

The goal of this section is to describe the two separate closed-form formulas that are proposed, one formula for the SPM $\eta_{\mathrm{SPM}}(f_i)$ contribution and one formula for the XPM contribution $\eta_{\mathrm{XPM}}(f_i)$. The total NLI is then obtained using Eq. (4.4). This Section only describes the resulting formulas. The detailed derivations of the formulas are carried out in Appendices A.3.2 and A.3.1.

The proposed closed-form approximation for the SPM contribution is (see Sec. A.3.2)

$$\eta_{\mathrm{SPM}}(f_i) \approx \frac{4}{9}\frac{\gamma^2}{B_i^2}\frac{\pi}{\phi_i\bar{\alpha}(2\alpha+\bar{\alpha})} \cdot \left[\frac{T_i-\alpha^2}{\alpha}\mathrm{asinh}\left(\frac{\phi_i B_i^2}{\pi\alpha}\right)+\frac{A^2-T_i}{A}\mathrm{asinh}\left(\frac{\phi_i B_i^2}{\pi A}\right)\right], \tag{4.8}$$

with $\phi_i = \frac{3}{2}\pi^2(\beta_2+2\pi\beta_3 f_i)$, $A=\alpha+\bar{\alpha}$ and $T_i=(\alpha+\bar{\alpha}-P_{\mathrm{tot}}C_{\mathrm{r}}f_i)^2$. The proposed closed-form approximation for the total XPM contribution is (see Sec. A.3.1)

$$\eta_{\mathrm{XPM}}(f_i) \approx \frac{32}{27}\sum_{k=1,k\neq i}^{N_{\mathrm{ch}}}\left(\frac{P_k}{P_i}\right)^2\frac{\gamma^2}{B_k\phi_{i,k}\bar{\alpha}(2\alpha+\bar{\alpha})} \cdot \left[\frac{T_k-\alpha^2}{\alpha}\mathrm{atan}\left(\frac{\phi_{i,k}B_i}{\alpha}\right)+\frac{A^2-T_k}{A}\,\mathrm{atan}\left(\frac{\phi_{i,k}B_i}{A}\right)\right], \tag{4.9}$$

with $\phi_{i,k}=2\pi^2(f_k-f_i)[\beta_2+\pi\beta_3(f_i+f_k)]$. The sum in Eq. (4.9) represents the summation over the XPM contribution of each individual interfering channel as in Eq. (4.1).

The parameter $\bar{\alpha}$ can be used to apply the proposed closed-formula in more general cases. Such cases include improved accuracy for non-uniform (tilted) launch power distributions, wavelength dependent attenuation and even the extension of the formula beyond 15 THz, i.e. beyond the triangular region of the Raman gain spectrum. The application of the formulas for optical bandwidths beyond 15 THz is discussed in more detail in Sec. 4.3. If not specified explicitly, it holds that $\bar{\alpha}=\alpha$. Eqs. (4.8) and (4.9) represent the first closed-form formulas that account for inter-channel stimulated Raman scattering, the dispersion slope and for arbitrary launch power distributions.

4.1.3 Comparison to published formulas in the absence of ISRS

The SPM contribution against channel bandwidth, obtained by numerically integrating Eq. (4.6) and by using its proposed approximation in closed-form Eq. (4.8), is shown in Fig. 4.3. For better comparison, the simulation parameters in this chapter are similar to the ones used in Sec. 3.7.2. A total optical bandwidth of 10.05 THz was assumed using a launch power of 0 dBm per channel. As an example, a single COI, centered at $f_i=-4040$ GHz, and a single interfering channel was transmitted over a 100 km long SMF span. The detailed simulation and fibre parameters can be found in Tab. 3.1. The proposed formula for the SPM contribution Eq. (4.8)

exhibits remarkable accuracy with and in the absence of ISRS throughout all symbol rates compared to numerically integrating Eq. (4.6). The very good accuracy suggests the validity of Eq. (4.8) and that the validity of the assumptions made in its derivation (see Appendix A.3.2).

For optical bandwidths that are within the C-band (< 5 THz), i.e. in the absence of ISRS and without considering the dispersion slope, the proposed formulas (4.8)(4.9) are comparible to those in Eq. (2.49) (see Sec. 2.6.3). To compare the newly derived formula to previous published results (in the absence of ISRS), Eq. (2.49), taken from [20, Eq. (39)] [21, Eq. (11)], is also shown in Fig. 4.3. For a fair comparison, the dispersion slope was included in the results of [20, Eq. (39)] [21, Eq. (11)], which do not account for the dispersion slope. Without ISRS, the result in [20, Eq. (39)] [21, Eq. (11)] is similar to the proposed formula Eq. (4.8) except for low symbol rates. This difference, of up to 1 dB, mainly stems from the assumed domain of integration with respect to frequencies (f_1, f_2)). The formula, derived in this Section, assumes a circular integration domain, whereas [20, Eq. (39)] [21, Eq. (11)] both assume a rectangular integration domain. A circular integration domain provides better accuracy for lower symbol rates and yields analytical solutions in terms of elementary functions as opposed to special functions [118].

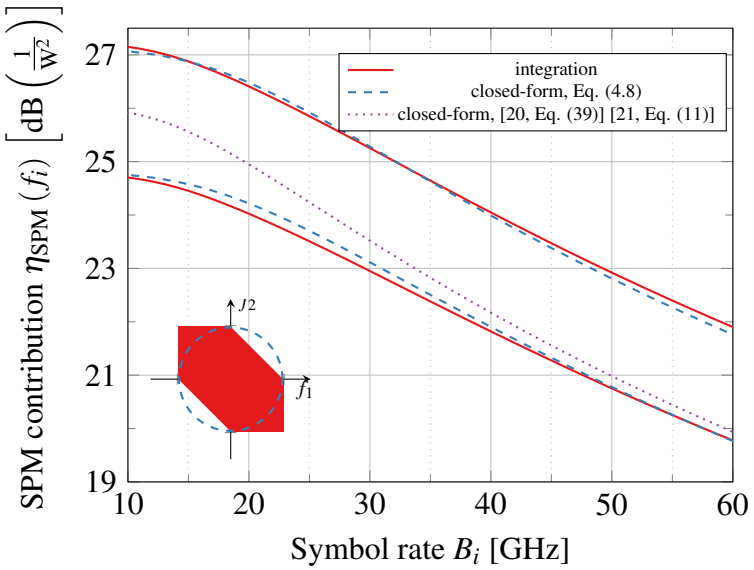

Figure 4.3: SPM contribution for $i = 25$ with $f_i = -4040$ GHz as a function of symbol rate (bandwidth), obtained from numerically solving the ISRS GN model in integral form (4.6) and its proposed approximation in closed-form (4.8). The inset shows the actual integration domain and its circlular approximation. For comparison the results of [20] [21] are shown, which both model SPM in the absence of ISRS.

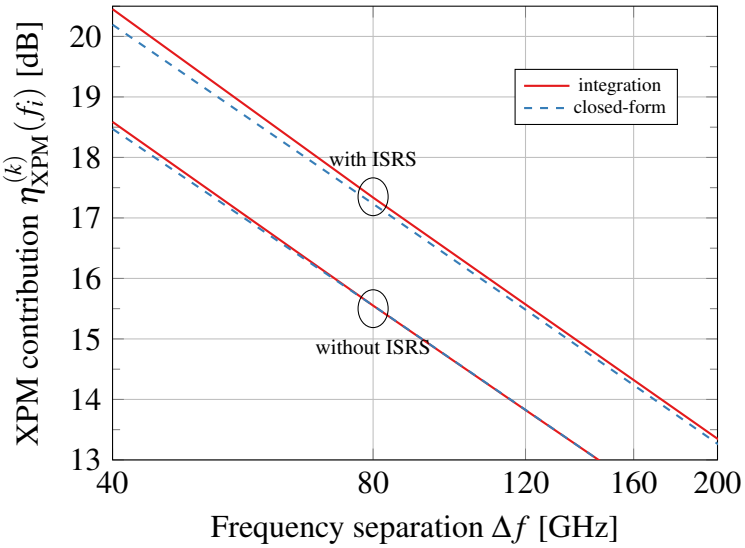

Figure 4.4: XPM contribution for channel $i = 25$ with $f_i = -4040$ GHz as a function of frequency separation between channel of interest (COI) and interferer (INF), obtained from numerically solving the ISRS GN model in integral form (4.6) and its proposed approximation in closed-form (4.9) (for $k \in \{26, 27, 28, 29, 30\}$). A WDM signal with an optical bandwidth of 10 THz is assumed with 0 dBm launch power per channel.

4.1.4 Discussion of key assumptions

The assumptions to derive the formulas for the SPM Eq. (4.8) and the XPM contribution Eq. (4.9) are now discussed in more detail. Additionally, bounds on the validity range are derived and described. The three key assumptions in the derivation of the formulas are:

Assumption 1): In the derivation of the XPM contribution Eq. (4.9), the frequency separation between the channel of interest and the interfering channel is much greater than half of the channel bandwidth, mathematically $|\Delta f| \gg \frac{B_k}{2}$.

Assumption 2): The impact of ISRS on the signal power profile is small. As a consequence, it can be approximated by a first-order Taylor series (with respect to the variable $x(\zeta) = P_{\mathrm{tot}} C_{\mathrm{r}} \bar{L}_{\mathrm{eff}}(\zeta)$) and higher order terms can be neglected.

Assumption 3): The signal power profile, in the presence of ISRS, is only a function of the total optical launch power and it is independent of its spectral distribution. This assumption has no impact on a uniform launch power distribution.

Assumption 1) is mathematically equivalent with the zeroth-order solution of the

inner integral, over f_2, in Eq. (4.6). In Appendix A.3.3, it is shown that the introduced relative approximation error of the XPM contribution, between a single COI and INT channel pair, is upper bounded by

$$\text{Rel. Err.} < 8\% \cdot \left(\frac{B_k}{\Delta f}\right)^2. \tag{4.10}$$

The channel spacing for an interfering channel that is adjacent to the channel of interest is $\Delta f = B_k$. The approximation error, caused by assumption 1, for those directly adjacent channels is *at most* $8\% = 0.3$ dB. The approximation error is smaller for non-Nyquist channel spacing, where significant guard bands are introduced between neighbouring channels. All other interfering channels have a channel spacing of $\Delta f \geq 2B_k$. For those channels, the relative approximation error is Rel. Err. $< 2\% = 0.08$ dB using Eq. (4.10). The reader is reminded that the total NLI on the channel of interest is a summation of all interfering channels (see Eq. (4.1)), where most channels exhibit relative approximation errors of Rel. Err. $<<$ 0.08 dB. Therefore, it can be concluded that the relative approximation error of assumption 1) on the *total* NLI is negligible.

Assumption 2) is valid when the impact of ISRS on the signal power profile can be considered small. This is required, as the signal power profile is described by a first-order Taylor series in the derivation of Eqs. (4.8)(4.9). The first-order approximation of the analytical solution of the Raman equations 2.28 is derived as

$$P_i^{(1)}(z) = \left(1 + \tilde{T}_i\right) e^{-\alpha z} - \tilde{T}_i e^{-(\alpha+\bar{\alpha})z}, \tag{4.11}$$

where $\tilde{T}_i = -\frac{P_{\text{tot}} C_r}{\bar{\alpha}} f_i$ and $\bar{\alpha} = \alpha$. Eq. (4.11) approximates the power profile in the presence of ISRS to first-order. The first-order profile is crucial in the derivation of the closed-form solutions in this section and derived in Appendix A.3.1. The channel powers for the highest and lowest frequency channels as a function of distance are shown in Fig. 4.5 using the Raman gain equations (2.27) and the first-order approximation (4.11). A 10 THz signal was assumed with a launch power of -2 dBm per channel. Fig. 4.5 shows that the first-order approximation of the signal power profile is in good agreement with the actual power profile. As a consequence, the first-order profile can be used in order to solve Eq. (4.6) analytically. Higher-order terms, with respect to ISRS, can be neglected. However, to quantify the induced approximation error, these higher order terms can be analysed. The analysis is carried out in Appendix A.3.4, where it was shown that higher-order terms can be neglected

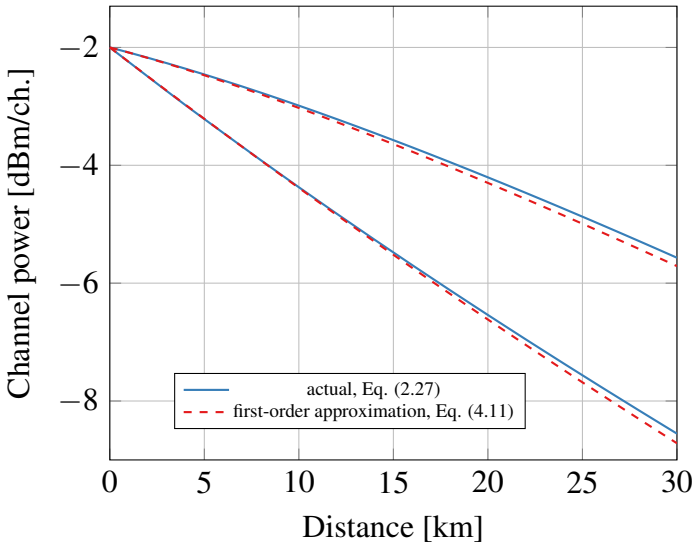

Figure 4.5: The power of the highest and lowest frequency channel as a function of distance. The results were obtained by numerically solving the Raman equations (2.27) and the first-order approximation (4.11). A launch power of -2 dBm per channel, signal bandwidth of 10 THz and fibre parameters $\alpha = 0.162\ \frac{\text{dB}}{\text{km}}$, $C_r = 0.0234\ \frac{1}{\text{W}\cdot\text{km}\cdot\text{THz}}$ were considered.

if

$$0.23 \cdot \Delta\rho\,(L)\,[\text{dB}] \ll 6. \tag{4.12}$$

with the ISRS power transfer between the outer channel of the WDM signal as in Eq. (3.8). In Figures 4.3 and 4.4, the ISRS power transfer is $\Delta\rho\,(L)\,[\text{dB}] = 6.3$ dB and Eq. yields $1.4 \ll 6$. Following Eq. (4.12), assumption 2) should introduce a small approximation error, which can be seen in Fig. 4.3 and 4.4 in the presence of ISRS.

Assumption 3) introduces no approximation error when the spectral launch power distribution is uniform. The impact of ISRS on the signal power profile is a function of the total optical launch power, mathematically expressed as $e^{-P_{\text{tot}}C_{\text{r}}L_{\text{eff}}(f_1+f_2-f_i)}$ in Eq. (4.6), and its spectral distribution, mathematically expressed as $\frac{1}{P_{\text{tot}}}\int G_{\text{Tx}}(\nu)e^{-P_{\text{tot}}C_{\text{r}}L_{\text{eff}}\nu}d\nu$ in (4.6). In the derivation of Eqs. (4.8)(4.9), it is assumed that the spectral launch power distribution is uniform over the optical bandwidth, mathematically $\int \frac{1}{P_{\text{tot}}}G_{\text{Tx}}(\nu)e^{-x\cdot\nu}d\nu = \frac{xB_{\text{tot}}}{2\sinh\left(\frac{xB_{\text{tot}}}{2}\right)}$. Therefore, small approximation errors are expected for non-uniform launch power distributions or for variably loaded transmission spectra. However, in Sec. 4.1.5.4, it is shown through numerical simulations that assumption 3) has negligible impact in the context of mesh optical networks, where fibre spans are variably loaded.

4.1.5 Numerical validation

The derived closed-form formulas for the SPM (4.8) and the XPM (4.9) contributions were validated via numerical split-step simulations (see. Sec. 2.3.4). For better comparison, the same simulation and transmission link parameters as in Sec. 3.7.2 (see Tab. 3.1) were used. The validation is first carried out for a point-to-point transmission scenario, with fully occupied signal spectrum, and subsequently for a mesh optical network scenario with variably loaded fibre spans (as in Sec. 3.6).

4.1.5.1 Transmission setup

The reader is referred to Sec. 3.7 for more details on the simulation setup. For the logarithmic step size distribution, two different number of steps were used. A total number of simulation steps of $0.25 \cdot 10^6$ was found to be sufficient for launch powers of up to 0 dBm per channel and $1 \cdot 10^6$ steps were sufficient for launch powers of up to 3 dBm/ch. Although a launch power of 3 dBm/ch is significantly (by 3 dB) beyond the optimum launch power, such a high launch power was simulated in order to test the limits of assumption 2) in Sec. 4.1.4, which states that the impact of ISRS has to be small.

Similar to Sec. 3.7, a WDM signal consisting of 251×40 GBd channels, spanning a total optical bandwidth of 10 THz, was considered. All channels within the WDM comb were entirely modulated with either Gaussian or uniform 64-QAM symbols.

The nonlinear interference coefficient was used as the figure of merit, estimated from the nonlinear SNR as $\eta_n(f_i) = \frac{\mathrm{SNR}_{\mathrm{NLI},i}}{P_i^3}$. To ease the NLI estimation in the split-step simulations and for a fair comparison between numerical simulation and the ISRS GN model, we consider ideal, noiseless and lumped amplifiers.

4.1.5.2 Single span transmission

The NLI coefficient after a single transmission span, using Eqs. (4.8)(4.9) and SSFM, is shown in Fig. 4.6a). Two different launch powers are shown, namely 0 dBm/ch. and 2 dBm/ch., resulting in ISRS power transfers of $\Delta\rho(L)\,[\mathrm{dB}] = 6.3$ dB and $\Delta\rho(L)\,[\mathrm{dB}] = 10.3$ dB, respectively. Additionally, Fig. 4.6a) shows the (unphysical) case of no ISRS for comparison. To more accurately validate the impact of ISRS on the NLI, Fig. 4.6b) shows the deviation of the NLI coefficient as a function of the ISRS power transfer. The results in both figures were obtained by split-step simulations, numerically integrating the ISRS GN model in integral form (3.6) and its proposed closed-form approximation (4.8)(4.9). As already shown in Sec. 3.7.2, the ISRS GN model in integral form matches the simulation results with negligible error. Minor deviations appear at the most outer channels which is due to the local white noise assumption (see Eq. (2.45)). The local white noise assumption

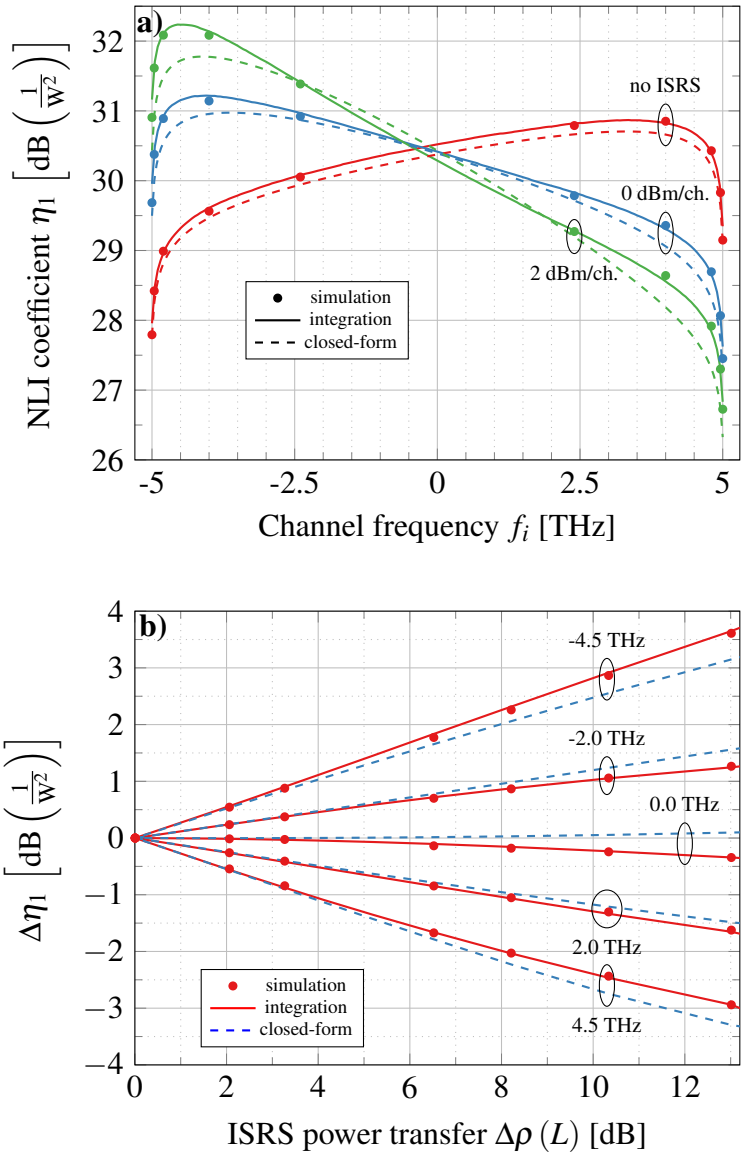

Figure 4.6: The NLI coefficient after one 100 km span as a function of channel frequency is shown in a). The deviation of the NLI coefficient after one span as a function of ISRS power transfer for different channels within the transmitted WDM signal is shown in b). The results were obtained by numerical simulations, numerically solving the ISRS GN model in integral form (3.6) and its proposed approximation in closed-form (4.8) and (4.9).

can be lifted by integrating the NLI PSD over the channel bandwidth of the COI.

It can be seen that Eqs. (4.8)(4.9) are in good agreement with the ISRS GN model in integral form (3.6) and the simulation results. In the absence of ISRS, the average deviation between closed-form formulas and simulation is 0.1 dB. This deviation stems from the XPM assumption (see Sec. 4.1.1). It can be concluded as the closed-form formulas predict the individual SPM and XPM contributions with neg-

ligible error, as shown in 4.3. When ISRS is accounted for, the average discrepancy is 0.1 dB for 0 dBm/ch. and 0.2 dB for 2 dBm/ch. launch power, respectively. This additional discrepancy arises from the assumption 2) in Sec. 4.1.4, which states that the impact of ISRS is assumed to be small. As the impact of ISRS is more significant at outer channels within the WDM signal, this assumption imposes larger approximation errors on those channels. Mathematically, higher order terms of the Taylor series describing ISRS become significant.

4.1.5.3 A point-to-point transmission scenario

After validating the closed-form formulas for single span transmission, their accuracy in a multi-span point-to-point transmission system was evaluated. The system under test is identical to the one used in Sec. 3.7.2, consisting of six spans of standard single mode fibre. The launch power was 0 dBm/ch. which is the optimum launch power for the centre channel in the presence of EDFAs with a noise figure of 5 dB. However to ease the validation, ASE noise was not considered in the simulation and noise figure was only considered in the choice of the launch power. At each fibre span the launch power was ideally recovered by means of gain flattening filters (see Sec. 3.2).

The NLI coefficient, using Eqs. (4.8)(4.9) and the SSFM, as a function of frequency is shown in Fig. 4.7a) and 4.7b) without and with ISRS, respectively. The unphysical case of not considering ISRS is only shown for comparison. The results were obtained by split-step simulations, the ISRS GN model (3.6), including the phased-array term, and the proposed formulas in closed-form (4.8)(4.9).

To study the impact of the coherent accumulation, expressed by the variable ε in Eq. (4.3), the closed-form approximation is considered with an incoherent ($\varepsilon = 0$) and a coherent ($\varepsilon \neq 0$) NLI accumulation of along the transmission path. The coherence factor, defined as in Sec. 4.1.1, for the studied system configuration is $\varepsilon = 0.15$ which was obtained in closed-form from [20]. The average gap between the closed-form, including a coherent accumulation, and the ISRS GN model in integral form is 0.1 dB and 0.2 dB without and with ISRS, respectively. The accuracy is similar to the single span case (see Fig. 4.6), indicating that Eq. (4.3) sufficiently approximates the coherent accumulation of NLI.

A majority of the NLI originates from the XPM contribution, which is accumulating incoherently. Therefore, Eq. 4.1.1 can be simplified by setting $\varepsilon = 0$, assuming an *incoherent* accumulation of NLI. The arising approximation error, of assuming an incoherent NLI accumulation, is 0.2 dB. Depending on accuracy requirements, this approximation error may be deemed negligible. It should be noted, however, that this accuracy loss (with respect to Gaussian modulation) increases

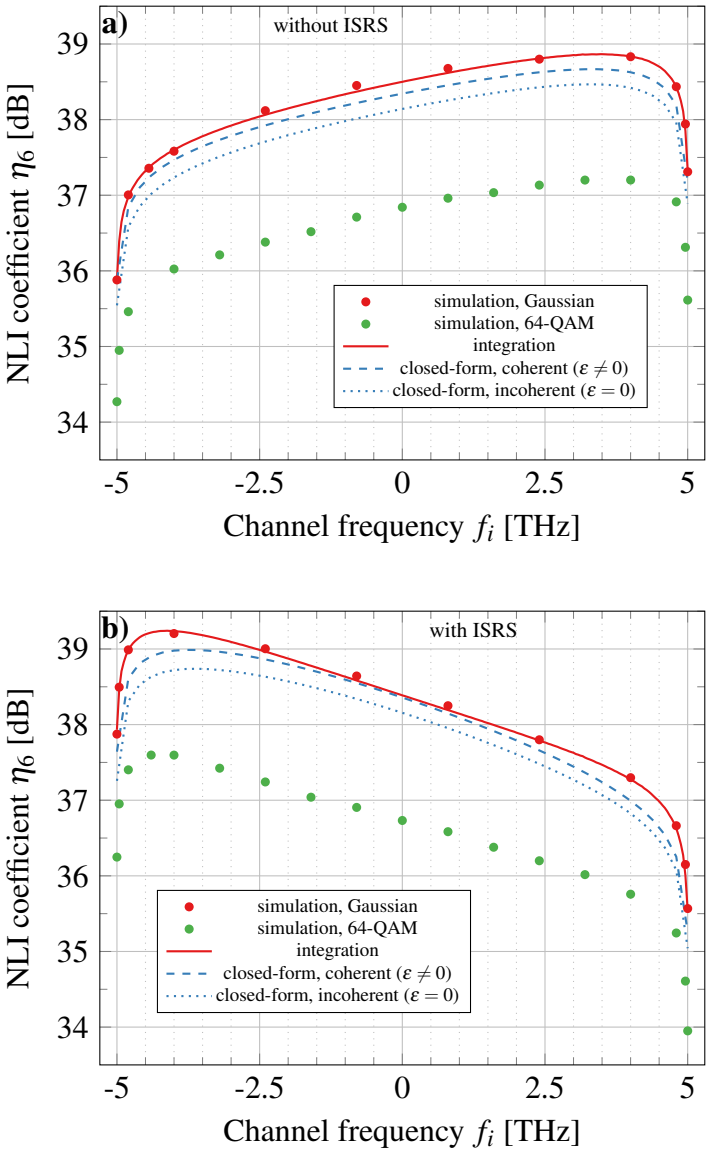

Figure 4.7: The distribution of the NLI coefficient after 6 spans (600 km) without a) and with b) ISRS. A launch power of 0 dBm/ch. was considered yielding an ISRS power transfer of $\Delta\rho\,(L)\,[\mathrm{dB}] = 6.3$ dB. The results were obtained by numerical simulations, the ISRS GN model in integral form (3.6) and its proposed approximation in closed-form (4.8) and (4.9), in coherent and incoherent form.

with the number of spans.

A key assumption of the model is that each frequency component carries a symbol drawn from a symmetric circular Gaussian distribution which leads to an overestimation of the NLI power with respect to square QAM formats. To compare the model predictions to a more practical modulation format, the NLI coefficient using 64-QAM symbols, obtained by the SSFM is shown in Fig. 4.7. The average gap between SSFM using 64-QAM and the closed-form approximation in coherent

form is 1.6 dB in both cases, without and with ISRS. This gap decreases with increasing accumulated dispersion, and hence, with increasing transmission distance. Additionally, state-of-the art transmission systems utilise probabilistic or geometric shaping which further decreases this gap as shaped signals partially resemble Gaussian modulated signals (see Sec. 2.2).

The proposed closed-form approximation appears to model the impact of ISRS on the NLI (SPM and XPM) with excellent accuracy in fully occupied point-to-point transmission scenarios. In can, therefore, be used for system design, optimisation and real-time performance estimations of ultra-wideband transmission point-to-point links.

4.1.5.4 A mesh optical network scenario

Next, the closed-form approximation of the SPM (4.8) and XPM (4.9) contribution was applied and validated in a mesh optical network transmission. As in Sec. 3.7 the fundamental difference in a mesh network, as opposed to a point-to-point transmission, is that: 1) not all channels within the optical WDM signal are transmitted along the *entire* lightpath and 2) fibre spans are variably loaded. At each ROADM, channels are added and dropped according to traffic demands and routing-wavelength allocations.

The transmission setup and the studied example is identical as the one studied in Sec. 3.7, where it was used to validated the ISRS GN model in integral form. In this section, the spectrum occupancy is assumed to be 80% and 90%, which means that 80% (or 90%) of the spectrum are always occupied.

The NLI coefficient, using Eqs. (4.8)(4.9) and the SSFM, for the network utilisation value of 80% is shown in Fig. 4.8a) and the network utilisation of 90% is shown in Fig. 4.8b). The ISRS power transfers for both cases were $\Delta\rho\,(L)\,[\mathrm{dB}] = 5$ dB and $\Delta\rho\,(L)\,[\mathrm{dB}] = 5.7$ dB, which is less than in the point-to-point case as less average power was launched into a span.

The fluctuating behaviour of the NLI coefficient is an immediate consequence of the variably loaded network edges, as shown in Fig. 3.7. The fluctuations are less pronounced in the case of 90 % network utilisation as a larger average spectral occupation leads to more averaging. The proposed closed-form approximation is in good agreement with the simulation results with an average discrepancy of 0.1 dB and 0.2 dB for 80% and 90% network utilisation, respectively. Assumption 3) in 4.1.4 appears to to have a negligible impact on the accuracy of the formula in variably loaded mesh optical networks, due to the good agreement to the SSFM. The average gap between the closed-form approximation and the SSFM using uniform 64-QAM is 1 dB which is less than in the point-to-point case (cf. Fig. 4.7) as

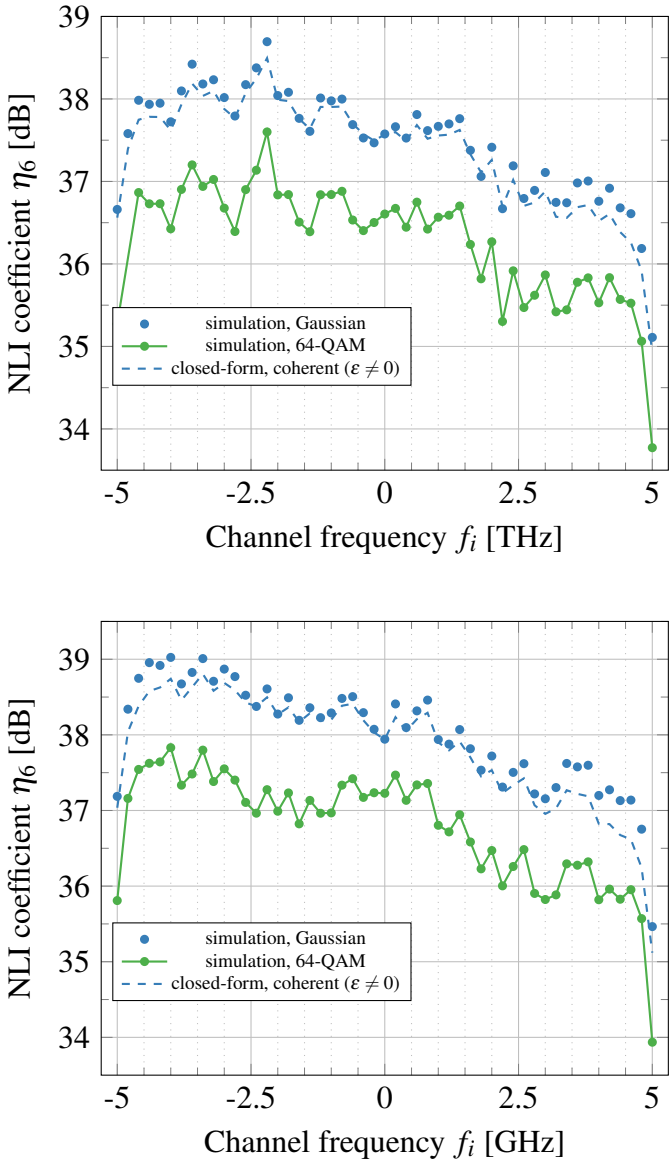

Figure 4.8: The NLI coefficient of every fifth channel (i.e. a channel of interest) after six spans where interfering channels are continuously added and dropped along the transmission with a network utilisation of 80% shown in a) and 90% shown in b). The results were obtained by numerical simulations and using the proposed closed-form approximation (4.8) and (4.9).

add/drop channels exhibit, in average, an higher amount of accumulated dispersion, due to their higher average transmission distance (history).

Based on the validation carried out in this section, it can be concluded that the proposed closed-form approximation models the NLI in mesh optical network scenarios with excellent accuracy. The results, therefore, enable the performance evaluation of complex light path configurations for an *entire* network topology, within only a few microseconds. This is an essential step in the modelling of optical net-

work performance in the ultra-wideband regime.

4.2 A modulation format correction formula for the Gaussian Noise model in the presence of inter-Channel stimulated Raman scattering

In the previous Sec. 4.1, a closed-form approximation of the ISRS GN model (see Sec. 3.5) was proposed. Although a significant result in modelling the NLI of ultra-wideband transmission systems, it does not account for the NLI dependence on the modulation format (see Sec. 2.6.4). The proposed closed-form, just as the conventional and the ISRS GN model (see Sec. 2.6.2 and Ch. 3), assumes a Gaussian constellation at the output of the transmitter. This signal Gaussianity assumption is the major source of inaccuracy for predicting higher order QAM constellations. As a consequence, the closed-form expressions derived in Sec. 4.1 overestimate the NLI for low cardinality formats and in optical links with low accumulated dispersion. As outlined in Sec. 2.6.4, significantly more complex models have been proposed to address and accounts for the modulation format dependence. In this section, a closed-form formula is derived that corrects for the modulation format dependence, in the presence of the dispersion slope and ISRS. The proposed formula represents an extension to the results in Sec. 4.1 to accurately account for non-Gaussian modulation formats.

In particular, a formula is proposed that corrects for the modulation format dependence in the XPM contributions of the total NLI. In Sec. 4.2.1, the general formalism for the modulation format correction of the NLI is reviewed. In Sec. 4.2.2, a generic modulation format correction formula is derived, that can be applied to generic transmission systems that are described by a link function. Moreover, it is shown that the modulation format correction can be approximated by two contributions, one originating from a single transmission span and one asymptotic contribution for a large number of spans. The asymptotic contribution is solved in closed-form for an arbitrary link function, making the result applicable for generic fibre systems using lumped, distributed or hybrid amplification schemes. In Sec. 4.2.4, the methodology is applied to the ISRS GN model in closed-form (see Sec. 4.1) to derive a closed-form formula that corrects for the modulation format dependence. The analytical result accounts for arbitrary number of spans, inter-channel stimulated Raman scattering, arbitrary launch power distributions and wavelength dependent dispersion and attenuation. In Sec. 4.2.5, the newly derived result is validated by means of numerical split-step simulations.

The results described in this section have been peer reviewed and published in

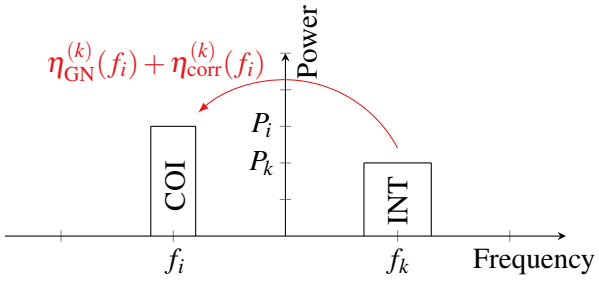

Figure 4.9: Illustration of the Gaussian (GN) NLI contribution and the modulation format correction on the channel of interest (COI) originating from a single interferer (INT). The channels exhibit arbitrary modulation formats, power levels, bandwidths and centre frequencies.

[P4].

4.2.1 General formalism for the modulation format correction

As discussed in Sec. 2.6.4, there are modulation format corrections for the self-phase modulation, cross-phase modulation and four-wave mixing contributions of the total NLI. In [117, 128], a complete set of formulas in integral form has been derived to correct for arbitrary modulation formats for SPM, XPM and FWM contributions. As in the closed-form approximation presented in Sec. 4.1.1 and similar to Sec. 2.6.5, we only account for the most dominant contribution, namely XPM. This is mathematically expressed as

$$\eta_n(f_i) = \eta_{\mathrm{GN},n}(f_i) + \eta_{\mathrm{corr.},n}(f_i), \tag{4.13}$$

where $\eta_{\mathrm{GN},n}$ is the NLI contribution arising from a Gaussian constellation and $\eta_{\mathrm{corr.},n}$ represents the modulation format correction term. For Gaussian modulated signals the correction term $\eta_{\mathrm{corr.},n}$ vanishes and Eq. (4.13) reduces to the GN model. It has been shown that, only considering the XPM modulation format correction, is sufficiently accurate with only a minor loss in accuracy [22, 31–33, 51]. The approach is particularly accurate in high dispersive fibres such as standard single mode fibre and systems with large symbol rates or large channel spacings. The accuracy of the proposed results are validated by numerical simulations in Sec. 4.2.5.

The XPM assumption, taking only XPM-like terms into account, evaluates the NLI over the COI bandwidth originating from a single interferer (INT). The XPM assumption including the modulation format correction is illustrated in Fig. 4.9. The total XPM correction is obtained by summing over all individual XPM corrections of each COI-INT pair present in the transmitted signal. Similar to Eq.

(4.1), the total XPM modulation format correction is

$$\eta_{\mathrm{corr},n}(f_i) = \sum_{k=1,k\neq i}^{N_{\mathrm{ch}}} \eta_{\mathrm{corr},n}^{(k)}(f_i), \tag{4.14}$$

where $\eta_{\mathrm{corr},n}^{(k)}(f_i)$ is the XPM correction of a single interfering channel k on channel i.

The dominant XPM modulation format correction term is given by [117, Eq. (17)]

$$\begin{aligned}\eta_{\mathrm{corr},n}^{(k)}(f_i) = \frac{80}{81}\left(\frac{P_k}{P_i}\right)^2 \frac{\gamma^2\Phi}{B_k^3}\int_{-\frac{B_i}{2}}^{\frac{B_i}{2}} df_1 \\ \cdot\left|\int_{-\frac{B_k}{2}}^{\frac{B_k}{2}} \mu\left(f_1+f_i, f_2+f_i+\Delta f, f_i\right)\sum_{m=0}^{n-1} e^{jmf_1(f_2+\Delta f)\phi} df_2\right|^2,\end{aligned} \tag{4.15}$$

where B_i and B_k are the bandwidth of COI i and INT k, respectively, $\Delta f = f_k - f_i$ is the channel frequency separation between COI and INT and $\phi = -4\pi^2\left[\beta_2 + \pi\beta_3(f_i+f_k)\right]L$ is the phase mismatch term accounting for coherent NLI accumulation. In deriving Eq. (4.15), it was assumed that the variation of the wavelength dependent dispersion is negligible over a single channel bandwidth, identical to the assumptions made in the derivation of Eq. 4.9. The variable $\mu\left(f_1, f_2, f_i\right)$ is the link function of a single span. An optical fibre transmission system that is described by the nonlinear Schrödinger equation can be, to first-order, described by a link function $\mu\left(f_1, f_2, f_i\right)$. The link function describes the nonlinear perturbation (i.e. the NLI) of three interacting frequencies on the frequency f_i after propagation. The variable $\Phi = \frac{\mathrm{E}\left[|X|^4\right]}{\mathrm{E}^2\left[|X|^2\right]} - 2$ is the excess kurtosis of the transmitted modulation format, where X are the transmitted symbols. It is the main parameter which captures the impact of the transmitted symbol sequence on the nonlinear interference power. The excess kurtosis of a few example modulation formats are listed in Table 2.3. Most modulation formats exhibit a negative excess kurtosis resulting in a negative modulation format correction $\eta_{\mathrm{corr},n}^{(k)}(f_i)$. This negative modulation format correction reduces the nonlinear interference, meaning that GN model approaches (for which $\Phi = 0$) are always conservative. The modulation format correction is smaller for more 'Gaussian-like' modulation formats, where the absolute value of $|\Phi|$ is smaller. This property does not only extend to the coordinates of the individual symbols, exploited by geometric constellation shaping but it also applies to probabilistically shaped formats as shown in [143].

In the following sections an approximation in closed-form of the modulation

format correction in integral form (4.15) is derived. This gives the advantage of increase prediction accuracy for non-Gaussian modulation formats without sacrificing computation complexity and execution time.

4.2.2 Modulation format correction for generic transmission systems in closed-form

In this section, an approximate solution of Eq. (4.15) for a generic transmission system is derived. The derivation of the proposed formula relies on two key assumptions. The first assumption is that the channel separation of two interfering channels (COI and INT) is much greater than the channel bandwidth, which allows to approximate $f_2 + \Delta f \approx \Delta f$ in (4.15). This is the same assumption that has been used in the derivation of Eq. (4.9) in Sec. 4.1. A detailed assessment of this assumption was carried out in A.3.3, where it was shown that this assumption has negligible impact on the total NLI. Using $f_2 + \Delta f \approx \Delta f$ in Eq. (4.15) results in

$$\begin{aligned}\eta_{\mathrm{corr},n}^{(k)}(f_i) \approx \tilde{\gamma} \int_{-\frac{B_i}{2}}^{\frac{B_i}{2}} df_1 \left|\mu\left(f_1+f_i, f_k, f_i\right)\right|^2 \\ \cdot \left|1+\sum_{m=1}^{n-1} \operatorname{sinc}\left(m\phi f_1 \frac{B_k}{2}\right) e^{jm\phi f_1 \Delta f}\right|^2,\end{aligned} \tag{4.16}$$

with $\tilde{\gamma} = \left(\frac{P_k}{P_i}\right)^2 \frac{80}{81} \frac{\gamma^2 \Phi}{B_k}$, which is introduced to simplify the notation.

Eq. (4.16) does not appear to have an analytical solution. However, in order to find an approximate solution, we analyse its asymptotic behaviour for a large number of fibre spans $n \to \infty$. For a large number of spans, the oscillation terms in Eq. (4.16) can be approximated by a Dirac delta function $\delta(x)$ as

$$\begin{aligned}&\lim_{n\to\infty} \left|1+\sum_{m=1}^{n-1} \operatorname{sinc}\left(m\phi f_1 \frac{B_k}{2}\right) e^{jm\phi f_1 \Delta f}\right|^2 \\ \approx &1+\delta(f_1) \lim_{n\to\infty} C_n,\end{aligned} \tag{4.17}$$

with a normalisation coefficient

$$C_n = \int_{-\infty}^{\infty} df_1 \left|\sum_{m=1}^{n-1} \operatorname{sinc}\left(m\phi f_1 \frac{B_k}{2}\right) e^{jm\phi f_1 \Delta f}\right|^2. \tag{4.18}$$

The sinc function is defined as $\operatorname{sinc}(x) = \frac{\sin(x)}{x}$. The normalisation coefficient C_n comes from the property $\int_{-\infty}^{\infty} \delta(x)\, dx = 1$ of the Dirac delta function.

The approximation (4.17) is the second key assumption in the derivation of

the proposed formula and it can be motivated as follows: For $f_1 = 0$, both sides of (4.17) yield infinity, making the 1 negligible and as a result it can be pulled out of the absolute square term. For $f_1 \neq 0$, the oscillating terms add mostly out-of-phase (deconstructively) and they are further damped by the $\frac{1}{f_1}$ decay in the $\mathrm{sinc}\,(x)$ function. Thus, the sum over the oscillating terms can be approximated by a Dirac delta function, the oscillating terms are negligible with respect to 1 and the 1 can be, again, pulled out of the absolute square.

Under the approximation as in (4.17), the modulation format correction can now be approximated by only two contributions. One modulation format correction originating in the first span and an asymptotic contribution originating in the limit of a large number of spans. The modulation format correction can be thus written as

$$\eta^{(k)}_{\mathrm{corr},n}(f_i) \approx \underbrace{\eta^{(k)}_{\mathrm{corr},1}(f_i)}_{\text{1st span corr.}} + \underbrace{\tilde{n} \cdot \eta^{(k)}_{\mathrm{corr},a}(f_i)}_{\text{asympt. corr.}} \tag{4.19}$$

with

$$\eta^{(k)}_{\mathrm{corr},1}(f_i) = \tilde{\gamma} \int_{-\frac{B_i}{2}}^{\frac{B_i}{2}} df_1 \left|\mu\left(f_1 + f_i, f_k, f_i\right)\right|^2 \tag{4.20}$$

$$\eta^{(k)}_{\mathrm{corr},a}(f_i) = \tilde{\gamma} \left|\mu\left(f_i, f_k, f_i\right)\right|^2 \cdot \lim_{n\to\infty} \Delta_n C_n \tag{4.21}$$

and

$$\tilde{n} = \begin{cases} 0, & \text{if } n = 1 \\ n, & \text{otherwise} \end{cases} \tag{4.22}$$

The asymptotic contribution $\eta^{(k)}_{\mathrm{corr},a}(f_i)$ is valid in the limit for a large number of spans. However, in order to calculate the modulation format correction for *any* number of spans, the asymptotic contribution is approximated by a Taylor series with respect to the number of spans and truncated to first-order. As the asymptotic contribution after one span must be zero (as this is covered by $\eta^{(k)}_{\mathrm{corr},1}(f_i)$), only its slope (in the asymptotic limit) must be calculated as in (4.21). As the span number is an integer variable, the slope is computed using the backward difference operator, defined as $\Delta_n f = f(n) - f(n-1)$. The asymptotic slope can be computed exactly and the necessary identity is derived in Appendix A.4.2.

Using the identity (A.30), derived in Appendix A.4.2, the asymptotic contri-

bution can be written *exactly* in closed-form as

$$\eta_{\mathrm{corr},a}^{(k)}(f_i) = \tilde{\gamma}|\mu(f_i,f_k,f_i)|^2 \cdot \frac{2\pi}{|\phi|B_k^2}\left[(2\Delta f - B_k)\ln\left(\frac{2\Delta f - B_k}{2\Delta f + B_k}\right) + 2B_k\right] \tag{4.23}$$

Eq. (4.23) represents a generic modulation format correction formula, valid in the asymptotic limit of a large span number. Remarkably, the asymptotic contribution does not require any further integration and it, therefore, represents a closed-form correction formula for *any* optical fibre transmission system described by a link function $\mu(f_1,f_2,f_i)$. Every transmission system that is accurately modelled by the NLSE or Manakov equation can be described by a link function. Eq. (4.23) can be universally applied to estimate the modulation format dependence and it is one of the main results in this Chapter.

To further increase the accuracy to an arbitrary number of spans, the integral, describing the modulation format correction contribution after a single span (4.20), must be solved. However, this integral resembles the mathematical structure of the GN model contribution $\eta_{\mathrm{GN},n}(f_i)$ (cf. (4.6)) In other words, if a closed-form approximation for the GN model contribution after one span exists for an arbitrary transmission system, a modulation format correction formula in closed-form for any number of spans immediately follows with the results in this paper using (4.19)(4.20)(4.23).

4.2.3 Link function of the ISRS GN model

Equations (4.19)(4.20)(4.23) can be used to derive a modulation format correction formula for the ISRS GN model for arbitrary span numbers. However, to derive a fully closed-form formula, the link function $\mu(f_1,f_2,f_i)$ of the underlying system is required. The link function of the ISRS GN model in analytical form is given by Eq. (3.6) as

$$\mu(f_1,f_2,f_i) = \int_0^L d\zeta\, \frac{P_{\mathrm{tot}}e^{-\alpha\zeta - P_{\mathrm{tot}}C_{\mathrm{r}}L_{\mathrm{eff}}\cdot(f_1+f_2-f_i)}}{\int G_{\mathrm{Tx}}(\nu)e^{-P_{\mathrm{tot}}C_{\mathrm{r}}L_{\mathrm{eff}}\nu}d\nu} \cdot e^{j\tilde{\phi}(f_1,f_2,f_i,\zeta)}, \tag{4.24}$$

where $\tilde{\phi} = -4\pi^2(f_1-f_i)(f_2-f_i)\left[\beta_2 + \pi\beta_3(f_1+f_2)\right]\zeta$. Eq. (4.24) can be used to calculate the nonlinear perturbation on f_i after one span for any arbitrary frequency triplet (f_1,f_2,f_i). Eq. (4.24) accounts for all occurring nonlinear mixing products, namely self-phase (SPM), cross-phase (XPM) and four-wave mixing (FWM) products. However, the proposed formulas (4.19)(4.20)(4.23), only correct for the

dominant mixing products which are XPM (see Sec. 4.1.1). This restricts the frequency triplets to the XPM domain which is (f_1+f_i, f_k, f_i) with $f_1 \in \left[-\frac{B_i}{2}, \frac{B_i}{2}\right]$. An approximation of the generic link function (4.24) for the XPM contribution has already been derived and utilised in the derivation of Eq. 4.9. The approximation is written as (cf. Eq. (A.18))

$$\mu\left(f_1+f_i, f_k, f_i\right) \approx -\frac{1+\tilde{T}_k}{-\alpha+j\phi_{i,k}f_1} + \frac{\tilde{T}_k}{-A+j\phi_{i,k}f_1} \tag{4.25}$$

where $\tilde{T}_k = -\frac{P_{\mathrm{tot}}C_{\mathrm{r}}}{\bar{\alpha}}f_k$, $\phi_{i,k} = -4\pi^2\left(f_k-f_i\right)\left[\beta_2+\pi\beta_3(f_i+f_k\right]$ and $A=\alpha+\bar{\alpha}$.

In order to obtain the modulation format correction of the ISRS GN model in closed-form, the approximated link function Eq. (4.25) must be substituted in Eqs. (4.20) and (4.23). As mentioned in Section 4.2.2, the integral, that needs to be executed in Eq. (4.20), resembles the GN model contribution after one span. This integral has already been solved in Sec. 4.1. Hence, the modulation format correction for the ISRS GN model can be obtained combining the result derived in this Section with Sec. 4.1.

4.2.4 Modulation format correction for the ISRS GN model in closed-form

Using the modulation correction formula for an arbitrary link function, derived in Sec. 4.2.2, combined with the approximated link function Eq. (4.25) of the ISRS GN model, yields a modulation format correction formula for the ISRS GN model in closed-form as

$$\begin{aligned}\eta_{\mathrm{corr.},n}\left(f_i\right) \approx \frac{80}{81}\Phi \sum_{k=1,k\neq i}^{N_{\mathrm{ch}}}\left(\frac{P_k}{P_i}\right)^2\frac{\gamma^2}{B_k}\Bigg\{&\frac{1}{\phi_{i,k}\bar{\alpha}\left(2\alpha+\bar{\alpha}\right)}\\ &\cdot\left[\frac{T_k-\alpha^2}{\alpha}\mathrm{atan}\left(\frac{\phi_{i,k}B_i}{\alpha}\right)+\frac{A^2-T_k}{A}\,\mathrm{atan}\left(\frac{\phi_{i,k}B_i}{A}\right)\right]\\ &+\frac{2\pi\tilde{n}T_k}{|\phi|\,B_k^2\alpha^2A^2}\left[\left(2\left|\Delta f\right|-B_k\right)\log\left(\frac{2\left|\Delta f\right|-B_k}{2\left|\Delta f\right|+B_k}\right)+2B_k\right]\Bigg\},\end{aligned} \tag{4.26}$$

with $\Delta f = f_k - f_i$, $\phi_{i,k} = -2\pi^2\left(f_k-f_i\right)\left[\beta_2+\pi\beta_3(f_i+f_k\right]$. The formula is applicable for lumped-amplified links for optical bandwidths of up to 15 THz, as this formula relies on the triangular Raman gain spectrum, similar to the approximations derived in Sec. 4.1. The results described in Sec. 4.3 can be used to apply Eq. (4.26) to larger bandwidths. The former summand in Eq. (4.26) corrects for the modulation format within a single span, while the latter summand corrects the modulation format contribution across multiple spans as described by Eq. (4.19).

The sum in (4.26) corrects for all interfering channels within the transmitted WDM signal.

4.2.5 Numerical validation

The proposed closed-form correction formula (4.26) was validated by numerical simulations over the entire C+L band, covering 10 THz optical bandwidth. The validation was carried out for two fibre types, one high dispersive standard single mode fibre (SMF) and one low dispersive non-zero dispersion-shifted fibre (NZDSF). The simulation parameters are shown in Table 4.1. The simulation setup was described in detail in Sec. 3.7. Inter-channel stimulated Raman scattering was included in the SSFM by applying a frequency dependent loss at every linear step, so that the signal power profile altered by ISRS, is obtained.

The launch powers were chosen to maximise the performance of the central channel assuming a 5 dB noise figure EDFA (see Sec. 2.4.1). Gaussian symbols, drawn from a circular-symmetric Gaussian distribution and uniform QPSK symbols were used in transmission. In the case of QPSK modulation, the channels of interest, centered at $f_i = 0$ THz and $f_i = -4.0$ THz, exhibit Gaussian modulation while the remainder of the channels were modulated with QPSK symbols. This was done for validation purposes and only for the results in this section 4.2.5. This approach offers a more precise validation, as the proposed formula only corrects for modulation formats of interfering channels (XPM terms). Therefore, all interfering channels were modulated with Gaussian symbols, which do not have a modulation format dependent contribution on the COI.

The SNR was estimated by comparing input and output symbols and the nonlinear interference coefficient was then estimated as $\eta_n(f_i) = \frac{\mathrm{SNR}_{\mathrm{NLI},i}}{P_i^3}$. In order to improve the simulation accuracy, four different data realisations were simulated and averaged for each transmission. Ideal, noiseless amplifiers were considered to ease the NLI computation and for a fair comparison between numerical simulation and modelling results. The EDFA noise figure was only considered in estimating the used launch power.

The nonlinear interference coefficient as a function of span numbers is shown in Fig. 4.10 and 4.11 for the channels with centre frequencies $f_i = -4.0$ THz and $f_i = 0$ THz. The results are shown for both fibre types and for the case with ISRS and without ISRS. The (unphysical) case of not considering ISRS is shown for comparison.

In the case of Gaussian modulation, the ISRS GN model in integral form (3.6) was used. In the case of QPSK modulation, the ISRS GN model in integral form was used with the modulation format correction in integral form Eq. (4.15)

Table 4.1: System parameters for Fig. 4.12 and 4.114.10

Parameters	SMF	NZDSF
Loss (α) [dB/km]	0.2	0.19
Dispersion (D) [ps/nm/km]	17.0	4.5
Dispersion slope (S) [ps/nm^2/km]	0.067	0.05
NL coefficient (γ) [1/W/km]	1.2	1.3
Effective core area [μm^2]	80	72
Raman gain slope (C_r) [1/W/km/THz]	0.028	0.031
Raman gain ($C_\mathrm{r} \cdot 14$ THz) [1/W/km]	0.39	0.44
Channel Launch Power (P_i) [dBm]	0	-2
Total Launch Power (P_tot) [dBm]	24	22
Symbol rate [GBd]	40	
Channel Bandwidth (B_i) [GHz]	40.004	
Channel spacing [GHz]	40.005	
Number of channels	251	
Optical bandwidth (B_tot) [THz]	10.05	
Reference Wavelength [nm]	1550	
Roll-off factor [%]	0.01	
Number of symbols [2^x]	17	
Simulation steps per span [10^6]	2.5	

(solid lines), as well as the modulation format correction formula in closed form Eq. (4.26) (dashed lines). This way, the accuracy of the closed-form modulation format correction can be estimated.

Unsurprisingly, and as already shown in Sec. 3.7.2, the ISRS GN model has remarkable accuracy with numerical simulations, exhibiting a negligible modelling error. In the case of QPSK modulation, the modulation format correction in integral form (4.16) models the impact of QPSK with good accuracy, despite one of the key assumptions made in its derivation (Assumption 1) in Sec. 4.1.4, mathematically $\Delta f \gg \frac{B_k}{2}$). The average deviation between the modulation format correction in integral form and the numerical simulation is 0.26 dB throughout the shown results. The error mostly stems from the XPM assumption and assumptions inherited from Eq. (4.15). The small impact of the assumption $\Delta f \gg \frac{B_k}{2}$ has been mathematically quantified in Appendix A.3.3.

The modulation format correction formula in closed-form (4.26) shows good accuracy for all number of spans. Throughout Fig. 4.10 and 4.11, the average absolute error is 0.45 dB between closed-form and numerical simulation. The majority

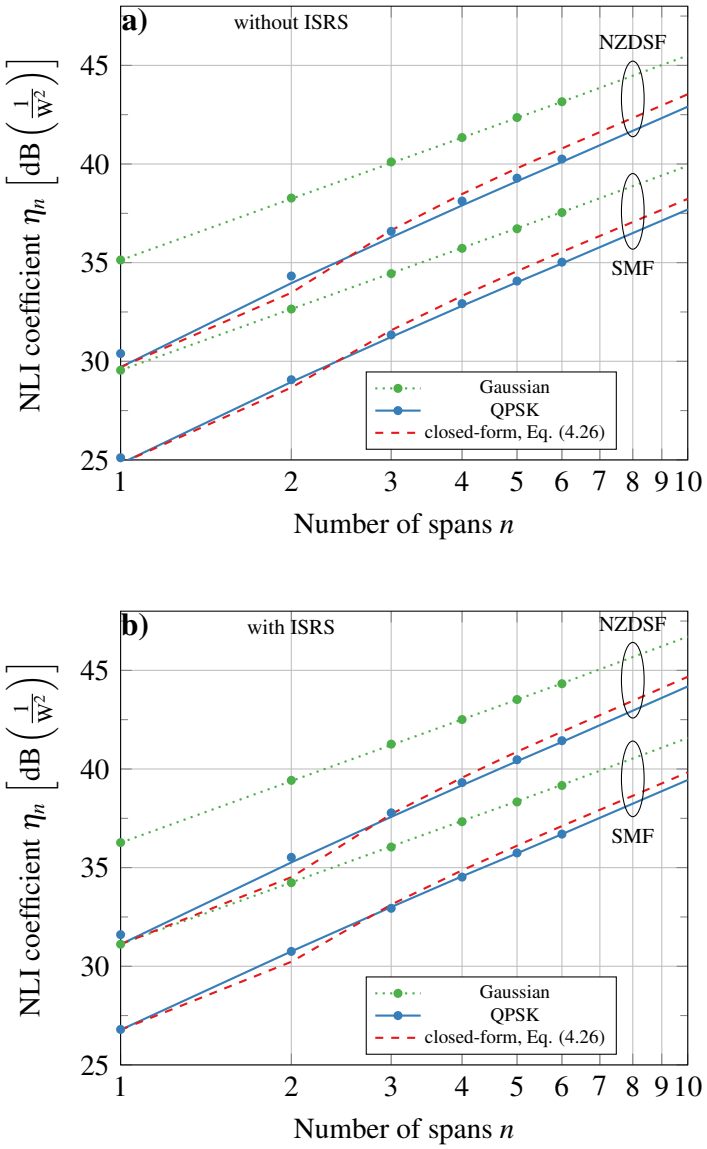

Figure 4.10: The nonlinear interference coefficent as a function of fibre spans for the channel centered at $f_i = -4.0$ THz. The results were obtained by split-step simulations (markers) and the ISRS GN model (3.6) with the modulation format correction in integral form (4.16) (solid lines). The ISRS GN model with the modulation format correction in closed-form (4.26) is shown in dashed lines. In the case of of QPSK, only the channel of interest exhibits Gaussian modulation for validation purposes.

of the mismatch can be traced back to the asymptotic assumption Eq. (4.17) and its linear approximation of the asymptotic contribution Eq. (4.21) with respect to the span number (see Sec. 4.2.2). The mismatch is smaller for an increasing number of spans, due to the assumption $n \to \infty$ in Eq. (4.17). Particularly, the error completely vanishes in the case of single span transmission and in the limit of infinite transmission spans. Not shown in the figures, the mismatch between modulation format

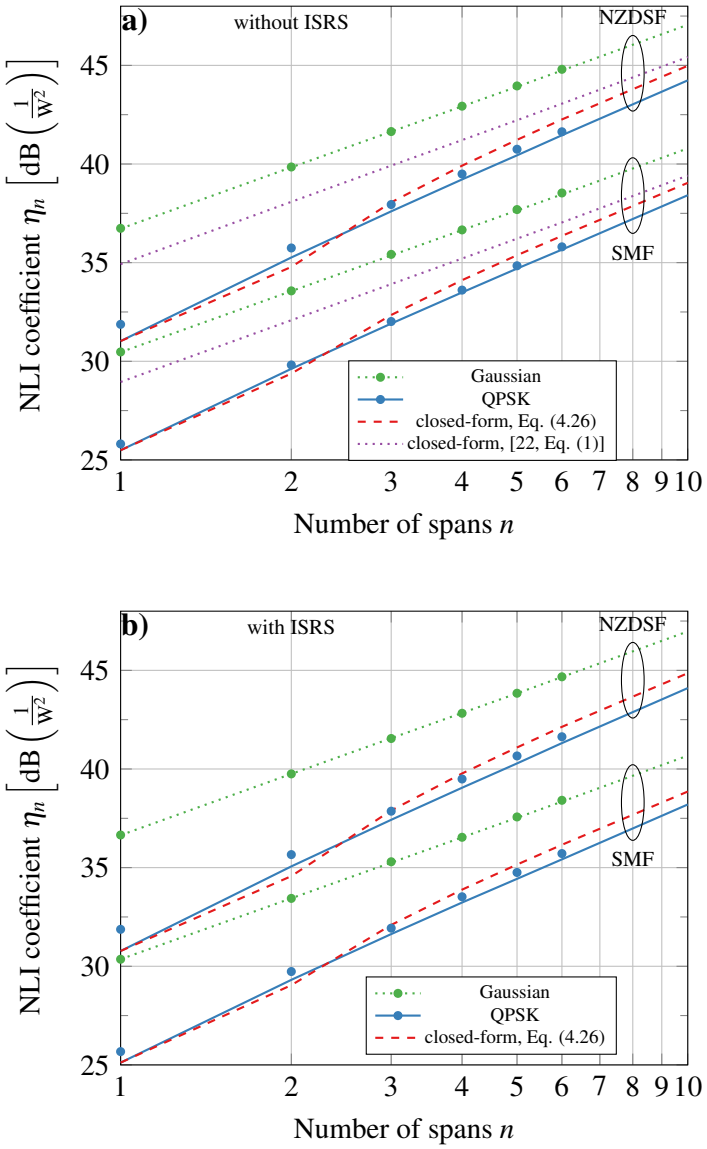

Figure 4.11: The nonlinear interference coefficent as a function of fiber spans for the channel centered at $f_i = 0$ THz. The results were obtained by split-step simulations (markers) and the ISRS GN model (3.6) with the modulation format correction in integral form (4.16) (solid lines). The ISRS GN model with the modulation format correction in closed-form (4.26) is shown in dashed lines. In the case of of QPSK, only the channel of interest exhibits Gaussian modulation for validation purposes. For comparison the result of [22, Eq. (1)] is shown, which proposed a modulation format correction formula in the absence of ISRS.

correction in closed-form and integral form is < 0.1 dB after 100 spans.

The result described in this section presents the first modulation format correction formula in the presence of ISRS. However, in the absence of ISRS (e.g. for optical bandwidths of at most 5 THz), modulation format correction formulas are already available in the literature. To compare our results to previously published

works in the absence of ISRS, [22, Eq. (1)] is shown in Fig. 4.11a), which proposes a modulation format correction formula in the absence of ISRS. As the result in [22] has been derived in the asymptotic limit of a large number of spans, it is inaccurate for the first few spans. Mathematically, this is because the result in [22] only approximates the asymptotic component in (4.19). The comparison shows that Eq. (4.26) is not only capable of correcting the modulation format in ISRS impaired systems, but it also more accurate than previously published results in the absence of ISRS.

4.2.6 The ISRS GN model for arbitrary modulation formats in closed-form

The next step is to combine the modulation format correction formula (4.26) with the ISRS GN model contribution in closed form derived in Sec. 4.1. The goal is to obtain a closed-form formula capable of predicting the total nonlinear SNR for arbitrary modulation formats. The formula for the *total* NLI coefficient as in Eq. (4.13) is

$$\begin{aligned}
\eta_n(f_i) \approx & \frac{4}{9}\frac{\gamma^2}{B_i^2}\frac{\pi n^{1+\varepsilon}}{\phi_i \bar{\alpha}(2\alpha+\bar{\alpha})} \\
& \cdot \left[\frac{T_i-\alpha^2}{\alpha}\operatorname{asinh}\left(\frac{\phi_i B_i^2}{\pi a}\right)+\frac{A^2-T_i}{A}\operatorname{asinh}\left(\frac{\phi_i B_i^2}{\pi A}\right)\right] \\
& + \frac{32}{27}\sum_{k=1,k\neq i}^{N_{\mathrm{ch}}}\left(\frac{P_k}{P_i}\right)^2\frac{\gamma^2}{B_k}\left\{\frac{n+\frac{5}{6}\Phi}{\phi_{i,k}\bar{\alpha}(2\alpha+\bar{\alpha})}\right. \\
& \cdot \left[\frac{T_k-\alpha^2}{\alpha}\operatorname{atan}\left(\frac{\phi_{i,k}B_i}{\alpha}\right)+\frac{A^2-T_k}{A}\operatorname{atan}\left(\frac{\phi_{i,k}B_i}{A}\right)\right] \\
& \left. + \frac{5}{3}\frac{\Phi\pi\tilde{n}T_k}{|\phi|B_k^2\alpha^2A^2}\left[(2|\Delta f|-B_k)\log\left(\frac{2|\Delta f|-B_k}{2|\Delta f|+B_k}\right)+2B_k\right]\right\},
\end{aligned} \tag{4.27}$$

with $\phi_i = \frac{3}{2}\pi^2(\beta_2+2\pi\beta_3 f_i)$, $T_k = (\alpha+\bar{\alpha}-P_{\mathrm{tot}}C_{\mathrm{r}}f_k)^2$, $\Delta f = f_k - f_i$, $\phi_{i,k} = -2\pi^2(f_k-f_i)[\beta_2+\pi\beta_3(f_i+f_k]$ and $A=\alpha+\bar{\alpha}$. Eq. (4.27) models the GN model contribution of the SPM and XPM contributions, as in Eqs. (4.8)(4.9), where the XPM terms are corrected for then modulation format dependence using Eq. (4.26).

The total NLI coefficient as a function of channel frequency with and without ISRS, obtained by Eq. (4.27) and the SSFM, is shown in Fig. 4.12. The results are shown for SMF and NZDSF. All transmitted channels are entirely modulated with either Gaussian, 16-QAM or 64-QAM symbols. It can be seen that Eq. (4.27) shows very good agreement with the numerical results. In both cases (with and without ISRS), the average mismatch between the closed-form model Eq. (4.27)

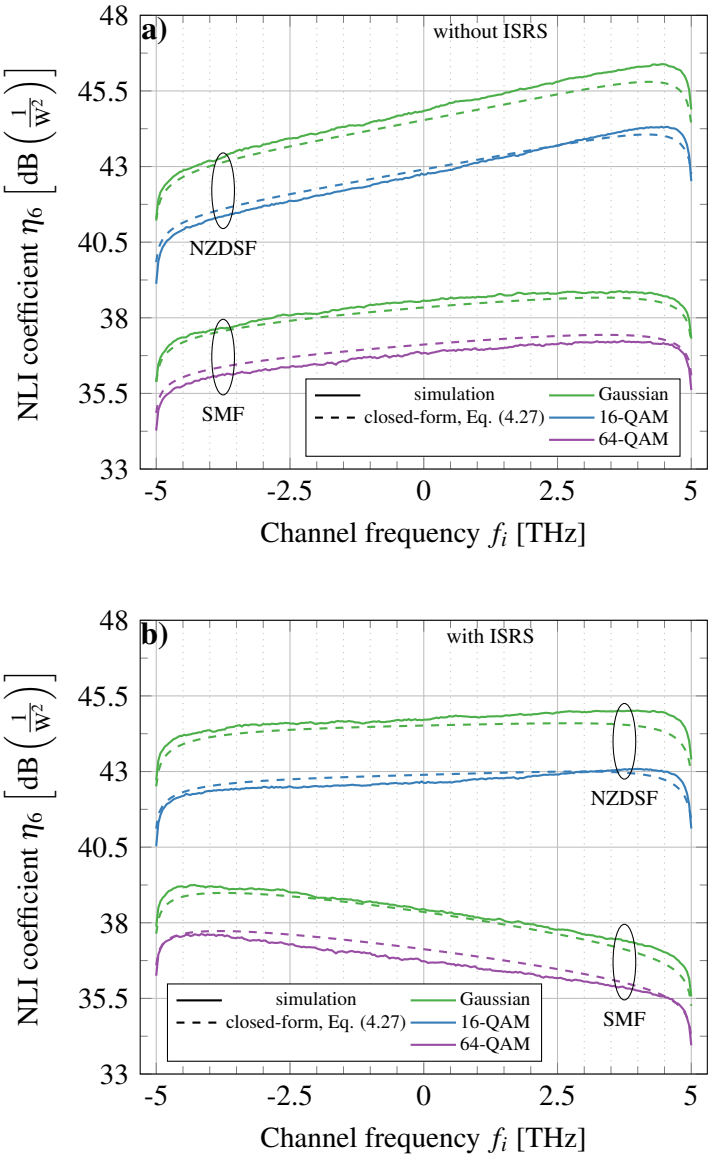

Figure 4.12: The nonlinear interference coefficient as a function of channel frequency for different modulation formats and fibre types after 6x100 km spans. The results were obtained by split-step simulations and in closed-form using Eq. (4.27). Figures a) and b) show the case without and with inter-channel stimulated Raman scattering, respectively.

and numerical simulation is 0.3 dB and 0.2 dB for SMF and NZDSF, respectively.

The analysis shows that the derived closed-form approximation (4.27) is capable of predicting nonlinear SNR of ultra-wideband optical transmission systems considering arbitrary modulation formats with good accuracy. This is a key result in the real-time modelling of next generation ultra-wideband transmission systems.

4.3 The ISRS GN model in closed-form extended to S+C+L band systems

The formulas in the previous Sections 4.1 and 4.2, are only applicable for optical bandwidths of up to 15 THz, as they rely on the triangular approximation of the Raman gain spectrum (see Fig. 2.7). The triangular approximation is key to yielding analytical approximation of the Raman gain equations (2.28) and, in turn, vital in the derivations of Eqs. (4.8)(4.9) and the modulation format correction (4.26). Therefore, real-time performance estimations for the entire SCL band, spanning a total optical bandwidth of approximately 20 THz, is not possible based on the results described in the previous sections of this chapter.

The analytical closed-form approximations in previous sections have been derived assuming a linear regression of the Raman gain spectrum. This assumption yields an analytical solution of the Raman equations (2.28), a key requirement to obtain a closed-form approximation for the NLI in the presence of ISRS. For bandwidths beyond 15 THz, the Raman gain spectrum cannot be accurately approximated as a linear function of frequency and an analytical solution of the Raman equations is not available This renders a fully analytical approach for the SNR estimation impossible. The goal of this section is a semi-analytical approach, which yields vast reductions in computation time compared to split-step simulations.

The approach uses the first-order description of the power transfer in the presence of ISRS, which was developed in Sec. 4.1. The power profile, to first-order, is fully characterised by three parameters which are α, $\bar{\alpha}$ and C_r. In the previous sections, we had that $\bar{\alpha} = \alpha$ for transmission systems with bandwidths below 15 THz and negligible variation of the fibre attenuation. However, in this Section, the three parameters (α, $\bar{\alpha}$, C_r) are redefined as channel dependent variables. These channel dependent parameters are then matched to the actual power profile of the respective channel i. The actual power profile $P_i(z)$ is obtained by numerically solving the Raman equations and matched to the power profile to first-order (with respect to ISRS)

$$P_i^{(1)}(z) = \left(1+\tilde{T}_i\right) e^{-\alpha_i z} - \tilde{T}_i e^{-(\alpha_i+\bar{\alpha}_i)z}, \tag{4.28}$$

where $\tilde{T}_i = -\frac{P_{\text{tot}} C_{r,i}}{\bar{\alpha}_i} f_i$. The matching of α_i, $\bar{\alpha}_i$ and $C_{r,i}$ can be carried out using standard regression techniques such as the Levenberg-Marquardt algorithm [144].

The channel power of the highest and lowest frequency component as a function of distance are shown in Fig. 4.13. The profiles are obtained by numerically solving the Raman gain equations (2.27) and using the first-order description of

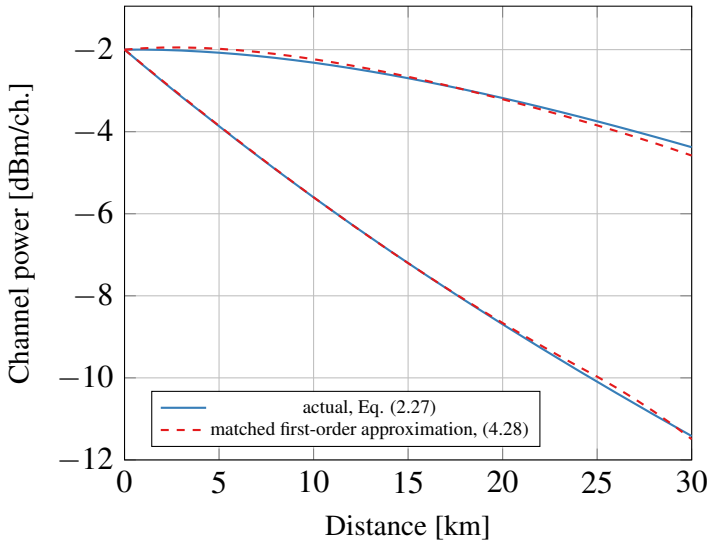

Figure 4.13: The power profile of the highest and lowest frequency channel as a function of distance. The profile are obtained by numerically solving the Raman gain equations (2.27) and using the first-order description of ISRS (4.28), where the parameters α_i, $\bar{\alpha}_i$ and $C_{r,i}$ are matched to the actual profile.

ISRS Eq. (4.28). The channel dependent parameters α_i, $\bar{\alpha}_i$ and $C_{r,i}$ were matched to the actual profile, using a standard least-squares algorithm. There is a good agreement between the actual power profile and the matched first-order approximation. This indicated that the approach of matching the parameters α_i, $\bar{\alpha}_i$ and $C_{r,i}$ is promising for predicting the arising nonlinear interference. The matched parameters can then be substituted in the closed-form formula to obtain the *total* nonlinear SNR (as in Eq. (4.27)) as

$$\begin{aligned}\mathrm{SNR}_{\mathrm{NLI},i}^{-1} \approx{}& \frac{4}{9}\frac{\pi\gamma^2 P_i^2 n^{1+\varepsilon}}{B_i^2\phi_i\bar{\alpha}_i(2\alpha_i+\bar{\alpha}_i)}\left[\frac{T_i-\alpha_i^2}{a_i}\operatorname{asinh}\left(\frac{\phi_i B_i^2}{\pi a_i}\right)+\frac{A_i^2-T_i}{A_i}\operatorname{asinh}\left(\frac{\phi_i B_i^2}{\pi A_i}\right)\right]\\ &+\frac{32}{27}\sum_{k=1,k\neq i}^{N_{\mathrm{ch}}}\frac{\gamma^2 P_k^2}{B_k}\\ &\left\{\frac{n+\frac{5}{6}\Phi}{\phi_{i,k}\bar{\alpha}_k(2\alpha_k+\bar{\alpha}_k)}\left[\frac{T_k-\alpha_k^2}{\alpha_k}\operatorname{atan}\left(\frac{\phi_{i,k}B_i}{\alpha_k}\right)+\frac{A_k^2-T_k}{A_k}\operatorname{atan}\left(\frac{\phi_{i,k}B_i}{A_k}\right)\right]\right.\\ &\left.+\frac{5}{3}\frac{\Phi\pi\tilde{n}T_k}{|\phi|B_k^2\alpha_k^2A_k^2}\left[(2|f_k-f_i|-B_k)\log\left(\frac{2|f_k-f_i|-B_k}{2|f_k-f_i|+B_k}\right)2B_k\right]\right\},\end{aligned} \tag{4.29}$$

where $T_i=(\alpha_i+\bar{\alpha}_i-P_{\mathrm{tot}}C_{r,i}f_i)^2$, $A_i=\alpha_i+\bar{\alpha}_i$, $\phi=-4\pi^2\left[\beta_2+\pi\beta_3(f_i+f_k)\right]L$, $\phi_i=\frac{3}{2}\pi^2\left(\beta_2+2\pi\beta_3 f_i\right)$, $\phi_{i,k}=-2\pi^2\left(f_k-f_i\right)\left[\beta_2+\pi\beta_3\left(f_i+f_k\right)\right]$.

Eq. (4.29) now extends the results discussed in previous Sec. 4.1 and 4.2.1

to bandwidths beyond 15 THz. However, this requires the numerical solution of the Raman equations and additional regression operations, which can be performed within a few seconds.

4.3.1 Numerical validation

The next step is to validate the proposed approach using split-step simulations. The validation was carried out for 452×40 GBd channels, occupying the entire S+C+L band (20 THz). The numerical validation in this section, represent the first numerical validation of perturbation models (see Sec. 2.6) over optical bandwidths of 20 THz. A Corning© SMF-28© ULL fibre was considered with experimentally measured fibre data for attenuation coefficient, shown in Fig. 4.14a), and the Raman gain spectrum, shown in Fig. 4.14b). Dispersion and nonlinearity parameters are $D = 18\frac{\text{ps}}{\text{nm}\cdot\text{km}}$, $S = 0.067\frac{\text{ps}}{\text{nm}^2\cdot\text{km}}$ ($\beta_2 = -22.6\frac{\text{ps}^2}{\text{km}}$ and $\beta_3 = 0.14\frac{\text{ps}^3}{\text{km}}$ at 1540 nm) and $\gamma = 1.2\frac{1}{\text{W}\cdot\text{km}}$.

Gaussian modulation, as well as uniform 64-QAM, were used as the symbol

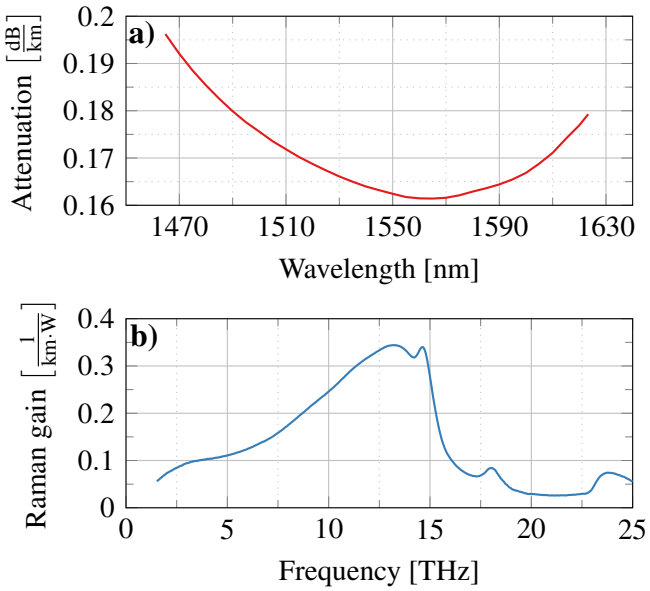

Figure 4.14: Experimentally measured attenuation coefficient and Raman gain spectrum of a Corning© SMF-28© ULL fibre.

constellations. The first was chosen to evaluate the accuracy of the Gaussian-like NLI contribution (cf. Sec. 4.1), while the latter was chosen to test the accuracy of the modulation format correction (cf. Sec. 4.2.4). A uniform channel launch power of -2 dBm was considered yielding a total optical power of 24.5 dB. A gap of 10 nm was assumed between S-and C-band and a gap of 5 nm between the C-and L-band. A sequence length of 2^{16} symbols were found to be sufficient for accurate simulations of up to 3 fibre spans. However, to further increase the simulation accuracy,

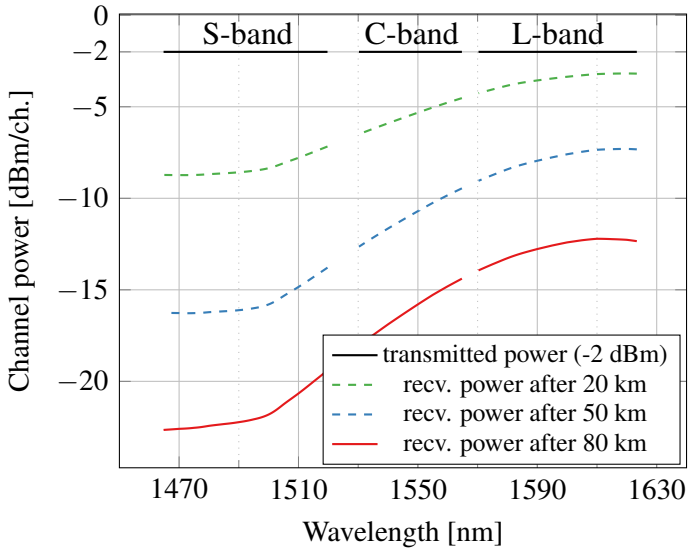

Figure 4.15: The power as a function of wavelength after several propagation distances. A launch power of -2 dBm per channel was assumed with experimentally measured fibre data of a Corning© SMF-28© ULL.

four independent data realisations were averaged (similar to cases simulated in Sec. 3.7.2, 4.1.5 and 4.2.5). Each data realisation (i.e. transmision) took 4.2 days on a single state-of-the-art GPU.

The power after several propagation distances within a span is shown in Fig. 4.15, where the signal power undergoes a complex interaction between the intrinsic fibre loss and ISRS. The sharp decrease of the Raman gain spectrum at frequency separations beyond 15 THz (approximately 120 nm) together with the non-uniform attenuation profile seem to offset each other, resulting in a relatively flat received power for low wavelengths in the S-band and high wavelengths in the L-band. Wavelengths in the C-band experience a linear tilt. This is a result of the coupling to all wavelengths in S- and L-band and the very low variation of the attenuation coefficient (maximum 0.04 dB/km) within the C-band.

The nonlinear SNR as a function of wavelength after 3×80 km, obtained using Eq. (4.29) and the SSFM, is shown in Fig. 4.16. As a check, results obtained with the ISRS GN model in integral form Eq. (3.5) are shown which exhibits a negligible error (<0.1 dB) compared to split-step simulations using Gaussian symbols. A Runge-Kutta method was used to numerically solve the Raman equations and a standard least mean squares algorithm was performed to minimise $\left|P_i(z) - P_i^{(1)}(z)\right|$ to obtain α_i, $\bar{\alpha}_i$ and $C_{r,i}$.

Numerical simulations as well as modelling predictions yield a relatively flat SNR across the wavelengths in S-and L-band. This is a consequence of the bal-

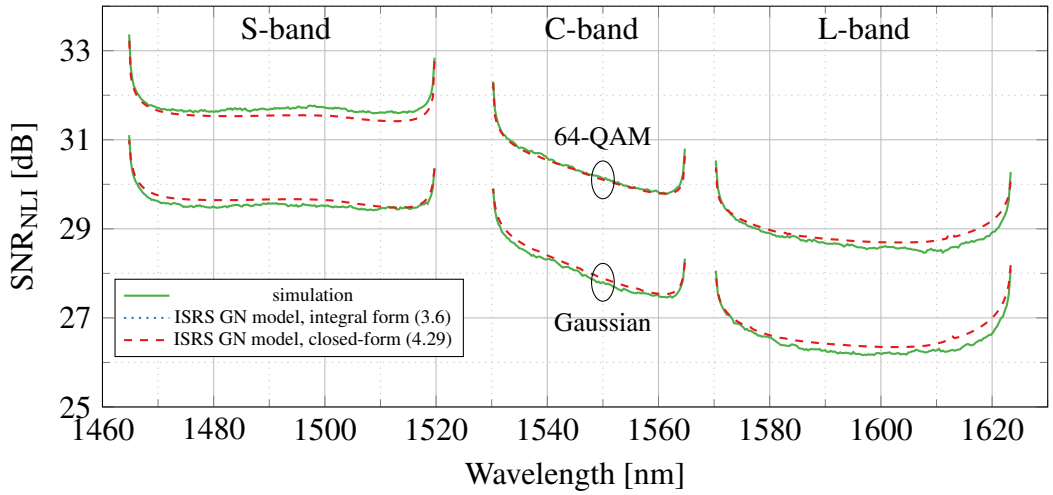

Figure 4.16: Nonlinear performance after 3×80 km transmission over the entire S+C+L band (20 THz, 158 nm) using a Corning© SMF-28© ULL with experimentally measured fibre data.

ancing effects between power tilt (see Fig. 4.15) and dispersion slope S (β_3). The power tilt shown in Fig. 4.15 results in increasing nonlinear interference towards longer wavelengths, while the dispersion slope weakens the nonlinear interference for longer wavelengths. Both effects result in a flat nonlinear SNR in the S-and L-bands for the given fibre parameters and the chosen launch power. The $\mathrm{SNR}_{\mathrm{NLI}}$ is tilted by 1.2 dB for wavelengths within the C-band as the power tilt occurring during propagation outweighs the effects of the dispersion slope. The nonlinear SNR of channels within the S-band is about 3.3 dB higher as compared to channels in the L-band due to the large power depletion, originating from ISRS and wavelength dependent attenuation.

The proposed closed-form has remarkable accuracy with an average mismatch of 0.1 dB and a maximum mismatch of 0.3 dB in the case of Gaussian symbols. The formula correctly predicts the impact of non-Gaussian modulation formats such as 64-QAM with an average and maximum mismatch of 0.1 and 0.3 dB, respectively. This validates that Eq. (4.29) can be applied in regimes beyond bandwidths of 15 THz with the approach described in this Section. The total simulation time to obtain the results in Fig. 4.16 was 33.6 days on a single state-of-the-art GPU. The total execution time using the semi-analytical closed-form approach was only a few seconds, where the majority of the time was required to numerically solve the Raman equations. This emphasises the major speed advantage of performance estimation approaches in closed-form.

The accuracy of Eq. (4.29) is expected to be maintained for different launch power distributions, modulation formats, fibre types and longer transmission dis-

tances, making the formula particularly useful for metro and long-haul transmission distances, where ultra-wideband simulations become unmanageable.

The analysis shows that the proposed closed-form approximation can be applied to S+C+L band transmission systems using QAM formats and optical bandwidths beyond 15 THz. The formula can be universally applied to account for arbitrary launch power distributions, span numbers, modulation formats and ultra-wideband effects such as wavelength dependent attenuation, dispersion and inter-channel stimulated Raman scattering.

4.4 Summary

In Chapter 3, the ISRS GN model was derived which accurately predicts the impact of ISRS on the nonlinear distortions. However, the ISRS GN model requires numerical integration with execution times of around a few minutes per channel. In this chapter, closed-form approximations of the ISRS GN model were derived to enable real-time performance estimations in sub-seconds. The formulae are key for time sensitive applications or optimisation problems with large solution space, such as dynamic launch power optimisation and RWA. To enable fast and accurate estimations with respect to arbitrary QAM formats, a closed-form approximation of the modulation format dependent NLI correction was derived. Finally, as both formulas are only valid to bandwidths of up to 15 THz, a semi-analytical approach was described that enable the formulas to be applied to bandwidths beyond 15 THz. The key results from this chapter are:

- A closed-form approximation of the ISRS GN model was derived, which enables to quantify nonlinear distortions in the presence of ISRS in sub-seconds. The new formula represents an extension of known closed-form approximations of the conventional GN model which are extended to account for ISRS and the dispersion slope. The formula was validated by numerical simulations for transmission in point-to-point links and mesh optical networks. The derived formula was found to be accurate within 0.2 dB compared to numerical simulations using Gaussian modulation. The work led to the publication of [P6].

- A modulation format correction formula in closed-form was derived in the presence of ISRS. This enables rapid, and yet accurate, estimations of the nonlinear penalty for arbitrary QAM constellations. The formula is valid for arbitrary span numbers and therefore also extends known formulas in the literature, to arbitrary span numbers, the dispersion slope and most importantly inter-channel stimulated Raman scattering. The proposed formula is vali-

dated by numerical simulations over 10 THz for a high dispersive SNR and a low dispersive non-zero dispersion-shifted fibre (NZDSF). Using 16 and 64-QAM, average deviations of 0.2 dB and 0.3 dB compared to numerical simulations have been found for NZDSF and SMF based spans, respectively. The formula is a key result in the modelling of nonlinear distortions in the ultra-wideband regime. A numerical simulation took 186 hours for a single transmission (four data realisations), while the closed-form formula was executed in sub-milliseconds. The work led to the publication of [P4].

- The derived formulas are based on analytical solutions to the Raman gain equations and can, therefore, only be applied to bandwidths of up to 15 THz. To overcome this limitation, a semi-analytical approach is described, based on parameter matching, to enable the application of the formulas to optical bandwidths beyond 15 THz. The formula is validated by a numerical simulation over 20 THz bandwidth (entire S+C+L band) with a maximum deviation of 0.3 dB for 64-QAM. The numerical simulation of a single transmission (four data realisations) took 16.8 days on a single state-of-the part GPU while the formula only required a few seconds execution time. The work led to the publication of [P19] and was 'top-scored'.

Chapter 5

Digital nonlinearity compensation: Practical limititations

According to the Shannon capacity formula Eq. (2.3), there are two main strategies to increase the throughput for transmission systems, which have been explored in this thesis. Firstly, the optical bandwidth can be increased in order to support more WDM channels and secondly, the SNR of the WDM channels can be maximised. In Chapters 3 and 4, the impact and the accurate modelling of physical fibre properties were discussed when the optical bandwidth is extended beyond the conventional C-band, that is currently used in most deployed systems. In this chapter, we focus on the second approach to increase the throughput of today's systems by increasing the SNR. In particular, the performance of digital nonlinearity compensation schemes (see Sec. 2.5) is reviewed. It is shown that the current modelling of such compensation schemes is incomplete and a new signal-noise interaction phenomenon is proposed. Incorporating the new phenomenon in the mathematical modelling, we are able to significantly enhance the performance prediction with respect to experiments of nonlinearily compensated systems. Based on the new formalism, we are also able to derive new optimum transceiver schemes that significantly outperform schemes that were, until now, thought to be optimum.

5.1 On the limits of digital back-propagation in the presence of transceiver noise

In this section, it is shown that nonlinear interactions between the signal and noise arising from the transceiver sub-system become significant in transmission systems that exhibit digital back-propagation or pre-distortion. These interactions have not been considered and completely overlooked in the published literature. The results in this section have been peer-reviewed and published in [P9, P15, P21, P25, P31].

5.1.1 Limitations of digital nonlinearily compensated systems

Several NLC algorithms based on DBP (see Sec. 2.5) have been proposed in the literature [24, 25, 40, 41, 103, 145–151] . It has been shown that significant SNR gains can be potentially achieved. In particular, significant gains in SNR can be achieved when full-field DBP (FF-DBP) is applied, where DBP is jointly applied to the entire optical signal. It should be noted that similar gains have been predicted when the digital-back propagation algorithm is applied at the transmitter side (DPC). However, the large theoretically predicted gains, of up to 9 dB in SNR, do not match the results of state-of-the art experiments using either NLC scheme. Reach increases of around 100% (from 640 km to 1280 km) have been experimentally demonstrated, when NLC is applied jointly to all received channels [44]. Similar reach gains of 100% (from 1530 km to 3060 km) and 200% (from 425 km to 1275 km) for shorter distances have been shown experimentally in the case of DPC [45, 46].

As already discussed in Sec. 2.5, two effects have been identified that are limiting the performance of digital NLC schemes, namely PMD and nonlinear signal noise interactions.

Digital NLC is able to fully compensate deterministic effects such as the nonlinear signal signal interactions. However, the algorithm is unable to fully compensate for stochastic effects, occurring during the the signal propagation. In numerical simulations it has been shown, that the stochastic nature of polarisation mode dispersion decreases the NLC gain, particularly if multiple channels are back-propagated [40, 147]. The latter is due to the fact that higher frequency spacings experience stronger PMD. However, is was shown that the polarization state can be tracked avoiding a significant NLC gain reduction due to PMD [152].

Second, another limiting effect is the nonlinear interaction between the signal and co-propagating ASE noise, which as been experimentally shown in [39] (see Sec. 2.5). It should be noted that although these beating terms are present in all transmission links, they are usually negligible compared to the nonlinear signal signal interference. However, when the signal signal interference is partially or fully mitigated, nonlinear interactions between ASE noise and the signal become significant.

However, it should be stressed that whether stochastic effects or nonlinear signal noise interactions impose a fundamental limitation on the achieved throughput is still an open research question. Despite the NLC gain degradation caused by PMD and interactions between the signal and ASE noise, theoretical predictions still substantially overestimate the experimentally achieved system performance (cf. [40, 41, 153]). This suggests that additional channel impairments must be considered in the modelling of transmission systems that exhibit NLC. In the next

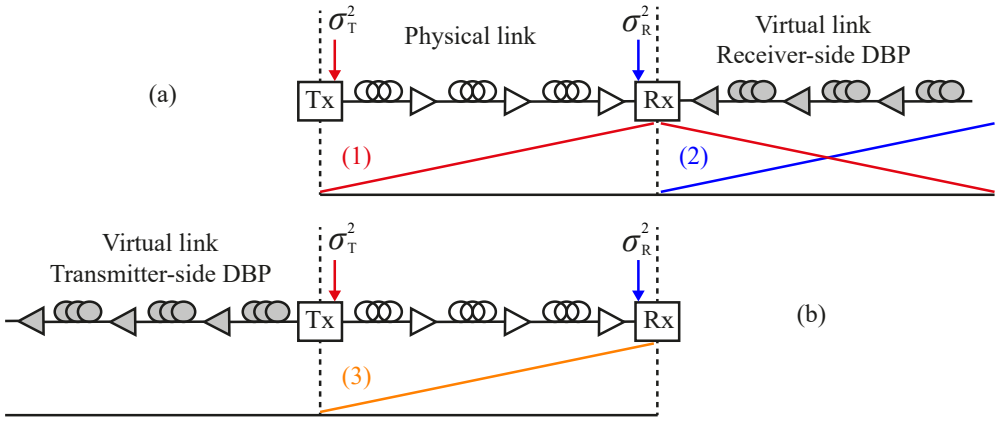

Figure 5.1: Nonlinear signal-noise interactions accumulation along transmission link for (a) receiver-side DBP and (b) transmitter-side DBP. The coloured lines show (1) nonlinear transmitter noise-signal beating, cancelled after DBP, (2) nonlinear receiver noise-signal beating, generated after DBP as: $3\tilde{\eta}_1\xi_{\mathrm{TRX}}\kappa_{\mathrm{R}}P^3$, and (3) nonlinear transmitter noise-signal beating, generated in transmission as: $3\tilde{\eta}_1\xi_{\mathrm{TRX}}(1-\kappa_{\mathrm{R}})P^3$.

sections, the goal is to account for this discrepancy by investigating the limits of DBP in realistic optical transmission systems, in which a limit on the maximum achievable SNR is imposed.

5.1.1.1 Nonlinear signal and transceiver noise interactions

An upper bound on the achievable SNR in coherent optical communication systems is set by the noise introduced by the transceiver subsystems [145]. Transceiver noise (TRX noise) is related to the back-to-back performance; the achievable SNR in the absence of any transmission medium. This phenomenological quantity combines all noise contributions from transmitter and receiver such as quantisation noise of analog-to-digital converters (ADC) or digital-to-analog converters (DAC) and noise from linear electrical amplifiers. Additionally, it includes noise from optical components such as optical amplifiers at the transceiver and laser RIN. In coherent transmission, the electrical drive signals in the transmitter are copied on the complex optical field envelope. Therefore, it is expected there are nonlinear interactions between the signal and, e.g., quantisation noise from the digital domain during fibre propagation. To date, these interactions have not been taken into account.

In the following, we develop an analytical framework in order to model nonlinear interactions between the signal and the transceiver noise. Note that the transceiver noise has origins in the optical, as well as in the digital, domains. If the signal co-propagates in a nonlinear medium with any noise contribution, nonlinear mixing products arise between the two. This mixing product, manifesting itself as nonlinear interference, approximately proportional to the joint propagation

distance. In the case of digital back-propagation or digital pre-distortion, the *physical* link is extended (doubled) by the *virtual* link (see Sec. 2.5). The virtual link exhibits inverse fibre parameters and, therefore, *reverses* a portion of the nonlinear interaction. The residual nonlinear interference, arising from nonlinear interactions between transceiver noise and signal, comes from the mismatched mixing products. In these cases the mixing product arising in the physical link are not fully reversed in the virtual link or vice versa.

The accumulation of nonlinear interactions between transceiver noise and the signal along the transmission link are schematically illustrated in Fig. 5.1, for DBP and DPC. The residual nonlinear interactions are dependent on whether the virtual link is placed at the transmitter or receiver and on the location at which the noise is introduced. The transceiver noise must be separated into two contributions, namely the transmitter noise σ_{T}^2 and the receiver noise σ_{R}^2.

In the case of DBP in Fig. 5.1a), the virtual link is located on the receiver side. Consequently, the nonlinear interaction between the signal and the transmitter noise accumulate along the physical link. After coherent detection, these interactions are completely reversed and cancelled in the virtual link. Therefore, the transmitter noise does not result in any residual nonlinear interference contributions and imposes no limitations on the DBP gain. On the other side, the receiver noise does not accumulate any nonlinear interactions in the physical link. However, the interactions between the signal and the receiver noise accumulate along the virtual link, leaving a residual nonlinear interference contribution. Therefore in the case of DBP, there is a noise contribution arising from nonlinear receiver noise signal interactions, limiting the DBP gain.

In the case of DPC in Fig. 5.1b), the virtual link is placed on the transmitter side. As a consequence, the receiver noise that is injected after the entire (virtual and physical) link, does not result in any nonlinear interactions with the signal. In other words, there are no nonlinear mixing products arising from the receiver noise. The nonlinear interaction between the signal and the transmitter noise, however, is not reversed in the virtual link as there is no virtual link following the physical transmission line. The nonlinear interference contribution, arising from the interactions between transmitter noise and signal, are not cancelled and therefore impose a limitation on the DPC gain.

If the nonlinearity compensation is divided between transmitter and receiver (split-NLC), the transceiver noise signal interactions become a function of the noise, both in transmitter and receiver. In literature, it has been suggested that an even split (50/50) of the virtual link between transmitter and receiver is optimal, as it minimises the amount of interactions between the signal and the ASE noise [41, 43,

105]. However, this is only true in the absence of transceiver noise, which is not negligible in most transmission systems. As a result, the optimum split ratio must be reevaluated based on the newly discovered interactions described in this Section. This reevaluation is described in Section 5.2.

If NLC is applied in the middle of the link (e.g. in the case of optical-phase conjugation), the beating between transmitter noise and signal in the first half of the link is inverted in the second half (and a virtual link is absent). It is, therefore, tempting to assume that NLC schemes that are located in the middle of the link would not suffer any SNR degradation from interactions between the signal and the transceiver noise. However, in practice, noiseless mid-link NLC may not be realisable and the uncompensated noise-signal interactions remain.

5.1.1.2 Analytical modelling

In this section, the analytical model describing the nonlinear interaction between the transceiver noise and the signal is derived. First, we separate the transceiver, denoted as SNR $\mathrm{SNR}_{\mathrm{TRX}}$ (see Eq. (2.37)), into a transmitter and receiver SNR contribution

$$\mathrm{SNR}_{\mathrm{TX}} = \frac{\mathrm{SNR}_{\mathrm{TRX}}}{1-\kappa_{\mathrm{R}}}, \tag{5.1}$$

and

$$\mathrm{SNR}_{\mathrm{RX}} = \frac{\mathrm{SNR}_{\mathrm{TRX}}}{\kappa_{\mathrm{R}}}, \tag{5.2}$$

where the ratio $\kappa_{\mathrm{R}} \in [0,1]$ is the relative amount of the receiver noise $\mathrm{SNR}_{\mathrm{RX}}$ on the total transceiver noise $\mathrm{SNR}_{\mathrm{TRX}}$.The noise power that is introduced at the transmitter and receiver, as illustrated in Fig. 5.1, is

$$\sigma_{\mathrm{T}}^2 = (1-\kappa_{\mathrm{R}})\,\kappa P, \tag{5.3}$$

and

$$\sigma_{\mathrm{R}}^2 = \kappa_{\mathrm{R}}\,\kappa P, \tag{5.4}$$

with $\kappa = \mathrm{SNR}^{-1}$ and channel launch power P. Eqs. (5.3) and (5.4) are used for notational convenience where the power dependency of κ is neglected. Both equations therefore do not imply that the transceiver noise is proportional to the power P. The arising nonlinear mixing terms can be calculated by using the formalism of the nonlinear interference coefficient (see Sec. 2.6). The nonlinear perturba-

tion is calculated by adding the transceiver noise contribution to the signal power. The nonlinear interference power arising from signal transceiver noise interactions $P_{\text{TRX-sig}}$ is then given as

$$P_{\text{TRX-sig}} = \tilde{\eta}_X \left(\sigma_{\text{T}}^2 + P\right)^3 - \tilde{\eta}_X P^3 + \tilde{\eta}_{n-X} \left(\sigma_{\text{R}}^2 + P\right)^3 - \tilde{\eta}_{n-X} P^3, \tag{5.5}$$

where the terms $-\tilde{\eta}_X P^3$ and $-\tilde{\eta}_{n-X} P^3$ denote the removal of signal signal interactions, as we are interested in nonlinear signal transceiver noise interactions. Eq. (5.5) considers any back-propagated bandwidth through the NLI coefficient. The variable η_X is the NLI coefficient after X fibre spans. Eq. (5.5) accounts for the residual interactions between the signal and transmitter (receiver) noise, when X spans are compensated by digital pre-distortion and the remaining $n-X$ spans are compensated by digital back-propagation. A schematic of the transmission line with its virtual links is shown in Fig. 2.13. Using Eqs. (5.3)(5.4), the coherent accumulation of NLI Eq. (2.47) and assuming that $\sigma_{\text{R}}^2 \ll P$ and $\sigma_{\text{T}}^2 \ll P$ yields

$$P_{\text{TRX-sig}} \approx 3 \left(\tilde{\eta}_X \sigma_{\text{T}}^2 + \tilde{\eta}_{n-X} \sigma_{\text{R}}^2\right) P^2 \tag{5.6}$$

$$= 3 \tilde{\eta}_1 \kappa \xi_{\text{TRX}} P^3, \tag{5.7}$$

where $\xi_{\text{TRX}} = (1-\kappa_{\text{R}}) X^{1+\varepsilon} + \kappa_{\text{R}} (n-X)^{1+\varepsilon}$ is the TRX noise beating accumulation factor. This factor depends on the digital compensation scheme (DPC, DBP or split-NLC), i.e., on the virtual link placement. In the case of DBP, where $X = 0$, we obtain $P_{\text{TRX-sig}} \approx 3\tilde{\eta}_1 \kappa \kappa_{\text{R}} n^{1+\varepsilon} P^3$ and all the residual signal transceiver noise interactions arise in the virtual link of DBP, as shown in Fig. 5.1a). In the case of DBP, where $X = n$, we obtain that $P_{\text{TRX-sig}} \approx 3\tilde{\eta}_1 \kappa (1-\kappa_{\text{R}}) n^{1+\varepsilon} P^3$ and all the residual signal transceiver noise interactions arise in the virtual link of the DPC block, as shown in Fig. 5.1b). The case of split-NLC and the optimisation of the split-ratio X is addressed in Sec. 5.2.

Eq. (5.7) can now be used to extend the SNR equation (2.53) to account for transceiver NSNI as

$$\text{SNR} = \frac{P}{(\eta_n - \tilde{\eta}_n) P^3 + \kappa P + N P_{\text{ASE}} + 3\tilde{\eta}_1 (\xi_{\text{ASE}} P_{\text{ASE}} + \xi_{\text{TRX}} \kappa P) P^2}. \tag{5.8}$$

Eq. (5.8) can be used to model arbitrary optical bandwidths that are digitally pre-distorted and back-propagated and is a key result in this chapter and in the research described in this thesis. Eq. (5.8) was validated by numerical simulations and experimental results described in the next Sec. 5.1.2.

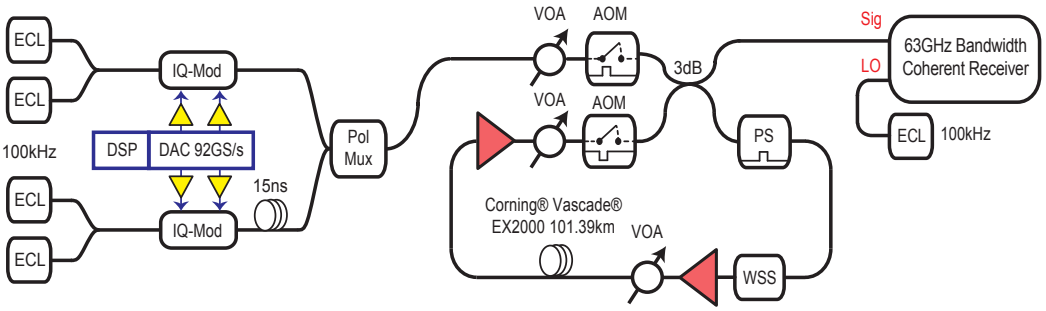

Figure 5.2: Experimental configuration to study nonlinear signal noise interactions.

5.1.2 Experimental validation of Eq. (5.8)

In this section, the formalism presented in Sec. 5.1.1 was validated by numerical simulations and experiments. The experiment was carried out in collaboration with L. Galdino and is described in [P15]. The experimental design, and the processing of the measurements were carried out jointly.In the following, the experimental setup is described in more detail. An schematic of the setup is shown in Fig. 5.2.

The transmitted signal consisted of a super channel made up of four subcarriers. Each dual-polarisation subcarrier was modulated with uniform 64-QAM at a symbol rate of 30 GBd. Four external cavity lasers with a linewidth of 100 kHz and a frequency spacing of 32 GHz were used as sources, separated into odd and even channels. The odd and even subcarriers were modulated using two separate IQ modulators, driven using spectrally shaped 64-QAM signals, with root raised cosine (RRC) filters with 0.1% roll-off from 92 GS/s DAC. Digital pre-emphasis was applied to the signal to compensate for the non-ideal frequency response of the transmitter components. The odd and even subcarriers were used in order to introduce a larger frequency spacing between channels that exhibit the same data pattern. The odd and even subcarriers were further decorrelated with a 15 ns delay. Subsequently, the odd and even channels were combined by a polarisation multiplexer to form a 4×30 GBd DP-64QAM super channel.

For transmission, a recirculating fibre loop was used, comprising a loop-synchronous polarisation scrambler (PS), a single span of 101.39 km Corning® Vascade® EX2000 fibre with a span loss of 16.2 dB, an EDFA with 5 dB noise figure, a wavelength selective switch (WSS) for adjustable gain flattening, and a second EDFA to overcome the loop loss components. The loop components exhibited a combined loss of 13.5 dB.

On the receiver side, a single digital coherent receiver was used to detect all four subcarriers. This was necessary to enable joint digital processing of all four channels. The received signal were passed to the coherent receiver together with

a local oscillator laser with a linewidth of 100 kHz. The coherent receiver consisted of a 90° optical hybrid, followed by balanced photo-detectors with 70 GHz electrical bandwidth. The combined signal was then digitised using two 160 GSa/s real-time digital sampling oscilloscopes with 63 GHz electrical analog bandwidth. The digital signal processing was carried out offline. The DSP chain consisted of receiver imbalance correction (which corrected the skew that was measured in advance using a frequency swept sine generated from the intradyne frequency offset between two lasers), digital back-propagation, adaptive equalisation, and carrier recovery. Finally, the received SNR was evaluated as the ratio between the variance of the transmitted symbols $E[|X|^2]$ and the variance of the noise σ^2, where $\sigma^2 = E[|X-Y|^2]$ and Y represents the received symbols after DSP.

5.1.2.1 Back-to-back characterisation

Back-to-back measurements were taken with the results shown in Fig. 5.3. Fig. 5.3a) shows the received SNR as a function of the optical SNR over both polarisations and Fig. 5.3b) shows the maximum achievable SNR SNR_{TRX} for all subcarriers within the super channel. Two cases were investigated. One where a single subcarrier was used and one where the entire super channel was simultaneously received with local oscillator tuned to the centre of the super channel. The subcarriers were then individually and digitally down-converted before they were passed to the DSP chain. For reference the ideal OSNR $= \frac{\mathrm{SNR}B_{\mathrm{ch}}}{12.5\mathrm{GHz}}$ is also shown. Fig. 5.3a) shows that the SNR is limited by the optical components until an OSNR of around 15 dB. For higher OSNR values than 15 dB, the SNR is limited by noise originating in the electrical components. The maximum achievable SNR can be extracted from Fig. 5.3a), shown separately in Fig. 5.3b). The maximum achievable SNR is lower for all subcarriers when transmitted as a super channel with respect to the single channel case. This is due to the frequency dependence of the electrical components. The outer channels of the super channel achieved a lower transceiver SNR for the same reason. It should be noted that if the LO is centred on each subcarrier and each subcarrier is received individually, then each subcarrier would have the same performance.

The main contributions to the transceiver noise were the DAC and the linear electrical amplifiers in the transmitter, and the ADC in the real time sampling oscilloscope at the receiver side. The DAC exhibited a measured effective number of bits (ENOB) of 5 bits over a 15 GHz carrier frequency, which corresponds to an SNR of approximately $6.02 \cdot \mathrm{ENOB} + 1.76 = 32$ dB. 15 GHz corresponds to the bandwidth of the spectrally shaped IQ drive signals. The noise figure of the linear, electrical amplifiers was 6 dB at a frequency of 15 GHz, therefore the maximum achievable

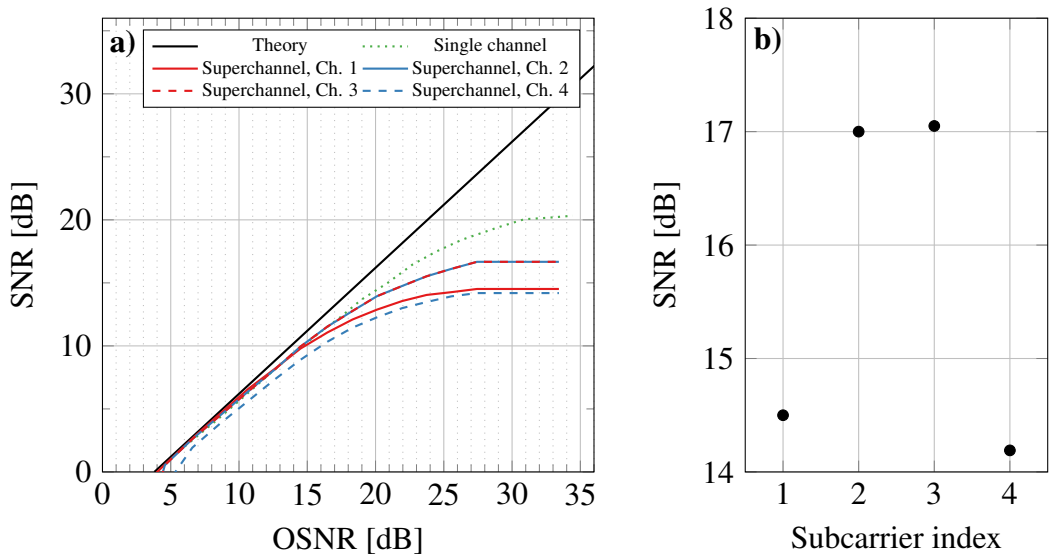

Figure 5.3: BTB measurements (a) SNR vs. OSNR for single channel and each subcarrier of the superchannel; (b) maximum archivable SNR for each subcarrier.

SNR originating from electrical components of the transmitter was approximately 26 dB. A further degradation of 2 dB was measured for applying pulse shaping. This degradation was caused as the pulse shaping increases the peak-to-average power ratio of the QAM signal. The ADCs in the real time sampling oscilloscope also exhibited a frequency dependent ENOB, which was 4.8 bits and 4.3 bits at a frequency of 15 GHz and 60 GHz, respectively. The residual transceiver noise originated from optical components, such as optical amplifiers and the limited bandwidth of the IQ modulators.

5.1.2.2 Transmission results

In order validate the theoretical predictions, described by Eq. (5.8), split-step simulations and the experimental setup of Sec. 5.1.2 was used for optical fibre transmission up to 5,000 km. As for the NLC algorithm, DBP was applied to the entire optical field as illustrated in Fig. 5.1a). For a better comparison, the transmission setup was numerically simulated (see Sec. 2.3.4) for two cases; one in the case of an ideal transceiver $\mathrm{SNR}_{\mathrm{TRX}} \to \infty$ and one with a finite maximum achievable transceiver SNR that coincided with the back-to-back measurements in Fig. 5.3b). The transceiver noise was assumed to be equally split between the transmitter and receiver, yielding $\kappa_{\mathrm{R}} = 0.5$ in Eq. (5.8). Additionally, transmission in the presence of polarisation-mode dispersion was considered in order to study the performance penalty of DBP in the presence of PMD. The PMD parameter was chosen to be $0.05\ \mathrm{ps}/\sqrt{\mathrm{km}}$, to match the specifications of the fibre used in the experimental setup. A linear PMD equaliser was used after the receiver-side DBP, assuming an exact

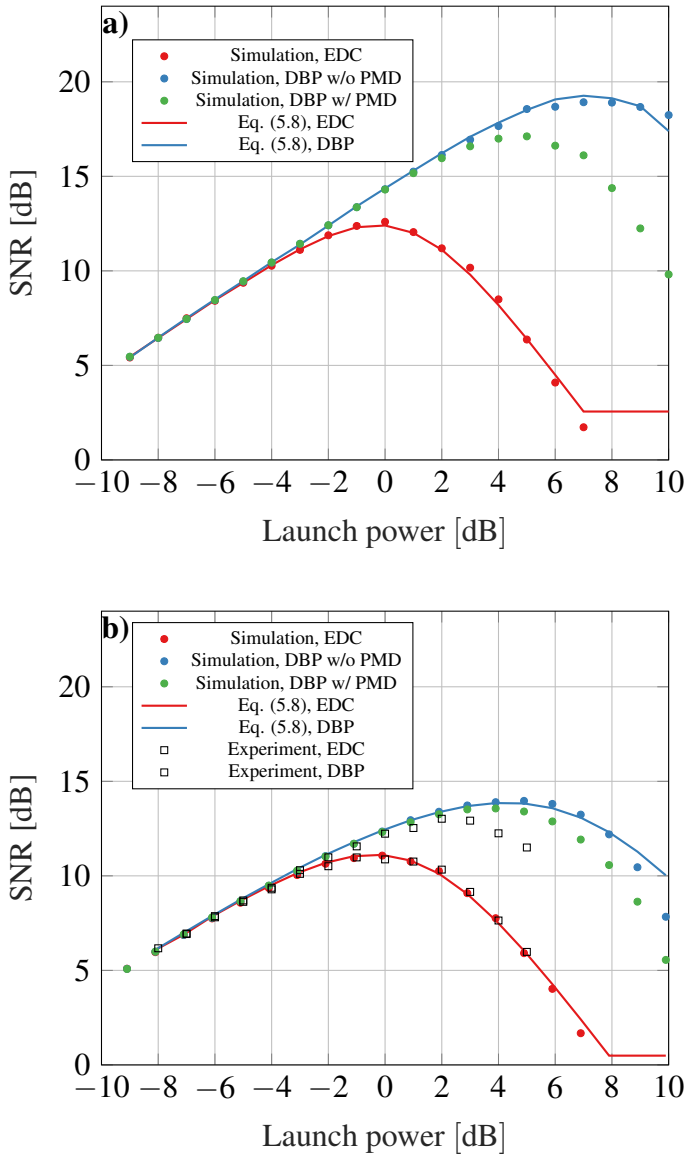

Figure 5.4: Received SNR against launch power over 5,000 km transmission (a) without transceiver noise and (b) with transceiver noise.

knowledge of the instantaneous PMD along the fibre propagation.

The received SNR as a function of the channel launch power is shown without and with transceiver noise in Fig. 5.4a) and 5.4b), respectively. The results were obtained for subcarrier 3 over a total propagation length of 5,000 km.

Fig. 5.4a) shows that, in the absence of transceiver noise, the SNR applying electronic dispersion compensation (EDC) is 12.4 dB at the optimum launch power of 0 dBm. EDC refers to electronic dispersion compensation, denoting that no NLC was applied. When DBP was applied in the absence of PMD, the SNR increased to 18.9 dB at 8 dBm launch power, yielding a DBP gain of 6.7 dB. However, when

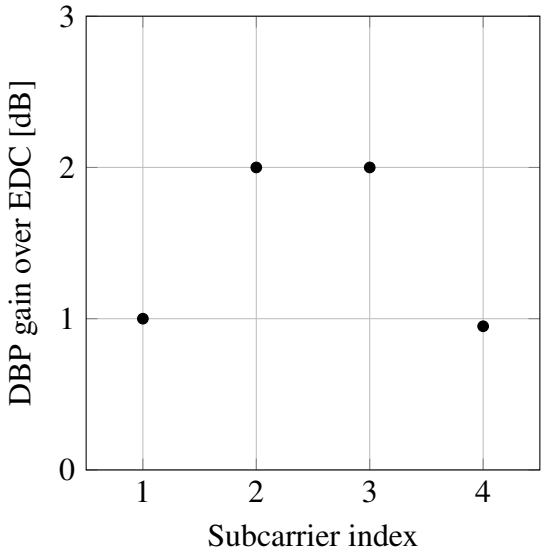

Figure 5.5: DBP gain over EDC for each subcarrier of the superchannel after 5,000 km of optical fiber transmission.

PMD was included in the numerical simulation, an SNR and DBP gain penalty of 2.2 dB was observed.

On the other hand, Fig. 5.4b) shows the transmission including the effect of the limited transceiver SNR. The transceiver SNR was $\mathrm{SNR}_{\mathrm{TRX}} = 17$ dB, as in Fig. 5.3b) for subcarrier 3. The analytical model Eq. (5.8) and the split-step simulation without PMD show a gain of 2.9 dB when DBP is applied. This is a significant gain reduction of 6.7 dB in DBP gain with respect to the case of no transceiver noise. The analytical model Eq. (5.8) exhibits remarkable accuracy compared to the numerical simulations, validating the theory presented in Sec. 5.1.1 and emphasising the significance of nonlinear signal transceiver noise interactions. When PMD is included in the simulation, an additional penalty of the DBP gain of 0.5 dB was observed. The experimental results obtained with the setup in Fig. 5.2 are also shown in Fig. 5.4b). The experimental results are in good agreement with the modelling results and the simulation results. Experimentally, a DBP gain in SNR of 2.0 dB was found compared to the 2.4 dB gain that was predicted by simulation. This slightly smaller gain in the experimental results at launch powers beyond 3 dBm may be due to the small mismatch of the dispersion values used in the DBP algorithm or the frequency-dependent ENOB of the receiver. The mismatch might also originate from the definition of the transceiver noise as in (5.3)(5.4) or from the assumption that the transceiver noise is evenly split between transmitter and receiver.

The experimentally measured SNR after a propagation distance of 5,000 km

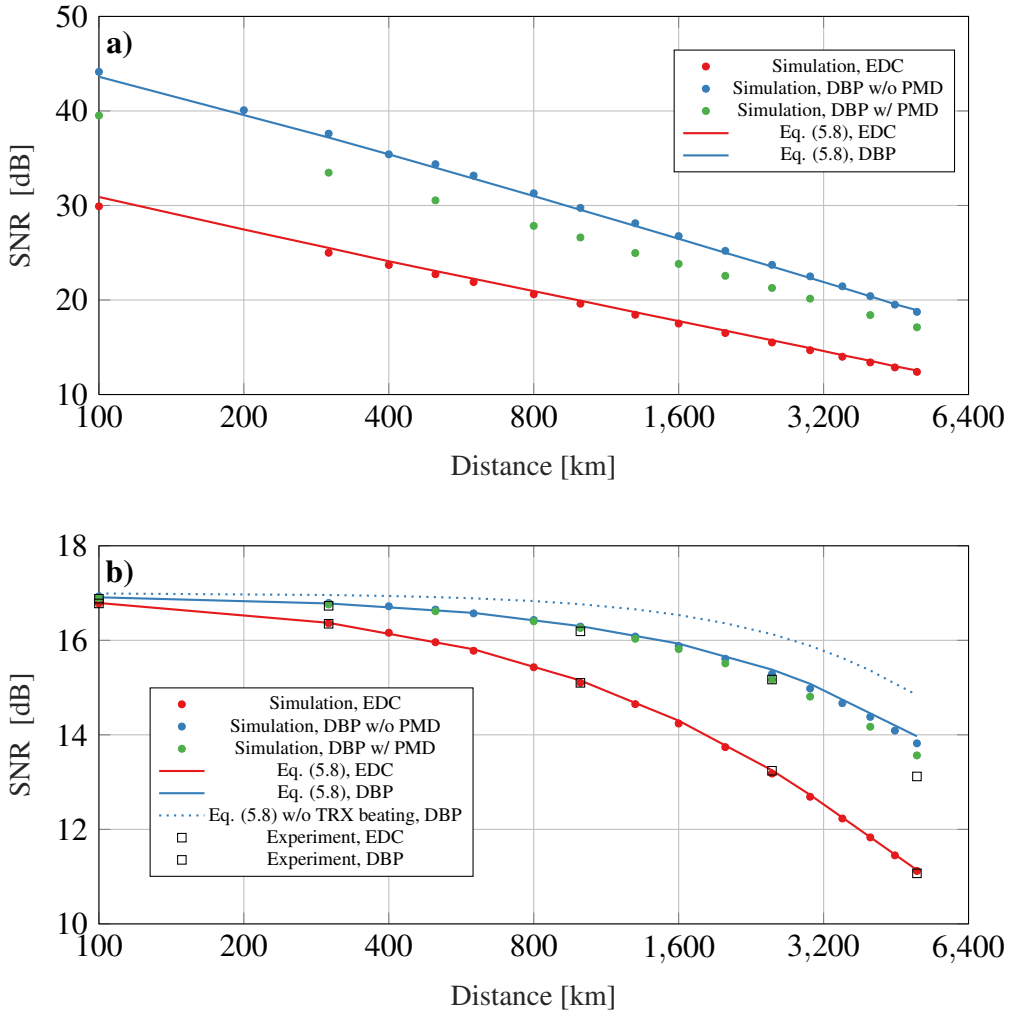

Figure 5.6: Received SNR vs. distance at optimum subcarrier launch power for (a) simulations and analytical model without transceiver noise and (b) experimental data, simulations and analytical model with transceiver noise

of each subcarrier is shown in Fig. 5.6. A DBP gain of 2 dB was measured for subcarrier 2 and 3, while the DBP gain for the outer subcarriers 1 and 4 was only 1 dB. This is because the transceiver noise is higher for those channels due to the frequency dependency of the electrical and optical equipment, as explained in Sec. 5.1.2.1 and shown in Fig. 5.3b)

To expand the comparison between analytical modelling, split-step simulations and experimental results, the SNR at (the respective) optimum launch power as a function of distance is shown in Fig. 5.6. The case of no transceiver noise is shown in Fig. 5.6a), while the case of including transceiver noise, and the experimental results, are shown in Fig. 5.6b). The analytical modelling of the transmission system using Eq. (5.8) is in good agreement with the numerical simulations for all transmission distances. In the case of no transceiver noise, the DBP gain reduces

as a function of distance. This is the result of increasing nonlinear interactions between the signal and co-propagating ASE noise. However, in the case of transceiver noise the DBP gain *increases* as a function of distance. This is a consequence of the linear transceiver noise contribution κP, as it limits the performance in high SNR regimes. The observation is supported by the experimental results. For this particular system, a 150% increase in reach (from 1,000 km to 2,500 km) was measured experimentally. The measured gain were in good agreement with the analytical model and the numerical simulations. The PMD was found to have a smaller impact that previously thought due to the transceiver noise limitation and the arising nonlinear interactions between the signal and the transceiver noise. The penalty due to PMD is almost negligible (<0.2 dB) for transmission distance of up to 2,500 km.

The results in this section, validate the theoretical model introduced in Sec. 5.1.1. The analytical results therefore enable a throughout study of the transceiver NSNI on transmission systems that employ digital NLC.

5.1.3 Implications on C-band systems

In the last section, the impact of transceiver noise signal interactions was investigated on a four channel system. However, it is important to quantify the impact of transceiver NSNI over the entire C-band. For this purpose the DBP gain with respect to EDC as a function of the back-propagated channels is shown after 1000 km transmission and after 10,000 km transmission in Fig. 5.7a) and 5.7b), respectively. The same system parameter used in Sec. 5.1.2 were considered, with a signal consisting of 155×32GBd channels spanning an optical bandwidth of 4.96 THz. A transceiver SNR of 24 dB was assumed. Additionally, the results were obtained for 3 different cases. First, the case of no transceiver noise was considered as a baseline comparison. Second, the case where the entire transceiver noise is introduced at the transmitter, which result in no nonlinear interactions between the signal and the transceiver noise. Finally, the case was studied where all transceiver noise was introduced at the receiver (receiver noise only), which includes nonlinear transceiver noise signal interactions. The last two cases were analysed to quantify the potential impact of the nonlinear transceiver noise signal interactions. In practice, the transceiver noise is partly introduced at the transmitter and at the receiver. Therefore, the performance of any realistic transceiver sub-system must lie between the two cases.

In the case of 1000 km transmission distance, shown in Fig. 5.7a), the transmitter noise reduced the DBP gain by 5 dB, with all channels back-propagated. It should be noted that this reduction comes from the transceiver noise alone (without nonlinear interactions) and from the NSNI between the signal and ASE noise. In the

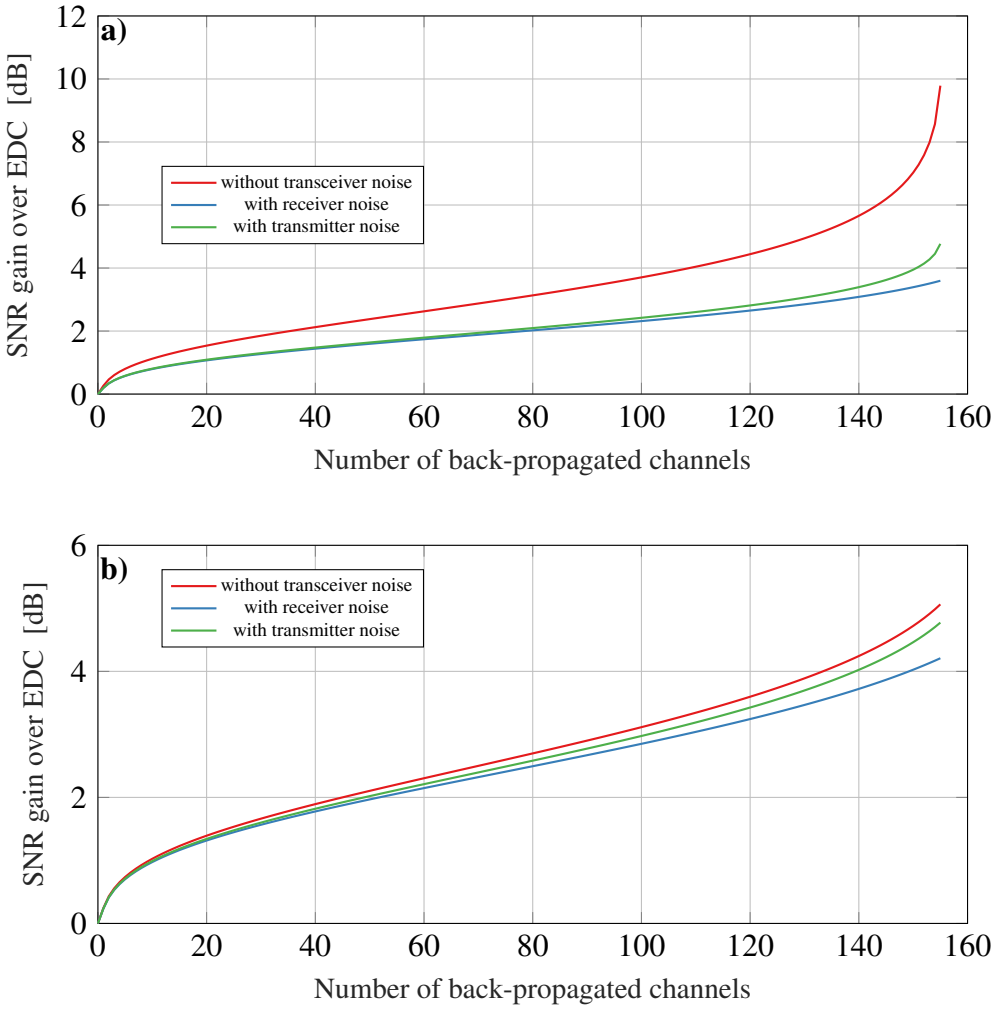

Figure 5.7: SNR gain as a function of back-propagated number of channels for transmission distance of (a) 1,000 km and (b) 10,000 km

case of transmitter noise only, there are no nonlinear interactions between the signal and transceiver noise (see Sec. 5.1.1). In the case of receiver noise only, where nonlinear interactions between transceiver noise and the signal occur, the DBP gain reduced further by 1.2 dB. This illustrates the significance and the impact of the transceiver noise signal interactions. As shown in Fig. 5.7a), these interactions become more significant, the more channels are digitally back-propagated.

Fig. 5.7b) shows the same transmission system with a transmission distance of 10,000 km. The gain reduction from an ideal transceiver sub-system to transmitter noise only (no transceiver noise signal interactions) was 0.3 dB. The DBP gain reduced further by an additional 0.5 dB for the receiver noise only case, where nonlinear interactions between the signal and the transceiver noise were present. For the case of 10000 km transmission distance, the impact of the transceiver noise

and its nonlinear beating is reduced compared to the case shown in Fig. 5.7a), as the transceiver noise impact, in general, is less dominant over longer transmission distances.

Due to the study in this section, it can be concluded that nonlinear interactions between transceiver noise and the signal become significant when the the majority of the optical signal is nonlinearity compensated for. The impact is particularly significant for shorter transmission distances, where the transceiver noise impact is more dominant with respect to other noise sources of the system. However, for single channel back-proagation or if only a few channels are back-propagated, the interactions between the transceiver noise and the signal are negligible.

5.2 On the optimum design of digital nonlinearity compensation

In this section, the newly derived Eq. (5.8) is utilised to derive an optimum split ratio between digital pre-distortion and digital back-propagation. The considered system is shown in Fig. 2.13, where X spans are pre-compensated at the transmitter and the remaining $n-X$ spans are digitally back-propagated at the receiver. The results of this section were peer reviewed and published in [P9].

To date, three different implementations have been proposed in the literature, depending on whether this virtual link is placed at the transmitter, receiver or evenly split between them. In the absence of transceiver noise, the performance difference between transmitter-side and receiver-side NLC lies only in the periodic arrangement of the optical amplifiers along the link [105]. This is mathematically described in ξ_{ASE} in Eq. (2.53). This is due to over-/under-compensated ASE noise-signal interactions that strongly depend on the specific location where each ASE noise contribution is introduced. For conventional links, where an optical amplifier is located after each span, DPC improves the transmission performance by up to one additional span. The gain in SNR decreases with distance and is approximately 0.2 dB after 20 spans and less than 0.1 dB after more than 45 spans [43].

Apart from transmitter and receiver-side NLC, it has been proposed in theoretical studies that the virtual link should be equally divided between transmitter and receiver [41, 43, 105]. This approach minimises the residual NSNI between signal and ASE noise and yields at least 1.5 dB improvement in SNR compared to conventional DBP, assuming full-field NLC and the absence of transceiver noise. However, it should be noted that, to date, there are no experimental demonstration of this potentially advantageous scheme.

The theoretical considerations in [41, 43, 105], expressed by Eq. (2.53), only

consider NSNI between the signal and ASE noise injected by optical amplifiers. Therefore, they do not generally apply for real transmission systems that further exhibit noise originating from non-ideal transceivers, as shown in Sec. 5.1.1. Due to the adverse impact of transceiver noise beating, the aim of this research was to revise the performance predictions of transmitter-side, receiver-side and split NLC.

The results in this Section were peer-reviewed and published in [P9].

5.2.1 Optimum split-ratio X_{opt}

To quantify the optimum split-ratio X_{opt} between digital pre-distortion and back-propagation, the accumulation factors that describe the residual signal noise beating are written as

$$\xi_{\mathrm{TRX}} = \underbrace{(1-\kappa_{\mathrm{R}})X^{1+\varepsilon}}_{\text{TX beating}} + \underbrace{\kappa_{\mathrm{R}}\,(n-X)^{1+\varepsilon}}_{\text{RX beating}}, \tag{5.9}$$

$$\xi_{\mathrm{ASE}} = \sum_{i=1}^{X-1} i^{1+\varepsilon} + \sum_{i=1}^{n-X} i^{1+\varepsilon}. \tag{5.10}$$

The NSNI factors (5.9)(5.10) describe the over and under-compensation of residual nonlinear signal noise mixing products. The minimisation of the NSNI accumulation factors Eqs. (5.10)(5.9) play a fundamental role in the derivation of the optimum split-ratio X_{opt}. Unfortunately, both accumulation factors minimise for different values of X. Therefore, it is necessary to define regimes where either NSNI contribution can be neglected. ASE noise beating can be typically neglected for short distances, which we refer to as the transceiver noise beating regime. On the other hand, TRX noise beating can be neglected for very long distances, which we refer to as the ASE noise beating regime. Both regimes have been studied separately with respect to their, optimum split X_{opt}, their optimum split NLC gains and approximate inequalities are derived that define both regimes. In the following Sections, it was assumed that the entire optical bandwidth is compensated for (i.e. $\tilde{\eta}_i = \eta_i$ in Eq. (5.8)).

5.2.1.1 The transceiver noise beating regime

The transceiver noise beating regime is defined as the regime, where the TRX noise beating is much stronger than the ASE noise beating at optimum launch power $\left(\kappa\xi_{\mathrm{TRX}}P_{\mathrm{opt}} \gg \xi_{\mathrm{ASE}}P_{\mathrm{ASE}}\right)$. In the TRX noise beating regime the SNR, including all

nonlinear signal noise interactions (see Sec. 5.1.1), Eq. (5.8) reduces to

$$\mathrm{SNR} = \frac{P}{\kappa P + nP_{\mathrm{ASE}} + 3\eta\,\kappa\xi_{\mathrm{TRX}}P^3}. \tag{5.11}$$

The optimum NLC split X_{opt}, that minimises ξ_{TRX} and maximises Eq. (5.11), is obtained by solving $\frac{\partial}{\partial X}\xi_{\mathrm{TRX}} = 0$. The optimum split is found to be

$$X_{\mathrm{opt}} = \left\lfloor \frac{n}{1+\left(\frac{1-\kappa_{\mathrm{R}}}{\kappa_{\mathrm{R}}}\right)^{\frac{1}{\varepsilon}}} \right\rceil, \tag{5.12}$$

with the optimum TRX noise beating accumulation factor

$$\xi_{\mathrm{TRX,opt}} = \frac{(1-\kappa_{\mathrm{R}})^{-\frac{1}{\varepsilon}} + \kappa_{\mathrm{R}}^{-\frac{1}{\varepsilon}}}{\left[(1-\kappa_{\mathrm{R}})^{-\frac{1}{\varepsilon}} + \kappa_{\mathrm{R}}^{-\frac{1}{\varepsilon}}\right]^{1+\varepsilon}} \cdot n^{1+\varepsilon}, \tag{5.13}$$

where $\lfloor x \rceil$ denotes the nearest integer function, the result of the quantisation of the number of spans. In the following this rounding is removed for notational convenience. It should be noted that the optimum NLC split ratio $\frac{X_{\mathrm{opt}}}{n}$ is only a function of the transceiver noise ratio and the coherence factor (see Sec. 2.6.2).

To quantify the gain of the optimum NLC scheme, using $X = X_{\mathrm{opt}}$, the gain in reach with respect to DBP ($X = 0$) was analysed. The TRX noise accumulation factor for DBP, using Eq. (5.11), is $\xi_{\mathrm{TRX,DBP}} = \kappa_{\mathrm{R}} n^{1+\varepsilon}$.

Substituting $\xi_{\mathrm{TRX,opt}}$ and $\xi_{\mathrm{TRX,DBP}}$ in Eq. (5.11), forcing $\mathrm{SNR}_{\mathrm{opt}} = \mathrm{SNR}_{\mathrm{DBP}}$ and solving for $\Delta n_{\max} = \frac{n_{\mathrm{opt}}}{n_{\mathrm{DBP}}}$ yields the reach increase of split NLC with respect to DBP. The result is

$$\Delta n_{\max} = \left\{ \frac{\kappa_{\mathrm{R}}\left[(1-\kappa_{\mathrm{R}})^{-\frac{1}{\varepsilon}} + \kappa_{\mathrm{R}}^{-\frac{1}{\varepsilon}}\right]^{1+\varepsilon}}{(1-\kappa_{\mathrm{R}})^{-\frac{1}{\varepsilon}} + \kappa_{\mathrm{R}}^{-\frac{1}{\varepsilon}}} \right\}^{\frac{1}{3+\varepsilon}}. \tag{5.14}$$

Similar to the optimum NLC split ratio, the gain in reach is only dependent on the transceiver noise ratio and the coherence factor. Eq. (5.14) yields the gain with respect to DBP. In order to obtain the reach gain compared to DPC ($X = n$), κ_{R} must be replaced by $1 - \kappa_{\mathrm{R}}$.

Typical transmission systems in recent years in optical communications have high dispersion coefficients and wide optical bandwidths that result in a small co-

herence factor. For dispersion parameters $D > 16$ ps/km/nm, attenuation coefficients $\alpha > 0.2$ dB/km, and optical bandwidths > 100 GHz, the coherence factor is $\varepsilon < 0.1$ for 80 km spans and EDFA amplification [20, Fig. 10]. For $\varepsilon \ll 1$ the optimum NLC split reduces to

$$X_{\text{opt}} = \begin{cases} 0 & \text{if } \kappa_{\text{R}} < 0.5, \\ \frac{n}{2} & \text{if } \kappa_{\text{R}} = 0.5, \\ n & \text{if } \kappa_{\text{R}} > 0.5, \end{cases} \tag{5.15}$$

and the TRX noise beating accumulation factor reduces to

$$\xi_{\text{TRX,opt}} = \begin{cases} \frac{1}{2^{1+\varepsilon}} \cdot n^{1+\varepsilon} & \text{if } \kappa_{\text{R}} = 0.5, \\ \min\left[1-\kappa_{\text{R}}, \kappa_{\text{R}}\right] \cdot n^{1+\varepsilon} & \text{otherwise.} \end{cases} \tag{5.16}$$

Eq. (5.15) shows that transmission systems with low coherence factors and lower transmitter noise than receiver noise should deploy transmitter-side NLC for maximum performance and vice versa when there is more transmitter noise. In other words, the virtual link should be placed where less transmitter or receiver noise is injected. This, perhaps surprising, result is due to the fact that only transceiver noise beating is considered in this section.

The split NLC gain in reach with respect to DBP for $\varepsilon \ll 1$ yields

$$\Delta n_{\max} = \begin{cases} 1 & \text{if } \kappa_{\text{R}} \leq 0.5, \\ \left(\frac{\kappa_{\text{R}}}{1-\kappa_{\text{R}}}\right)^{\frac{1}{3+\varepsilon}} & \text{if } \kappa_{\text{R}} > 0.5. \end{cases} \tag{5.17}$$

There is no split NLC reach gain with respect to DBP for $\kappa_{\text{R}} < 0.5$, as DBP is already the optimum itself. When κ_{R} is replaced by $1-\kappa_{\text{R}}$, (5.17) gives the split NLC reach gain with respect to DPC due to symmetry reasons. It is apparent from (5.17) that transmission systems with a low coherence factor ε and equally divided transceiver noise ($\kappa_{\text{R}} = 0.5$) exhibit no gain compared to DBP in the TRX noise beating regime. However, split NLC gains are significant, when the transceiver noise is unequally divided between transmitter and receiver.

The split NLC reach gain with respect to DBP (Eq. (5.14) and its approximation Eq. (5.17)) are shown in Fig. 5.8 as a function of coherence factor for a variety of transceiver noise ratios. Only transceiver ratios $\kappa_{\text{R}} \geq 0.5$ are shown. For lower transceiver noise ratios the plot can be interpreted as the split NLC gain with respect to DPC when κ_{R} is replaced by $1-\kappa_{\text{R}}$. Fig. 5.8 is sufficient to estimate whether the coherence factor can be considered small and the approximation (5.17) can be

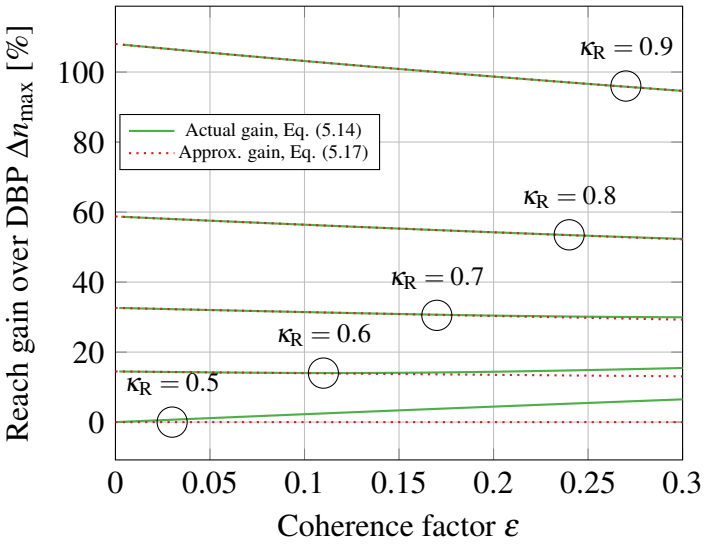

Figure 5.8: Reach increase of split NLC with respect to DBP as function of the coherence factor for a variety of transceiver noise ratios. Shown are the exact gain from Eq. (5.14) and its approximation for small ε from Eq. (5.17).

used. Eq. (5.17) serves as an excellent approximation for most of the cases except for high coherence factors combined with a transceiver noise ratio close to 0.5. The plot also shows that the split NLC reach gain is larger for systems with a larger imbalance between the amount of noise injected by transmitter and receiver. For example, when more noise is injected at the receiver and $\varepsilon \ll 1$, the receiver noise beating can be fully elimated by placing the complete virtual link at the transmitter. This will result in transmitter noise beating (occurring in the physical link) which will be smaller than the eliminated receiver noise beating.

In the following, a simple inequality is derived to determine whether a transmission system is operated in the TRX noise beating regime. First, we start with the condition that ASE noise beating is negligible compared to TRX noise beating at optimum launch power

$$\xi_{\mathrm{ASE}} P_{\mathrm{ASE}} \ll \xi_{\mathrm{TR}} \kappa P_{\mathrm{opt}}. \tag{5.18}$$

Inequality (5.18) is then expanded as

$$\xi_{\mathrm{ASE}} P_{\mathrm{ASE}} \leq \xi_{\mathrm{ASE,DBP}} P_{\mathrm{ASE}} \ll \xi_{\mathrm{TR,opt}} \kappa P_{\mathrm{opt}} \leq \xi_{\mathrm{TR}} \kappa P_{\mathrm{opt}}, \tag{5.19}$$

with $\xi_{\mathrm{ASE,DBP}} = \sum_{i=1}^{n} i^{1+\varepsilon}$. It is sufficient to consider the inner inequality in (5.19) in order to show that Eq. (5.18) holds. The inner inequality in (5.19) is the approx-

imation in Appendix A.5. The result is

$$\mathrm{SNR}_{\mathrm{EDC,ideal}}\,[\mathrm{dB}] \gg \frac{2}{3}\left(\frac{\mathrm{SNR}_{\mathrm{TRX}}}{\min\left[1-\kappa_{\mathrm{R}},\kappa_{\mathrm{R}}\right]}\right)[\mathrm{dB}] - 6.5\mathrm{dB}, \tag{5.20}$$

where $(\cdot)\,[\mathrm{dB}]$ means conversion to decibel scale and $\mathrm{SNR}_{\mathrm{EDC,ideal}}$ is the SNR at optimum launch power with electronic dispersion compensation only and no transceiver noise, which can be calculated as

$$\mathrm{SNR}_{\mathrm{EDC,ideal}} = \frac{1}{\sqrt[3]{\frac{27}{4}P_{\mathrm{ASE}}^2\eta_1 n^{3+\varepsilon}}}. \tag{5.21}$$

When the inequality in Eq. (5.20) is satisfied, the corresponding system is operating in the transceiver noise beating regime and the optimum split ratio and reach gain reported in this section apply.

5.2.1.2 The ASE noise beating regime

In this section the regime is discussed where the TRX noise beating is negligible with respect to the ASE noise beating at optimum launch power $\left(\kappa\xi_{\mathrm{TRX}}P_{\mathrm{opt}} \ll \xi_{\mathrm{ASE}}P_{\mathrm{ASE}}\right)$. This regime has already been studied in the literature [41, 43, 105] and is, therefore, only briefly covered. In the ASE noise beating regime the SNR (5.8) reduces to

$$\mathrm{SNR} = \frac{P}{nP_{\mathrm{ASE}} + 3\tilde{\eta}_1\xi P^2 P_{\mathrm{ASE}}}, \tag{5.22}$$

with the optimum NLC split given as $X_{\mathrm{opt}} = \left\lceil \frac{n}{2} \right\rceil$, where $\lceil x \rceil$ denotes the ceiling function with the optimum ASE noise beating accumulation factor [43, Eq. (7)]

$$\xi_{\mathrm{ASE,opt}} = \left(\frac{n}{2}\right)^{1+\varepsilon} + 2\sum_{i=1}^{\frac{n}{2}-1} i^{1+\varepsilon}. \tag{5.23}$$

Similar to Sec. 5.2.1.1, the gain of split NLC is compared to the performance of DBP. The gain in reach $\Delta n_{\max} = \frac{n_{\mathrm{opt}}}{n_{\mathrm{DBP}}}$ can be expressed as

$$\Delta n_{\max} = 2^{\frac{1+\varepsilon}{3+\varepsilon}}. \tag{5.24}$$

The split NLC reach increase is only a function of the coherence factor with $\Delta n_{\max} = 25\%$ for $\varepsilon \ll 1$. This means that a reach increase of 25% is expected for typical high bandwidth transmission systems in optical fibre communications.

Similarly to section 5.2.1.1, an inequality is derived to determine whether a transmission system is operated in the ASE noise beating regime. First, we start

with the condition that TRX noise beating is negligible compared to ASE noise beating

$$\xi_{\mathrm{ASE}} P_{\mathrm{ASE}} \gg \xi_{\mathrm{TRX}} \kappa P_{\mathrm{opt}}, \tag{5.25}$$

which is then expanded to (for $\varepsilon \ll 1$)

$$\xi_{\mathrm{ASE}} P_{\mathrm{ASE}} > \xi_{\mathrm{ASE,opt}} P_{\mathrm{ASE}} \approx \frac{1}{2} \xi_{\mathrm{ASE,DBP}} P_{\mathrm{ASE}} \gg \xi_{\mathrm{TRX,max}} \kappa P_{\mathrm{opt}} > \xi_{\mathrm{TRX}} \kappa P_{\mathrm{opt}}. \tag{5.26}$$

Considering only the inner inequality to prove Eq. (5.25) and using the result derived in Appendix A.5 yields

$$\mathrm{SNR}_{\mathrm{EDC,ideal}}\,[\mathrm{dB}] \ll \frac{2}{3} \left(\frac{\mathrm{SNR}_{\mathrm{TRX}}}{\max\left[1-\kappa_{\mathrm{R}}, \kappa_{\mathrm{R}}\right]} \right) [\mathrm{dB}] - 9.5\mathrm{dB}, \tag{5.27}$$

with $\mathrm{SNR}_{\mathrm{EDC,ideal}}$ as in Eq. (5.22). When inequality (5.27) holds, the corresponding transmission system is operated in the ASE noise beating regime and the optimum split ratio and the reach gain reported in this section apply.

5.2.2 Numerical validation

The next step is to validate the theory described in Sec. 5.2.1 by means of numerical split-step simulations (see Sec. 2.3.4). The transmitted signal was a 3×32 GBd system with a channel spacing of 32.001 GHz (Nyquist-spacing). The transmission line, comprised of SMF based spans, with parameters as in Tab. 3.1. The step-size was logarithmically distributed with 800 steps per 80 km span length. The noise figure of the EDFAs was set to 4 dB. The symbol constellation was uniform 256-QAM.

Additive white Gaussian noise was added at transmitter and receiver to emulate a finite transceiver SNR and nonlinearity compensation was carried out as schematically shown in Fig. 2.13. The nonlinear interference coefficient and the coherence factor were obtained in closed-form from [20, Eq. (13) and Eq. (23)] with the modulation format dependent correction from [22, Eq. (2)]. The values were $\tilde{\eta}_1 = 26.2$ dB and $\varepsilon = 0.108$.

To test the theory presented in section 5.2.1, a system with a transceiver noise that is equally divided between transmitter and receiver ($\kappa_{\mathrm{R}} = 0.5$), shown in Sec. 5.2.2.1, and a system with an unequal division of transceiver noise ($\kappa_{\mathrm{R}} = 0.8$), shown in Sec. 5.2.2.2, were simulated.

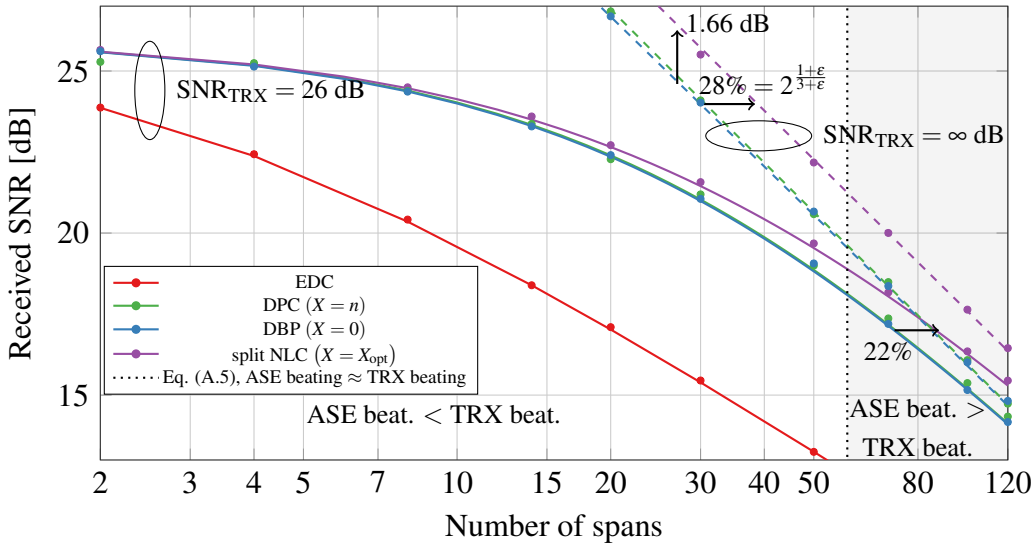

Figure 5.9: SNR at optimum launch power as a function of span number obtained by simulation (markers) and Eq. (5.8) (lines) for 256-QAM. The case with an infinite transceiver SNR (solid lines) and a finite transceiver SNR of 26 dB (dashed lines) are shown. The transceiver noise is equally divided between transmitter and receiver ($\kappa_{\mathrm{R}} = 0.5$).

5.2.2.1 Equal transmitter and receiver noise contribution

First, the case of an equal contribution of transceiver noise between transmitter and receiver ($\kappa_{\mathrm{R}} = 0.5$) is studied. The received SNR was evaluated at optimum launch power, as a function of distance and is shown in Fig. 5.9. The lines represent the analytical model estimated by Eq. (5.8) at optimum launch power for EDC, DBP ($X = 0$), DPC ($X = n$) and split NLC with the optimum split NLC of $X_{\mathrm{opt}} = \lceil \frac{n}{2} \rceil$ between transmitter and receiver. A split of $X = \lceil \frac{n}{2} \rceil$ is the optimum for a system where the transceiver noise is equally divided between transmitter and receiver. For comparison, the same transmission system without transceiver noise (SNR$_{\mathrm{TRX}} = \infty$ dB) is shown with dashed lines and the point where ASE noise beating approximately equals TRX noise beating is shown with a black vertical dashed line. For the given system parameters, both beating contributions are approximately equal at 58 spans according to Eq. (A.52) in the Appendix.

Further, in the case of a finite transceiver SNR, there is negligible performance difference between DPC and DBP, as they only differ for short distances due to an advantage of one span in favour of DPC in the ASE noise beating contribution [43, Fig. 2]. However, short transmission distances are dominated by TRX noise beating where both perform the same (cf. Eq. (5.9) with $\kappa_{\mathrm{R}} = 0.5$). Moreover, as predicted in Section 5.2.1.1, there is negligible gain of split NLC when TRX noise beating is dominant.

At 72 spans, the reach increase of split NLC compared to DBP is 22%. Even at such a long transmission distance, the gain was not fully converged to the case of $\mathrm{SNR}_{\mathrm{TRX}} = \infty$ dB. According to (A.52), at least 580 spans are required for the TRX noise beating to be one order of magnitude lower than ASE noise beating. Such distances are not of practical interest, which illustrates the importance of transceiver noise beating in real systems. Inequality (A.52) can be further used to estimate the impact of a different transceiver SNR.

Fig. 5.9 shows that systems with a transceiver SNR of 26 dB are usually operated in the TRX noise beating regime for short, medium and long-haul distances and in a mixed regime for transatlantic and transpacific distances. Split NLC only proves useful in the latter case for transmission systems with *equally* divided transceiver noise.

5.2.2.2 Unequal transmitter and receiver noise contributions

In this section the same optical transmission system as in the previous section is simulated but with 20% of the transceiver noise injected at the transmitter and 80% injected at the receiver ($\kappa_{\mathrm{R}} = 0.8$). Unequal contributions of transceiver noise (e.g. more transmitter as receiver noise) are more likely to be present in realistic transmission systems. The received SNR was evaluated at optimum launch power, as a function of distance and is shown in Fig. 5.10a). Further, a NLC split of $X = \lceil \frac{n}{2} \rceil$ and the optimum split X_{opt} obtained by taking the maximum of all possible splits $X \in [0, n]$ are shown. The absolute SNR, as well as the SNR gain, predictions of the model are in very good agreement with the simulation results. Fig. 5.10a) shows that optimum split NLC yields significant increase in reach with respect to DBP throughout all distances. For instance, in the TRX noise beating regime a reach gain of 56% is achieved (from 5 to 8 spans). This is in stark contrast to the case of equal division of transceiver noise in the previous section and confirms the theory presented in section 5.2.1. In the TRX noise beating regime the optimum NLC split is $X = n$ which is equivalent to the DPC case. As shown in Fig. 5.10a) DPC outperforms DBP up to approximately 30 spans where the amount of ASE noise beating becomes comparable to the amount of TRX noise beating. As the coherence factor is quite low ($\varepsilon = 0.108$), the simple Eq. (5.17) accurately predicts the reach gain, yielding a reach increase of 56% for this example. The DPC curve starts to approach the DBP curve with a residual gap as the TRX noise beating contribution is significant up to this point. Consequently, the optimum NLC split ratio at 120 spans is 56% with a gain of 1.34 dB in SNR with respect to DBP.

The split NLC gain with respect to DBP as a function of the NLC split ratio is shown in Fig. 5.10b) for 16, 34 and 120 spans. The gain of optimum split NLC

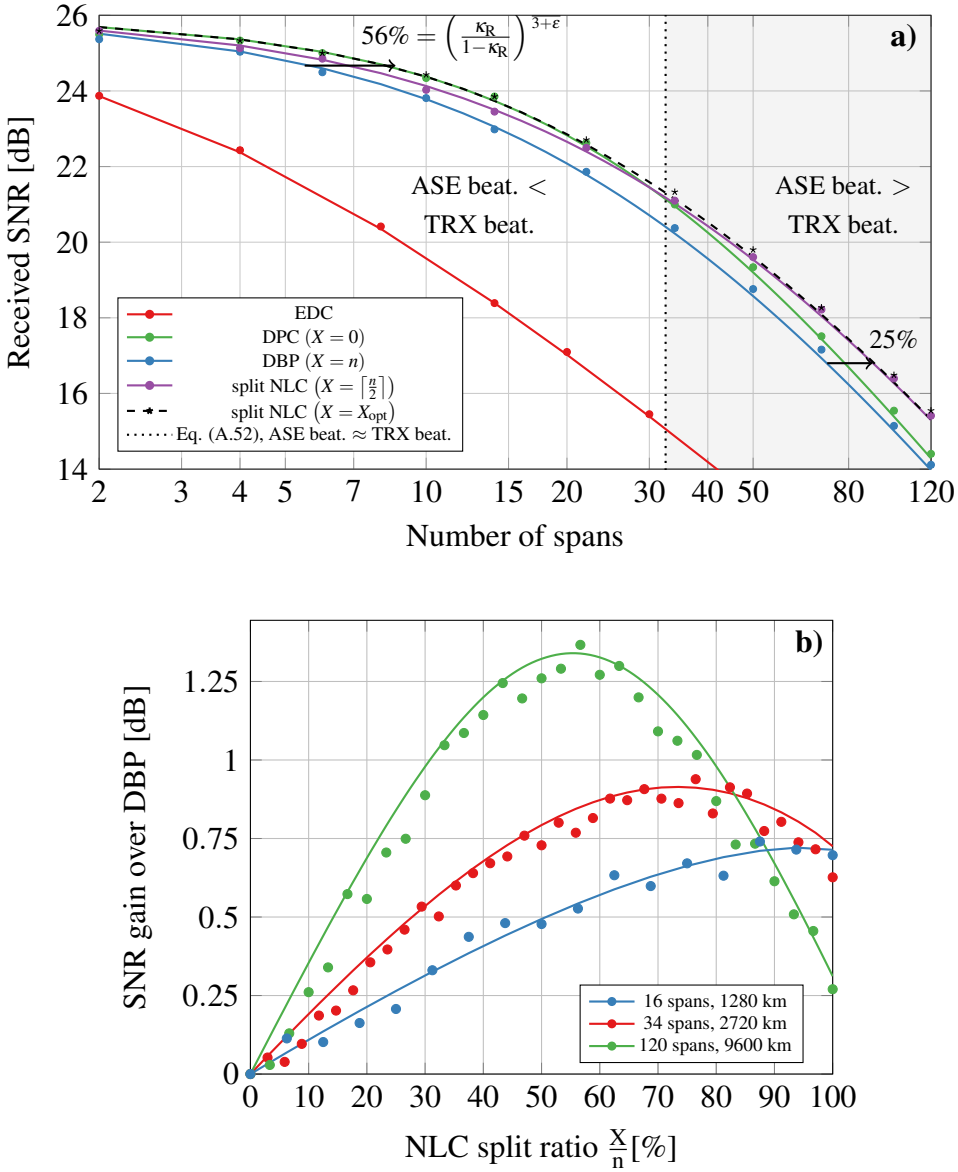

Figure 5.10: a) SNR at optimum launch power as a function of span number and the SNR as a function of NLC split ratio b) obtained by simulation (markers) and Eq. (5.8) (lines) for 256-QAM. The transceiver SNR is 26 dB and the transceiver noise is unequally divided between transmitter and receiver ($\kappa_R = 0.8$).

is 0.74 dB at 16 spans. As the ASE noise beating becomes more significant, the optimum split ratio slowly shifts from $X = n$ to $X = \lceil \frac{n}{2} \rceil$. At 34 spans, where the amount of ASE noise beating is approximately equal to the amount of TRX noise beating, the relative optimum NLC split ratio is 73%. For longer distances the ASE noise beating contribution becomes more dominant and the optimum NLC split ratio is with 54% close to $X = \lceil \frac{n}{2} \rceil$.

It might be surprising that the gain in reach decreases with transmission distance (e.g., from 56% at 5 spans to 25% at 70 spans) but this is accompanied by gain in SNR increases with distance (e.g., from 0.4 dB at 5 spans to 1.1 dB at 70 spans). Split NLC appears to yield higher SNR gains for longer distances and higher reach gains for shorter distances. This effect can be explained by the linear transceiver noise term κP in Eq. (5.8). Different received SNR values are affected differently by the linear transceiver noise contribution and as a result the SNR gains for short distances are not visible. Hence, the gain in SNR as a figure of merit may be a misleading quantity for comparing nonlinearity compensation techniques in systems that are impaired by transceiver noise. From that perspective, reach increase evaluated at the same received SNR is a fairer figure of merit, as the linear transceiver noise affects both distances equally.

5.3 Summary

For the first time, a formula for the SNR Eq. (5.8) has been proposed that accounts for the nonlinear interaction between signal and TRX noise. It was shown that those interactions, which has not been accounted for in the past, are significant in systems that deploy digital nonlinearity compensation. The theoretical model was validated by numerical and experimental results. Furthermore, enabled by the newly derived formula, new optimum nonlinearity compensation schemes were proposed, outperforming previous designs by around 25%. The analytical results can be used to estimate ultimate performance limits for nonlinearilty compensated, optical transmission systems. The key results from this chapter are:

- It is shown that the known interactions between the signal and co-propagating ASE noise are not sufficient for the accurate modelling of systems that perform digital nonlinearity compensation. However, it was shown through simulation and experiment, that interactions between the signal and transceiver noise are significant and cannot be neglected. Novel mathematical descriptions for the SNR are derived to include such interactions. On the contrary to previous publications, it was shown that those interactions are significant for transmission systems that deploy digital NLC. The results were validated by

numerical and experimental demonstrations. The work led to the publication of [P15].

- A new NLC scheme was proposed where the DBP and DPC algorithm is split between transmitter and receiver. Enabled by the new formula, formulas for the optimum split between transmitter and receiver and the expected gains are derived. It is shown that the optimum split depends on the transmission distance and the ratio of the transmitter and receiver noise. The scheme outperforms previously proposed designs that suggested an equal split between transmitter and receiver to be optimal. The new design outperforms previous designs by 25% in reach increase. The work led to the publication of [P9].

Chapter 6

Conclusions and future work

In this thesis, two main strategies to increase the capacity of single-mode optical fibre transmission systems were studied. These are to use the large low-loss transmission window by expanding the optical bandwidth and, second, increasing the channel SNR by means of digital signal processing to further increase the achieved throughput per channel. The main contributions of this thesis are the advanced mathematical models of nonlinear distortions arising in transmission. The proposed models can be used in order to design optimum system architectures, improve system operation and to quantify expected capacity gains for ultra-wideband transmission systems in the nonlinear regime.

First, the impact of inter-channel stimulated Raman scattering was studied in Chapter 3. This is important as ISRS is a significant physical impairment for optical bandwidths beyond the C-band and its understanding is key for the design of ultra-wideband transmission systems. In Chapter 3, the first analytical model was derived that enables to quantify the effect of ISRS on the nonlinear interference. The model was validated by experiments with an optical bandwidth of 9 THz, occupying the C+L band. A good agreement was found between the proposed model and the experimental results with an average deviation of 0.4 dB. The model was extended to account for strong ISRS power transfers and distributed Raman amplified systems, denoted as the ISRS GN model. The ISRS GN model was further extended to account for variably loaded spans, for accurate predictions in mesh optical network scenarios. The models were verified by extensive numerical simulations with negligible errors between split-step simulations and the ISRS GN model. The analytical model proposed in this Chapter are key for offline design nd the static optimisation of ultra-wideband transmission systems. It was shown that the model can be used to quantify the gains in total capacity that can be expected by extending the optical bandwidth beyond the C-band (5 THz). It was shown that, for 15 THz optical bandwidth, the impact of ISRS on the achievable information rate is around 40% using

a single modulation format across the optical spectrum and gain flattening filters at each span to prevent ISRS from accumulating along the transmission path. However, this degradation can be reduced to only 10% when adaptive modulation formats are used that are tailored to each channel within the optical signal. The results showed that ISRS does not present an insurmountable obstacle and that fourfold capacity gains can be achieved using the entire S+C+L band (20 THz) with respect to using the C-band only. Therefore, extending the optical bandwidth represents a viable option in order to cope with the ever increasing throughout demands.

However, the ISRS GN model, proposed in Chapter 3, is not suitable for real-time performance estimations or optimisation problems with very large sample spaces. This is because the results derived in Ch. 3 rely on numerical integrations that cannot be carried out in sub-second execution times. To overcome this limitation, closed-form solutions of the ISRS GN model were derived in Chapter 4, that do not require numerical integrations and, therefore, enable real-time performance estimates. The results represent the first closed-form formula capable of predicting the impact of ISRS on the NLI for arbitrary launch power distributions. The proposed closed-form formula was validated by numerical simulations showing a maximum deviation of 0.2 dB between simulations and the ISRS GN model in closed-form. Additionally, the formula was applied to transmission scenarios in mesh optical networks, showing its applicability and validity in physical layer aware network designs and optimisation. The formulas can, therefore, be used to derive novel RWA algorithms for ultra-wideband networks in the presence of ISRS. In Sec. 4.2.1, a formula for the modulation format correction was derived, extending the ISRS GN model in closed-form to accurately predict the NLI dependence on the transmitted modulation format. Deviations of 0.3 dB and 0.2 dB were found between the formula and 16-QAM transmission for high dispersive (SMF) and low dispersive (NZDSF) fibre systems, respectively. Finally in Sec. 4.3, a semi-analytical approach is proposed that enables the ISRS GN model in closed-form to be applied for optical bandwidths beyond 15 THz. A significant result that enables real-time optimisation for optical networks that utilise uniform or shaped QAM formats over S+C+L band systems and beyond.

After addressing the viability of bandwidth extension, the capacity limitation using digital pre-distortion and back-propagation was studied in Chapter 5. A new formula was derived to account for the nonlinear interactions between the signal and noise arising from the transceiver sub-system. Through analytical calculations, numerical simulations and experimental results, it was shown for the first time that these nonlinear interactions between transceiver noise and signal are performance limiting in systems that deploy digital nonlinearity compensation. The results chal-

lenge previous studies that suggested that interactions between the signal and co-propagating ASE noise are an ultimate performance limitation in such systems. The implications of the transceiver noise signal beating on C-band transmission systems were discussed, showing the impact of nonlinear TRX signal beating for multi channel NLC. In Sec. 5.2.1, an optimum digital nonlinearity compensation scheme was derived, enabled by the new formula. Contrary to suggestions in previous studies, it was shown that evenly splitting digital pre-distortion and back-propagation between the transceiver is not optimal. It was shown that the optimum split-ratio depends on the amount of noise that is introduced at the transmitter and the receiver and additionally on the transmission distance. Reach gains of around 25% could be achieved using the improved and optimal split ratio with respect to designs published in the literature. These results are significant in the prediction of fundamental capacity limitations of optical fibre systems that deploy nonlinearity compensation.

In overall conclusion, this thesis provides new mathematical models and fundamental contributions in the field of modelling nonlinear distortions in optical fibre systems. The results in this thesis enable the quantification of ultimate transmission performance of optical networks. More importantly, the proposed models pave the way to derive optimum system designs, optimisation strategies and advanced transceiver architectures for ultra-wideband optical networks in the nonlinear regime, key to further increasing the stunning capacity improvements of optical fibre systems, that underpin the unprecedented throughput demands of our modern societies.

6.1 Future work

The work presented in this thesis gives rise to additional research questions which are elaborated on below

- The new mathematical models proposed in Chapters 3 and 4 are capable of predicting the impact of inter-channel stimulated Raman scattering on the nonlinear distortions for single-mode fibres. However in multi-mode fibres, the signal propagates within different modes that are grouped into mode group traveling at different mode group velocities. To date, it is unclear whether a similar methodology can be applied to multi-mode fibres, where different amounts of ISRS occurs within and between propagating mode groups. Further investigations and potential extensions are required in order to apply the theory derived in the thesis to multi-mode fibres.

- In terms of the impact of ISRS on the nonlinear distortions, it was shown that through proper use of gain flattening filters and adaptive modulation formats, the impact of ISRS can be limited to a capacity degradation of around 10% for 15 THz optical bandwidth. However, further investigations must be carried out to explore additional techniques to mitigate the impact of ISRS, especially in the context of wavelength routing. Optical-phase conjugation (OPC) might be a potential candidate as OPC devices are able to invert the optical spectrum around its centre frequency. This might aid to balance the impact of ISRS on the overall spectrum as high frequency channels are swapped into low frequency channels after the OPC device. This could help to reduce the significant frequency dependence of the SNR that is imposed by ISRS and the received SNR exhibits a smaller tilt across the optical spectrum.

- In Chapter 4, closed-form approximations are proposed that are suitable for real-time performance estimates in ultra-wideband mesh optical networks. In Sec. 5.2.2, it is shown how ISRS alters the nonlinear distortions in a mesh optical network scenario. The work can be extended by including the derived formulas into network layer algorithms, such as routing and spectrum assignment (RWA). As ISRS imposes a significant frequency dependence on the received SNR, it is necessary to revise RWA algorithms to minimise the impact of ISRS in mesh optical networks.

- In Chapter 5, it was shown how nonlinear interactions between the signal and the transceiver noise are significant in systems, that deploy digital nonlinearity compensation. Based on the new derived model, a design was proposed that minimises these interactions, resulting in significant gains with respect

to previously proposed schemes. However, the design proposed in Sec. 5.2.1 is based on numerical simulations and analytical modelling. An experimental demonstration would not only further validate the derived theory, but also outperform experimentally shown NLC gains previously reported in the published literature.

Appendix A

Derivations

A.1 Derivation of Eq. (3.5)

In this section, Eq. (3.5) is derived for one span based on the nonlinear Schrödinger equation (NLSE) and a first-order regular perturbation approach (see Sec. 2.6). The derivation was peer-reviewed and published in [P8]. Instead of a constant attenuation coefficient α, as in the conventional GN model (2.44), a generic frequency and distance dependent gain coefficient $g(z,f)$ is used to model the effect of inter-channel stimulated Raman scattering. For the sake of brevity, only the key derivation steps are outlined.

We begin with the NLSE in the frequency domain, as in Eq. (2.6)

$$\frac{\partial}{\partial z}Q(z,f) = \widetilde{\Gamma}(z,f)Q(z,f) + j\gamma Q(z,f) * Q^*(z,-f) * Q(z,f), \tag{A.1}$$

with $\widetilde{\Gamma}(z,f) = \frac{g(z,f)}{2} + j2\pi^2\beta_2 f^2 + j\frac{4}{3}\pi^3\beta_3 f^3$ and $u(x) * v(x)$ denoting the convolution operation. The complex envelope of the electric field $Q(z,f)$ is expanded in a regular perturbation series with respect to the nonlinearity coefficient γ (see Sec. 2.6). The series is then truncated to first-order and we have

$$Q(z,f) = Q^{(0)}(z,f) + \gamma Q^{(1)}(z,f). \tag{A.2}$$

Inserting (A.2) in (2.7), we obtain

$$Q^{(0)}(z,f) = Q(0,f)\cdot e^{\Gamma(z,f)}, \tag{A.3}$$

with $\Gamma(z,f) = \int_0^z \widetilde{\Gamma}(\zeta,f)\,d\zeta$ as the solution for the zeroth-order terms and a linear

ordinary differential equation for the first-order terms as

$$\frac{\partial}{\partial z}Q^{(1)}(z,f) = \widetilde{\Gamma}(z,f)Q^{(1)}(z,f) + \tilde{Q}(z,f), \tag{A.4}$$

with $\tilde{Q}(z,f) = jQ^{(0)}(z,f) * Q^{(0)*}(z,-f) * Q^{(0)}(z,f)$. The initial condition for the first-order solution is $E^{(1)}(0,f) = 0$ and we obtain

$$E^{(1)}(z,f) = e^{\Gamma(z,f)} \int_0^z \frac{Q(\zeta,f)}{e^{\Gamma(\zeta,f)}} d\zeta, \tag{A.5}$$

as the solution of (A.4). The result is identical to Eq. (2.42). In order to compute $\tilde{Q}(z,f)$, we assume that the input signal can be modelled as a periodic Gaussian process as in Eq. (2.43). For notational convenience, we write nf_0 as f_n and $\sum_{n=\infty}^{\infty}$ as $\sum_{\forall n}$ for the remainder of this derivation. Using (2.43), $Q(z,f)$ can be written as

$$\begin{aligned}\tilde{Q}(z,f) = jf_0^{\frac{3}{2}} \sum_{\forall m}\sum_{\forall n}\sum_{\forall k} \sqrt{G_{\mathrm{Tx}}(f_m)G_{\mathrm{Tx}}(f_n)G_{\mathrm{Tx}}(f_k)} \\ \xi_m \xi_n^* \xi_k \delta\left(f - f_m + f_n - f_k\right) e^{\Gamma(z,f_m)+\Gamma^*(z,f_n)+\Gamma(z,f_k)}.\end{aligned} \tag{A.6}$$

To first order, it can be shown that only non-degenerate frequency triplets in (A.6) contribute to the nonlinear interference power. Degenerate frequency triplets merely introduce a constant phase shift of the first-order solution $Q^{(1)}(z,f)$, which cancels out when the PSD of $Q^{(1)}(z,f)$ is computed. For more details, the reader is referred to [116, Ch. IV.B and IV.D]. Therefore, we neglect degenerate frequency triplets in order to keep the derivation concise. Similar to [116], we define the triplets of non-degenerate frequency components as

$$A_i = \left\{(m,n,k) : [m-n+k] = i \,\text{and}\, [m \neq n \,\text{or}\, k \neq n]\right\}, \tag{A.7}$$

and rewrite (A.6) as

$$\begin{aligned}\tilde{Q}(z,f) = jf_0^{\frac{3}{2}} \sum_{\forall i} \delta\left(f - f_i\right) \sum_{\forall (m,n,k)\in A_i} \xi_m \xi_n^* \xi_k \\ \sqrt{G_{\mathrm{Tx}}(f_m)G_{\mathrm{Tx}}(f_n)G_{\mathrm{Tx}}(f_k)} e^{\Gamma(z,f_m)+\Gamma^*(z,f_n)+\Gamma(z,f_k)}.\end{aligned} \tag{A.8}$$

Inserting (A.8) in (A.5) yields the first-order solution as

$$\begin{aligned} Q^{(1)}(z,f) &= j f_0^{\frac{3}{2}} e^{\Gamma(z,f)} \sum_{\forall i} \delta\left(f-f_i\right) \\ &\sum_{\forall (m,n,k)\in A_i} \xi_m \xi_n^* \xi_k \sqrt{G_{\mathrm{Tx}}(f_m) G_{\mathrm{Tx}}(f_n) G_{\mathrm{Tx}}(f_k)} \\ &\int_0^z d\zeta \; e^{\Gamma(\zeta,f_m)+\Gamma^*(\zeta,f_n)+\Gamma(\zeta,f_k)-\Gamma(\zeta,f_m-f_n+f_k)}. \end{aligned} \tag{A.9}$$

In order to obtain the nonlinear interference power, we compute the average PSD of the first-order solution $\gamma Q^{(1)}(z,f)$. Similar to [116, Ch. IV.D], the average PSD of (A.9) multiplied by γ is

$$\begin{aligned} G_{\mathrm{NLI}}(z,f) &= 2\gamma^2 f_0^3 e^{2\mathrm{Re}[\Gamma(z,f)]} \sum_{\forall i} \delta\left(f-f_i\right) \\ &\sum_{\forall (m,n,k)\in A_i} G_{\mathrm{Tx}}(f_m) G_{\mathrm{Tx}}(f_n) G_{\mathrm{Tx}}(f_k) \\ &\left| \int_0^z d\zeta \; e^{\Gamma(\zeta,f_m)+\Gamma^*(\zeta,f_n)+\Gamma(\zeta,f_k)-\Gamma(\zeta,f_m-f_n+f_k)} \right|^2. \end{aligned} \tag{A.10}$$

In the following, we transform the inner summation appearing in (A.10) into a summation over two independent variables. For the non-degenerate set A_i, we have that $f_m - f_n + f_k = f_i$ and for a given frequency triplet (f_i, f_m, f_k) it follows that $f_n = f_m + f_k - f_i$. Therefore, (A.10) can be written as

$$\begin{aligned} G(z,f) &= 2\gamma^2 f_0^3 e^{2\mathrm{Re}[\Gamma(z,f)]} \sum_{\forall i} \delta\left(f-f_i\right) \\ &\sum_{\forall m} \sum_{\forall k} G_{\mathrm{Tx}}(f_m) G_{\mathrm{Tx}}(f_k) G_{\mathrm{Tx}}(f_m+f_k-f) \\ &\left| \int_0^z d\zeta \; e^{\Gamma(\zeta,f_m)+\Gamma^*(\zeta,f_m+f_k-f)+\Gamma(\zeta,f_k)-\Gamma(\zeta,f)} \right|^2. \end{aligned} \tag{A.11}$$

Finally, we define the normalised signal power profile of a frequency component as $\rho(z,f) = e^{\int_0^z g(\zeta,f)d\zeta}$ and rewrite (A.11) as an integral expression by letting $f_0 \to 0$

$$\begin{aligned} G(z,f) &= 2\gamma^2 \rho(z,f) \int df_1 \int df_2 \\ &G_{\mathrm{Tx}}(f_1) G_{\mathrm{Tx}}(f_2) G_{\mathrm{Tx}}(f_1+f_2-f) \\ &\left| \int_0^z d\zeta \sqrt{\frac{\rho(\zeta,f_1)\rho(\zeta,f_2)\rho(\zeta,f_1+f_2-f)}{\rho(\zeta,f)}} e^{j\phi(f_1,f_2,f,\zeta)} \right|^2. \end{aligned} \tag{A.12}$$

As (A.12) was derived for single polarization, $2\gamma^2$ must be replaced by $\frac{16}{27}\gamma^2$ to

obtain the nonlinear interference power for dual polarization. Furthermore, the term $\rho(z,f)$ outside of the integral can be removed when each frequency is amplified corresponding to its respective loss at the receiver. In practice, this can be realized with the use of adaptive gain flattening filters. The result is Eq. (3.5).

A.2 Derivation of Eq. (3.11)

This section includes details of the derivation of Eq. (3.11). Starting from the ISRS GN model as in Eq. (3.5) and inserting the normalised signal power profile of the

entire transmission distance (3.10) yields

$$
\begin{aligned}
G(f) &= \frac{16}{27}\gamma^2 \int df_1 \int df_2 \; G_{\mathrm{Tx}}(f_1) G_{\mathrm{Tx}}(f_2) G_{\mathrm{Tx}}(f_1+f_2-f) \\
&\Bigg| \int_0^{nL} d\zeta \; S_k(f_1,f_2,f)\, e^{j\phi(f_1,f_2,f,\zeta)} \\
&\cdot \sqrt{\frac{\sum_{k=1}^{n} G_k\left[\mathrm{mod}_L(z), f_1\right] \Pi\left(\frac{z-kL+\frac{1}{2}L}{L}\right)}{\sum_{k=1}^{n} G_k\left[\mathrm{mod}_L(z), f\right] \Pi\left(\frac{z-kL+\frac{1}{2}L}{L}\right)}} \\
&\cdot \sqrt{\sum_{k=1}^{n} G_k\left[\mathrm{mod}_L(z), f_2\right] \Pi\left(\frac{z-kL+\frac{1}{2}L}{L}\right)} \\
&\cdot \sqrt{\sum_{k=1}^{n} G_k\left[\mathrm{mod}_L(z), f_1+f_2-f\right] \Pi\left(\frac{z-kL+\frac{1}{2}L}{L}\right)} \Bigg|^2 \\
&= \frac{16}{27}\gamma^2 \int df_1 \int df_2 \; G_{\mathrm{Tx}}(f_1) G_{\mathrm{Tx}}(f_2) G_{\mathrm{Tx}}(f_1+f_2-f) \\
&\Bigg| \sum_{k=1}^{n} \int_{(k-1)L}^{kL} d\zeta \; \frac{1}{S_1(f_1,f_2,f)} e^{j\phi(f_1,f_2,f,\zeta)} \\
&\cdot \sqrt{\frac{\sum_{k=1}^{n} G_k\left[\mathrm{mod}_L(z), f_1\right] \Pi\left(\frac{z-kL+\frac{1}{2}L}{L}\right)}{\sum_{k=1}^{n} G_k\left[\mathrm{mod}_L(z), f\right] \Pi\left(\frac{z-kL+\frac{1}{2}L}{L}\right)}} \\
&\cdot \sqrt{\sum_{k=1}^{n} G_k\left[\mathrm{mod}_L(z), f_2\right] \Pi\left(\frac{z-kL+\frac{1}{2}L}{L}\right)} \\
&\cdot \sqrt{\sum_{k=1}^{n} G_k\left[\mathrm{mod}_L(z), f_1+f_2-f\right] \Pi\left(\frac{z-kL+\frac{1}{2}L}{L}\right)} \Bigg|^2 \\
&= \frac{16}{27}\gamma^2 \int df_1 \int df_2 \; G_1(f) \\
&\left| \sum_{k=1}^{n} \int_0^{L} d\zeta \; S_k(f_1,f_2,f) \frac{P_{\mathrm{tot},k} e^{-\alpha z - P_{\mathrm{tot},k} C_{\mathrm{r}} L_{\mathrm{eff}}(f_1+f_2-f)}}{\int G_k(\nu) e^{-P_{\mathrm{tot},k} C_{\mathrm{r}} L_{\mathrm{eff}} \nu} d\nu} e^{j\phi\left(f_1,f_2,f,\zeta+\tilde{L}_k\right)} \right|^2,
\end{aligned}
\tag{A.13}
$$

with $S_k(f_1,f_2,f) = \sqrt{\frac{G_k(f_1)G_k(f_2)G_k(f_1+f_2-f)}{G_k(f)}}$ and $\tilde{L}_k = \sum_1^{k-1} L_k$. The result in Eq. (A.13) resembles the ISRS GN model extended for variably loaded spans, as in Eq. (3.11).

A.3 Derivation of the ISRS GN model in closed-form

A.3.1 Derivation of the XPM contribution Eq. (4.9)

In this section, the closed-form approximation of the XPM contribution (4.9) is derived. The derivation was peer-reviewed and published in [P6]. The derivation consists of finding an analytical approximation of the integral form Eq. (4.6) which models the nonlinear interference caused on channel i by a single interfering channel k.

For notational brevity, we define $x(\zeta) = P_{\text{tot}} C_{\text{r}} \bar{L}_{\text{eff}}(\zeta)$ with $\bar{L}_{\text{eff}}(\zeta) = \frac{1-e^{-\bar{\alpha}\zeta}}{\bar{\alpha}}$. To increase the potential parameter space and enable regression approaches, a separate effective length $\bar{L}_{\text{eff}}$ is kept in the ISRS term. This allows for a more general application of the proposed formula e.g. for the application for optical bandwidths beyond 15 THz (see Sec. 4.3). Additionally, a pre-factor of $\frac{32}{27}\frac{\gamma^2}{B_k^2}\left(\frac{P_k}{P_i}\right)^2$ is suppressed throughout the derivation. For the ISRS term, the optical power is assumed to be uniformly distributed over the transmitted bandwidth yielding $\int \frac{1}{P_{\text{tot}}} G_{\text{Tx}}(\nu) e^{-x\cdot\nu} d\nu = \frac{xB_{\text{tot}}}{2\sinh\left(\frac{xB_{\text{tot}}}{2}\right)}$. Eq. (4.6) is then written as

$$
\begin{aligned}
\eta_{\text{XPM}}^{(k)}(f_i) &= \int_{-\frac{B_i}{2}}^{\frac{B_i}{2}} df_1 \int_{-\frac{B_k}{2}}^{\frac{B_k}{2}} df_2 \, \Pi\left(\frac{f_1+f_2}{B_k}\right) B_{\text{tot}} \\
&\cdot \left| \int_0^L d\zeta \, \frac{x e^{-\alpha\zeta - x\cdot(f_1+f_2+f_i+\Delta f)}}{2\sinh\left(\frac{xB_{\text{tot}}}{2}\right)} e^{j\phi(f_1+f_i, f_2+f_i+\Delta f, f_i, \zeta)} \right|^2 \\
&\approx \int_{-\frac{B_i}{2}}^{\frac{B_i}{2}} df_1 \int_{-\frac{B_k}{2}}^{\frac{B_k}{2}} df_2 \left| \int_0^L d\zeta \, \frac{xB_{\text{tot}} e^{-\alpha\zeta - x\cdot(f_1+f_i+\Delta f)}}{2\sinh\left(\frac{xB_{\text{tot}}}{2}\right)} \right. \\
&\left. \cdot \, e^{j\phi(f_1+f_i, f_i+\Delta f, f_i, \zeta)} \right|^2 \\
&= 2B_k \int_0^{\frac{B_i}{2}} df_1 \left| \int_0^L d\zeta \, \frac{xB_{\text{tot}} e^{-\alpha\zeta - x\cdot(f_1+f_i+\Delta f)}}{2\sinh\left(\frac{xB_{\text{tot}}}{2}\right)} \right. \\
&\left. \cdot e^{j\phi(f_1+f_i, f_i+\Delta f, f_i, \zeta)} \right|^2,
\end{aligned}
\tag{A.14}
$$

where $\Delta f = f_k - f_i$ is the (centre) frequency separation between channel k and i. In Eq. (A.14), it is assumed that the frequency separation is much larger than half of the bandwidth of channel k (i.e. $|\Delta f| \gg \frac{B_k}{2}$). This assumption allows to approximate $f_2 + \Delta f \approx \Delta f$ and has only a minor accuracy impact on the phase mismatch term ϕ for channels that are close to the COI as addressed in detail in Appendix A.3.3. It has negligible impact on the ISRS term (the signal power profile) and the dispersion slope as both are essentially constant over one channel bandwidth B_k. Additionally, the term $\Pi\left(\frac{f_1+f_2}{B_k}\right)$ was neglected in Eq. (A.14).

For the phase mismatch factor ϕ, we obtain

$$\begin{aligned}
&\phi\left(f_1+f_i,f_i+\Delta f,f_i,\zeta\right)\\
&=-4\pi^2 f_1\Delta f\left[\beta_2+\pi\beta_3(f_1+2f_i+\Delta f)\right]\zeta\\
&\approx-4\pi^2 f_1\Delta f\left[\beta_2+\pi\beta_3(2f_i+\Delta f)\right]\zeta\\
&=-4\pi^2 f_1\left(f_k-f_i\right)\left[\beta_2+\pi\beta_3(f_i+f_k\right]\zeta\\
&=\phi_{i,k}f_1\zeta,
\end{aligned}\tag{A.15}$$

with $\phi_{i,k}=-4\pi^2\left(f_k-f_i\right)\left[\beta_2+\pi\beta_3(f_i+f_k\right]$ and where it was assumed that the impact of the dispersion slope is constant over one channel bandwidth B_i. Eq. (A.15) shows that the XPM assumption and a slowly varying group velocity dispersion, essentially leads to a modification rule of the GVD parameter β_2 to account for the dispersion slope.

In order to simplify Eq. (A.14), the ISRS term is expanded into a Taylor series and truncated to first-order, assuming weak ISRS. The validity range of this approximation is analysed in Appendix A.3.4. Additionally, it is assumed that the signal power profile is constant over one channel bandwidth B_i, mathematically $e^{-x\cdot(f_1+f_i+\Delta f)}\approx e^{-x\cdot(f_i+\Delta f)}=e^{-x\cdot f_k}$. The Taylor expansion of the ISRS term is then given by

$$\frac{B_{\text{tot}}xe^{-x\cdot f_k}}{2\sinh\left(\frac{B_{\text{tot}}}{2}x\right)}=1-f_kx+\mathcal{O}(x^2),\tag{A.16}$$

and the signal power profile (to first-order) as

$$\frac{B_{\text{tot}}xe^{-\alpha\zeta-x\cdot f_k}}{2\sinh\left(\frac{B_{\text{tot}}}{2}x\right)}\approx\left(1+\tilde{T}_k\right)e^{-\alpha\zeta}-\tilde{T}_ke^{-A\zeta},\tag{A.17}$$

with $\tilde{T}_k=-\frac{P_{\text{tot}}C_{\text{r}}}{\bar{\alpha}}f_k$ and $A=\alpha+\bar{\alpha}$. Enabled by the first-order assumption of ISRS,

the following simplification is obtained

$$\begin{aligned}
&\left| \int_0^L d\zeta \, \frac{B_{\text{tot}} x e^{-\alpha\zeta - x\cdot f_k}}{2\sinh\left(\frac{B_{\text{tot}}}{2}x\right)} e^{j\phi_{i,k} f_1 \zeta} \right|^2 \\
&\approx \left| \int_0^L d\zeta \, \left[\left(1+\tilde{T}_k\right) e^{-\alpha\zeta} - \tilde{T}_k e^{-A\zeta} \right] e^{j\phi_{i,k} f_1 \zeta} \right|^2 \\
&\approx \left| -\frac{1+\tilde{T}_k}{-\alpha + j\phi_{i,k} f_1} + \frac{\tilde{T}_k}{-A + j\phi_{i,k} f_1} \right|^2 \\
&= \frac{T_k + \phi_{i,k}^2 f_1^2}{\alpha A^2 + \left(2\alpha A + \bar{\alpha}^2\right)\phi_{i,k}^2 f_1^2 + \phi_{i,k}^4 f_1^4},
\end{aligned} \tag{A.18}$$

where $T_k = \left(\alpha + \bar{\alpha} - P_{\text{tot}} C_{\text{r}} f_k\right)^2$ and it was assumed that $e^{-\alpha L} \ll 1$. Substituting the simplification Eq. (A.18) in Eq. (A.14) and using the exact integral identities (A.38) and (A.39) yields

$$\begin{aligned}
&2B_k \int_0^{\frac{B_i}{2}} df_1 \left| \int_0^L d\zeta \, \frac{x B_{\text{tot}} e^{-\alpha\zeta - x\cdot f_k}}{2\sinh\left(\frac{x B_{\text{tot}}}{2}\right)} e^{j\phi_{i,k} f_1 \zeta} \right|^2 \\
&\approx \frac{2B_k}{\phi_{i,k}\bar{\alpha}\left(2\alpha + \bar{\alpha}\right)} \cdot \left[\frac{T_k - \alpha^2}{\alpha} \operatorname{atan}\left(\frac{\phi_{i,k} B_i}{2\alpha}\right) \right. \\
&\left. + \frac{A^2 - T_k}{A} \operatorname{atan}\left(\frac{\phi_{i,k} B_i}{2A}\right) \right].
\end{aligned} \tag{A.19}$$

In order to obtain the XPM contribution of channel k on channel i, the suppressed pre-factor $\frac{32}{27}\frac{\gamma^2}{B_k^2}\left(\frac{P_k}{P_i}\right)^2$ must be included. Finally, $\phi_{i,k}$ is redefined and the individual XPM contributions $\eta_{\text{XPM}}^{(k)}(f_i)$ are summed up in order to obtain the total XPM contribution $\eta_{\text{XPM}}(f_i)$ as in Eq. (4.9).

A.3.2 Derivation of the SPM contribution Eq. (4.8)

In this section, the closed-form SPM contribution of the NLI Eq. (4.8) is derived. The derivation was peer-reviewed and published in [P6]. The derivation consists of finding an analytical approximation of the integral expression Eq. (4.6) which models the nonlinear interference caused by channel i on itself. The reader is reminded that, for the SPM contribution, a factor of $\frac{1}{2}$ must be multiplied to (4.6). For notational brevity, we define $x(\zeta) = P_{\text{tot}} C_{\text{r}} \bar{L}_{\text{eff}}(\zeta)$ with $\bar{L}_{\text{eff}}(\zeta) = \frac{1-e^{-\bar{\alpha}\zeta}}{\bar{\alpha}}$ and a pre-factor of $\frac{16}{27}\frac{\gamma^2}{B_i^2}$ is suppressed throughout the derivation.

The NLI coefficient of the SPM contribution is then written as

$$\begin{aligned}\eta_{\mathrm{SPM}}(f_i) &\approx \int_{-\frac{B_i}{2}}^{\frac{B_i}{2}} df_1 \int_{-\frac{B_i}{2}}^{\frac{B_i}{2}} df_2 \\ &\cdot \left| \int_0^L d\zeta \, \frac{xB_{\mathrm{tot}} e^{-\alpha\zeta - xf_i}}{2\sinh\left(\frac{xB_{\mathrm{tot}}}{2}\right)} e^{j\phi(f_1+f_i, f_2+f_i, f_i, \zeta)} \right|^2 \\ &\approx \int_{-\frac{B_i}{2}}^{\frac{B_i}{2}} df_1 \int_{-\frac{B_i}{2}}^{\frac{B_i}{2}} df_2 \frac{T_i + \phi_i^2 f_1^2 f_2^2}{\alpha A^2 + (2\alpha A + \bar{\alpha}^2)\,\phi_i^2 f_1^2 f_2^2 + \phi_i^4 f_1^4 f_2^2},\end{aligned} \tag{A.20}$$

with $\phi_i = -4\pi^2(\beta_2 + 2\pi\beta_3 f_i)$ and where the first-order description of ISRS was used and it was assumed that the signal power profile and the dispersion slope are constant over one channel bandwidth B_i (see Appendix A.3.1).

Eq. (A.20) can be solved exactly in terms of elementary functions over a closed circular integration domain. The radius of the circular domain is chosen such that its area equals that of the actual integration domain, as proposed in [118]. The actual integration domain and its approximated circular domain are shown as insets in Fig. 4.3. Exploiting the circular domain approximation, Eq. (A.3.1) is recast in polar coordinates and solved using the integral identities (A.40) and (A.41) as

$$\begin{aligned}\eta_{\mathrm{SPM}}(f_i) &\approx 4 \int_0^{\sqrt{\frac{3}{\pi}}\frac{B_i}{2}} dr \int_0^{\frac{\pi}{2}} d\phi \\ &\frac{r T_i + \frac{\phi_i^2}{4} r^5 \sin^2(\phi)}{\alpha A^2 + \frac{\phi_i^2}{4}(2\alpha A + \bar{\alpha}^2) r^4 \sin^2(\phi) + \frac{\phi_i^4}{16} r^8 \sin^4(\phi)} \\ &= \int_0^{\sqrt{\frac{3}{\pi}}\frac{B_i}{2}} dr \, \frac{4\pi}{\bar{\alpha}(2\alpha + \bar{\alpha})} \\ &\cdot \left(\frac{T_i - \alpha^2}{\alpha^2} \frac{r}{\sqrt{1 + \frac{\phi_i^2}{4\alpha^2} r^4}} + \frac{A^2 - T_i}{A^2} \frac{r}{\sqrt{1 + \frac{\phi_i^2}{4A^2} r^4}} \right) \\ &= \frac{2\pi}{\phi_i \bar{\alpha}(2\alpha + \bar{\alpha})} \\ &\cdot \left[\frac{T_i - \alpha^2}{a} \operatorname{asinh}\left(\frac{3\phi_i B_i^2}{8\pi a} \right) + \frac{A^2 - T_i}{A} \operatorname{asinh}\left(\frac{3\phi_i B_i^2}{8\pi A} \right) \right]\end{aligned} \tag{A.21}$$

In order to obtain the SPM contribution, the suppressed pre-factor $\frac{16}{27}\frac{\gamma^2}{B_i^2}$ must be included and ϕ_i is redefined in order to the final result Eq. (4.8).

A.3.3 Addressing assumption 1) in Sec. 4.1.4

In this section, the assumption 1) in Section 4.1.4 is addressed in more detail. The derivation was peer-reviewed and published in [P6]. Assumption 1) states that the channel separation between COI and INT has to be much greater than half of the channel bandwidth $|\Delta f| \gg \frac{B_k}{2}$. To mathematically quantify the impact of the assumption, we start with the XPM contribution as in Eq. (4.6). For simplification, ISRS is neglected and $\tilde{\phi}_{i,k} = -4\pi^2 [\beta_2 + \pi\beta_3(f_i + f_k]$ similar to Appendix A.3.1. For notational brevity, the pre-factor $\frac{32}{27}\frac{\gamma^2}{B_k^2}\left(\frac{P_k}{P_i}\right)^2$ is not shown, as it does not alter the analysis in this section. The NLI coefficient is then given as

$$\tilde{\eta}_{\mathrm{XPM}}^{(k)}(f_i) = \int_0^{\frac{B_i}{2}} df_1 \int_{-\frac{B_k}{2\Delta f}}^{\frac{B_k}{2\Delta f}} df_2 \frac{2\Delta f}{\alpha^2} \frac{1}{1+\tilde{\mu} f_1^2 (f_2+1)^2}, \tag{A.22}$$

with $\tilde{\mu} = \frac{\tilde{\phi}_{i,k}^2 \Delta f^2}{\alpha^2}$ and where it was assumed that $e^{-\alpha L} \ll 1$ and $\Pi\left(\frac{f_1+f_2}{B_k}\right)$ was neglected as in Appendix A.3.1.

As the channel spacing is at least $\Delta f > \frac{B_k}{2}$, the inner integration variable in Eq. (A.22) varies as $f_2 \in [-1,1]$. Therefore, the integrand in Eq. (A.22) is expanded into a converging Taylor series and truncated after second-order

$$\int_{-\frac{B_k}{2\Delta f}}^{\frac{B_k}{2\Delta f}} df_2 \frac{2\Delta f}{1+\tilde{\mu} f_1^2 (f_2+1)^2} \approx \underbrace{\frac{2B_k}{\tilde{\mu} f_1^2 + 1}}_{\text{zeroth-order}} + \underbrace{\frac{\tilde{\mu} f_1^2 \left(3\tilde{\mu} f_1^2 - 1\right) B_k^2}{6\Delta f^2 \left(\tilde{\mu} f_1^2 + 1\right)^3}}_{\text{second-order}}, \tag{A.23}$$

where the first-order term yields zero after integration. Mathematically, the assumption $|f_k - f_i| = |\Delta f| \gg \frac{B_k}{2}$ (or simply $f_2 = 0$) in 4.1.4 *coincides* with the zeroth-order approximation of the integral over the variable f_2. The relative error can be therefore obtained by analysing the higher-order terms. Inserting the Taylor approximation Eq. (A.23) in Eq. (A.22) and solving the integrals using Eq. (A.42) and Eq. (A.43) yields

$$\tilde{\eta}_{\mathrm{XPM}}^{(k)}(f_i) \approx \frac{B_k B_i}{\alpha^2 \mu} \cdot \left\{ \underbrace{\operatorname{atan}(\mu)}_{\text{zeroth-order}} + \underbrace{\frac{B_k^2}{12\Delta f^2}\left[\operatorname{atan}(\mu) - \frac{\mu\left(2\mu^2+1\right)}{\left(\mu^2+1\right)^2}\right]}_{\text{second-order}} \right\}, \tag{A.24}$$

with $\mu = \frac{|\tilde{\phi}_{i,k}||\Delta f|B_i}{2\alpha}$. The zeroth-order term in Eq. (A.24) is identical to the proposed closed-form (A.3.2) in the absence of ISRS. Finally, the relative error, caused by Assumption 1) in Section 4.1.4 is obtained by normalising the second-order term by the zeroth-order term. Therefore, the relative error is given by

$$\text{Rel. Err.} = \frac{1}{12}\frac{B_k^2}{\Delta f^2}\left[1 - \frac{\mu\left(2\mu^2+1\right)}{\left(\mu^2+1\right)^2 \operatorname{atan}(\mu)}\right] < \frac{1}{12}\frac{B_k^2}{\Delta f^2}. \tag{A.25}$$

Eq. (A.25) can be reliable used to quantify the approximation error caused by Assumption 1).

A.3.4 Derivation of the validity range

In order to derive a validity range of the weak ISRS assumption, the ISRS term to first-order is compared to the ISRS term to second-order at a frequency component f_k. The first-order approximation is then valid when the second-order term is negligible. The derivation was peer-reviewed and published in [P6]. The second coefficient of the Taylor series, as in Eq. (A.16), is given by

$$\tilde{T}_k^{(2)} = \frac{f_k^2}{2} - \frac{B^2}{24}. \tag{A.26}$$

Requiring that the second-order term is negligible to the first-order approximation yields

$$|f_k x| \gg \left|\tilde{T}_k^{(2)} x^2\right| = \left|\frac{f_k^2}{2} - \frac{B_{\text{tot}}^2}{24}\right| x^2. \tag{A.27}$$

The channel that is most impacted by ISRS is the channel with center frequency $f_k = \frac{B}{2}$ for which we will evaluate Eq. (A.27) and obtain

$$B_{\text{tot}} P_{\text{tot}} L_{\text{eff}} C_r = 0.23 \cdot \Delta\rho\,(L)\,[\text{dB}] \ll 6, \tag{A.28}$$

where $\Delta\rho\,(L)\,[\text{dB}]$ is the ISRS power transfer between the outer channels of the transmitted signals as in Eq. (3.8).

A.4 Derivation of modulation format correction

A.4.1 Derivation of Eq. (4.16)

This section presents the key steps in the derivation of Eq. (4.16). The derivation was peer-reviewed and published in [P4]. For the sake of brevity, the derivation is carried out for the *integrand* of (4.16). Starting from the integrand in (4.15) and

assuming that $f_2+\Delta f \approx \Delta f$ for the link function μ, we have that

$$\begin{aligned}
&\left|\int_{-\frac{B_k}{2}}^{\frac{B_k}{2}} \mu\left(f_1+f_i, f_2+f_i+\Delta f, f_i\right) \sum_{m=0}^{n-1} e^{jmf_1(f_2+\Delta f)\phi} df_2\right|^2 \\
&\approx \left|\mu\left(f_1+f_i, f_k, f_i\right) \int_{-\frac{B_k}{2}}^{\frac{B_k}{2}} \sum_{m=0}^{n-1} e^{jmf_1(f_2+\Delta f)\phi} df_2\right|^2 \\
&= \left|\mu\left(f_1+f_i, f_k, f_i\right)\right|^2 \\
&\cdot \left|B_k + \sum_{m=1}^{n-1} e^{jmf_1\Delta f\phi} \int_{-\frac{B_k}{2}}^{\frac{B_k}{2}} e^{jmf_1f_2\phi} df_2\right|^2 \\
&= B_k^2 \left|\mu\left(f_1+f_i, f_k, f_i\right)\right|^2 \\
&\cdot \left|1 + \sum_{m=1}^{n-1} \frac{e^{jmf_1\Delta f\phi}}{jmf_1\phi B_k} \left(e^{jmf_1\frac{B_k}{2}\phi} - e^{-jmf_1\frac{B_k}{2}\phi}\right)\right|^2 \\
&= B_k^2 \left|\mu\left(f_1+f_i, f_k, f_i\right)\right|^2 \\
&\cdot \left|1 + \sum_{m=1}^{n-1} \operatorname{sinc}\left(mf_1\frac{B_k}{2}\phi\right) e^{jmf_1\Delta f\phi}\right|^2 .
\end{aligned} \tag{A.29}$$

Eq. (A.29) is then used in order to derive (4.16).

A.4.2 Identity used to derive Eq. (4.23)

In this section, an identity for $\lim_{n\to\infty}\Delta_n C_n$ is derived in order to obtain a closed-form formula for the asymptotic modulation format correction contribution Eq. (4.21). The asymptotic differential normalisation coefficient can be calculated exactly and no approximations are needed. The derivation was peer-reviewed and published in [P4].

For notational brevity, the identity is derived for arbitrary parameters a and b which reads

$$\begin{aligned}
C_\infty^{'} &= \lim_{n\to\infty} \Delta_n \int_{-\infty}^{\infty} dx \left|\sum_{m=1}^{n} \operatorname{sinc}\left(max\right) e^{jmbx}\right|^2 \\
&= \frac{\pi}{a^2}\left[(b-a)\ln\left(\frac{b-a}{a+b}\right) + 2a\right].
\end{aligned} \tag{A.30}$$

We start proving Eq. (A.30) by executing the backward differential operator with respect to the span number. For this purpose, the identity

$$\Delta_n \left(\sum_{m=1}^{n} f(m)\right)^2 = f^2(n) + 2\sum_{m=1}^{n-1} f(n) f(m), \tag{A.31}$$

is used, which can be easily proven by induction. In the context of Eq. (A.30), we have that $\lim_{n\to\infty} f^2(n) = 0$ and $n-1 \approx n$ due to large n. We can therefore solve the discrete derivative as

$$\begin{aligned}
C_\infty^{'} &= \lim_{n\to\infty} \Delta_n \int_{-\infty}^{\infty} dx \left| \sum_{m=1}^{n} \operatorname{sinc}(max)\, e^{jmbx} \right|^2 \\
&= \lim_{n\to\infty} \int_{-\infty}^{\infty} dx \frac{1}{2a^2 n x^2} \sum_{m=1}^{n} \frac{1}{m} \{ \\
&\quad [\sin(mc_2x) + \sin(mc_1x)]\,[\sin(nc_2x) + \sin(nc_1x)] \\
&\quad + [\cos(mc_2x) - \cos(mc_1x)]\,[\cos(nc_2x) - \cos(nc_1x)]\} \\
&= \lim_{n\to\infty} \int_{-\infty}^{\infty} dx \frac{1}{2a^2 n x^2} \sum_{m=1}^{n} \frac{1}{m} \{ \\
&\quad [\sin(mc_2x) + \sin(mc_1x)]\,[\sin(nc_2x) + \sin(nc_1x)] \\
&\quad + [\sin(mbx + nc_1x) + \sin(mbx - nc_1x)] \\
&\quad \cdot [\sin(max) - \sin(max)]\,\},
\end{aligned} \tag{A.32}$$

with $c_1 = a+b$ and $c_2 = a-b$, which are defined for the sake of a concise notation. The last step in Eq. (A.32) was obtained using trigonometric identities. Using the exact integral solution $\int_{-\infty}^{\infty} dx \frac{\sin(ax)\sin(bx)}{x^2} = \frac{\pi}{2}(|a+b| - |a-b|)$ yields

$$\begin{aligned}
C_\infty^{'} = \lim_{n\to\infty} \frac{\pi}{2a^2 n} \sum_{m=1}^{n} \frac{1}{m} \{ \\
- |mc_2 - nc_2| + |mc_1 + nc_2| + |mc_2 + nc_1| - |mc_1 - nc_1|\}.
\end{aligned} \tag{A.33}$$

To resolve the absolute value operations in Eq. (A.33), we identify that $b \geq 0$, $a \geq 0$ and $b \geq a$, resulting in $c_1 \geq 0$ and $c_2 \leq 0$. The conditions are met by default as the minimum feasible channel spacing is $\Delta f \geq \frac{B_k}{2}$ and the result is invariant to the sign of b. Applying the conditions results in

$$\begin{aligned}
C_\infty^{'} = \lim_{n\to\infty} \frac{\pi}{2a^2 n} \sum_{m=1}^{n} \frac{1}{m} \\
\{b(m-n) + (n+m)a + |mc_1 - n|c_2||\}.
\end{aligned} \tag{A.34}$$

Eq. (A.34) can be written as two distinct series, which are solved separately in the

following. The first series is exactly written and solved as

$$\begin{aligned}&\lim_{n\to\infty}\frac{\pi}{2a^2n}\sum_{m=1}^{n}\frac{1}{m}\left\{b\left(m-n\right)+\left(n+m\right)a\right\}\\&=\lim_{n\to\infty}\left[\frac{\pi}{2a^2}c_1-\left|c_2\right|\mathrm{Har}\left(n\right)\right],\end{aligned}\tag{A.35}$$

with $\mathrm{Har}\left(n\right)$ being the n'th harmonic number. The second series can be written and exactly solved as

$$\begin{aligned}&\lim_{n\to\infty}\frac{\pi}{2a^2n}\sum_{m=1}^{n}\frac{1}{m}\left|mc_1-n\left|c_2\right|\right|\\&=\lim_{n\to\infty}\frac{\pi}{2a^2}\left(\sum_{m=1}^{\left\lfloor\frac{n\left|c_2\right|}{c_1}\right\rfloor}\frac{\left|c_2\right|}{m}-\frac{c_1}{n}+\sum_{m=\left\lceil\frac{n\left|c_2\right|}{c_1}\right\rceil}^{n}\frac{c_1}{n}-\frac{\left|c_2\right|}{m}\right)\\&=\lim_{n\to\infty}\frac{\pi}{2a^2}\left\{\left|c_2\right|\mathrm{Har}\left(\left\lfloor\frac{n\left|c_2\right|}{c_1}\right\rfloor\right)-\left|c_2\right|\mathrm{Har}\left(n\right)\right.\\&\left.+\left|c_2\right|\mathrm{Har}\left(\left\lceil\frac{n\left|c_2\right|}{c_1}\right\rceil\right)+\frac{c_1}{n}\left(n-\left\lceil\frac{n\left|c_2\right|}{c_1}\right\rceil-\left\lfloor\frac{n\left|c_2\right|}{c_1}\right\rfloor\right)\right\}\\&=\lim_{n\to\infty}\frac{\pi}{2a^2}\left[2\left|c_2\right|\mathrm{Har}\left(\frac{n\left|c_2\right|}{c_1}\right)-\left|c_2\right|\mathrm{Har}\left(n\right)+c_1-2\left|c_2\right|\right],\end{aligned}\tag{A.36}$$

where it was used that $\lim_{n\to\infty}\left\lceil\frac{nc_2}{c_1}\right\rceil=\lim_{n\to\infty}\left\lfloor\frac{nc_2}{c_1}\right\rfloor=\lim_{n\to\infty}\frac{nc_2}{c_1}$. Both series can be further simplified by recalling that $\lim_{n\to\infty}\mathrm{Har}\left(n\right)=\lim_{n\to\infty}\log\left(n\right)+\gamma$, with γ being the Euler-Mascheroni constant.

Combining Eq. (A.35) and Eq. (A.36) yields the final result

$$\begin{aligned}C_\infty'&=\lim_{n\to\infty}\frac{\pi}{a^2}\left\{\left|c_2\right|\mathrm{Har}\left(\frac{n\left|c_2\right|}{c_1}\right)-\left|c_2\right|\mathrm{Har}\left(n\right)+2a\right\}\\&=\frac{\pi}{a^2}\left[\left|c_2\right|\ln\left(\frac{\left|c_2\right|}{c_1}\right)+2a\right]\\&=\frac{\pi}{a^2}\left[\left(b-a\right)\ln\left(\frac{b-a}{a+b}\right)+2a\right],\end{aligned}\tag{A.37}$$

which proves the identity in Eq. (A.30). Therefore, Eq. (A.30) can be used to write Eq. (4.21) in closed-form as Eq. (4.23), without imposing any additional assumptions.

A.4.3 Integral identities

This section contains the integral identities that were used in order to derive the proposed closed-form expressions in Sec. 4.1.

$$\begin{aligned}&\int_0^X dx\,\frac{1}{a+bx^2+x^4}\\&=\frac{\sqrt{2}}{c\sqrt{b-c}}\operatorname{atan}\left(\frac{\sqrt{2}X}{\sqrt{b-c}}\right)-\frac{\sqrt{2}}{C\sqrt{b+c}}\operatorname{atan}\left(\frac{\sqrt{2}X}{\sqrt{b+c}}\right),\end{aligned}\tag{A.38}$$

$$\begin{aligned}&\int_0^X dx\,\frac{x^2}{a+bx^2+x^4}\\&=\frac{\sqrt{b+c}}{\sqrt{2}c}\operatorname{atan}\left(\frac{\sqrt{2}X}{\sqrt{b+c}}\right)-\frac{\sqrt{b-c}}{\sqrt{2}c}\operatorname{atan}\left(\frac{\sqrt{2}X}{\sqrt{b-c}}\right),\end{aligned}\tag{A.39}$$

with $c=\sqrt{b^2-4a}$.

$$\begin{aligned}&\int_0^{\frac{\pi}{2}} dx\frac{1+a\sin^2(x)}{1+b\sin^2(x)+c\sin^4(x)}\\&\qquad=\frac{\pi}{\sqrt{(2)}\tilde{a}}\left\{j\frac{[a(\tilde{a}-c)+2c]}{\tilde{b}}+\frac{[a(\tilde{a}+c)-2c]}{\tilde{c}}\right\},\end{aligned}\tag{A.40}$$

where $\tilde{a}=\sqrt{b^2-4c}$, $\tilde{b}=\sqrt{b(A-b)+c(A-b+2)}$, $\tilde{c}=\sqrt{b(A+b)+c(A+b-2)}$ and $j=\sqrt{-1}$.

$$\int_0^X dx\frac{x}{\sqrt{1+a^2x^4}}=\frac{1}{2a}\operatorname{asinh}\left(aX^2\right),\tag{A.41}$$

$$\int_0^X \frac{1}{a^2x^2+1}dx=\frac{\operatorname{atan}(aX)}{a},\tag{A.42}$$

$$\int_0^X \frac{x^2\left(3a^2x^2-1\right)}{\left(a^2x^2+1\right)^3}dx=\frac{\operatorname{atan}(aX)}{a^3}-\frac{X\left(2a^2X^2+1\right)}{a^2\left(a^2X^2+1\right)^2}.\tag{A.43}$$

A.5 Approximation of NSNI regimes

In this section, an approximation is derived on when nonlinear ASE noise interactions are negligible with respect to transceiver noise signal interactions. The derivation was peer-reviewed and published in [P15]. For the derivation, we start by deriving the optimum launch power P_{opt} in Eq. (5.8), which is

$$P_{\text{opt}}=\frac{\xi_{\text{ASE}}P_{\text{ASE}}\phi}{6\xi_{\text{TRX}}\kappa_{\text{R}}},\tag{A.44}$$

with

$$\phi = 2\cosh\left[\frac{1}{3}\operatorname{acosh}(\Gamma)\right] - 1, \tag{A.45}$$

$$\Gamma = \frac{18n^{3+2\varepsilon}\kappa_{\mathrm{R}}^2}{\xi_{\mathrm{ASE}}^3 P_{\mathrm{ASE}}^2 \tilde{\eta}_1} - 1. \tag{A.46}$$

For typical parameter values in optical communication, we have that $\Gamma \gg 1$. Furthermore, the relations $\cosh(x) \approx \exp(x)/2$ for $x \gg 0$ and $\operatorname{acosh}(\Gamma) \approx \ln(2\Gamma)$ for $\Gamma \gg 1$. Therefore, we can do the following approximation $\phi \approx (2\Gamma)^{\frac{1}{3}} - 1$. Using the approximation yields the approximate optimum launch power as

$$P_{\mathrm{opt}} \approx \left(\frac{P_{\mathrm{ASE}}}{6N^{\varepsilon}\kappa_{\mathrm{R}}\eta}\right)^{\frac{1}{3}} - \frac{\xi_1 P_{\mathrm{ASE}}}{6N^{1+\varepsilon}\kappa_{\mathrm{R}}}. \tag{A.47}$$

The ASE noise signal beating is negligible with respect to the transceiver noise signal beating if

$$\xi_{\mathrm{ASE,DBP}} P_{\mathrm{ASE}} \ll n^{1+\varepsilon}\kappa_{\mathrm{R}} P_{\mathrm{opt}}. \tag{A.48}$$

Inserting (A.47) in (A.48) and rearranging yields

$$(7\xi_{\mathrm{ASE,DBP}})^3 P_{\mathrm{ASE}}^2 \tilde{\eta}_1 \ll 36n^{3+2\varepsilon}\kappa_{\mathrm{R}}^2. \tag{A.49}$$

When $\varepsilon \approx 0$, $\xi_{\mathrm{ASE,DBP}}$ can be approximated as $\xi_{\mathrm{ASE,DBP}} \approx n(n+1)/2$, and assuming that $N \gg 1$, yielding $\xi_{\mathrm{ASE,DBP}} \approx n^2/2$. Under these conditions, (A.49) can be expressed as

$$\left(\frac{4}{27P_{\mathrm{ASE}}^2\tilde{\eta}_1 n^3}\right)^{\frac{1}{3}} \gg \frac{7}{6(3\kappa_{\mathrm{R}})^{\frac{2}{3}}}, \tag{A.50}$$

where we recognise the left-hand side of (A.50) as Eq. (2.38) with $\kappa = 0$, i.e., the SNR when EDC only is applied in the absence of any transceiver limitation, which we denote by $\max_P(\mathrm{SNR}_{\mathrm{EDC,ideal}})$. Furthermore, assuming that the transceiver noise is equally split between transmitter and receiver, $\mathrm{SNR}_{\mathrm{TR}} = 2/\kappa_{\mathrm{R}}$, and (A.50) becomes

$$\max_P(\mathrm{SNR}_{\mathrm{EDC,ideal}}) \gg \frac{7}{6^{\frac{5}{3}}}\mathrm{SNR}_{\mathrm{TRX}}^{\frac{2}{3}}. \tag{A.51}$$

Converting (A.51) to a decibel scale yields

$$\max_{P}(\mathrm{SNR}_{\mathrm{EDC,ideal}})[\mathrm{dB}] \gg \frac{2}{3}\mathrm{SNR}_{\mathrm{TRX}}[\mathrm{dB}] - 4.5\mathrm{dB}. \tag{A.52}$$

Acronyms

ADC analog-to-digital converters 61

AIR achievable information rate 38

ASE amplified-spontaneous emission 6

AWGN additive white Gaussian noise 25

COI channel of interest 69

DAC digital-to-analog converters 61

DBP digital back-propgatation 59

DPC digital pre-compensation 59

DSP digital signal processing 25

ECL external cavity lasers 82

EDC electronic dispersion compensation 150

EDFA Erbium-doped fibre amplifier 54

EGN enhanced Gaussian Noise 71

FWM four-wave mixing 46

GFF gain-flattening filter 78

GN Gaussian Noise 5

GPU graphical processing unit 24

GVD group velocity dispersion 43

I inphase component 37

INT interfering channel 69

ISRS inter-channel stimulated Raman scattering 10

MI mutual information 38

NLC nonlinearity compensation 6

NLI nonlinear interference 18

NSNI nonlinear signal noise interactions 6

NLSE nonlinear Schrödinger equation 40

NZDSF non-zero dispersion-shifted fibre 140

OFDM orthogonal frequency devision multiplexing 68

PMD polarisation mode dispersion 52

PSD power spectral density 37

Q quadrature component 37

QAM quadrature amplitude modulation 29

RIN relative intensity noise 56

ROADM reconfigurable optical add-drop multiplexer 69

RP1 regular first-order perturbation 62

RWA routing-wavelength allocations 69

SMF standard single mode fibre 14

SNR signal-to-noise ratio 14

SPM self-phase modulation 46

SS-ASE spectrally-shaped amplified spontaneous emission 82

SSFM split-step Fourier method 16

TDFA Thulium-doped fibre amplifier 55

TRX transceiver 24

WDM wavelength devision multiplexing 14

XPM cross-phase modulation 46

List of Symbols

f_c	carrier frequency	s^{-1}
$\hat{Q}(t)$	complex valued, electric field	$\mathrm{V\,m}^{-1}$
$\frac{\partial}{\partial x} f(x)$	partial derivative	
$Q(t)$	complex envelope of electric field	$\mathrm{V\,m}^{-1}$
$\mathrm{MI}(X,Y)$	mutual information	bit
$p_{X,Y}(x,y)$	joint probability distribution	
$p_X(x)$	marginal probability distribution	
C	capacity	
SNR	signal-to-noise ratio	
$p_{\mathrm{MB}}(x)$	Maxwell-Boltzmann probability distribution	
λ_{MB}	shaping parameter	
z	distance	m
α	loss coefficient	$\mathrm{Np\,m}^{-1}$
j	imaginary unit	
β_2	GVD parameter	$\mathrm{s}^2\,\mathrm{m}^{-1}$
β_3	GVD parameter slope	$\mathrm{s}^3\,\mathrm{m}^{-1}$
T	reference time	s
γ	nonlinearity coefficient	$\mathrm{W}^{-1}\,\mathrm{m}^{-1}$
T_{R}	Raman time constant	s
λ_{ref}	reference wavelength	m
v_g	group velocity	$\mathrm{m\,s}^{-1}$
n_2	nonlinear refractive index	$\mathrm{m}^2\,\mathrm{W}^{-1}$
A_{eff}	effective core area	m^2
f	frequency	s^{-1}
$\mathscr{F}$	Fourier transform	
$*$	convolution	
$P(z,f)$	power	
ω	angular frequency	s^{-1}
L	fibre span length	m

D	chromatic dispersion parameter	$\mathrm{s\,m^{-2}}$
c	speed of light in vacuum	$\mathrm{m\,s^{-1}}$
R_b	symbol rate	$\mathrm{s^{-1}}$
T_s	symbol duration	s
$H(f)$	transfer function	
L_eff	effective length	m
Q_0	initial field envelope	$\mathrm{V\,m^{-1}}$
ϕ_0	initial optical phase	
$\phi(L,T)$	optical phase,symbol=	
Q_1	field envelope of channel 1	$\mathrm{V\,m^{-1}}$
P_1	power of channel 1	W
Q_k	field envelope of channel k	$\mathrm{V\,m^{-1}}$
P_k	power of channel k	W
f_k	centre frequency of channel k	$\mathrm{s^{-1}}$
$\rho(z,f)$	relative power profile	
P_tot	total optical power	
C_r	Raman gain slope	$\mathrm{s\,W^{-1}\,m^{-1}}$
$G_\mathrm{Tx}(f)$	signal power spectral density	W s
Q_x	field envelope of x polarisation	$\mathrm{V\,m^{-1}}$
Q_y	field envelope of y polarisation	$\mathrm{V\,m^{-1}}$
Δz	step size	m
$\hat{L}$	linear operator	
$\hat{N}$	nonlinear operator	
P_ASE	ASE noise power	W
n_sp	spontaneous emission factor	
h	Planck constant	$\mathrm{m\,kg^2\,s^{-1}}$
B_ref	reference bandwidth	$\mathrm{s^{-1}}$
G	gain	
F_n	noise figure	
P_p1	power of first pump	W
λ_p1	wavelength of first pump	m
f_p1	frequency of first pump	$\mathrm{s^{-1}}$
P_p1	loss coefficient at λ_{p1}	m
P_p2	power of second pump	W
λ_p2	wavelength of second pump	m
f_p2	frequency of second pump	$\mathrm{s^{-1}}$
P_p2	loss coefficient at λ_{p2}	m
X	number of spans used for DPC	

n	number of tranmission spans	
κ	transceiver noise coefficient	
$\mathrm{SNR}_{\mathrm{TRX}}$	transceiver (back-to-back) SNR	
P_{NLI}	nonlinear interference power	W
η_n	nonlinear interference coefficient after n spans	W^{-2}
$\mathrm{SNR}_{\mathrm{opt}}$	SNR at opimum launch power	
P_{opt}	opimum launch power	
$Q^{(0)}(f)$	zeroth order solution of field envelope	$\mathrm{V\,m}^{-1}$
$Q^{(1)}(f)$	first order solution of field envelope	$\mathrm{V\,m}^{-1}$
$\hat{\Gamma}(f)$	complex propagation constant	m^{-1}
ξ_n	circular, complex Gaussian distributed symbol	
$\delta(f)$	Dirac delta function	
B_{ch}	Channel bandwidth	s^{-1}
$G(f)$	PSD of NLI	W s
B_{tot}	total optical bandwidth	s^{-1}
ε	coherence factor	
N_{ch}	number of WDM channels	
$\mathrm{Har}(x)$	harmonic number	
$\eta_{\mathrm{SPM}}(f_i)$	SPM contribution of NLI	W^{-2}
$\eta_{\mathrm{XPM}}^{(k)}(f_i)$	NLI contribution of ch. k on ch. i	W^{-2}
$\eta_{\mathrm{XPM}}(f_i)$	total XPM contribution on ch. i	W^{-2}
$\eta_{\mathrm{XPM,\,GN}}^{(k)}(f_i)$	Gaussian XPM contribution	W^{-2}
$\eta_{\mathrm{XPM,\,corr.}}^{(k)}(f_i)$	mod. format correction for XPM terms	W^{-2}
Φ	excess kurtosis	
ξ_{ASE}	ASE signal noise beating accumulation factor	
$\tilde{\eta}_i$	NLI coefficient for compensated spectrum	W^{-2}
$l_{\mathrm{GFF}}(f)$	loss of gain flattening filter	
$G_{\mathrm{EDFA}}(f)$	EDFA gain	
$\alpha_{\mathrm{eff},i}$	effective attenuation coefficent of channel i	$\mathrm{Np\,m}^{-1}$
$\phi(f_1, f_2, f, z)$	phase mismatch factor	
$G_k(z, f)$	signal PSD of span k	W s
$P_{\mathrm{tot},k}$	total optical power of span k	W
L_k	length of span k	m
S_i	set of interering channels	
$\mathrm{SNR}_{\mathrm{NLI}}$	nonlinear SNR	
B_k	bandwidth of ch. k	s^{-1}
$g_i(f)$	pulse shape of ch. i	
ϕ_i	phase mismatch factor	$\mathrm{s}^2\,\mathrm{m}^{-1}$

$\phi_{i,k}$	phase mismatch factor	$\mathrm{s\,m^{-1}}$
T_i	tilt factor of ch. i	$\mathrm{m^{-2}}$
$\tilde{T}_i$	tilt factor of ch. i	$\mathrm{m^{-2}}$
$P_i^{(1)}(z)$	first order power profile	
$\Delta\rho()$	ISRS power transfer	
$\mu(f_1, f_2, f)$	link function	m
C_n	normalisation coefficient	$\mathrm{s^{-1}}$
$\eta_{\mathrm{corr},1}^{(k)}$	mod. format. correction for 1 span	$\mathrm{W^{-2}}$
$\eta_{\mathrm{corr},a}^{(k)}$	asymptotic mod. format corr.	$\mathrm{W^{-2}}$
$\tilde{n}$	reduced span number	
Δ_n	discrete derivative	
ϕ	phase mismatch factor	$\mathrm{s^2}$
$\tilde{\phi}(f_1, f_2, f, z)$	phase mismatch factor	
$\bar{\alpha}$	loss coefficient	$\mathrm{Np\,m^{-1}}$
A	loss coefficient	$\mathrm{Np\,m^{-1}}$
σ_{T}^2	transmitter noise	W
σ_{R}^2	receiver noise	W
$\mathrm{SNR_{TX}}$	transmitter SNR	
$\mathrm{SNR_{RX}}$	receiver SNR	
κ_{R}	TX-RX noise ratio	
$P_{\text{TRX-sig}}$	TRX signal beating noise power	W
ξ_{TRX}	TRX signal noise beating accumulation factor	
OSNR	optical SNR	
x_{opt}	optimum NLC split ratio	
$\xi_{\mathrm{TRX,opt}}$	optimum TRX signal noise beating acc. factor	
$\xi_{\mathrm{TRX,DBP}}$	DBP TRX signal noise beating acc. factor	
$\xi_{\mathrm{ASE,opt}}$	optimum ASE signal noise beating acc. factor	
$\xi_{\mathrm{ASE,DBP}}$	DBP ASE signal noise beating acc. factor	
$\Delta n_{\max}$	gain in reach	
$\mathrm{SNR_{EDC,ideal}}$	optimum SNR without TRX noise	

Bibliography

[1] J.-X. Cai, Y. Cai, C. Davidson, A. Lucero, H. Zhang, D. Foursa, O. Sinkin, W. Patterson, A. Pilipetskii, G. Mohs, and N. Bergano, "20 Tbit/s capacity transmission over 6,860 km," in *Optical Fiber Communications Conference (OFC)*, Optical Society of America, 2011. PD.PB4.

[2] J.-X. Cai, H. Zhang, H. G. Batshon, M. Mazurczyk, O. V. Sinkin, Y. Sun, A. Pilipetskii, and D. G. Foursa, "Transmission over 9,100 km with a capacity of 49.3 Tb/s using variable spectral efficiency 16 QAM based coded modulation," in *Optical Fiber Communications Conference (OFC)*, Optical Society of America, 2014. PD.Th5B.4.

[3] J.-X. Cai, Y. Sun, H. G. Batshon, M. Mazurczyk, H. Zhang, D. G. Foursa, and A. N. Pilipetskii, "54 Tb/s transmission over 9,150 km with optimized hybrid Raman-EDFA amplification and coded modulation," in *European Conference on Optical Communication (ECOC)*, Optical Society of America, sep 2014. PD3.3.

[4] J.-X. Cai, H. G. Batshon, M. V. Mazurczyk, O. V. Sinkin, D. Wang, M. Paskov, W. Patterson, C. R. Davidson, P. Corbett, G. Wolter, T. Hammon, M. Bolshtyansky, D. Foursa, and A. Pilipetskii, "70.4 Tb/s capacity over 7,600 km in C+L band using coded modulation with hybrid constellation shaping and nonlinearity compensation," in *Optical Fiber Communications Conference (OFC)*, Optical Society of America, sep 2017. PD.Th5B.2.

[5] J.-X. Cai, H. G. Batshon, M. V. Mazurczyk, O. V. Sinkin, D. Wang, M. Paskov, W. W. Patterson, C. R. Davidson, P. C. Corbett, G. M. Wolter, T. E. Hammon, M. A. Bolshtyansky, D. G. Foursa, and A. N. Pilipetskii, "70.46 Tb/s over 7,600 km and 71.65 Tb/s over 6,970 km transmission in C+L band using coded modulation with hybrid constellation shaping and nonlinearity compensation," *Journal of Lightwave Technology*, vol. 36, pp. 114–121, jan 2018. PD.Th5B.2.

[6] A. Ghazisaeidi, I. F. d. Jauregui Ruiz, R. Rios-Muller, L. Schmalen, P. Tran, P. Brindel, A. C. Meseguer, Q. Hu, F. Buchali, G. Charlet, and J. Renaudier, "65Tb/s transoceanic transmission using probabilistically-shaped DM-64QAM," in *European Conference on Optical Communication (ECOC)*, vol. 36, pp. 114–121, Optical Society of America, Sep. 2016. PD.Th.3.C.4.

[7] M. Ionescu, D. Lavery, A. Edwards, E. Sillekens, L. Galdino, D. Semrau, R. Killey, W. Pelouch, S. Barnes, and P. Bayvel, "74.38 Tb/s transmission over 6300 km single mode fiber with hybrid EDFA/Raman amplifiers," in *Optical Fiber Communications Conference (OFC)*, vol. 36, pp. 114–121, Optical Society of America, Sep. 2019. PD.Th.3.C.4.

[8] M. Mazurczyk, D. G. Foursa, H. G. Batshon, H. Zhang, C. R. Davidson, J.-X. Cai, A. Pilipetskii, G. Mohs, and N. S. Bergano, "30 Tb/s transmission over 6,630 km using 16QAM signals at 6.1 bits/s/Hz spectral efficiency," in *European Conference on Optical Communication (ECOC)*, vol. 36, pp. 114–121, Optical Society of America, Sep. 2012. PD.Th.3.C.2.

[9] M. Salsi, P. Tran, S. Bigo, P. Brindel, L. Schmalen, J. Renaudier, H. Mardoyan, R. Rios-Muller, G. Charlet, and A. Ghazisaeidi, "38.75 Tb/s transmission experiment over transoceanic distance," in *European Conference on Optical Communication (ECOC)*, vol. 36, pp. 114–121, Optical Society of America, Sep. 2013. PD.3.E.2.

[10] M. C. F. and A. N. Pinto, "Attenuation fitting functions," *Microwave and Optical Technology Letters*, vol. 51, no. 10, pp. 2294–2296, 2009.

[11] G. Agrawal, *Nonlinear Fiber Optics*. Elsevier Science Publishing Co Inc, 2012.

[12] R. H. Stolen and E. P. Ippen, "Raman gain in glass optical waveguides," *App. Phys. Lett.*, vol. 22, no. 6, pp. 276–278, 1973.

[13] FiberLabs, "Amp-52xx-sb s-band amplifier," 2019.

[14] J. W. Dawson, L. S. Kiani, P. H. Pax, G. S. Allen, D. R. Drachenberg, V. V. Khitrov, D. Chen, N. Schenkel, M. J. Cook, R. P. Crist, and M. J. Messerly, "E-band Nd3+ amplifier based on wavelength selection in an all-solid microstructured fiber," in *Optics Express*, vol. 25, pp. 6524–6538, March 2017.

[15] E. M. Dianov, "Bismuth-doped optical fibers: a challenging active medium for near-IR lasers and optical amplifiers," *Light: Science & Applications*, vol. 1, 2012.

[16] S. Firstov, S. Alyshev, M. Melkumov, K. Riumkin, A. Shubin, and E. Dianov, "Bismuth-doped optical fibers and fiber lasers for a spectral region of 1600–1800 nm," *Optics Lett.*, vol. 39, no. 24, pp. 6927–6930, 2014.

[17] I. Roberts, J. M. Kahn, J. Harley, and D. W. Boertjes, "Channel power optimization of WDM systems following Gaussian noise nonlinearity model in presence of stimulated Raman scattering," *J. Lightw. Technol.*, vol. 35, pp. 5237–5249, Dec. 2017.

[18] M. Cantono, D. Pilori, A. Ferrari, and V. Curri, "Introducing the generalized GN-model for nonlinear interference generation including space/frequency variations of loss/gain," *ArXiv e-prints*, 2017.

[19] D. J. Ives, A. Lord, P. Wright, and S. J. Savory, "Quantifying the impact of non-linear impairments on blocking load in elastic optical networks," in *Optical Fiber Communication Conference*, p. W2A.55, Optical Society of America, 2014.

[20] P. Poggiolini, "The GN model of non-linear propagation in uncompensated coherent optical systems," *J. Lightw. Technol.*, vol. 30, pp. 3857–3879, Dec. 2012.

[21] P. Johannisson and E. Agrell, "Modeling of nonlinear signal distortion in fiber-optic networks," *J. Lightw. Technol.*, vol. 32, pp. 3942–3950, Dec 2014.

[22] P. Poggiolini, G. Bosco, A. Carena, V. Curri, Y. Jiang, and F. Forghieri, "A simple and effective closed-form GN model correction formula accounting for signal non-Gaussian distribution," *J. Lightw. Technol.*, vol. 33, pp. 459–473, Jan. 2015.

[23] C. V. Networking, "Index: Forecast and methodology, 2016–2021," tech. rep., June 6, 2017.

[24] E. Ip, "Nonlinear compensation using backpropagation for polarization-multiplexed transmission," *Journal of Lightwave Technology*, vol. 28, pp. 939–951, mar 2010.

[25] T. Tanimura, M. Nölle, J. K. Fischer, and C. Schubert, "Analytical results on back propagation nonlinear compensator with coherent detection," *Optics Express*, vol. 20, p. 28779, dec 2012.

[26] C. E. Shannon, "A mathematical theory of communication," *Bell System Technical Journal*, vol. 27, no. 3, pp. 379–423, 1948.

[27] A. Splett, C. Kurtzke, and K. Petermann, "Ultimate transmission capacity of amplified optical fiber communication systems taking into account fiber nonlinearities," in *1993 The European Conference on Optical Communication (ECOC)*, 1993.

[28] H. Louchet, A. Hodzic, and K. Petermann, "Analytical model for the performance evaluation of DWDM transmission systems," *IEEE Photonics Technology Letters*, vol. 15, pp. 1219–1221, Sept 2003.

[29] J. Tang, "The channel capacity of a multispan DWDM system employing dispersive nonlinear optical fibers and an ideal coherent optical receiver," *J. Lightw. Technol.*, vol. 20, p. 1095, Jul. 2002.

[30] P. Johannisson and M. Karlsson, "Perturbation analysis of nonlinear propagation in a strongly dispersive optical communication system," *J. Lightw. Technol.*, vol. 31, pp. 1273–1282, Apr. 2013.

[31] A. Mecozzi and R.-J. Essiambre, "Nonlinear Shannon limit in pseudolinear coherent systems," *J. Lightw. Technol.*, vol. 30, pp. 2011–2024, Jun. 2012.

[32] M. Secondini and E. Forestieri, "Analytical fiber-optic channel model in the presence of cross-phase modulation," *IEEE Photon. Technol. Lett.*, vol. 24, pp. 2016–2019, Nov. 2012.

[33] R. Dar, M. Feder, A. Mecozzi, and M. Shtaif, "Properties of nonlinear noise in long, dispersion-uncompensated fiber links," *Opt. Express*, vol. 21, p. 25685, Oct. 2013.

[34] P. Serena and A. Bononi, "A time-domain extended Gaussian noise model," *J. Lightw. Technol.*, vol. 33, pp. 1459–1472, Apr. 2015.

[35] A. R. Chraplyvy, "Limitations on lightwave communications imposed by optical-fiber nonlinearities," *Journal of Lightwave Technology*, vol. 8, pp. 1548–1557, Oct 1990.

[36] A. R. Chraplyvy, "Optical power limits in multi-channel wavelength-division-multiplexed systems due to stimulated Raman scattering," *Electronics Letters*, vol. 20, pp. 58–59, January 1984.

[37] H. D. Kim and C.-H. Lee, "Capacities of WDM transmission systems and networks limited by stimulated Raman scattering," *IEEE Photonics Technology Letters*, vol. 13, pp. 379–381, April 2001.

[38] A. R. Sarkar, M. N. Islam, and M. G. Mostafa, "Performance of an optical wideband WDM system considering stimulated Raman scattering, fiber attenuation and chromatic dispersion," *Optical and Quantum Electronics*, vol. 39, no. 8, pp. 659–675, 2007.

[39] D. Rafique and A. D. Ellis, "Impact of signal-ase four-wave mixing on the effectiveness of digital back-propagation in 112 gb/s pm-qpsk systems," *Opt. Express*, vol. 19, pp. 3449–3454, Feb 2011.

[40] G. Gao, X. Chen, and W. Shieh, "Influence of PMD on fiber nonlinearity compensation using digital back propagation," *Optics Express*, vol. 20, p. 14406, j doi = 10.1364/oe.20.014406, publisher = The Optical Society, 2012.

[41] A. D. Ellis, M. E. McCarthy, M. A. Z. Al-Khateeb, and S. Sygletos, "Capacity limits of systems employing multiple optical phase conjugators," *Opt. Express*, vol. 23, pp. 20381–20393, aug 2015.

[42] M. A. Z. Al-Khateeb, M. McCarthy, C. Sánchez, and A. Ellis, "Effect of second order signal–noise interactions in nonlinearity compensated optical transmission systems," *Opt. Lett.*, vol. 41, pp. 1849–1852, Apr 2016.

[43] D. Lavery, D. Ives, G. Liga, A. Alvarado, S. J. Savory, and P. Bayvel, "The benefit of split nonlinearity compensation for single-channel optical fiber communications," *IEEE Photonics Technology Letters*, vol. 28, pp. 1803–1806, sep 2016.

[44] R. Maher, D. Lavery, D. Millar, A. Alvarado, K. Parsons, R. Killey, and P. Bayvel, "Reach enhancement of 100% for a DP-64QAM super-channel using MC-DBP," in *Optical Fiber Communication Conference*, OSA, 2015.

[45] E. Temprana, E. Myslivets, L. Liu, V. Ataie, A. Wiberg, B. Kuo, N. Alic, and S. Radic, "Two-fold transmission reach enhancement enabled by transmitter-side digital backpropagation and optical frequency comb-derived information carriers," *Optics Express*, vol. 23, p. 20774, jul 2015.

[46] E. Temprana, E. Myslivets, V. Ataie, B. P. P. Kuo, N. Alic, V. Vusirikala, V. Dangui, and S. Radic, "Demonstration of coherent transmission reach tripling by frequency-referenced nonlinearity pre-compensation in EDFA-only SMF link," in *ECOC 2016; 42nd European Conference on Optical Communication*, pp. 1–3, Sept 2016.

[47] E. Ip, A. P. T. Lau, D. J. F. Barros, and J. M. Kahn, "Coherent detection in optical fiber systems," *Opt. Express*, vol. 16, pp. 753–791, Jan 2008.

[48] S. J. Savory, "Digital filters for coherent optical receivers," *Opt. Express*, vol. 16, pp. 804–817, Jan 2008.

[49] P. Poggiolini, A. Carena, V. Curri, G. Bosco, and F. Forghieri, "Analytical modeling of nonlinear propagation in uncompensated optical transmission links," *IEEE Photon. Technol. Lett.*, vol. 23, pp. 742–744, Jun. 2011.

[50] F. R. Kschischang and S. Pasupathy, "Optimal nonuniform signaling for gaussian channels," *IEEE Transactions on Information Theory*, vol. 39, pp. 913–929, May 1993.

[51] R. Dar, M. Feder, A. Mecozzi, and M. Shtaif, "Accumulation of nonlinear interference noise in fiber-optic systems," *Opt. Express*, vol. 22, pp. 14199–14211, Jun. 2014.

[52] R. Dar, M. Shtaif, and M. Feder, "New bounds on the capacity of the nonlinear fiber-optic channel," *Opt. Lett.*, vol. 39, pp. 398–401, Jan 2014.

[53] M. Secondini and E. Forestieri, "Scope and limitations of the nonlinear shannon limit," *Journal of Lightwave Technology*, vol. 35, no. 4, pp. 893–902, 2017.

[54] K. J. Blow and D. Wood, "Theoretical description of transient stimulated raman scattering in optical fibers," *IEEE Journal of Quantum Electronics*, vol. 25, pp. 2665–2673, Dec 1989.

[55] F. Forghieri, R. W. Tkach, and A. R. Chraplyvy, "Effect of modulation statistics on Raman crosstalk in WDM systems," *IEEE Photon. Technol. Lett.*, vol. 7, pp. 101–103, Jan. 1995.

[56] K.-P. Ho, "Statistical properties of stimulated Raman crosstalk in WDM systems," *J. Lightw. Technol.*, vol. 18, pp. 915–921, Jul. 2000.

[57] M. I. Hayee and A. E. Willner, "Pre- and post-compensation of dispersion and nonlinearities in 10-Gb/s WDM systems," *IEEE Photonics Technology Letters*, vol. 9, pp. 1271–1273, Sep. 1997.

[58] R. J. Essiambre, G. Kramer, P. J. Winzer, G. J. Foschini, and B. Goebel, "Capacity limits of optical fiber networks," *Journal of Lightwave Technology*, vol. 28, pp. 662–701, Feb 2010.

[59] P. Mitra and J. Stark, "Nonlinear limits to the information capacity of optical fibre communications," *Nature*, vol. 411, pp. 1027–1030, 2001.

[60] S. Walker, "Rapid modeling and estimation of total spectral loss in optical fibers," *Journal of Lightwave Technology*, vol. 4, pp. 1125–1131, Aug 1986.

[61] S. R. Nagel, J. B. MacChesney, and K. L. Walker, "An overview of the modified chemical vapor deposition (MCVD) process and performance," *IEEE Transactions on Microwave Theory and Techniques*, vol. 30, pp. 305–322, Apr 1982.

[62] A. J. Antos and D. K. Smith, "Design and characterization of dispersion compensating fiber based on the lp01 mode," *Journal of Lightwave Technology*, vol. 12, pp. 1739–1745, Oct 1994.

[63] Y. Akasaka, R. Sugizaki, A. Umeda, I. Oshima, and K. Kokura, "Dispersion-compensating fiber with w-shaped index profile," in *Optical Fiber Communications Conference*, p. ThH3, Optical Society of America, 1995.

[64] J. Mora, A. Diez, M. V. Andres, P. Y. Fonjallaz, and M. Popov, "Tunable dispersion compensator based on a fiber bragg grating written in a tapered fiber," *IEEE Photonics Technology Letters*, vol. 16, pp. 2631–2633, Dec 2004.

[65] K. Iwashita and N. Takachio, "Chromatic dispersion compensation in coherent optical communications," *Journal of Lightwave Technology*, vol. 8, pp. 367–375, Mar 1990.

[66] D. J. Richardson, "Filling the light pipe," *Science*, vol. 330, no. 6002, pp. 327–328, 2010.

[67] A. D. Ellis, J. Zhao, and D. Cotter, "Approaching the non-linear Shannon limit," *Journal of Lightwave Technology*, vol. 28, pp. 423–433, Feb 2010.

[68] J. P. Gordon, "Theory of the soliton self-frequency shift," *Opt. Lett.*, vol. 11, pp. 662–664, Oct 1986.

[69] F. M. Mitschke and L. F. Mollenauer, "Discovery of the soliton self-frequency shift," *Opt. Lett.*, vol. 11, pp. 659–661, Oct 1986.

[70] G. Bosco, A. Carena, V. Curri, R. Gaudino, P. Poggiolini, and S. Benedetto, "Suppression of spurious tones induced by the split-step method in fiber systems simulation," *IEEE Photonics Technology Letters*, vol. 12, pp. 489–491, May 2000.

[71] F. Shimizu, "Frequency broadening in liquids by a short light pulse," *Physical Review Letters*, vol. 19, pp. 1097–1100, Nov. 1967.

[72] R. R. Alfano and S. L. Shapiro, "Observation of self-phase modulation and small-scale filaments in crystals and glasses," *Physical Review Letters*, vol. 24, pp. 592–594, Mar. 1970.

[73] M. N. Islam, J. R. Simpson, H. T. Shang, L. F. Mollenauer, and R. H. Stolen, "Cross-phase modulation in optical fibers," *Opt. Lett.*, vol. 12, pp. 625–627, Aug 1987.

[74] M. Shtaif, "Analytical description of cross-phase modulation in dispersive optical fibers," *Opt. Lett.*, vol. 23, pp. 1191–1193, Aug 1998.

[75] S. Tariq and J. C. Palais, "A computer model of non-dispersion-limited stimulated Raman scattering in optical fiber multiple-channel communications," *J. Lightw. Technol.*, vol. 11, pp. 1914–1924, Dec. 1993.

[76] Q. Lin and G. P. Agrawal, "Vector theory of stimulated raman scattering and its application to fiber-based raman amplifiers," *J. Opt. Soc. Am. B*, vol. 20, pp. 1616–1631, Aug 2003.

[77] M. Zirngibl, "Analytical model of Raman gain effects in massive wavelength division multiplexed transmission systems," *Electron. Lett.*, vol. 34, pp. 789–790, Apr. 1998.

[78] D. N. Christodoulides and R. B. Jander, "Evolution of stimulated Raman crosstalk in wavelength division multiplexed systems," *IEEE Photonics Technology Letters*, vol. 8, pp. 1722–1724, Dec 1996.

[79] C. Antonelli, M. Shtaif, and A. Mecozzi, "Modeling of nonlinear propagation in space-division multiplexed fiber-optic transmission," *Journal of Lightwave Technology*, vol. 34, no. 1, pp. 36–54, 2016.

[80] C. R. M. P. K. A. Wai and H. H. Chen, "Stability of solitons in randomly varying birefringent fibers," *Optics Lett.*, vol. 16, no. 16, pp. 1231–1233, 1991.

[81] C. R. Menyuk and B. S. Marks, "Interaction of polarization mode dispersion and nonlinearity in optical fiber transmission systems," *Journal of Lightwave Technology*, vol. 24, pp. 2806–2826, July 2006.

[82] P. Serena, C. Lasagni, S. Musetti, and A. Bononi, "On numerical simulations of ultra-wideband long-haul optical communication systems," *Journal of Lightwave Technology*, vol. 38, no. 5, pp. 1019–1031, 2020.

[83] H. Ono, M. Yamada, T. Kanamori, S. Sudo, and Y. Ohishi, "1.58-um band gain-flattened erbium-doped fiber amplifiers for wdm transmission systems," *J. Lightwave Technol.*, vol. 17, p. 490, Mar 1999.

[84] J. X. Cai, Y. Sun, H. Zhang, H. G. Batshon, M. V. Mazurczyk, O. V. Sinkin, D. G. Foursa, and A. Pilipetskii, "49.3 Tb/s transmission over 9100 km using C+L EDFA and 54 Tb/s transmission over 9150 km using hybrid-Raman EDFA," *J. Lightw. Technol.*, vol. 33, pp. 2724–2734, Jul. 2015.

[85] B. Cole and M. L. Dennis, "S-band amplification in a thulium doped silicate fiber," in *OFC 2001. Optical Fiber Communication Conference and Exhibit. Technical Digest Postconference Edition (IEEE Cat. 01CH37171)*, vol. 2, pp. TuQ3–TuQ3, March 2001.

[86] K. Minoguchi, S. Okamoto, F. Hamaoka, A. Matsushita, M. Nakamura, E. Yamazaki, and Y. Kisaka, "Experiments on stimulated Raman scattering in S- and L-bands 16-QAM signals for ultra-wideband coherent WDM systems," in *Optical Fiber Communication Conference*, p. Th1C.4, Optical Society of America, 2018.

[87] F. Hamaoka, K. Minoguchi, T. Sasai, A. Matsushita, M. Nakamura, S. Okamoto, E. Yamazaki, and Y. Kisaka, "150.3-tb/s ultra-wideband (s, c, and l bands) single-mode fibre transmission over 40-km using >519Gb/s/a PDM-128QAM signals," in *2018 European Conference on Optical Communication (ECOC)*, pp. 1–3, Sep. 2018.

[88] S. V. Firstov, K. Riumkin, S. Alyshev, M. M., and E. M. Dianov, "Broadband optical amplifier for a wavelength region of 1515 - 1775 nm," in *Optical Fiber Communication Conference*, p. W2A.22, Optical Society of America, 2017.

[89] C. R. S. Fludger, V. Handerek, and R. J. Mears, "Pump to signal RIN transfer in Raman fiber amplifiers," *J. Lightwave Technol.*, vol. 19, p. 1140, Aug 2001.

[90] V. E. Perlin and H. G. Winful, "Optimal design of flat-gain wide-band fiber Raman amplifiers," *J. Lightw. Technol.*, vol. 20, pp. 250–254, Feb 2002.

[91] M. Tan, P. Rosa, S. T. Le, M. A. Iqbal, I. D. Phillips, and P. Harper, "Transmission performance improvement using random DFB laser based raman amplification and bidirectional second-order pumping," *Opt. Express*, vol. 24, pp. 2215–2221, Feb 2016.

[92] A. D. Ellis, M. Tan, A. Iqbal, M. A. Z. Al-Khateeb, V. Gordienko, G. Saavedra, S. Fabbri, M. F. C. Stephens, M. E. McCarthy, A. Perentos, I. D. Phillips, D. Lavery, G. Liga, R. Maher, P. Harper, N. Doran, S. K. Turitsyn, S. Sygletos, and P. Bayvel, "4 Tb/s transmission reach enhancement using 10×400 Gb/s super-channels and polarization insensitive dual band optical phase conjugation," *J. Lightwave Technol.*, vol. 34, pp. 1717–1723, Apr 2016.

[93] J. A.-C. nón, "Quasi-lossless transmission using second-order Raman amplification and fibre bragg gratings," *Opt. Express*, vol. 12, pp. 4372–4377, Sep 2004.

[94] J. Bromage, "Raman amplification for fiber communications systems," *J. Lightw. Technol.*, vol. 22, p. 79, Jan. 2004.

[95] W. S. Pelouch, "Raman amplification: An enabling technology for long-haul coherent transmission systems," *Journal of Lightwave Technology*, vol. 34, pp. 6–19, Jan 2016.

[96] A. Ghazisaeidi, I. F. de Jauregui Ruiz, L. Schmalen, P. Tran, C. Simonneau, E. Awwad, B. Uscumlic, P. Brindel, and G. Charlet, "Submarine transmission systems using digital nonlinear compensation and adaptive rate forward error correction," *J. Lightw. Technol.*, vol. 34, pp. 1886–1895, Apr. 2016.

[97] A. Sano, T. Kobayashi, S. Yamanaka, A. Matsuura, H. Kawakami, Y. Miyamoto, K. Ishihara, and H. Masuda, "102.3-Tb/s C- and extended L-band all-Raman transmission over 240 km using PDM-64QAM single carrier FDM with digital pilot tone," in *OFC/NFOEC*, pp. 1–3, March 2012.

[98] M. Ionescu, D. Lavery, A. Edwards, E. Sillekens, L. Galdino, D. Semrau, R. I. Killey, W. Pelouch, S. Barnes, and P. Bayvel, "74.38 Tb/s transmission over 6300 km single mode fiber with hybrid EDFA/Raman amplifiers," in *2019 Optical Fiber Communications Conference and Exhibition (OFC)*, pp. 1–3, March 2019.

[99] E. Ip and J. M. Kahn, "Compensation of dispersion and nonlinear impairments using digital backpropagation," *Journal of Lightwave Technology*, vol. 26, pp. 3416–3425, oct 2008.

[100] D. S. Millar, S. Makovejs, C. Behrens, S. Hellerbrand, R. I. Killey, P. Bayvel, and S. J. Savory, "Mitigation of fiber nonlinearity using a digital coherent receiver," *IEEE Journal of Selected Topics in Quantum Electronics*, vol. 16, pp. 1217–1226, sep 2010.

[101] N. V. Irukulapati, H. Wymeersch, P. Johannisson, and E. Agrell, "Stochastic digital backpropagation," *IEEE Transactions on Communications*, vol. 62, pp. 3956–3968, nov 2014.

[102] N. Fontaine, S. Randel, P. Winzer, A. Sureka, S. Chandrasekhar, R. Delbue, R. Ryf, P. Pupalaikis, and X. Liu, "Fiber nonlinearity compensation by digital backpropagation of an entire 1.2-Tb/s superchannel using a full-field spectrally-sliced receiver," in *39th European Conference and Exhibition on Optical Communication (ECOC 2013)*, Institution of Engineering and Technology, 2013.

[103] R. Dar and P. J. Winzer, "On the limits of digital back-propagation in fully loaded WDM systems," *IEEE Photonics Technology Letters*, vol. 28, pp. 1253–1256, jun 2016.

[104] E. Temprana, E. Myslivets, B. P.-P. Kuo, N. Alic, and S. Radic, "Transmitter-side digital back propagation with optical injection-locked frequency referenced carriers," *Journal of Lightwave Technology*, vol. 34, pp. 3544–3549, aug 2016.

[105] D. Lavery, R. Maher, G. Liga, D. Semrau, L. Galdino, and P. Bayvel, "On the bandwidth dependent performance of split transmitter-receiver optical fiber nonlinearity compensation," *Optics Express*, vol. 25, p. 4554, feb 2017.

[106] P. Poggiolini, G. Bosco, A. Carena, V. Curri, Y. Jiang, and F. Forghieri, "The gn-model of fiber non-linear propagation and its applications," *Journal of Lightwave Technology*, vol. 32, pp. 694–721, Feb 2014.

[107] R. Dar, M. Feder, A. Mecozzi, and M. Shtaif, "Inter-channel nonlinear interference noise in WDM systems: Modeling and mitigation," *J. Lightw. Technol.*, vol. 33, pp. 1044–1053, Mar. 2015.

[108] A. Vannucci, P. Serena, and A. Bononi, "The rp method: a new tool for the iterative solution of the nonlinear schrodinger equation," *J. of Lightw. Technol.*, vol. 20, pp. 1102–1112, Jul. 2002.

[109] G. Bosco, P. Poggiolini, A. Carena, V. Curri, and F. Forghieri, "Analytical results on channel capacity in uncompensated optical links with coherent detection," *Opt. Express*, vol. 19, pp. B440–B451, Dec. 2011.

[110] T. Hasegawa, Y. Yamamoto, and M. Hirano, "Optimal fiber design for large capacity long haul coherent transmission," *Opt. Express*, vol. 25, pp. 706–712, Jan. 2017.

[111] V. Anagnostopoulos, C. T. Politi, C. Matrakidis, and A. Stavdas, "Physical layer impairment aware wavelength routing algorithms based on analytically calculated constraints," *Optics Communications*, vol. 270, pp. 247–254, Feb. 2007.

[112] R. Dar, "Analytical and semi-analytical models for nonlinear transmission," in *ECOC 2016; 42nd European Conference on Optical Communication*, pp. 1–3, Sep. 2016.

[113] A. Carena, V. Curri, G. Bosco, P. Poggiolini, and F. Forghieri, "Modeling of the impact of nonlinear propagation effects in uncompensated optical coherent transmission links," *J. Lightw. Technol.*, vol. 30, pp. 1524–1539, May 2012.

[114] P. Poggiolini and Y. Jiang, "Recent advances in the modeling of the impact of nonlinear fiber propagation effects on uncompensated coherent transmission systems," *J. Lightw. Technol.*, vol. 35, pp. 458–480, Feb. 2017.

[115] C. Kurtzke, "Kapazitätsgrenzen digitaler optischer Übertragungssysteme," *PhD thesis*, 1995.

[116] P. Poggiolini, G. Bosco, A. Carena, V. Curri, Y. Jiang, and F. Forghieri, "A detailed analytical derivation of the GN model of non-linear interference in coherent optical transmission systems," *ArXiv e-prints*, 2012.

[117] A. Carena, G. Bosco, V. Curri, Y. Jiang, P. Poggiolini, and F. Forghieri, "EGN model of non-linear fiber propagation," *Opt. Express*, vol. 22, p. 16335, Jun. 2014.

[118] S. J. Savory, "Approximations for the nonlinear self-channel interference of channels with rectangular spectra," *IEEE Photon. Technol. Lett.*, vol. 25, pp. 961–964, May 2013.

[119] X. Chen and W. Shieh, "Closed-form expressions for nonlinear transmission performance of densely spaced coherent optical OFDM systems," *Opt. Express*, vol. 18, pp. 19039–19054, Aug. 2010.

[120] Q. Zhuge, B. Châtelain, and D. V. Plant, "Comparison of intra-channel nonlinearity tolerance between reduced-guard-interval CO-OFDM systems and Nyquist single carrier systems," in *OFC/NFOEC*, pp. 1–3, Mar. 2012.

[121] F. Zhang, Q. Zhuge, and D. V. Plant, "Fast analytical evaluation of fiber nonlinear noise variance in mesh optical networks," *IEEE/OSA Journal of Optical Communications and Networking*, vol. 9, pp. C88–C97, April 2017.

[122] W. Shieh, H. Bao, and Y. Tang, "Coherent optical OFDM: theory and design," *Opt. Express*, vol. 16, pp. 841–859, Jan. 2008.

[123] A. Bononi and P. S. N. Rossi, "Performance dependence on channel baudrate of coherent single-carrier WDM systems," in *39th European Conference and Exhibition on Optical Communication (ECOC 2013)*, pp. 1–3, Sept 2013.

[124] L. B. Du and A. J. Lowery, "Optimizing the subcarrier granularity of coherent optical communications systems," *Opt. Express*, vol. 19, pp. 8079–8084, Apr. 2011.

[125] P. Poggiolini, A. Nespola, Y. Jiang, G. Bosco, A. Carena, L. Bertignono, S. M. Bilal, S. Abrate, and F. Forghieri, "Analytical and experimental results on system maximum reach increase through symbol rate optimization," *J. Lightw. Technol.*, vol. 34, pp. 1872–1885, Apr. 2016.

[126] E. Agrell, A. Alvarado, G. Durisi, and M. Karlsson, "Capacity of a nonlinear optical channel with finite memory," *J. Lightwave Technol.*, vol. 32, pp. 2862–2876, Aug 2014.

[127] B. Chen, C. Okonkwo, D. Lavery, and A. Alvarado, "Geometrically-shaped 64-point constellations via achievable information rates," in *2018 20th International Conference on Transparent Optical Networks (ICTON)*, pp. 1–4, July 2018.

[128] Y. Jiang and P. Poggiolini, "The EGN model of nonlinear propagation in coherent optical transmission systems and its applications," *PhD Thesis, Politecnico di Torino*, 2014.

[129] A. Nespola, S. Straullu, A. Carena, G. Bosco, R. Cigliutti, V. Curri, P. Poggiolini, M. Hirano, Y. Yamamoto, T. Sasaki, J. Bauwelinck, K. Verheyen, and F. Forghieri, "GN-Model validation over seven fiber types in uncompensated PM-16QAM Nyquist-WDM links," *IEEE Photon. Technol. Lett.*, vol. 26, pp. 206–209, Jan. 2014.

[130] J. X. Cai, H. G. Batshon, H. Zhang, M. Mazurczyk, O. V. Sinkin, D. G. Foursa, and A. N. Pilipetskii, "Transmission performance of coded modulation formats in a wide range of spectral efficiencies," in *OFC 2014*, pp. 1–3, Mar. 2014.

[131] A. Nespola, M. Huchard, G. Bosco, A. Carena, Y. Jiang, P. Poggiolini, and F. Forghieri, "Experimental validation of the EGN-model in uncompensated optical links," in *Optical Fiber Communication Conference (OFC)*, p. Th4D.2, Optical Society of America, 2015.

[132] L. Galdino, G. Liga, G. Saavedra, D. Ives, R. Maher, A. Alvarado, S. Savory, R. Killey, and P. Bayvel, "Experimental demonstration of modulation-dependent nonlinear interference in optical fibre communication," in *ECOC 2016; 42nd European Conference on Optical Communication*, pp. 1–3, Sept 2016.

[133] V. E. Zakharov and L. A. Ostrovsky, "Modulation instability: The beginning," *Physica D: Nonlinear Phenomena*, vol. 238, pp. 540–548, 3 2009.

[134] J. P. Gordon and L. F. Mollenauer, "Phase noise in photonic communications systems using linear amplifiers," *Opt. Lett.*, vol. 15, pp. 1351–1353, Dec 1990.

[135] P. Serena, "Nonlinear signal noise interaction in optical links with nonlinear equalization," *Journal of Lightwave Technology*, vol. 34, pp. 1476–1483, March 2016.

[136] *Nonlinear fiber optics*. Elsevier.

[137] S. Norimatsu and T. Yamamoto, "Waveform distortion due to stimulated Raman scattering in wide-band WDM transmission systems," *J. Lightw. Technol.*, vol. 19, pp. 159–171, Feb. 2001.

[138] M. Tan, P. Rosa, S. T. Le, V. V. Dvoyrin, M. A. Iqbal, S. Sugavanam, S. K. Turitsyn, and P. Harper, "RIN mitigation and transmission performance enhancement with forward broadband pump," *IEEE Photonics Technology Letters*, vol. 30, pp. 254–257, Feb 2018.

[139] M. Cantono, J. L. Auge, and V. Curri, "Modelling the impact of SRS on NLI generation in commercial equipment: an experimental investigation," in *Optical Fiber Communication Conference*, p. M1D.2, Optical Society of America, 2018.

[140] I. Roberts, J. M. Kahn, J. Harley, and D. Boertjes, "Corrections to "Channel power optimization of WDM systems following Gaussian noise nonlinearity model in presence of stimulated Raman scattering"," *Journal of Lightwave Technology*, vol. 36, pp. 2309–2309, June 2018.

[141] D. J. Ives, P. Bayvel, and S. J. Savory, "Adapting transmitter power and modulation format to improve optical network performance utilizing the gaussian noise model of nonlinear impairments," *J. Lightw. Technol.*, vol. 32, pp. 4087–4096, Nov 2014.

[142] D. J. Ives, A. Alvarado, and S. J. Savory, "Adaptive transceivers in nonlinear flexible networks," in *ECOC 2016; 42nd European Conference on Optical Communication*, pp. 1–3, Sept 2016.

[143] T. Fehenberger, A. Alvarado, G. Böcherer, and N. Hanik, "On probabilistic shaping of quadrature amplitude modulation for the nonlinear fiber channel," *J. Lightw. Technol.*, vol. 34, pp. 5063–5073, Nov 2016.

[144] D. Marquardt, "An algorithm for least-squares estimation of nonlinear parameters," *SIAM Journal Applied Mathematics*, vol. 11, pp. 431–441, 1963.

[145] R. Maher, A. Alvarado, D. Lavery, and P. Bayvel, "Increasing the information rates of optical communications via coded modulation: a study of transceiver performance," *Scientific Reports*, 2016.

[146] X. Chen, S. Chandrasekhar, S. Randel, W. Gu, and P. Winzer, "Experimental quantification of implementation penalties from limited ADC resolution for Nyquist shaped higher-order QAM," in *Optical Fiber Communication Conference*, p. W4A.3, Optical Society of America, 2016.

[147] G. Liga, C. B. Czegledi, T. Xu, E. Agrell, R. I. Killey, and P. Bayvel, "Ultra-wideband nonlinearity compensation performance in the presence of PMD," in *ECOC 2016; 42nd European Conference on Optical Communication*, pp. 1–3, Sep. 2016.

[148] R. J. Essiambre and P. J. Winzer, "Fibre nonlinearities in electronically predistorted transmission," in *2005 31st European Conference on Optical Communication, ECOC 2005*, vol. 2, pp. 191–192 vol.2, Sept 2005.

[149] Z. Tao, L. Dou, W. Yan, L. Li, T. Hoshida, and J. C. Rasmussen, "Multiplier-free intrachannel nonlinearity compensating algorithm operating at symbol rate," *J. Lightwave Technol.*, vol. 29, pp. 2570–2576, Sep 2011.

[150] A. Ghazisaeidi and R. J. Essiambre, "Calculation of coefficients of perturbative nonlinear pre-compensation for Nyquist pulses," in *2014 The European Conference on Optical Communication (ECOC)*, pp. 1–3, Sept 2014.

[151] M. Secondini, D. Marsella, and E. Forestieri, "Enhanced split-step Fourier method for digital backpropagation," in *2014 The European Conference on Optical Communication (ECOC)*, pp. 1–3, Sept 2014.

[152] C. B. Czegledi, G. Liga, D. Lavery, M. Karlsson, E. Agrell, S. J. Savory, and P. Bayvel, "Digital backpropagation accounting for polarization-mode dispersion," *Optics Express*, vol. 25, p. 1903, jan 2017.

[153] X. Liang and S. Kumar, "Multi-stage perturbation theory for compensating intra-channel nonlinear impairments in fiber-optic links," *Opt. Express*, vol. 22, pp. 29733–29745, Dec 2014.